Problems of physical movement in soil genesis: Application of meteoric Beryllium-10 as a component of multi-tracer analysis

A DISSERTATION

SUBMITTED TO THE FACULTY OF

UNIVERSITY OF MINNESOTA

BY

Nicolas Adam Jelinski

IN PARTIAL FULFILLMENT OF THE REQUIREMENTS

FOR THE DEGREE OF

DOCTOR OF PHILOSOPHY

Kyungsoo Yoo

December, 2014

Acknowledgements

This work would not have been possible without the support and guidance of my advisor, Kyungsoo Yoo, and my committee, Ed Nater, Brandy Toner and Jeff Coulter. Throughout my graduate program, they supported and encouraged new perspectives and ideas, and always pushed me to pursue them.

A special thank you to a significant group of collaborators for assisting in my work to two field sites (Cyrus, MN and Abisko, SE): Sharon Papiernik, Tom Schumacher, David Lobb, Sheng Li and Jonatan Klaminder for seeing the promise in the application of a novel tracer at well-established study sites and assisting with sample and site selection. Thanks also to Dave Swanson for providing the opportunity to conduct fieldwork at a third site (Midas Lake, AK) and the many discussions we had about cryoturbation and permafrost-affected soils in the field. My thanks goes to Jane Willenbring for opening her laboratory and introducing me to the internal workings of the fabulous isotope Beryllium-10.

For great discussions about soils and many other things: Beth Fisher, Charlotte Riggs, and Salli Dymond. For help in the laboratory and field: Marta Roser, Patrick Connerton, Kalei Holt, and Fleur Nicklen.

This work was supported by many sources: A University of Minnesota Graduate School Fellowship and Grant-In-Aid, a National Science Foundation Graduate Research Fellowship, and a Seed Grant from Purdue University's PRIME Lab.

Lastly, a special thanks to all of my family and friends for their unwavering support as I have pursued this goal and many others.

Dedication

Dedicated to JB and Maeda…thank you!

Abstract

The physical movement of soil materials plays a globally important role in soil genesis, but knowledge of the rates and patterns of these processes and their relationship to soil morphology has lagged behind an understanding of soil chemical processes. In this study, I analyze two separate problems related to physical movement in soil genesis - that of *eroded phase* soils and *cryoturbated* soils. In each of these cases, I circumscribe these genetic problems and subsequently apply meteoric Beryllium-10 (^{10}Be) as a critical component of multi-tracer suites at specific study sites.

Eroded phase soils: I first re-evaluate the general conceptual framework of soil production and connect it to problems of eroded soil genesis in agricultural landscapes underlain by unconsolidated parent materials (Chapter 1). Then, I explore factors related to the identification and description of eroded phase soils by analyzing the distribution of eroded phase soils in the SSURGO database for the Conterminous U.S (Chapter 2). Lastly, at a field site near the town of Cyrus in west-central Minnesota, I utilize meteoric ^{10}Be to derive rates and depths of total post-settlement erosion by developing numerical conversion models (Chapter 3).

Cryoturbated soils: I describe the distribution of cryoturbated soils and gelic materials across a landscape in the central Brooks Range Alaska, a study that prompted the application of ^{10}Be in a multi-tracer suite to understand physical movement processes in Arctic patterened ground (Chapter 4). Through the application of this tracer suite, I constrain rates of material movement in a non-sorted circle (NSC) near Abisko, Sweden. In addition to estimating movement rates throughout the NSC with other tracers, meteoric

^{10}Be allows - for the first time - an estimate of the surficial residence time of cryoturbated parcels now in the subsurface (Chapter 5).

The results of this work show that the application of meteoric ^{10}Be and other isotopic, elemental and morphological tracers in studies of soil genesis holds significant promise for elucidating long-standing problems related to the physical movement of soil materials.

Table of Contents

List of Tables

List of Figures

CHAPTER 1

A generalized concept of soil production for agricultural lands in the Anthropocene

1.1. Introduction

The development of concepts of soil loss tolerance in the 1970s-1980s was accompanied by the realization that little was known about rates of soil formation, in contrast to the extensive model development and large body of data that had been collected on soil erosion (McCormack et al., 1979). At the time, several types of "soil formation" processes were considered in the development of soil loss tolerance recommendations, most prominently those related to A horizon formation, particularly in the United States (Hall et al., 1982, Bui et al., 2011). The rate of soil formation from consolidated igneous, metamorphic, or sedimentary bedrock was, until the mid-late 1980s, an anecdotal enigma to which little data was attached. In the past 3 decades, several conceptual and technical breakthroughs have allowed the quantification of rates of soil formation from consolidated rock materials or saprolite, most notably first with the work of E.B. Alexander, who utilized catchment-scale weathering fluxes in outflow waters to estimate rates of rock weathering and soil formation (Alexander 1985, Alexander, 1988). Approximately 10 years later, the cosmogenic radionuclides (CRN) ^{10}Be and ^{26}Al were first applied to quantitatively estimate rates of soil formation from saprolite (termed "soil production") on soil-mantled hillslopes (Heimsath et al., 1997, Heimsath et al., 2000). Since these landmark studies, an explosion in the quantification of CRN-derived soil production rates has taken place (Dixon et al., 2012, Heimsath et al., 2012, Larsen et al., 2014).

This newly acquired abundance of soil production rates has led to direct comparisons of CRN-derived rates of soil production to the sustainability of agricultural

soils as balanced against measures of soil erosion (Montgomery, 2007, Verheijen et al., 2009, Bui et al., 2011) and, thus, the central thesis that rates of soil production derived from CRN studies can be used to understand the sustainability of agricultural soils at large scales across diverse agricultural systems. This central thesis is based on implicit but critical assumptions: 1) that the terminology surrounding soil production is well defined and generalizable; 2) that a generalizable theoretical framework for the process and context of soil production across earth systems has been developed; and 3) that the surficial geology is not relevant in generalizing the concept of soil production and soil production function to agricultural landscapes. These three assumptions have been only anecdotally explored (Montgomery, 2007, Verheijen et al., 2009, Bui et al., 2011, Heimsath, 2014). In the following analysis we explore each of these assumptions more carefully, attempt to define them more explicitly, and consider the contextual meaning of soil production in the face of agricultural management and the consequences that this holds for the long-term sustainability of soils.

1.2. Assumption 1: A well-defined terminology?

Although the term "*soil production*" seems generally innocuous, accessible, and generalizable, its use can lead to confusion when applied outside of the strictly defined system states and framework in which empirical CRN soil production rates are derived.

1.2.1 The three-tiered, three-boundary regolith-bedrock framework

We adopt the regolith-bedrock framework of Yoo and Mudd (2008) to place other

definitions in context (Fig 1.1). In this idealized 3-tiered framework (3TF), regolith-bedrock systems are represented as a three-tiered, three-boundary system, where regolith is defined as "the blanket of unconsolidated rock-material of whatever origin, residual or transported, that mantles solid rock" (Chesworth, 2008).

These represent a Physically Disturbed Zone (PDZ), a physically undisturbed but Chemically Altered Zone (CAZ), and unweathered bedrock (Yoo and Mudd, 2008, Fig 1.1). For simplification and generalization purposes here, the CAZ is also taken to include any mantle of originally transported but subsequently non-physically disturbed regolith (i.e. thick deposits of alluvium, colluvium, eolian or glacial materials extending beyond the PDZ). In reality, regolith-bedrock systems may exhibit highly variable depths of each tier, and tiers may be missing in other cases, but the formal definition of the three-tiered system is flexible enough to accommodate the totality of all regolith-bedrock systems.

In its strictest definition, the PDZ/CAZ boundary (η) is characterized by the deepest depth of physical disturbance of regolith materials, disturbances which are caused by both biotic and abiotic mechanisms. Yoo and Mudd (2008) provide a definition for the PDZ where:

$$\vec{q}_{PDZ} \neq 0 \qquad (1)$$

where q_{PDZ} is the volume of materials crossing a unit contour line per unit time [$L^2\ T^{-1}$], in this case referring only to gross movements, which is equivalent to a more general statement:

$$\vec{r}_{m,PDZ} \neq 0 \qquad (2)$$

where $r_{m,PDZ}$ is the displacement magnitude [L] (relative to the baseline datum so excluding tectonics) of an individual particle or aggregate m.

Using this same framework, the CAZ is defined physically and chemically:

$$\vec{r}_{m,CAZ} = 0 \qquad (3a)$$

and

$$\delta_{w,CAZ} \neq 0 \qquad (3b)$$

where $r_{m,CAZ}$ is the displacement magnitude [L] (relative to the baseline datum so excluding tectonics) of an individual particle or aggregate m, and $\delta_{w,CAZ}$ is the mass loss of element w (the boundary is placed at the deepest depth where no detectable mass loss of any element can be detected, Yoo and Mudd, 2008)

1.2.2 Geomorphic and pedologic uses of the term "soil" within the three-tiered framework

In the literature on soil production, the definition of "soil" is most closely associated with the "colluvial soil mantle" or PDZ from the 3TF (Yoo and Mudd, 2008). This can cause confusion across general readership as this definition differs widely (in many systems) from the genetic-agronomic definition of soil, which is generally defined as the portion of the regolith that: "shows evidence of horizonation and is capable of supporting rooted plants in natural environments. The depths of these substrates considered soil are often limited to 2m in terrestrial systems for the practical purposes of survey and mapping" (Johnson and Johnson, 2010, including definitions from Soil Survey Staff, 1993 and Soil

Survey Staff, 1999).

With respect to genetic horizons, the geomorphic definition of "soil" (the colluvial soil mantle or PDZ) typically includes at least A horizons and may or may not include portions of genetic Bt or Bw horizons (Yoo and Mudd, 2008). Other examples include spodosols in Upper Michigan and the Czech Republic where the PDZ is generated by return cycles of tree throw and include the Bhs or Bsm horizons (Samonil et al., 2013). In old, well-mixed tropical soils with large termite populations, the PDZ may extend well into C horizons or past traditional definitions of soil depth (Morras et al., 2009). The examples above have included only biotic mechanisms of soil disturbance, but is also true for abiotic mechanisms, particularly those due to differential frost heave and cryotrubation in permafrost-affected soils, where mixing includes material from O, A and Bg horizons (Jelinski, 2013).

1.2.3 Formal definition of the term "soil production" with reference to 3TF

Thus if we adopt an idealized 3TF such as that at Tennessee Valley, CA, where the soil production rates were first empirically quantified with CRN (Heimsath et al., 1997, Yoo and Mudd, 2008), then "soil" in the term "soil production" is equivalent to the PDZ and includes the well-mixed (bioturbated) genetic A horizon overlying saprolite. "Soil" thickness in this case is equivalent to PDZ thickness, and the soil production function being quantified is the downward migration (with reference to the arbitrary datum z=0) of the lower PDZ boundary (η):

$$p = -\frac{\partial \eta}{\partial t} \qquad (4)$$

where p is the soil production rate [L T^{-1}], (downward migration of the boundary results in a positive soil production rate) with the additional constraints of steady-state PDZ thickness:

$$\frac{\partial h_{PDZ}}{\partial t} = 0 \text{, so that } \frac{\partial \eta}{\partial t} = \frac{\partial \zeta}{\partial t} \quad (5)$$

therefore, most frameworks imply that the migration of the PDZ is uni-directionally downward:

$$\frac{\partial \eta}{\partial t} < 0 \quad (6)$$

which, under steady-state assumptions, also implies no upbuilding processes (relative to the arbitrary datum, so excluding tectonics) such as volumetric expansion or the deposition of eolian, colluvial, alluvial or glacially derived materials:

$$\frac{\partial \zeta}{\partial t} < 0 \quad (7)$$

The final constraint is that the CAZ is composed of non-transported (saprolitic/residual) material.

This specialized and highly technical definition is inadvertently but unfortunately attached to the seemingly accessible term “soil production”, and thus is the cause of confusion when extrapolated without regard to the underlying conceptual framework. Unresolved questions arise from this realization, such as: what is the meaning of soil production for regolith-bedrock systems characterized by deep unconsolidated sediment

materials?

1.3. Assumption 2: A generalizable conceptual framework?

As described above, the process of *soil production*, in its central concept, is ultimately defined by the physical incorporation of regolith materials into the colluvial soil layer or Physically Disturbed Zone (Fig 1.1). Thus, the PDZ-CAZ boundary definition (η) becomes a critical factor in the generalization of the central concept of soil production. Here, we develop a generalizable mechanism describing how the PDZ-CAZ boundary is set by the combination of material strengths and disturbance stresses that independently vary with depth. This mechanistic view highlights the notion that consideration of surficial geology is critical in constraining the applicability of CRN-based soil production rates and soil production function in agricultural landscapes.

1.3.1 Initial assumptions

According to mechanical concepts of material strength, applied stresses, and failure theories (Holtz, 2010), we provide four initial assumptions about the regolith system in order to proceed with the definition:

1. The regolith fabric (solid material component) is idealized as a highly complex but rigid, unified body composed of planes of weakness between individual particles or aggregates. These particles are tortuously connected, and variously cemented or non-cemented.

2. The regolith fabric is idealized as failing in a brittle manner across planes of weakness

between individual particles or aggregates.

3. Only linear displacement is considered. Angular displacement (rotation) is not considered as disturbance.

4. For transported regolith materials, the initial movement in transport is not considered a disturbance. Disturbances considered must be cyclical or have at least a theoretically definable return frequency (below).

Under these assumptions, we define failure of the soil fabric along a plane of weakness (and hence linear displacement) as occurring when one of the three major applied stress components (σ_C – normal compressive stress, σ_T – normal tensile stress, or τ – shear stress) from a disturbance mechanism exceeds the material strength (here defined as the ultimate compressive, tensile or shear test strength, due to assumption of brittle failure mechanism), so that failure and linear displacement occurs whenever:

$$\tau_{\max} > S_{USS} \quad (8a)$$

OR

$$\sigma_{C,\max} > S_{UCS} \quad (8b)$$

OR

$$\sigma_{T,\max} > S_{UTS} \quad (8c)$$

where τ_{max} is the maximum applied shear stress, $\sigma_{C,max}$ is the maximum applied normal compressive stress, $\sigma_{T,max}$ is the maximum applied normal tensile stress, and S_{USS}, S_{UCS}, and S_{UTS} are the ultimate shear, compressive and tensile strengths, equivalent to failure stresses for brittle failure mechanisms (Holtz, 2010). Maximum applied stresses are necessary here because only a single event which satisfies eqns 8a-8c is necessary for failure under the assumptions above, and other metrics (such as average applied stresses over a certain time period) would not adequately capture failure-producing stresses in

some cases.

1.3.2 Definition 1 - Disturbance-threshold definition

In the following formalized definition of the PDZ, we focus on *soil disturbance mechanisms*, without implying any specific form or direction of material movement (i.e. -turbation, lateral flux), actors (bio-turbation), or material type (pedo-).

We begin with the case of a 1-dimensional profile discretized into I depth increments [L] of length Δz, which we observe over J discretized time increments [T]. At each time increment, we assign a binary score to a matrix U:

$$U_{ij} = \begin{cases} 1 \text{ if } \tau_{\max} > S_{USS} \text{ OR } \sigma_{C,\max} > S_{UCS} \text{ OR } \sigma_{T,\max} > S_{UTS} \\ 0 \text{ if } \tau_{\max} < S_{USS} \text{ OR } \sigma_{C,\max} < S_{UCS} \text{ OR } \sigma_{T,\max} < S_{UTS} \end{cases} \quad (9)$$

for depth increment i and time increment j. We then populate a binary matrix:

$$\begin{pmatrix} U_{11} & \cdots & U_{1j} \\ \vdots & \ddots & \vdots \\ U_{i1} & \cdots & U_{ij} \end{pmatrix}$$

and define a disturbance frequency-depth distribution:

$$f_i = \frac{\sum_{j=1}^{J} U_{ij}}{J} \quad (10)$$

where f_i is the disturbance frequency [T^{-1}] for depth increment i.

Then, in the strict interpretation, the PDZ/CAZ boundary η is defined:

$$\eta = \min_z, f_i \text{ where } f_i > 0 \quad (11a)$$

where η, then represents the lowest depth ($\min_z$) where f_i meets the defined criteria. In

practice, however, it may be necessary to define a low frequency threshold (α), instead of 0 for f_i, below which disturbance can be considered negligible compared to overlying layers so that the PDZ/CAZ boundary (η) is the lowest depth where:

$$\eta = \min_z, f_i \text{ where } f_i > \alpha \qquad (11b)$$

where $\min_z$, f_i represents the lowest depth ($\min_z$) where f_i meets the defined criteria. Over a 2-dimensional area of study, then, we have a population of 1-dimensional profiles (χ_{tot}), the average of which is the average PDZ depth (by definition 1) across 2-dimensional space.

$$\bar{\eta} = \frac{\sum_{\chi=1}^{\chi_{tot}} \eta_\chi}{\chi_{tot}} \qquad (12)$$

where η_χ is η evaluated at profile χ and χ_{tot} is the total number of profiles evaluated in 2-dimensional space.

The process of disturbance of the regolith to incorporate it into the PDZ (the central concept of soil production) is therefore the result of three factors: 1) the depth profile of the material strength of the soil body (or individual components – aggregate, etc.), 2) the depth profile of applied stress (by disturbance mechanisms) and 3) the timescale of observation. Because this binary definition depends only on frequency, however, high-magnitude low-frequency disturbance events are not separated from low-magnitude, low-frequency events and may be missed if α is set too high. Nonetheless, these types of events (i.e. tree throw) can be critical for determining PDZ depth, soil genesis and sediment production (Walther et al., 2009). Thus, we develop a second operational definition of the PDZ, where we consider net particle movement, below.

1.3.3 Definition 2 – Mixing-threshold definition

We present a second definition of the PDZ/CAZ boundary (η) based on displacement or mixing velocities, starting from the net linear displacement of idealized individual particles, to particle populations and depth-distributions of mixing velocities.

By our initial assumptions and definitions above, a disturbance must be associated with a linear displacement. For an individual particle or aggregate m, the net displacement magnitude in any timestep is:

$$r_{m,ij} = \sqrt{(x_f - x_i)^2 + (y_f - y_i)^2 + (z_f - z_i)^2} \qquad (13)$$

where $r_{m,j}$ is the displacement magnitude [L] (representing net displacement because time is discretized) for particle m originating in depth increment i and time increment j and x_f, x_i are the final and initial positions of particle m (same for y and z dimensions).

We make an additional assumption that soil properties are perfectly homogenous in a direction parallel to the ground surface (i.e. the soil properties are controlled by horizon). In that case, mixing in properties is accomplished only by the component of the displacement vector that is normal to the ground surface r_n, which in the simplest case of a flat surface is r_z.

For a population of individual particles or aggregates (M_{tot}) originating in depth increment i, a mean displacement magnitude normal to horizon planes over time period j, termed the "average mixing magnitude" [L] can be determined where:

$$\overline{r}_{n,ij} = \frac{\sum_{m=1}^{M_{tot}} r_n}{M_{tot}} \qquad (14)$$

where $r_{n,ij}$ is the average mixing magnitude [L] for the population of particles originating in depth increment i over time increment j.

Then, the average mixing velocity [L T^{-1}] for particles originating in depth increment i over the total time of observation J can be determined:

$$\bar{v}_{n,i} = \frac{\sum_{j=1}^{J} r_{n,ij}}{J} \quad (15)$$

Plotting $v_{n,i}$ on a 1-dimensional depth distribution as with f_i, above, will separate high-magnitude/low-frequency events from low-magnitude/low frequency events, and α can be set with more confidence as low frequency events with low mixing displacements will be negligible.

1.3.4 Predictions and system types

Matshushi et al. (2008) developed a conceptual framework for the description and prediction of temporal-mechanical relationships for central-concept three-tiered systems based on the propagation of a weathering front and subsequent shear strength reduction. In the Matsushi model, the initial strength value of the surficial material is constant and is considered the failure (termed "erosion") threshold, which is a set value.

Here, we extend this and define at any depth (z) or depth increment (i) the threshold for mechanical failure as a function of both the applied stress profile of the disturbance mechanisms at work in the soil (Fig 1.2). This can be used to understand predictive models of PDZ thickness. Based on the definitions above, we can define a theoretical

maximum applied stress envelope over time period t=0 to t=J (below shown just for the case of shear, but valid for normal stresses (compressive and tensile) as well which are characteristic of the disturbance mechanism at work over the period of observation:

$$\tau_{\max,i} = \max_j, \tau_{\max,ij} \qquad (16)$$

where $\max_j$, $\tau_{max,ij}$ is the maximum value of τ_{max} across all time periods j at depth increment i.

Next, we define theoretical material strength curves, which, for a predictive model can be represented by the material strength curve at time J:

$$S_{USS,i} = S_{USS,iJ} \qquad (17)$$

The lower depth of the PDZ (η) defined as in section 3.2, above, is determined by the intersection of the material strength profile and the maximum applied stress profile for each type of stress/strength relationship (i.e. tensile/shear/compressive - Fig 1.2). This mechanism, regardless of material context, determines the depth of the colluvial soil mantle or PDZ. The result of this conceptual framework is that material strength and disturbance mechanisms interact in all systems, regardless of material context, to determine the depth of the colluvial soil mantle or PDZ.

For the purposes of predictive models, we define systems as *strength*-limited and *mechanism*-limited. The maximum applied stress and materials strength (for the case of shear) at the lower PDZ boundary (η) are $\tau_{max,\eta}$ and $S_{USS,\eta}$, respectively. In a *strength*-limited system the downward migration of the PDZ boundary (z=η) is limited by the strength of the material below (z=η+Δz) and requires strength reduction to proceed (Fig 1.2C):

$$\tau_{\max,\eta} < S_{USS,\eta+\Delta z} \text{ and } \tau_{\max,\eta+\Delta z} < S_{USS,\eta+\Delta z} \quad (18)$$

In contrast, in a *mechanism*-limited system, the downward migration of the PDZ boundary is limited only by the depth that the applied stress reaches (Fig 1.2A) even though the stress at the depth of η may exceed the material strength at the depth of η+Δz:

$$\tau_{\max,\eta} > S_{USS,\eta+\Delta z} \text{ and } \tau_{\max,\eta+\Delta z} < S_{USS,\eta+\Delta z} \quad (19)$$

Based on our definitions - in contrast to "central-concept" strength-limited systems - in mechanism-limited systems PDZ depth is constrained solely by depth of stress propagation by disturbance mechanisms at work in the soil. In this case, PDZ thickness will keep pace with high magnitude surficial removals as long as the disturbance mechanism continues to propagate downward with the same maximum applied stress envelope. Alternatively, the PDZ can be thickened with a change in mechanism that extends deeper into the regolith. The major advantage of this generalized approach is that we are not restricted to evolving, steady-state hillslopes, but can apply this definition across soil and regolith-bedrock systems.

1.4. Assumption 3: Materials context of agricultural lands

Placing CRN-derived soil production rates into context and utilizing them to determine the sustainability of soils has resulted in a number of statements where authors clearly recognize the limitations in the systems that these may apply to:

"In evaluating the long-term effects of agricultural soil erosion,

there is a fundamental difference between floodplain agriculture, where annual flooding refreshes mineral soils, and upland agriculture, where soils gradually thin and lose productivity as soil erosion outpaces soil production."

- Montgomery (2007, p. 13268-13269)

This statement implicitly ignores upland agriculture in deep unconsolidated materials, where the entrainment of material from below as the PDZ migrates downward also refreshes soils.

"[The]…assumption is that "natural" soil erosion rates equate to soil formation rates. This implies a meta-stable situation where all soils are in dynamic equilibrium in terms of quantity (mass/volume). Clearly, young soils or any soil that could accumulate under current conditions, and thereby improve the soil regulation, production, and habitat functions, would not be in dynamic equilibrium. Nevertheless, soil formation rates form the best basis upon which to establish tolerable rates of soil erosion."

- Verheijen et al. (2009, p. 26)

"In-theory, at equilibrium or when a steady-state balance exists in a landscape, the net rate of erosion is equal to the rate of soil

> formation…although steady-state assumptions do not hold over all landscape settings, deviations have limited influence on results…"
>
> - Bui et al. (2011, p. 140)

This statement mixes the imprecise term "soil formation" with central concepts of soil production, and discusses only whether or not steady-state assumptions hold – which does not address materials context issues.

Nonetheless, in all of the above studies, CRN-derived soil production estimates were applied to a wide range of agricultural lands balanced against soil erosion to understand the sustainability of agricultural soils. The intense interest in applying CRN-derived soil production rates to agricultural soils, begs the question of understanding the materials context of agricultural lands in particular. Below, we evaluate the materials context of agricultural lands at three spatial scales: regional, continental and global.

1.4.1 Regional context example: Depth to bedrock of cultivated lands in Minnesota and Iowa

Together, Minnesota and Iowa contain > 13% of cultivated area in the continental U.S. (USDA-NASS, 2013) and, except for the Paleozoic Plateau or Driftless Area (Prior, 1991) of southeastern Minnesota and northwestern Iowa, are broadly characterized by landscapes on deep deposits of transported eolian, alluvial and glacial drift (Sollins et al., 2009). We estimated the distribution of cultivated lands in the region across differing depths of unconsolidated deposits by utilizing the 2012 National Cultivated Layer

(USDA-NASS, 2013) and depth to bedrock layers from the Minnesota and Iowa Geological Surveys (Fig 1.3, Table 1.1). Assuming that any residual saprolite was stripped from the landscape during repeated cycles of glaciation and glacial erosion, the depth to bedrock indicates the depth of unconsolidated materials from the land surface. This analysis revealed that > 90% of the cultivated lands in this region are underlain by transported, unconsolidated sediments > 10m thick (Fig 1.3, Table 1.1).

1.4.2 Continental context example: Surficial material type in the conterminous U.S.

To evaluate the relationship between croplands and surficial materials continental US, we utilized the Map Database for Surficial Materials in the Conterminous United States (Soller et al., 2009) and classified individual materials categories into those that were most likely to be characterized by consolidated and unconsolidated parent materials. All surficial materials mapped as "residual", "patchy", or "exposed rock" were classified as landscapes characterized by consolidated materials, while all other material categories (including "colluvial", "alluvial", "glacial" and "eolian" materials) were classified as landscapes characterized by unconsolidated materials (Fig 1.4, Table 1.1).

We then utilized the 2013 national cultivated layer dataset (USDA-NASS, 2013), to analyze the materials context of cultivated lands. Spatial patterns of agricultural lands in the United States generally follow the distribution of unconsolidated parent materials (glacial materials, alluvium or colluvium in valleys) with a smaller proportion of agricultural lands on consolidated parent materials (Fig 1.4). When pixels mapped as potentially consolidated materials at the national scale were matched to those at the

regional scale, above we found that our estimate of large-scale estimate of consolidated materials accounted for regional croplands with depth to bedrock ~ 5m (Fig 1.4, Table 1.1), so it is likely that even this analysis is conservative.

1.4.3 Global Context: Croplands and Topographic Ruggedness Index (TRI)

Due to the paucity of spatial data on the distribution of surficial materials or depth to bedrock at a global scale, we evaluated the distribution of global croplands with respect to the topographic roughness index (TRI). In doing so, we made a reasonable assumption that highly rugged regions are likely to be characterized by consolidated materials, while low-gradient landscapes are most likely to be characterized by unconsolidated materials. We utilized global TRI spatial data from Gruber (2012), where after Gaussian convolution, TRI was derived from a global DEM as:

$$TRI = \ln\left(\frac{\max(z) - \min(z)}{\sqrt{A}} * 100\right) \quad (20)$$

where z is surface elevation and A is the total area of a 5x5 pixel neighborhood (Gruber, 2012).

We followed Gruber (2012) and utilized 5 categories of TRI corresponding to Flat (TRI 0-1.5: e.g. Central California Valley, Southeastern U.S. Coastal Plain), Undulating (TRI 1.5-2.5: i.e. Eastern U.S. Piedmont, Palouse Hills), Hilly (TRI 2.5-3.5: i.e. Ozarks), Mountainous (TRI 3.5-4.5: i.e. Central Appalachians, Sierra Nevada) and Rugged (TRI > 4.5: i.e. Central Rockies, Olympic Mountains) landscapes. Categorizing familiar example landscapes to TRI class confirms our assumption that landscapes in the two lowest TRI classes are highly likely to be characterized by unconsolidated materials, while those

landscapes falling into the Hilly, Mountainous and Rugged classes are highly likely to be characterized by consolidated materials.

We then reclassified a probabilistic global croplands data layer (Ramankutty et al., 2008) into a binary layer by reclassifying all pixels in the original data with > 50% probability of being cropland as cropland and all pixels with < 50% probability as non-cropland. The results of our analysis show that over 84% of global croplands fall into the lowest two TRI categories (Fig 1.5, Table 1.1), meaning they are highly likely to be characterized by unconsolidated materials. The remaining 16% of global croplands are in the upper three TRI classes and likely to be characterized by consolidated materials (Fig 1.5, Table 1.1). Broad trends in continental distributions of croplands by TRI class are generally consistent except for Australia/Oceania, which have a high proportion of croplands in TRI class 4 due to mountain agriculture in Indonesia. Other global regions of mountain agriculture lie across the Mediterranean and North Africa, as well as the Ethiopian and Mexican highlands (Fig 1.5). Nonetheless, on a global scale, these are of minor importance in spatial extent relative to the intensively cultivated but flat or undulating landscapes of the North American Great Plains, the European and Asian Steppes, the Indus and Ganges floodplains, the Argentinian Pampas, and other similar landscapes (Fig 1.5).

Taken together, the results of our analysis at multiple spatial scales suggests, at the very least, that the majority of global agricultural lands are characterized in landscapes underlain by unconsolidated materials (sometimes extremely deep) that do not fit well into the central concept of soil production, as defined. The PDZ depth in most of these

landscapes, is most likely mechanism and not strength limited, based on our previous definitions. At the very least, these results suggest caution in the sweeping, widespread application of CRN-derived soil production rates, or at least the restriction of the application of these rates to problems of soil sustainability to appropriate geographic areas.

1.5. Discussion and conclusions

The geomorphic central concept of soil production and the ability to quantify it with CRN relies heavily upon specific assumptions in systems underlain by consolidated bedrock. Nonetheless, the desire to extend the results of CRN-derived soil production to understand the sustainability of soils across global agricultural systems has resulted in the application of these concepts well outside of the realm of systems for which they were initially intended.

There is considerable room to consolidate existing research on all aspects of PDZ thickness processes in agricultural settings and cast them in a unified, coherent geomorphic context such as that presented in this work. It is likely that most agricultural systems are mechanism limited, and that weathering is relatively unimportant for PDZ thickness maintaining processes, which may deepen through tillage disturbance at the same rate as removals (Fig 1.6A). In systems approaching strength limitation, however, changes in weathering rate may be extremely important in understanding long-term sustainability (Fig 1.6B).

Agricultural systems are geomorphically unique because they are characterized by

strong erosive forcing, large-magnitude short-scale volumetric change due to tillage, enhanced rates of chemical weathering and nearly instantaneous mixing. Physical denudation through surficial erosion rates in conventional agricultural systems tends to be orders of magnitude greater than in natural systems (Montgomery, 2007), Due to tillage management and machinery considerations, agricultural management has a significant effect on soil bulk density and volumetric change. These seasonal effects are dependent upon tillage management, but can account for changes in bulk density of 16-25% in the upper soil (Aikins and Afuakwa, 2012). There is significant evidence that agricultural management, with intense physical management and fertility maintenance through nutrient additions has an effect on weathering rates at a mineral scale (McGahan et al., 2003). In agricultural systems approaching *strength* limitation, changes in weathering rate may be extremely important in understanding the long-term sustainability of the colluvial soil mantle (Fig 1.6B).

Nonetheless, we suggest that based on our analyses future studies must be very explicit about defining soil production and decide whether or not it applies to the systems under consideration. We caution against using blanket meta-analyses which balance erosion and production data to make conclusions about soil sustainability on large scales. Instead, measurements of sustainability need to be more broad and inclusive (and models more nuanced) if we are to accurately predict the future outcomes of soil sustainability in conventional agricultural systems. Recently, advances have been made in deconfounding concepts of singular values for tolerable erosion rates to multiple values that each focus on a separate goal (maintenance of colluvial soil mantle thickness, maintenance of crop

productivity, and reduction of off-site impacts) (Li et al., 2009). Work on tolerable erosion rates has not progressed significantly over the last 3 decades (Li et al., 2009, Bui et al., 2011), but it is time that more focus is given to defining these rates more quantitatively so that spatial information on the sustainability of agricultural systems can be harnessed and evaluated at large scales. This will begin with clarifying and properly utilizing the fantastic advances in the measurement of soil production and soil thickness processes from the geomorphic community and critically evaluating its meaning and magnitude in a range of agricultural systems.

Regional: Cultivated Lands in Minnesota and Iowa

Depth to Bedrock	Total (km^2)	Percent (%)	References
0 - 1 m	6,305	3.5	Minnesota Depth to Bedrock: Olsen, B.M. and J.M. Mossler (1982); Iowa Depth to Bedrock: Witzke et al. (2010); Cultivated Lands: USDA-NASS (2013)
1 - 2 m	2,028	1.1	
2 - 5 m	8,814	5.0	
5 – 10 m	18,576	10.4	
10-50 m	36,750	20.7	
50-100 m	51,841	29.1	
> 100 m	53,610	30.1	
Total	177,923	100.0	

Continental: Cultivated Lands in the Continental U.S.

Surficial Materials	Total (km^2)	Percent (%)	References
Unconsolidated	1,084,589	81	Surficial Geology: Soller et al. (2009) Cultivated Lands: USDA-NASS (2013)
Consolidated	254,409	19	
Total	1,338,999	100	

Global: Cultivated Lands

TRI Class	Total (km^2)	Percent (%)	References
0 - 1.5 – Flat	6,333,390	54.7	Topographic Ruggedness Index: Gruber (2012) Croplands: Ramankutty et al. (2008)
1.5 – 2.5 – Undulating	3,484,442	30.1	
2.5 – 3.5 – Hilly	1,298,732	11.2	
3.5 – 4.5 – Mountainous	44,569	3.8	
> 4.5 – Rugged	19,689	0.2	
Total	11,581,941	100	

Table 1.1. Materials and geomorphic context of agricultural lands at multiple scales.

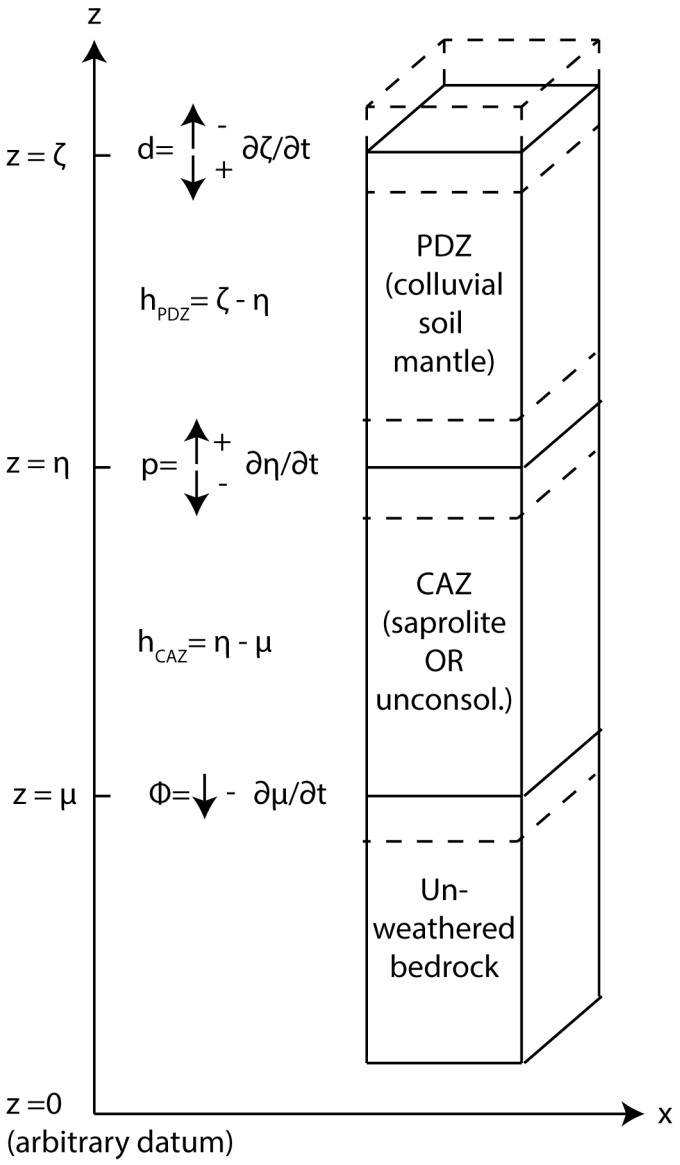

Figure 1.1. Representation of the three-tiered regolith-bedrock system (adapted from Yoo and Mudd, 2008). Following conventions, d is defined as positive up, while p and Φ are positive down. In the generalized form, both d and p are bi-directional, while Φ is uni-directional.

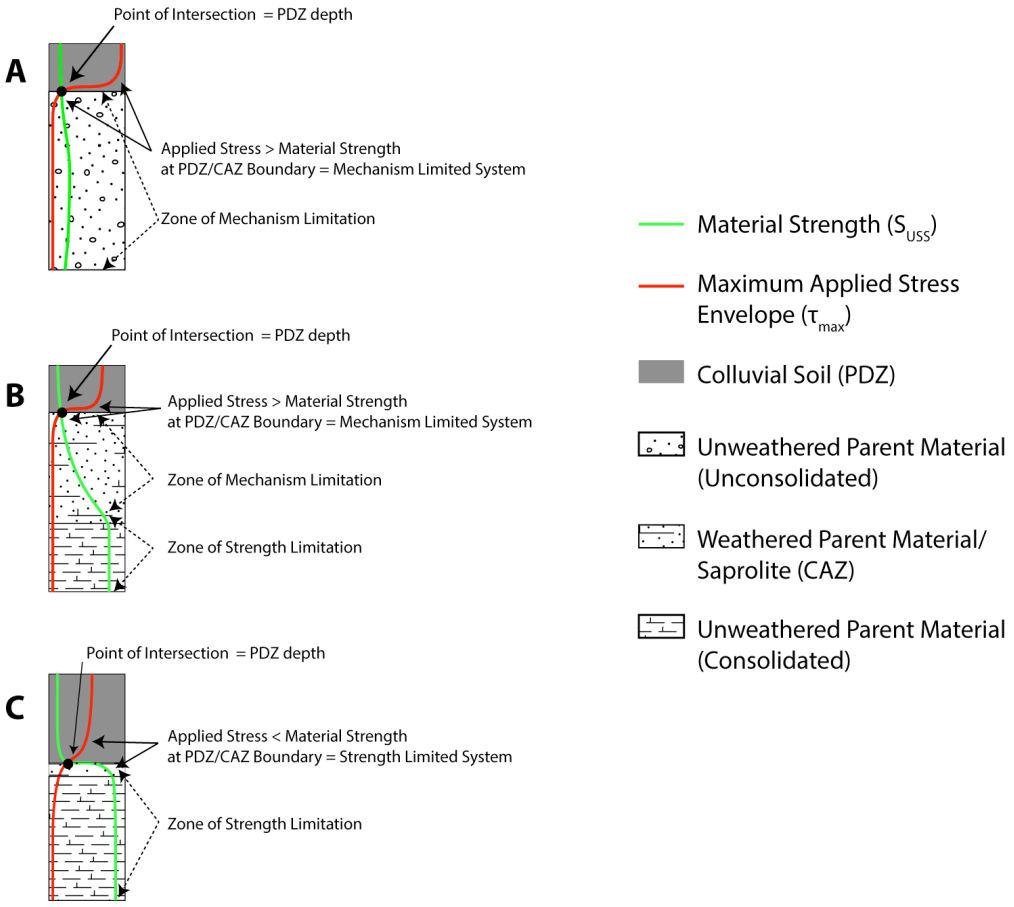

Figure 1.2. Hypothetical interactions between material strength and applied stresses for predictive models of PDZ depth and limitations to PDZ thickness.

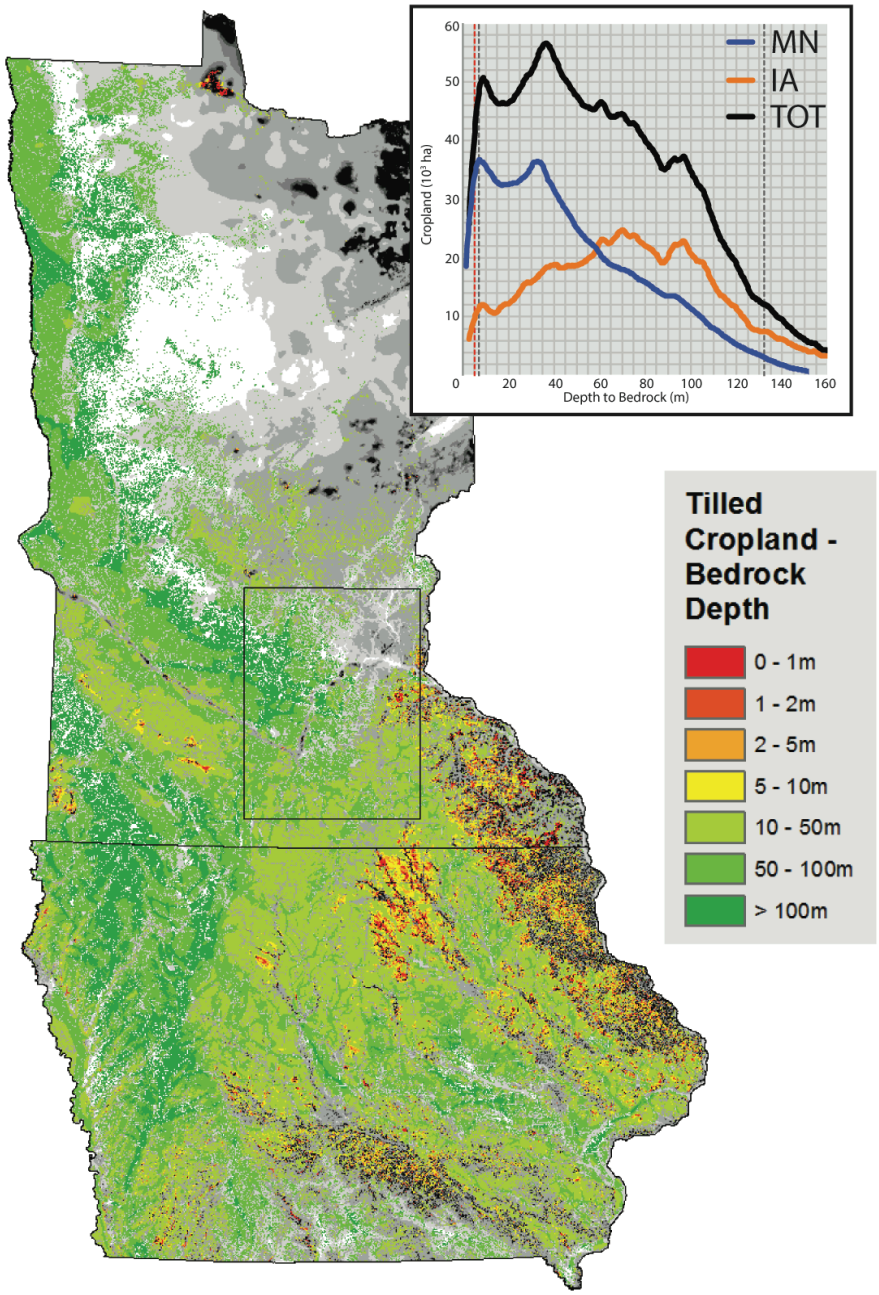

Figure 1.3. Regional distribution of croplands and depth to bedrock (thickness of unconsolidated materials) in Minnesota and Iowa, U.S.A. Inset: cropland distributions with depth to bedrock, black dotted lines = 95% inclusion. Data from Olsen et al. (1982) and USDA-NASS (2013).

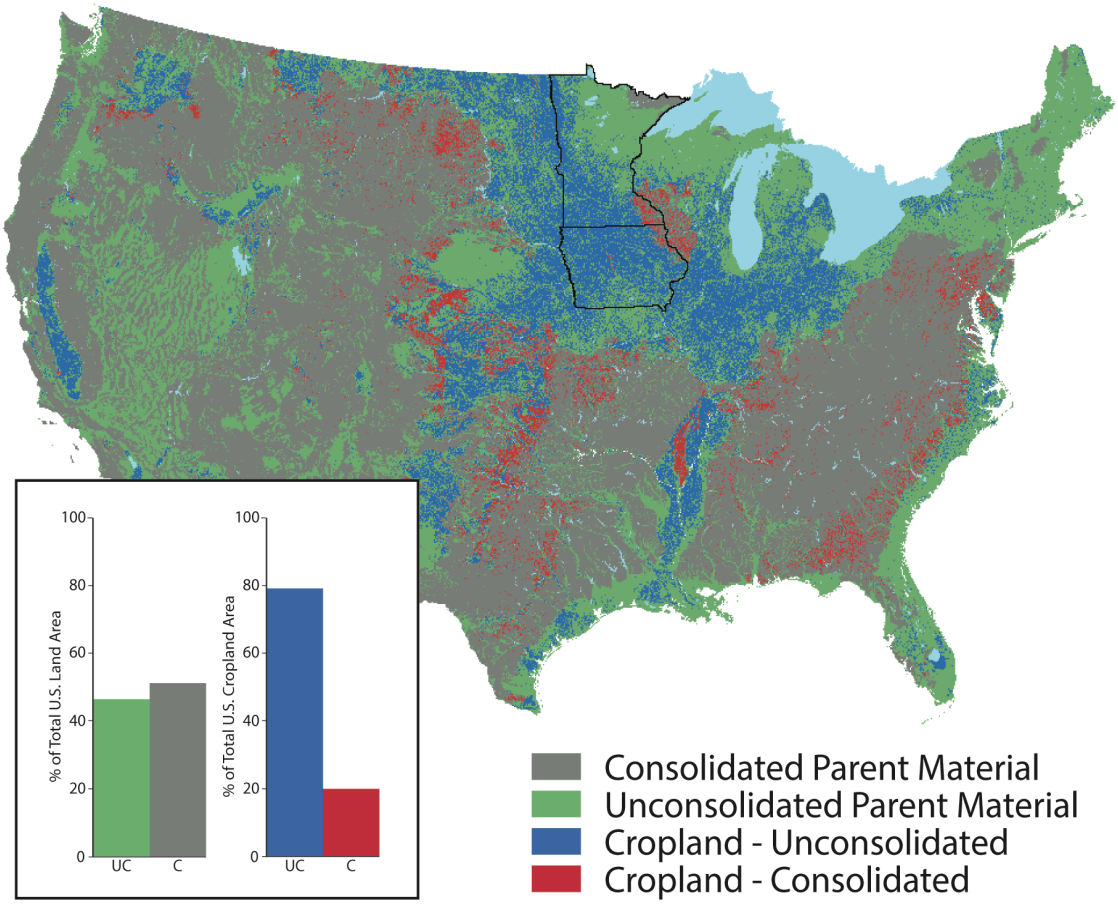

Figure 1.4. Distribution of croplands in relation to consolidated and unconsolidated surficial materials in the conterminous U.S. Inset: Histograms of material type for total land area (L) and croplands (R), UC = unconsolidated, C = consolidated. Data from Soller et al. (2009) and USDA-NASS (2013).

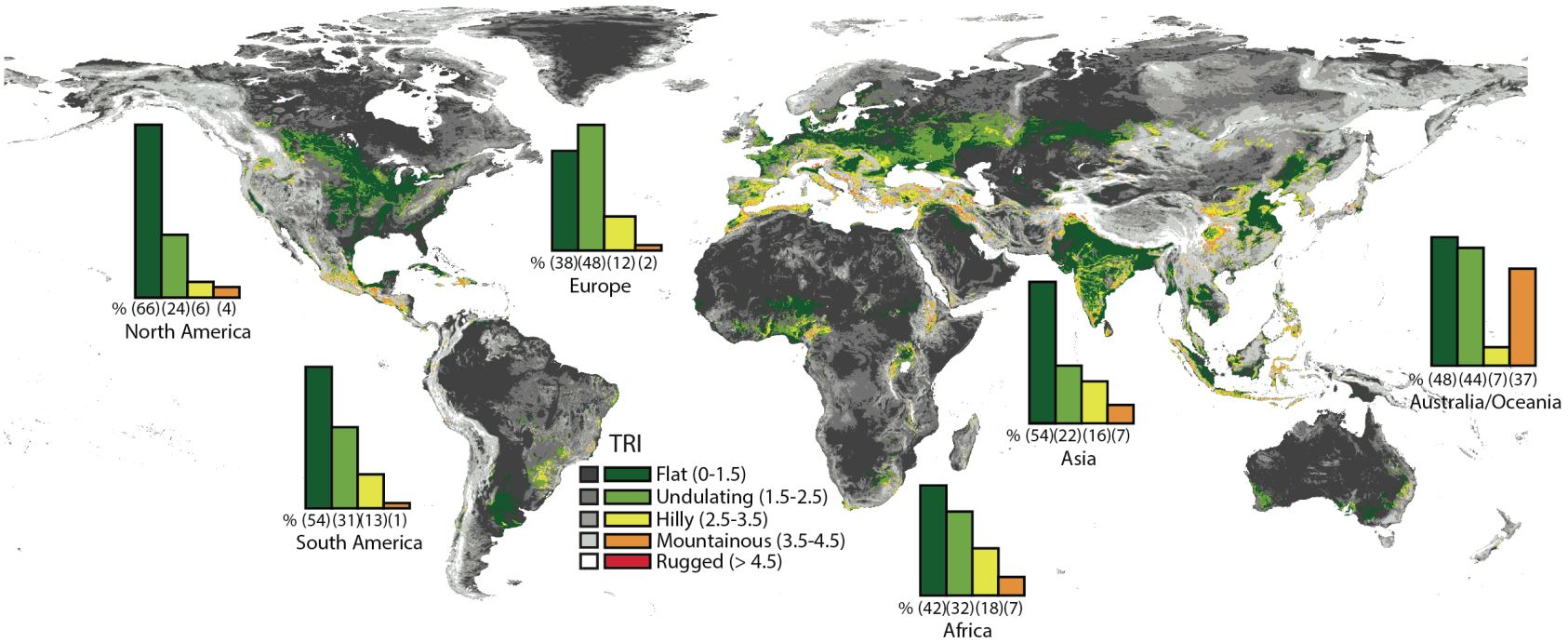

Figure 1.5. Global distributions of topographic ruggedness index (TRI) classes (grayscale) and TRI classes for croplands (color). Index histograms show normalized class distributions by continent. Data from Gruber (2012) and Ramankutty et al. (2008).

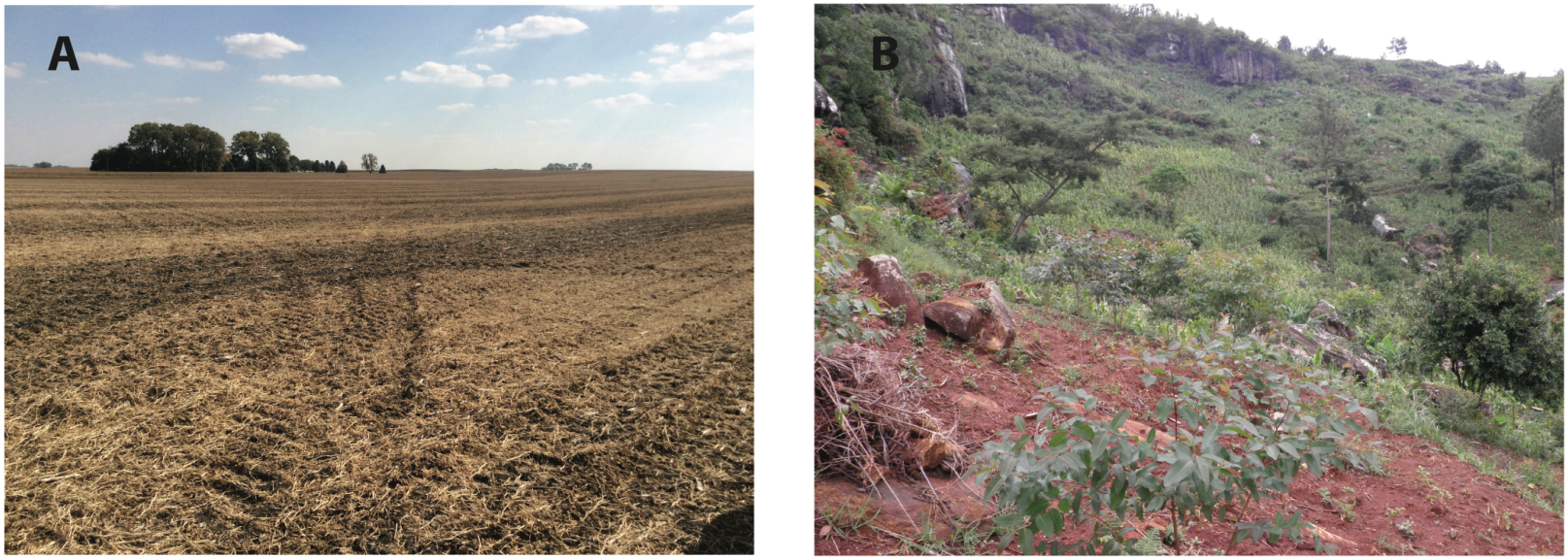

Figure 1.6. Examples of geomorphic and materials context of global agricultural lands. (A) Annually tilled uplands of central Iowa, U.S.A. – depth of unconsolidated material > 50m, topographic ruggedness index (TRI) < 1. (B) Bi-annually tilled uplands of the West Usambara mountains, Tanzania – depth of unconsolidated material < 1m, TRI ~ 4.

CHAPTER 2

The Distribution and Genesis of Eroded Phase Soils in the Continental United States

2.1. Introduction

The study and mapping of eroded soils as a unique pedological entity is a complex but important task in understanding the connections between land-use, erosion severity and crop productivity across a wide range of scales (Larson et al., 1985). Information on the distribution and severity of eroded soils has been used to predict the response of crop yields to soil erosion (Bakker et al., 2004), sediment yields (Trimble, 1975) and past land-use histories (Richter and Markewitz, 2001). However, the description, identification, classification and mapping of eroded soils is a complex activity requiring multiple levels of abstraction (Soil Survey Division Staff, 1993). Mapping erosion prevalence and severity has been a major focus of the United States soil survey, which was uniquely poised to do so because survey activities took place within a reasonable timeframe after the conversion of largely natural landscapes to intensive agricultural land-use in the Continental U.S. following European Settlement (Miller et al., 1985). The description and classification of eroded phase soils require an impressive, broad-scale understanding and integration of soil-landscape relationships and pedon morphologies (Olson, 1987) and thus represents a significant effort of lasting value.

2.1.1 Terminology and classification of eroded phases in soil survey

Critical terminology for interpreting the distribution of eroded phase soils is the distinction between *erosion types*, *erosion classes*, and *erosion phases*. Only erosion phases are ultimately identified and delineated as discrete map units, but erosion types and classes are closely related to phase and are integral to phase development and

identification in most cases.

Erosion *types* or kinds refer to recognizable features that indicate ongoing erosive processes. These types are grouped into water-generated types (sheet, rill, gully, and tunnel), wind-generated, and colluvial (landslips, i.e. mass movement). The erosion types represented in the U.S. soil survey (Soil Survey Division Staff, 1993) are a subset of the globally recognized types of erosion (Zachar, 1982), and represent those which have the greatest effect on soil properties and management over human timescales in the continental U.S. Tillage is an important mechanism of erosion that can cause extensive soil loss in some landscapes (Li et al., 2007) but was not emphasized in the U.S. soil survey because the effects include both material removal and extensive mixing, which in the short-term results in less dramatic morphological modification than water, wind or gravity-driven erosion. Nonetheless, in some landscapes, tillage erosion can account for soil loss on the same order of magnitude as that from water or wind erosion (Papiernik et al., 2005).

Erosion *classes* are an estimate of the degree to which surficial accelerated erosion (i.e. excluding landslip and tunnel types) has removed material from the upper horizons of the soil profile. Class 1 is defined as having lost < 25% of original A and E horizons (or of the upper 20cm if the original A/E were < 20cm), Class 2 has lost 25-75% of the same increments, Class 3 has lost > 75% and Class 4 has lost 100% or more of the original (Soil Survey Division Staff, 1993). Erosion classes are generally related to erosion types. For example, typical evidence of class 1 may be a few rills, an accumulation of sediment at the base of slopes, small areas where the plow layer contains

subsurface material, some widely spaced rills or gullies without a measurable reduction in thickness between the features. Erosion classes 3 and 4 may be extensively characterized by gullying (Soil Survey Division Staff, 1993).

Erosion *phases* (as with other phase designations in soil survey) are recognized on the basis of differences in potential use, management or performance. Therefore, an eroded phase is recognized only if the properties of the soil material that remains changes one of these interpretations for the purposes of the survey at hand (Soil Survey Division Staff, 1993). Under these definitions, therefore, there is no prescribed erosion type or class that is required to delineate a particular erosion phase. However, erosion classes and phases are generally closely linked because most soils have a large number of physical and chemical properties affected by erosion (Larson et al., 1985). There are 3 recognized water erosion phases (slightly eroded, moderately eroded and severely eroded) and 2 erosion phases specific to wind (eroded (blown) and severely eroded (blown)). Additionally, gullied phases are named only when gullies occupy < 10% of the map unit. When gullies occupy > 10% of the map unit, no phases of existing soil series are utilized and the map unit is instead named as a complex or association of soil and gullied land (Soil Survey Staff, 1993).

Slightly eroded phases are not distinguished from uneroded areas in most surveys, but represent a situation where the soil properties have changed to require a slight modification of management. Slightly eroded phases are generally associated with Class 1 erosion. Moderately eroded phases (or just eroded phases in most surveys) have undergone changes in soil properties that result in major differences in management or

management response and are generally associated with Class 2 erosion. Severely eroded phases require a change in land use intensity, extensive reclamation or property restoration efforts, significantly reduced productivity or major engineering limitations. Severely eroded phases are generally associated with some gullying and class 3 erosion. Eroded (blown), or moderately wind eroded phases are those map units where management but not suitability differs from that of the uneroded soil. Severely wind eroded (severely blown) phases are characterized by both accumulations, removal and the shifting of soil materials around the area, which have caused differences in suitability in the absence of extensive reworking or extensive management (Soil Survey Division Staff, 1993).

The purposes of this study were to (i) determine the extent and spatial distribution of eroded phase soils in the continental U.S., (ii) examine the relationship between the mapping of eroded phase soils by political boundaries, physiographic boundaries, and currently cultivated lands, (iii) redefine and clarify the terminology used to describe, classify and map eroded phases of soils with reference to the Soil Survey Manual, (iv) discuss the factors related to the genesis of eroded phase soils as defined and (v) to revisit the implications of eroded phase soils and the importance of mapping efforts.

2.2. Methods and Data Sources

The SSURGO database (Soil Survey Staff, 2014) was utilized in state tiles to map the distribution of eroded phase soils in the continental United States. State databases were mined for SSURGO polygons containing the word "eroded" (case insensitive),

indicative of eroded phase map units and “gullied” (case insensitive), indicative of gullied phases or complexes using standard SQL queries in ArcGIS 10.2. Severely eroded polygons were extracted from the database by querying the subset of map units containing the word “eroded” with the word “severe*” (wild card, case insensitive).

The intersection of eroded polygons and cultivated/uncultivated pixels in the 2013 National Cultivated Layer (USDA-NASS, 2013, 30m resolution) was used to determine the extent of eroded soils on currently cultivated and uncultivated lands. The 2013 National Cultivated Layer is a binary (cultivated or uncultivated) spatial raster dataset generated by combining the previous five years (2009-2013) of the USDA-NASS Cropland Data Layer (CDL). If a pixel was cultivated in at least two of the previous five years it was assigned to the cultivated class (USDA-NASS, 2013). Checks on land area and land area standards utilized data from the U.S. Census Bureau (U.S. Census Bureau, 2010).

In addition to state boundaries, the boundaries of Level 3 Ecoregions (USEPA, 2013) were utilized to understand broad geographical patterns in eroded phase soils, and the relationship of these soils to currently cultivated lands in various physiographic settings. Eighty-five EPA Level 3 Ecoregions are delinated in the continental United States based on consistent patterns in biotic and abiotic phenomena, and are of an appropriate scale for regional analysis (Omernik, 1995). EPA Level I, II and IV Ecoregions were determined to be too coarsely or finely delineated to yield scale-appropriate regional results in this analysis.

A global 30-arc second resolution raster of terrain ruggedness (Gruber, 2012) was

utilized to determine the average Terrain Ruggedness Index (TRI) for each region as a measure of topographic heterogeneity. Topographic ruggedness index is a scaled version of a neighborhood area normalized elevation difference (Melton, 1965, Gruber, 2012) and can be used to broadly classify global landscapes into flat (TRI = 0 – 1.5), undulating (TRI = 1.5 – 2.5), hilly (TRI = 2.5 – 3.5), mountainous (TRI = 3.5 – 4.5) and rugged (TRI > 4.5). In relation to well known global landforms, the flat class encompasses regions such as the Ganges-Indus Plains and the Hudson Bay Lowlands, the undulating class to the Piedmont and non-glaciated Northern Plains of the U.S., the hilly class to portions of the U.S. Midwestern Driftless Area, the mountainous class to most of the Appalachian and Rocky mountains, and the rugged class to the most extreme core of the Canadian Rockies, Brooks Range, Alps, and Himalayas.

Polygon map unit names in each state (Table 2.1) were combined to determine the total number of unique eroded map units (inclusive of slope class and additional phase names (i.e. stony/rock/etc) for each named series). The series names for each map unit (and the first named occurring series in a complex) were extracted and queried against the Official Series Description Database (Soil Survey Staff, 2014). These series names were compiled and analyzed for family textural classifications and taxonomy. To determine examples of mapping criteria for eroded soils at the county level, published and archived soil surveys (ranging in age from 1958 - 2005) were mined for representative series in which an uneroded and eroded profile were described in the same county.

The distribution of erosion classes in the Dust Bowl county surveys of Joel (1937) was analyzed in relationship to eroded phase soils in the SSURGO database, using

digitized maps created from the original hand-drawn products by the Historical GIS Lab at the University of Saskatchewan (Cunfer, 2011). The 85 erosion class combinations in the Dust Bowl survey (Joel, 1937) were generalized into the following classes (Removal: Water only, Removal: Wind only, Removal: Wind and Water, Removal and Accumulation: Predominantly removal, Removal and Accumulation: Predominantly accumulation, Accumulation only) by projecting an average A horizon depth from the average of official series descriptions from the study region in the current SSURGO data (7 cm) to the proportions of topsoil removed in the original survey classes. For those classes which had both removal and accumulation co-occuring, the removal depth range was subtracted from the accumulation depth range:

$$T = A - R \qquad (21)$$

Where T is the total erosion or removal (cm), A is the accumulated depth range (cm), and R is the removal depth range (cm). Classes which had a T value of < 0 (negative) were considered to have predominantly removal, whereas classes with a T value of ≥ 0 (positive) were considered to have predominantly accumulation. All statistical analyses were performed in R (R Core Development Team, 2014).

2.3. Results

2.3.1 Distribution of eroded phase soils by state

In the continental U.S., 462,979 km^2 of eroded phase soils have been mapped (Fig 2.1) of

which Iowa (40,200 km^2 – 28% of total land area), Missouri (39,000 km^2 – 22% of total land area), Nebraska (30,800 km^2 – 16% of total land area), Illinois (30,100 km^2 – 21% of total land area) and Georgia (28,500 km^2 – 19% of total land area) are the top five states in terms of total mapped area, accounting for 36% of the U.S. total (Table 2.1). The states with the highest proportion of total mapped area as eroded phases are Iowa (28%), Indiana (26%), Tennessee (24%), Kentucky (23%), Mississippi (21%), Missouri (21%) and Illinois (21%) (Table 2.1). Eroded phase soils account for 6.3% of the total mapped area in the continental United States (Table 2.1).

In total, 125,769 km^2 (27.2%) of eroded phase soils are currently under cultivation, and of the 1,338,999 km^2 of lands under cultivation in the continental U.S., 9.4% lie on mapped eroded soils (Table 2.2). Iowa (24,565 km^2 – 61% of cultivated land mapped as eroded), Nebraska (17,312 km^2 – 56% of cultivated land mapped as eroded), Illinois (14,637 km^2 – 50% of cultivated land mapped as eroded), Missouri (10,541 km^2 – 27% of cultivated land mapped as eroded), Wisconsin (9,932 km^2 – 41% of cultivated land mapped as eroded) and Indiana (9,413 km^2 – 39% of cultivated land mapped as eroded) are the top states in terms of total eroded area mapped on currently cultivated soils (Table 2.2).The states with the highest proportion of eroded soils currently under cultivation are South Dakota (63%), Iowa (61%), Minnesota (61%), Nebraska (56%) and Michigan (54%). The states with the highest proportions of cultivated soils on eroded lands are Tennessee (37%), Missouri (27%), Wisconsin (27%), Iowa (25%) and Kentucky (23%) (Table 2.2).

The number of unique, eroded map units (including complexes with series names

in different orders, unique slope classes and other phases) totaled 15,202 (Table 2.1). By state boundaries, the number of unique eroded phase map units is significantly related to the amount of currently cultivated land on eroded phase soils ($R^2 = 0.84$, $p < 0.001$) and the total eroded phase mapped ($R^2 = 0.61$, $p < 0.001$), but not the total mapped area or total cultivated area in each state ($p > 0.4$) (Fig 2.2). Extracting series names and the first named series in the case of complexes resulted in 2265 unique, named series with recognized, mapped eroded phases. Of these named series, 42% (943) are Alfisols, 24% (541) are Mollisols, and 14% (305) are Ultisols. Andisols (< 1%), Aridisols (4%), Entisols (6%), Inceptisols (8%), Vertisols (2%) and Spodosols (1%) make up the remaining 20% (Table 2.3). Together, the clayey (fine), fine-loamy, fine-silty and coarse-silty textural classes make up over 85% of the eroded series with assigned textural classes (Table 2.3).

Soils mapped as severely eroded are most prevalent in Kentucky (9,135 km^2), Mississippi (6,316 km^2), West Virginia (6,138 km^2), Illinois (6,081 km^2) and Indiana (6,025 km^2) (Fig 2.3). States vary widely in the total proportion of eroded soils mapped as severely eroded. For example, 100% of West Virginia's eroded phase soils are classified as severely eroded (Table 2.1). In contrast, < 1% of Wisconsin's eroded phase soils are classified as severely eroded. The top 5 states in percentage of total eroded soils classified as severely eroded are West Virginia (100%), North Dakota (47%), Kentucky (39%), Tennessee (32%) and Louisiana (31%). In sum, 72,690 km^2 (16%) of eroded phase soils are mapped as severely eroded (Table 2.1). The total area of severely eroded soils mapped in each state is significantly related to the total area of eroded soils mapped

($R^2 = 0.47$, $p < 0.001$).

Gullied lands occupy 12,846 km^2 in the continental U.S. (0.2% of total land area/mapped area, Fig 2.3, Table 2.1). Over 68% of the mapped gullied lands (8,716 km^2) in the continental U.S. are in Mississippi (3,107 km^2), Wyoming (2,149 km^2), Oklahoma (1,393 km^2), Tennessee (1,207 km^2) and California (860 km^2) (Table 2.1). Twenty-five other states have mapped gullied lands, which make up the remaining 32%. States which have gullied lands as the greatest proportions of the sum of their gullied and eroded lands are Wyoming (95%), North Dakota (91%), Montana (52%), Colorado (20%) and Nevada (20%) (Table 2.2).

2.3.2 Distribution of eroded phase soils by ecoregion: cultivation and terrain ruggedness

Level III ecoregions are defined with reference to both biotic and abiotic properties (USEPA, 2013), and as such represent natural physiographic boundaries instead of the county and state political boundaries of SSURGO data. Level III Ecoregions with the largest area of mapped eroded phase land area are the Piedmont (portions of: AL, GA, SC, NC, VA) 57,448 km^2, the Western Corn Belt Plains (portions of: IA, MN, MO, NE) 55,876 km^2, the Interior Plateau (portions of: AL, TN, KY, IL, IN, OH) 37,481 km^2, the Southeastern Plains (portions of: TN, MS, AL, FL, GA, SC, NC, VA, MD) 36,446 km^2 and the Central Irregular Plains (portions of: IA, MO, KS, OK) 32,692 km^2 (Table 2.4). Ecoregions with the highest proportion of eroded soils are the Driftless Area of the Upper Midwest (45.1%), the Mississippi Valley Loess Plains (37.7%), Piedmont (34.6%), Interior Plateau (30.3%) and the Central Irregular Plains

(28.6%) (Fig 2.4).

The relationships between the proportion of cultivated land area by ecoregion and the proportion of eroded phase area by ecoregion (Fig 2.5), reveals important breaks at the 85th percentile of each metric. These can be used to divide the plot into 4 quadrants, pertaining to different combinations of proportions of cultivated lands and eroded phase soils which are related to current land-use and land-use histories (Fig 2.5). Type I ecoregions have a low proportion of cultivated land and a low proportion of mapped eroded phase soils. Ecoregions included here are those that do not (and have never) had extensive areas of land in agriculture, such as the North Central Hardwood Forests and the Arkansas Valley ecoregions. Type II ecoregions include those ecoregions that are under intensive cultivation but have had or continue to have a low proportion of eroded phase soils. These ecoregions include the Lake Agassiz Plain, the Central Great Plains, the Mississippi Alluvial Plains, and the Central California Valley. Type III ecoregions are intensively used for agriculture and have a large proportion of mapped eroded phase soils. These 5 ecoregions lie predominantly in the Corn Belt and include the Western, Central, and Eastern Corn Belt Plains, the Southeastern Wisconsin till plains, and the Interior Valleys and Hills of Tennessee and Kentucky. Lastly, Type IV ecoregions are areas with extensive areas of land mapped as eroded, but with a low proportion of land area currently under cultivation, including well known cases such as the Midwestern Driftless Area (Trimble, 2013) and Piedmont of the Eastern U.S. (Trimble, 2008).

Generalized statistics by type further underline the relationship of these groupings to land-use histories. Type IV Ecoregions have an average of 33% of their total area

mapped as eroded, with only 15% of their total area cultivated, 16% of the eroded phase soils cultivated, and 36% of cultivated lands on eroded phase soils. Type III Ecoregions have an average of 23% of their total area mapped as eroded, with 62% of their total area cultivated, 55% of the eroded phase soils cultivated, and 20% of cultivated lands on eroded phase soils. Type II Ecoregions have an average of 5% of their total area mapped as eroded, with only 53% of their total area cultivated, 46% of the eroded phase soils cultivated, and 4% of cultivated lands on eroded phase soils. Lastly Type I Ecoregions have an average of 2% of their total area mapped as eroded, with 10% of their total area cultivated, 11% of the eroded phase soils cultivated, and 3% of cultivated lands on eroded phase soils (Table 2.4 and Table 2.5).

Maximum average TRI for ecoregions was 4.51 (North Cascades) and the minimum was < 0.001 (Southern Florida Coastal Plain), with a continental average of 2.14 +/- 1.18 (Table 2.4). Trends in average TRI values and % of ecoregion cultivated show that the majority of extensively cultivated ecoregions lie below an average TRI of 2.5 (with two major exceptions: the Columbia Plateau (containing the Palouse Hills) and the Willamette Valley ecoregions, both in Washington state), with a steady decline from the lowest gradient ecoregions (Fig 2.6). In contrast, ecoregions with the highest percentage of mapped eroded phase soils in terms of total area show a peak at an average TRI between 1 and 2.

2.4. Discussion and Conclusions

2.4.1 Historical aspects of erosion-affected land related to the distribution and extent of

SSURGO eroded phase soils in the continental U.S.

Various estimates of erosion-affected soils in the continental United States have been produced, however differences in methodology, terminology and extent preclude direct comparisons (Larson et al., 1983). For example, Bennett (1939) estimated that 428 million ha (4.28×10^6 km^2) of land was affected by erosion in the continental United States, 120 million ha of which (1.20×10^6 km^2) was on cultivated lands. The total area of eroded phase soils mapped in the SSURGO database (0.46×10^6 km^2, Table 2.1) is an order of magnitude lower than Bennett's estimates. The discrepancies between these estimates are likely due to several factors: (1) Bennett's 1939 estimates are coarse and are derived from extremely broad generalizations of regional landscapes (Miller et al., 1985), which may have led to an overestimation of erosion-affected land area relative to the SSURGO data, which is of much finer scale; (2) the Bennett (1939) estimate includes wind-eroded soils in close temporal time to the peak of the Dust Bowl era (a minor component of SSURGO eroded phase soils for morphological reasons); (3) many of the surveys made in the SSURGO database were finalized decades after the extremely intensive land-use that occurred in the late 19th century and early 20th century, which may have been captured in Bennett's estimates; (4) the designation of eroded phases ultimately is dependent on interpretation and perceived impact of erosion on soil properties, which makes the delineation of eroded phase soils much more conservative than erosion-affected soils in general (Soil Survey Division Staff, 1993). Thus, eroded phase soils may be viewed as a subset of erosion-affected soils.

The importance of the third point above (time of survey relative to time of most

intensive land-use, is perhaps best reflected in the differences between the distributions of eroded phase soils in the Piedmont ecoregion in contrast to the Corn Belt regions of southern Minnesota, Iowa, Illinois, Missouri and Indiana (Type III Ecoregions: Fig 2.1, Fig 2.4). County-level surveys in the Northern Piedmont (Type 1 Ecoregion: Maryland and Virginia, Fig 2.4 and Fig 2.5), and Piedmont (Type IV Ecoregion, Fig 2.4 and Fig 2.5) were finalized 100-200 years (Northern Piedmont, Craven, 2006) or 60-100 years (Piedmont, Trimble 1975, Trimble, 2008b) after the most intensive peak in land-use and subsequent large-scale land abandonment. In stark contrast, county-level surveys in the Corn Belt states were finalized during a period of continuing intensification of agricultural land-use on the landscape. These differences are manifested in the patchy distribution of eroded soils driven by county political boundaries in the Piedmont region and relatively seamless mapping of eroded phase soils in the Corn Belt states (Fig 2.1). Nonetheless, the fact that eroded phase soils could be extensively mapped in the Piedmont when surveys were finalized testifies to the extensive losses that occurred on that landscape (Trimble, 1975) up to a century before and the suitability of Ultisol morphology in particular to the identification and delineation of eroded phases (see below).

In addition to the Piedmont, other type IV ecoregions (Fig 2.5, Table 2.4) have well documented histories of intensive land-use and erosive forcings followed by land abandonment and recovery such as the Upper Mississippi Valley Hill Country (Trimble, 2013) and Mississippi Valley Loess Hills (Hilgard, 1860). Additionally, these ecoregions lie in TRI categories where both agricultural land-use and erosive forcings remain at

moderate levels, resulting in high erosion risk and the identification of many eroded phase map units. All of these Type IV ecoregions have in common tremendous agricultural expansion and intensification of land-use at the time of European settlement followed by de-intensification by the 20th century as the soils could not support continued intensive agricultural land-use (typically due to fragipans, highly erodable loess, or low depth to bedrock, i.e. Craven, 2006, Trimble, 2008).

2.4.2 Morphological identification of eroded soils

An eroded phase soil is a morphological state of a soil profile that has changed over time relative to a previous reference state. In this context, accurately defining eroded soils depends on the ability to choose an appropriate reference state (Olson, 1994). Thus, the question of defining a reference state becomes critical in the mapping and delineation of eroded phase soils (Soil Survey Division Staff, 1993). The two major issues involved in choosing reference states are related to space-for-time substitutions and landscape heterogeneity (Olson, 1994, Ellert and Betany, 1995, Jelinski and Kucharik, 2009). Space-for-time substitutions assume that differences between two sites are due solely to time since management change and not spatial variability, which may or may not be an appropriate assumption in some landscapes (Jelinski and Kucharik, 2009). For the purposes of soil survey, the soil survey manual differentiates between *natural* erosion and *accelerated* erosion (Soil Survey Division Staff, 1993). Natural erosion is considered to be that occuring under natural climatic, topographic and biotic forcings. Natural erosion is a process affecting (and involved in) soil formation, and may occur on timescales

consistent with, or highly incongruent with other soil forming processes (Johnson et al., 1990), however, properties related to natural erosion are part of the definition of soil taxa, not a basis for the identification of erosion phases (Soil Survey Division Staff, 1993). In contrast, accelerated erosion is defined as erosional forcing over and above natural erosion, predominantly due to anthropogenic factors such as intensive agronomic practices, grazing or logging (Soil Survey Division Staff, 1993).

In the soil survey manual (Soil Survey Division Staff, 1993) the "uneroded" profile is referred to as a reference in most cases, but this terminology can be highly confusing (Olson and Beavers, 1987) and, as discussed above, the distinction made between natural and accelerated erosion is implicit in the term. The reference state of a soil profile (at a previous timepoint) has also been variously termed a "virgin", or "uncultivated" profile in the United States (Rhoton and Tyler, 1992, Graveel et al., 2002, Papiernik et al., 2007) and the "Etalon" (French - standard) in Eastern Europe (Zachar, 1982). Here, the use of the term Etalon is applied to specifically identify a particular reference state relative to which a putative eroded soil profile will be compared. This term is preferred as it is free from biases and hidden meanings (the soil to which an eroded profile is compared may not always be uneroded, virgin, or uncultivated (Olson and Beavers, 1987)), and stands simply for an object or standard of comparison. Its non-English origins also allow the term to be used in a precise manner when speaking specifically of a comparative unit soil profile.

Developing an appropriate conceptual model for the etalon can prove difficult, particularly in intensively utilized landscapes, where undisturbed soils do not exist

extensively and those that are left may have biased properties (Mokma et al., 1996). In intensively cultivated landscapes, for example, uncultivated soils or even uneroded soils may not be available as etalon profiles (Olson et al., 2013), but the etalons selected must still contain key morphological indicators that are below the plow layer in order to be useful in the field. Etalon selection must be done with care, particularly in intensively cultivated landscapes, because reference pedons are often biased towards a particular difference (too wet, dry, or rocky). For similar reasons, fence-rows and cemeteries can also be biased, but sometimes these may be the only options (Kreznor et al., 1989). The appropriateness of space-for-time substitution depends heavily on the heterogeneity of soil bodies across the landscape as well as the variation in depth of key morphologies or material layers (Wilson et al., 2010).

Because changes in morphology that relate to the identification of eroded phase soils must rely on key morphological indicators in the etalon profile, the term Key Etalon Morphologies (KEMs) is proposed, which refer to those indicators that are robust enough to apply across the landscape and recognize in individual profiles. Any of the five soil forming factors may cause an etalon/eroded relationship that is reliant on space-for-time substitutions to be unrepresentative when applied across a landscape. For this reason, adjustments to KEM properties must be accounted for when estimating depth of erosion by morphology alone. Key etalon field morphologies can be illustrated by using the Relative Horizon Distinctness (RHD) Index of Bilzi and Ciolkosz (1977a and Ciolkosz, 1977b). The RHD combines comparative field descriptions of soil texture, color, structure and other morphologies (effervescence, etc) to determine a single number index

for the difference between adjacent horizons or between all horizons and a parent material (Bilzi and Ciolkosz, 1977a). Inter-horizon differences in morphology are assigned unit changes and the total of these changes is summed to determine the single-number RHD for two horizons (Bilzi and Ciolkosz, 1977b). A reasonable marker used in an etalon/eroded comparison should have an RHD of at least 6, which based on RHD scoring can only result from multiple changes in soil texture, color, and structure and is fairly robust. Although this number remains an arbitrary criteria, it is useful for identifying KEM number and strength in the following discussion.

Soil with KEMs that are driven by surficial horizons (i.e. Mollisols and the Mollic epipedon, particularly Hapludolls) may have weak or no subsurface KEMs that can be used as morphological metrics for identifying erosion depth (Fig 2.7). Soils with no KEMs will be difficult to map as eroded phases due to problems of etalon definition, and these typically include weakly developed Hapludolls (Fig 2.7A, 2.7B), Entisols (Fig 2.8E), some Inceptisols and Oxisols (Fig 2.8F). In the case of the Hapludolls, this can make them difficult to identify as eroded phases and also highly susceptible to classification change (typically to Inceptisols or Entisols) (Mokma et al., 1996, Veenstra and Burras, 2011). In some cases, organic carbon concentrations have been used to identify eroded phases, however this may be unadvisable because without quantification of the proportion of SOC lost to decomposition, quantification of erosion class can be difficult (Kimble et al., 2001, Jankauskas et al., 2007).

Besides truncation, the mixing of subsurface materials with surface materials in the plow layer of cultivated soils has been used as another common indicator. This, of

course, requires that the subsurface materials be of sufficiently different physical and or chemical composition than the surficial materials to be a reliable indicator, such as the case with Bk horizons in Calciudolls (Fig 2.7C, Papiernik et al., 2007) or argillic horizons in Argiudolls (Fig 2.7D). However, mixing of subsoil materials alone is not sufficient criteria to define an eroded phase soil (or erosion class) unless those materials lie below a KEM boundary in the etalon that is below plow depth (Olson, 1994). For example, Figure 2.7A shows a Hapludoll (Clarion) with a single KEM that is at the boundary between a cambic and parent material, whereas the single KEM in Figure 2.7C in a Calciudoll lies at the Ap/Bk boundary. If the plow layer is exactly at the original A/Bk boundary in the etalon, then the mixing of subsurface Bk material into the plow layer is an indication of erosion, however if the plow layer reaches deeper than the original A horizon, mixing of material could occur even if no accelerated erosion was occurring.

Alfisols and Ultisols have argillic, kandic, or natric horizons and therefore typically have at least 2 KEMs (Fig 2.8A), with Fragi- great groups perhaps demonstrating the most robust KEMs and morphological distinctness of all soil taxa, often with 3 KEMs (Fig 2.8B and 2.8D). In contrast Pale- great groups which do not exhibit significant clay decreases at the bottom of the argillic horizon may only have a single KEM (Fig 2.8C). Other important examples of strong KEMs include lithologic discontinuities, paralithic and lithic contacts. The selection of etalons, KEMs and morphological criteria for the delineation of eroded phases varies strongly by survey region and soil type (Table 2.6). However, common themes in a selection of eroded criteria from county-level surveys in the U.S. shows that many KEMs that have been

developed into eroded criteria are dependent upon changing depths to a subsurface diagnostic (and subsequent morphologic property change), thinning of A horizon materials, mixing of subsurface materials and depth to lithic or paralithic contacts (Table 2.6).

2.4.3 Genesis of eroded phase soils.

Aspects of the canonical soil forming factors (Jenny, 1941) relevant to the genesis of eroded phase soils are by definition those that cause accelerated erosion over and above natural erosion rates encompassed in etalon morphology.

Climate. The major climatic variables in the two most important equations for predicting water (RUSLE) and wind erosion (RWEQ) are rainfall energy and wind speed, however unless abrupt climatic change influences the erosive forcing of these factors, changes in other factors (predominantly the biotic factor) through management are necessary to allow these climatic forces to cause accelerated erosion above and beyond natural erosion rates which are contained in the Etalon concept (Zachar, 1982, Soil Survey Division Staff, 1993). Of all climatic factors, rainfall energy and intensity is perhaps the most important climatic variable related to the physical removal of soil material by water, a relationship emphasized in the revised Universal Soil Loss (RUSLE) equation (Renard et al., 1997). The relative importance of water and wind erosion (and thus the erodibility of entire landscapes) is driven by climate and at large scales climate averages have been utilized to compute iso-erodent maps (Renard et al., 1997).

Organisms. When anthropogenic forcings are included in the biotic factor,

humans have the greatest effect on accelerated soil erosion through both direct soil movement (Wilkinson, 2005) and also indirectly through the management and extensive change of flora and fauna relative to natural systems (Foster et al., 1985). Tillage is the major extensive, direct soil disturbance that takes place on a global scale and is more energy intensive and efficient at moving soil material than any natural pedoturbative processes (Lindstrom et al., 2000, Yoo et al, 2005). Tillage erosion is a distinctly anthropogenic component of the genesis of eroded phase soils and is the "hidden" erosion in many agricultural landscapes, an unavoidable consequence of intensive agricultural land use (Li et al., 2011). Therefore, the genesis of eroded phase soils almost always requires the complete removal or reduction of surface vegetative cover or destruction of the litter layer. In some systems tillage erosion has been estimated to be responsible for almost quadruple the amount of soil movement from some points on the landscape than wind and water erosion combined (Li et al., 2007). Tillage erosion is critical for the genesis of eroded phase soils because it includes both mixing and downslope mass movement (not just surface movement) away from a point, which has dramatic effects on soil morphology (DeAlba et al., 2004). Conventional agricultural management is typically characterized by extensive changes in the type of vegetative cover, leaving soils exposed to other accelerated erosive forcings. In contrast, management systems that emphasize maintaining vegetative cover can result in erosion rates within the range of natural systems, which would not allow an eroded soil to develop (Montgomery, 2007).

Topography. Even at very large scales, the topographic signal on the distribution of eroded phase soils is strong (Fig 2.6). While cultivated area shows a continuous

decline from the lowest gradient ecoregions, the proportion of eroded soils has a peak between a TRI of 1-2 (Fig 2.6). This demonstrates that physiographic regions with TRIs ~ 1-2 carry a significant risk of widespread erosion at a landscape scale because slope gradients are low enough to encourage cultivation but high enough to exert a considerable erosive forcing on the landscape under intensive use.

Topographic position on the landscape is also central to the concept of eroded soils. Because (by definition), eroded phase soils are those that have undergone accelerated erosion and are truncated, eroded phase soils can only exist where soil loss exceeds accumulation. Therefore, at a hillslope scale, eroded phase soils will only be mapped on convex or linear hillslope positions (summit to backslope). Sediment receiving (concave) accumulation positions (backslope to toeslope) by definition cannot be delineated eroded phase soils, even though they may be erosion-affected (Pennock, 1997). The exception to this is wind eroded phases (severely blown), which typically occur on low gradient landscapes due to high wind speeds, but can be characterized by both removals and accumulations of shifting dunes and blowing material (Joel, 1937, Soil Survey Division Staff, 1993). Topography also plays a central role in all mechanistic equations for the three major erosive forcings (water, wind and tillage), and therefore is critical to the location, mapping and identification of eroded soils (Renard et al., 1997, Lindstrom et al., 2000, Blanco and Lal, 2008).

Although topography exerts an influence on erosion magnitude at multiple scales, changes in topography must be more extreme than typically observed changes alone to cause accelerated erosion. Excluding intensive construction sites, even extensive changes

in topography due to tillage erosion tend to flatten rather than steepen the landscape (Li et al., 2008). Therefore topography, like climate, plays a secondary role in causing accelerated erosion after changes in biotic factors.

Parent material. The particle size distribution and mineralogy of soil parent materials play a large role in determining the erodibility of soil materials (Renard et al., 1997). Particle size distribution are included in all of the erosion prediction equations as it drives important physical factors such as soil texture, aggregation and cohesiveness, all of which play a role in erosion severity. Family particle size may be least influential in the case of tillage erosion, but can still play a strong role, as cloddiness (large clods rolling downhill), particularly in hand-tilled agricultural systems (Zhang et al., 2004). The observation that 73% of eroded phase soils have etalon family particle size classes of fine, fine-loamy and fine-silty (Table 2.3) is not surprising as these 3 family classes all have the majority of their particle size distributions lying between geometric mean diameters of 0.009 and 0.07 μm (Shirazi and Boersma, 1984) (the logarithms of which are -2.1 to -1.2), which is the peak in the RUSLE erodibility factor (K) in relationship to particle size (Renard et al., 1997).

Time. The timing of surveys relative to major changes in erosive forcings resulting in accelerated erosion can play a significant role in the identification and delineation of eroded phase soils. This timing interacts with soil type and morphology as well. For example, a soil with no KEMs that may be identified as eroded at one time period may (under the influence of different land-use) recover A horizon thickness or SOC and be unidentifiable as an eroded phase at a later period. This would result in two

different distributions of eroded phase soils. Conversely, soils with many or distinct KEMs related to fragic soil properties or fragipans (Fig 2.8) may be irreversibly truncated for practical purposes and be identifiable as eroded phase soils (assuming there is etalon representation) for millennia. Additionally, with temporal changes in land-use patterns, time may also be associated with a drift in etalon availability or morphology, which can influence erosion estimates and the delineation of eroded phases by morphology alone.

2.4.4 SSURGO eroded phase case studies

Figure 2.9 details 4 case studies at a sub-national level that demonstrate some of these important issues related to the identification and mapping of eroded phase soils.

Case Study 1: West Feliciana Parish, Louisiana and Wilkinson County, Mississippi. Figure 2.9A shows a major difference in the mapping of eroded phase soil across political boundaries. One contributing factor here may be that Mississippi as a state survey area has extensive areas of eroded lands (largely in the Mississippi Valley Loess Plains Ecoregion), so mapping of eroded phase soils was a priority. In contrast, Louisiana is comprised largely of low gradient landscapes and has relatively small extent of mapped eroded phase area (Table 2.1); consequently, mapping eroded soils was not a priority, even in West Feliciana Parish, which contains part of the Mississippi Valley Loess Plains ecoregion.

Case Study 2: Yellow Medicine, Renville and Chippewa Counties, MN: Figure 2.9B shows part of three counties (Yellow Medicine, Chippewa and Renville) in southwestern Minnesota which demonstrate the importance of soils which are sensitive to

classification changes (Hapludolls) in their eroded phase. Eroded soils are mapped on very similar landscape positions in all three counties (Fig 2.9B), but in Yellow Medicine and Renville, the eroded series are mapped as Ves-Storden, classified as Eutrudepts, whereas in Chippewa county soils on similar landscape positions are mapped as Doland-Swanlake, Hapludolls. Three of the series in these complexes (Ves, Doland and Swanlake) are highly sensitive to classification changes from Mollisols to Inceptisols or Entisols (Hapludolls and Calciudolls) (Mokma et al., 1996, Veenstra and Burras, 2011). The difference along the county boundary therefore reflects whether priority was placed on viewing the soils as "eroded Mollisols" or "eroded, but Inceptisols", with very few morphological differences, in reality.

Case Study 3: Hardin County Iowa and Central Iowa. Iowa has perhaps the most consistently mapped eroded phase soils in the continental U.S., at multiple scales, which seamlessly overlay county boundaries (Fig 2.9C and 2.9D). The attention to consistency and landscape scale factors can be seen (eroded phase soils are mapped on the same landscape units across political boundaries) so that geomorphic features can be discerned from eroded phase distributions alone (Fig 2.9C and 2.9D). This is due mainly to the very high importance of specific soils information for land values and agricultural production in the state of Iowa in general, and central Iowa in particular.

Case Study 4: The Dust Bowl Counties. Wind erosion presents a difficult problem in the mapping of eroded phase soils, highlighted by the case of the 20 Dust Bowl Counties (Fig 2.9E). In 1936, the USDA conducted an extensive, detailed survey of the 20 county heart of the dust bowl in Texas, Oklahoma, Kansas and Colorado (Fig 2.9E).

The original 1937 publication of the survey results (Joel, 1937) revealed that a significant proportion of the land was affected by both erosion and accumulation (expected in the largely flat landscapes of the high plains ecoregion (Ave TRI = 1.18). Wind erosion is unique in that flat landscapes are conducive to high wind velocities, wind erosion and sediment reworking. The combined effects of removal and accumulation make the mapping of eroded soils more difficult as the etalon becomes more difficult to define. In the original survey, ~ 74% of the lands surveyed were affected by both removal and accumulation, while only 20% were affected by removal only (Table 2.7). SSURGO eroded phase soils are not particularly well aligned with any classification from the 1936 Dust Bowl surveys (Table 2.7). None of the Texas counties have eroded map units, demonstrating a strong difference in mapping philosophy between political boundaries (Fig 2.9E). The reason for these discrepancies in an area that is historically extensively eroded (such as the heart of the Dust Bowl counties) is due to these multiple factors. Additional factors include the fact that the surveys for many of these counties were finalized in the 1970s and 1980s, 30-40 years after the major events of the Dust Bowl. This time period, particularly in a Mollisol dominated landscape with few to no robust KEMs may have minimized the ability to map eroded phases. In contrast, eroded soils in the Piedmont (primarily driven by water erosion and with stronger KEMs (Ultisols and Alfisols) have been consistently mapped well after a century of the most intensive land use (Trimble, 1975).

2.4.5 Erosion severity and crop yield effects. The effects of erosion on crop yields are

generally negative and have been summarized mechanistically as 1) decreases in water storage or available water capacity, 2) decreases in nutrient availability and 3) physical limitations to root growth (Foster et al., 1985). Changes in organic matter due to erosion are linked to both loss of water storage capacity and nutrient availability (Hudson, 1994, Woomer et al., 1994). Changes due to the loss of organic matter are perhaps the most easily replaceable with improved management, whereas changes in depth to a root-restricting layer may be considered relatively irreversible in the timescales under consideration (Wolman, 1985).

Experimental designs for studying the effects of erosion on crop yields have traditionally relied upon topsoil removals or additions, topographic transects, or comparative plots (Bakker et al., 2004). Each of these methods present challenges that make studies unrepresentative of real conditions because soil property change is either too abrupt (as in topsoil removal or addition experiments – no mixing) or utilize space-for-time substitutions and are susceptible to variation in soil properties across the landscape (transect and comparative plot) (Meyer et al., 1985, Bakker et al., 2004). Recent meta-analyses of yield-normalized and erosion adjusted as depth of soil loss (in cm) have shown that the apparent effects of erosion on crop yields are highly dependent on experimental design (Fig 2.10, Bakker et al., 2004). On average addition and desurfacing experimental designs show yield normalized losses of 27% per 10cm of soil loss, whereas transect and comparative plot experimental designs show yield normalized losses of 11% and 5%, respectively (Fig 2.10). When the genesis of eroded soils is understood, the reasons for these strong experimental differences become apparent. Soil

desurfacing experiments provide an example of very sudden truncation, exposing subsoil properties with no mixing of topsoil materials. On the other hand, the comparative plot method uses space-for time substitution and results in much greater incorporation of surficial materials as erosion proceeds (Bakker et al., 2004). Additionally, in some cases (because the comparative plot method depends on a wide spatial distribution), differences in management due to land ownership may affect or even ameliorate some effects of the most highly eroded plots. For example, in Graveel et al., (2002) the severely eroded plots had twice the amount of N and P fertilizer applied as the slightly or moderately eroded plots. The transect method lies somewhere in between these two extremes, as it is effectively a space-for-time substitution, but also is heavily influenced by landscape heterogeneity which may increase the apparent effect of erosion severity (Bakker et al., 2004).

Although general trends can be revealed from meta-analyses, it is well known that the relationship between erosion and yield change is highly complex and dependent on soil type (Hall et al., 1985). Linking diagnostic horizons and soil classification to more specific relationships between erosion and yield has been an object of study at the intersection of pedology and agronomy. It is generally recognized that only three diagnostic horizons tend to enhance crop growth (2 surface – mollic and histic and 1 subsurface – cambic) (Hall et al., 1985). In contrast to the cambic horizon, most subsurface diagnostic horizons are restrictive to root growth or detrimental to crop yields (Pennock, 1997), thus as these key morphologies and horizons move upward in the profile due to truncation from accelerated forcing, a depression in crop yields occurs

(Graveel et al., 2002, Bakker et al., 2004).

2.4.6 Conclusions

The distribution of eroded phase soils in the SSURGO database represents an important characterization of erosion-affected lands in the United States that can be highly useful when caveats are understood. It is important to avoid the temptation to see these maps as permanent, as they are static (Veenstra and Burras, 2011) and spatial and temporal trends in accelerated erosion remain highly dynamic (USDA, 2013). The U.S. soil survey was uniquely poised to take advantage of the timeframe of its inception to map eroded phase soils, and the distribution of these map units have proven valuable for studies of the effects of erosion on crop yields, sediment losses, and land-use histories. The structure and execution of the U.S. soil survey at a county level provided the extensive local field experience and high-level, integrative activities that are required to map eroded phases in high detail over large spatial extents and is unlikely to be replicated in the future.

However, novel tools that integrate remote sensing spectral data with soil properties and erosion metrics may provide new ways to integrate dynamic information on eroded soils (Vagen et al., 2013). Additionally, novel markers such as meteoric ^{10}Be (Harden et al., 2002) and fly-ash (Olson et al., 2013) may provide independent estimates of total truncation or erosion depth, which can be subsequently matched up with morphology, providing quantitative assessments at large scale in fine detail. Mapping eroded phase soils remains important as soil information is compiled, digitized and improved in food insecure developing countries (Lal and Stewart, 2011), and lessons

learned from the U.S. experience will be critical to produce efficient strategies for mapping eroded soils for use in research and land management far into the future.

	Total		Eroded Soils					
	Land Area[1]	Non-Water Mapped[2]	Eroded Phase Mapped (km^2)[2]	% of Total Land Area[1,2]	% of Total Mapped Area[2]	# Unique Eroded Map Units[2]	Eroded - Severe (km^2)[2]	% Severe
Alabama	131,426	130,908	19,944	15.2	14.7	1,011	2,820	14.1
Arizona	294,311	287,789	1,512	0.5	0.5	33	126	8.3
Arkansas	134,856	134,368	2,310	1.7	1.7	122	50	2.1
California	403,932	379,282	14,554	3.6	3.8	860	1,367	9.4
Colorado	268,626	241,108	2,285	0.9	0.9	65	120	5.3
Connecticut	12,548	12,496	-	-	-	-	-	-
Delaware	5,061	5,034	-	-	-	-	-	-
Florida	139,670	133,445	184	0.1	0.1	12	30	16.2
Georgia	149,976	149,339	28,531	19.0	18.7	654	5,535	19.4
Idaho	214,314	162,094	354	0.2	0.2	38	8	2.3
Illinois	143,959	143,413	30,080	20.9	20.6	1,078	6,081	20.2
Indiana	92,895	92,481	24,323	26.2	26.0	961	6,025	24.8
Iowa	144,700	144,164	40,246	27.8	27.6	976	3,955	9.8
Kansas	211,900	211,793	12,540	5.9	5.9	179	85	0.7
Kentucky	102,895	102,833	23,720	23.1	22.6	717	9,135	38.5
Louisiana	112,825	110,147	112	0.1	0.1	8	35	31.0
Maine	79,930	79,590	757	0.9	0.8	28	6	0.8
Maryland	25,315	25,177	1,624	6.4	5.1	133	200	12.3
Massachusetts	20,306	20,220	-	-	-	-	-	-
Michigan	147,122	146,739	2,724	1.9	1.8	502	232	8.5
Minnesota	206,189	207,987	10,010	4.9	4.6	302	30	0.3
Mississippi	121,489	120,685	26,467	21.8	21.1	555	6,316	23.9
Missouri	178,414	178,094	38,697	21.7	21.4	411	2,485	6.4
Montana	376,978	360,853	400	0.1	0.1	20	-	-
Nebraska	199,098	198,641	30,782	15.5	15.4	298	976	3.2
Nevada	284,445	270,502	872	0.3	0.3	28	-	-
New Hampshire	23,227	20,263	-	-	-	-	-	-
New Jersey	19,210	19,074	341	1.8	1.6	65	12	3.4
New Mexico	314,308	295,278	3,506	1.1	1.2	71	668	19.1
New York	122,284	114,503	836	0.7	0.7	173	139	16.6
North Carolina	126,161	125,542	15,392	12.2	11.2	470	365	2.4
North Dakota	178,647	179,205	22	0.0	0.0	6	10	46.9
Ohio	106,055	105,760	14,358	13.5	13.4	957	669	4.7
Oklahoma	177,847	177,215	14,419	8.1	8.0	315	3,806	26.4
Oregon	248,628	162,102	75	0.0	0.0	11	-	-
Pennsylvania	116,073	115,733	4,202	3.6	3.6	294	123	2.9
Rhode Island	2,707	2,744	-	-	-	-	-	-
South Carolina	77,982	77,942	9,324	12.0	11.5	356	1,467	15.7
South Dakota	196,539	196,227	742	0.4	0.4	19	-	-
Tennessee	106,752	107,710	26,127	24.5	23.7	1,410	8,436	32.3
Texas	678,049	682,294	13,445	2.0	1.9	353	1,497	11.1
Utah	212,749	151,013	2,672	1.3	1.7	194	71	2.7
Vermont	23,957	23,872	30	0.1	0.1	5	-	-
Virginia	102,548	102,131	12,672	12.4	11.9	801	3,228	25.5
Washington	172,348	154,003	1,342	0.8	0.9	165	251	18.7
West Virgina	62,362	62,202	6,138	9.8	9.8	133	6,138	100.0
Wisconsin	140,662	140,144	24,199	17.2	16.6	1,063	195	0.8
Wyoming	251,488	235,389	110	0.0	0.0	6	-	-
Continental U.S.	7,663,759	7,299,525	462,979	6.0	6.3	15,202	72,690	15.7

Table 2.1. Area, distribution and proportions of eroded phase soils by state and in the conterminous U.S.
[1]U.S. Census Bureau;
[2]SSURGO Database (USDA-NRCS, 2014).

	Cultivated Lands					Gullied Lands	
	Area (km^2)[3]	% of Total Land Area[1,3]	On Eroded Phase (km^2)[2,3]	% of Total Eroded Cultivated[2,3]	% on Eroded Phase[1,2]	Area (km^2)[3]	%Gullied Eroded + Gullied[2,3]
Alabama	7,790	5.9	1,391	7.0	17.9	170	0.8
Arizona	7,614	2.6	25	1.6	0.3	192	11.2
Arkansas	28,246	20.9	175	7.6	0.6	84	3.5
California	40,489	10.0	433	3.0	1.1	860	5.6
Colorado	33,915	12.6	854	37.4	2.5	585	20.4
Connecticut	690	5.5	-	-	-	-	-
Delaware	2,073	41.0	-	-	-	-	-
Florida	11,457	8.2	21	11.3	0.2	3	1.8
Georgia	19,161	12.8	1,608	5.6	8.4	154	0.5
Idaho	21,572	10.1	104	29.4	0.5	15	4.2
Illinois	89,733	62.3	14,637	50.2	16.3	-	-
Indiana	47,789	51.4	9,413	38.7	19.7	63	0.3
Iowa	97,823	67.6	24,565	61.0	25.1	323	0.8
Kansas	98,314	46.4	6,077	48.5	6.2	5	0.0
Kentucky	12,316	12.0	2,866	12.1	23.3	93	0.4
Louisiana	19,562	17.3	6	5.4	0.0	-	-
Maine	1,247	1.6	24	3.2	1.9	-	-
Maryland	5,538	21.9	346	21.3	6.2	-	-
Massachusetts	532	2.6	-	-	-	-	-
Michigan	34,443	23.4	1,477	54.2	4.3	2	0.1
Minnesota	80,100	38.8	6,111	61.0	7.6	-	-
Mississippi	18,138	14.9	1,108	4.2	6.1	3,107	10.5
Missouri	38,759	21.7	10,541	27.2	27.2	57	0.1
Montana	50,720	13.5	7	1.7	0.0	428	51.7
Nebraska	75,540	37.9	17,312	56.2	22.9	54	0.2
Nevada	1,709	0.6	2	0.2	0.1	213	19.7
New Hampshire	120	0.5	-	-	-	-	-
New Jersey	2,008	10.5	45	13.3	2.3	-	-
New Mexico	7,924	2.5	199	5.7	2.5	431	11.0
New York	13,517	11.1	200	23.9	1.5	-	-
North Carolina	21,646	17.2	2,511	16.3	11.6	116	0.7
North Dakota	89,924	50.3	7	32.4	0.0	228	91.2
Ohio	38,185	36.0	3,024	21.1	7.9	1	0.0
Oklahoma	34,033	19.1	2,207	15.3	6.5	1,393	8.8
Oregon	12,461	5.0	30	40.2	0.2	-	-
Pennsylvania	14,387	12.4	907	21.6	6.3	1	0.0
Rhode Island	55	2.0	-	-	-	-	-
South Carolina	8,226	10.5	156	1.7	1.9	210	2.2
South Dakota	64,275	32.7	471	63.4	0.7	22	2.9
Tennessee	11,633	10.9	4,321	16.5	37.1	1,207	4.4
Texas	94,171	13.9	1,074	8.0	1.1	495	3.5
Utah	6,257	2.9	175	6.6	2.8	170	6.0
Vermont	913	3.8	0	1.3	0.0	-	-
Virginia	6,613	6.4	735	5.8	11.1	14	0.1
Washington	24,398	14.2	659	49.1	2.7	-	-
West Virgina	406	0.7	5	0.1	1.2	-	-
Wisconsin	36,985	26.3	9,932	41.0	26.9	-	-
Wyoming	5,593	2.2	6	5.7	0.1	2,149	95.1
Continental U.S.	1,338,999	17.5	125,769	27.2	9.4	12,846.4	2.7

Table 2.2. Area, distribution and proportion of gullied lands and eroded phase soils on cultivated lands by state and in the conterminous U.S. [1]U.S. Census Bureau; [2]SSURGO Database (USDA-NRCS, 2014); [3]2013 National Cultivated Layer (USDA-NASS 2014)

	Class	# Named Soil Series[1,2]	Frequency (%)
Order	**Alfisols**	943	41.6
	Mollisols	541	23.9
	Ultisols	305	13.5
	Inceptisols	170	7.5
	Entisols	130	5.7
	Aridisols	92	4.1
	Vertisols	42	1.9
	Spodosols	31	1.4
	Andisols	11	0.5
Family Particle Size Classes	Very Fine	22	1.0
	Fine	644	28.4
	Clayey - Total	**697**	**30.8**
	Fine-loamy	592	26.1
	Coarse-loamy	200	8.8
	Loamy - Total	**792**	**35.0**
	Fine-silty	418	18.5
	Coarse-silty	63	2.8
	Silty - Total	**481**	**21.2**
	Sandy	**84**	**3.7**
	Skeletal Classes	**119**	**5.3**
	Ashy,Pumiceous or Medial	**11**	**0.5**
All Mapped Eroded Phase Soils	**Total**	**2265**	**100**

Table 2.3. Distribution of officially named series with eroded phases by order and family particle size class. [1]USDA-NRCS Official Series Descriptions; [2]SSURGO Database (USDA-NRCS, 2014).

		Total	Eroded Soils		
Type	Ecoregion	Total Area[1]	Eroded Phase Mapped (km^2)[2]	% of Total Area[1,2]	TRI (Mean)
Type IV Ecoregions: > 85th %tile Eroded, < 85th %tile Cultivated	Driftless Area	47,386	21,390	45.1	2.11
	Mississippi Valley Loess Plains	51,810	19,551	37.7	1.16
	Piedmont	166,117	57,448	34.6	1.67
	Interior Plateau	123,527	37,481	30.3	1.84
	Central Irregular Plains	114,323	32,692	28.6	1.21
	Southern CA/N Baja Coast	20,955	3,842	18.3	3.03
	Type IV Total	**524,119**	**172,404**	**32.9**	**1.84**
Type III Ecoregions: > 85th %tile Eroded, > 85th %tile Cultivated	Interior River Valleys and Hills	120,448	30,049	24.9	1.13
	Western Corn Belt Plains	228,143	55,876	24.5	1.13
	Southeastern WI Till Plains	31,350	7,095	22.6	1.22
	Eastern Corn Belt Plains	86,858	18,961	21.8	0.85
	Central Corn Belt Plains	76,510	11,309	14.8	0.59
	Type III Total	**543,309**	**123,290**	**22.7**	**0.98**
Type II Ecoregions: < 85th %tile Eroded, > 85th %tile Cultivated	Central Great Plains	274,963	28,352	10.3	1.21
	S MI/N IN Drift Plains	53,035	2,153	4.1	0.89
	Huron/Erie Lake Plains	31,595	917	2.9	0.26
	Lake Agassiz Plain	45,060	516	1.1	0.22
	Central California Valley	46,490	446	1.0	0.79
	Northern Glaciated Plains	134,806	983	0.7	0.74
	Mississippi Alluvial Plain	116,119	415	0.4	0.17
	Type II Total	**702,068**	**33,783**	**4.8**	**0.61**
Type I Ecoregions: < 85th %tile Eroded, < 85th %tile Cultivated	Western Allegheny Plateau	81,440	11,126	13.7	2.23
	Texas Blackland Prairies	43,382	5,771	13.3	1.12
	Southeastern Plains	328,885	36,446	11.1	1.14
	Erie Drift Plain	30,960	3,372	10.9	1.87
	Ridge and Valley	116,716	12,671	10.9	2.85
	Southwestern Appalachians	37,995	3,982	10.5	2.43
	Central CA Fthills & Cstal Mtns	76,679	7,231	9.4	3.25
	Cross Timbers	88,188	8,304	9.4	1.58
	Southern California Mountains	15,838	1,240	7.8	4.02
	North Central Hardwood Forests	88,910	5,978	6.7	1.11
	Flint Hills	27,932	1,647	5.9	1.48
	Northern Piedmont	31,365	1,791	5.7	2.09
	Arkansas Valley	28,422	1,474	5.2	2.14
	East Central Texas Plains	55,753	2,866	5.1	1.05
	Blue Ridge	46,595	1,768	3.8	3.43
	Northern Allegheny Plateau	46,510	1,412	3.0	2.94
	Ozark Highlands	106,391	2,898	2.7	1.93
	Boston Mountains	14,178	332	2.3	2.90
	Wasatch and Uinta Mountains	45,693	842	1.8	3.82
	Columbia Plateau	83,131	1,369	1.6	2.78
	Acadian Plains and Hills	45,250	633	1.4	2.15
	High Plains	288,320	3,964	1.4	1.19
	Southwestern Tablelands	198,829	2,521	1.3	1.94
	Sierra Nevada	53,103	656	1.2	4.07
	South Central Plains	152,132	1,738	1.1	1.03
	Chihuahuan Deserts	164,060	1,797	1.1	2.16
	Eastern Great Lakes Lowlands	40,302	434	1.1	1.77

Table 2.4. Area, distribution and proportions of eroded phase soils by ecoregion and ecoregion type. [1]U.S. EPA; [2]SSURGO Database (USDA-NRCS, 2014).

		Total	Eroded Soils		
Type	Ecoregion	Total Area[1]	Eroded Phase Mapped (km^2)[2]	% of Total Area[1,2]	TRI (Mean)
Type I Ecoregions: < 85th %tile Eroded, < 85th %tile Cultivated	Madrean Archipelago	39,650	375	0.9	3.03
	Coast Range	54,250	393	0.7	3.46
	Central Appalachians	62,050	418	0.7	3.02
	Central Basin and Range	308,790	2,052	0.7	3.10
	Arizona/New Mexico Mountains	110,910	674	0.6	3.25
	Atlantic Coastal Pine Barrens	14,308	81	0.6	0.69
	Klamath Mtns/CA Coast Range	48,358	255	0.5	4.11
	Nebraska Sand Hills	59,123	268	0.5	1.42
	Middle Atlantic Coastal Plain	78,476	302	0.4	0.20
	Snake River Plain	53,627	199	0.4	2.17
	Northeastern Coastal Zone	42,067	130	0.3	2.01
	Ouachita Mountains	26,895	75	0.3	2.46
	Arizona/New Mexico Plateau	146,859	363	0.2	2.53
	Mojave Basin and Range	127,690	312	0.2	3.28
	Northern Lakes and Forests	191,883	443	0.2	1.36
	Northern Basin and Range	140,198	321	0.2	2.97
	Eastern Cascades Slopes & Fthills	53,257	122	0.2	3.15
	Colorado Plateaus	136,575	300	0.2	3.23
	Sonoran Basin and Range	118,370	217	0.2	2.46
	Northwestern Glaciated Plains	174,882	320	0.2	1.74
	Western Gulf Coastal Plain	75,406	136	0.2	0.07
	North Cascades	30,395	47	0.2	4.52
	Northwestern Great Plains	357,584	507	0.1	2.15
	Southern Rockies	145,702	197	0.1	3.70
	Southern Texas Plains	53,423	69	0.1	1.07
	Northern Rockies	81,961	106	0.1	3.91
	North Central Appalachians	26,727	32	0.1	2.89
	Edwards Plateau	74,964	89	0.1	1.86
	Middle Rockies	164,462	171	0.1	3.72
	Southern Coastal Plain	141,414	112	0.1	0.25
	Northeastern Highlands	124,197	75	0.1	3.06
	Cascades	58,854	32	0.1	3.92
	Blue Mountains	70,911	26	0.0	3.61
	Willamette Valley	14,885	3	0.0	2.62
	Wyoming Basin	132,682	16	0.0	2.64
	Idaho Batholith	60,283	0	0.0	4.16
	Southern Florida Coastal Plain	22,533	-	0.0	0.00
	Northern Minnesota Wetlands	22,829	-	0.0	0.32
	Puget Lowland	16,970	-	0.0	2.75
	Canadian Rockies	18,880	-	0.0	4.26
	Type I Total	**6,020,239**	**133,500**	**2.2**	**2.41**
	Continental U.S.	**7,789,735**	**462,976**	**5.9**	**2.14**

Table 2.4 (Cont). Area, distribution and proportions of eroded phase soils by ecoregion and ecoregion type. [1]U.S. EPA; [2]SSURGO Database (USDA-NRCS, 2014).

		Cultivated Lands				
Type	Ecoregion	Area (km^2)[3]	% of Total Area[1,3]	On Eroded Phase (km^2)[2,3]	% of Total Eroded Cultivated[2,3]	% on Eroded Phase[1,2]
Type IV Ecoregions: > 85th %tile Eroded, < 85th %tile Cultivated	Driftless Area	16,590	35.0	8,707.7	40.7	52.5
	Mississippi Valley Loess Plains	10,057	19.4	4,260.1	21.8	42.4
	Piedmont	7,939	4.8	3,022.4	5.3	38.1
	Interior Plateau	12,450	10.1	3,274.8	8.7	26.3
	Central Irregular Plains	31,254	27.3	8,693.8	26.6	27.8
	Southern CA/N Baja Coast	370	1.8	108.9	2.8	29.4
	Type IV Total	**78,660**	**15.0**	**28,067.8**	**16.3**	**35.7**
Type III Ecoregions: > 85th %tile Eroded, > 85th %tile Cultivated	Interior River Valleys and Hills	54,265	45.1	10,910.8	36.3	20.1
	Western Corn Belt Plains	161,361	70.7	37,306.8	66.8	23.1
	Southeastern WI Till Plains	14,241	45.4	3,455.8	48.7	24.3
	Eastern Corn Belt Plains	50,732	58.4	8,296.2	43.8	16.4
	Central Corn Belt Plains	55,945	73.1	7,239.7	64.0	12.9
	Type III Total	**336,544**	**61.9**	**67,209.3**	**54.5**	**20.0**
Type II Ecoregions: < 85th %tile Eroded, > 85th %tile Cultivated	Central Great Plains	124,216	45.2	12,616.7	44.5	10.2
	S MI/N IN Drift Plains	23,362	44.0	1,030.6	47.9	4.4
	Huron/Erie Lake Plains	18,492	58.5	566.1	61.7	3.1
	Lake Agassiz Plain	32,589	72.3	371.4	72.0	1.1
	Central California Valley	32,386	69.7	111.9	25.1	0.3
	Northern Glaciated Plains	83,982	62.3	633.3	64.4	0.8
	Mississippi Alluvial Plain	61,909	53.3	216.6	52.2	0.3
	Type II Total	**376,937**	**53.7**	**15,546.6**	**46.0**	**4.1**
Type I Ecoregions: < 85th %tile Eroded, < 85th %tile Cultivated	Western Allegheny Plateau	3,817	4.7	148.6	1.3	3.9
	Texas Blackland Prairies	8,589	19.8	621.5	10.8	7.2
	Southeastern Plains	45,182	13.7	3,510.8	9.6	7.8
	Erie Drift Plain	6,382	20.6	849.0	25.2	13.3
	Ridge and Valley	8,637	7.4	1,001.4	7.9	11.6
	Southwestern Appalachians	727	1.9	280.4	7.0	38.6
	Central CA Fthills & Cstal Mtns	3,520	4.6	197.1	2.7	5.6
	Cross Timbers	5,040	5.7	340.0	4.1	6.7
	Southern California Mountains	32	0.2	8.5	0.7	26.5
	North Central Hardwood Forests	28,924	32.5	2,939.8	49.2	10.2
	Flint Hills	4,503	16.1	439.9	26.7	9.8
	Northern Piedmont	5,307	16.9	287.9	16.1	5.4
	Arkansas Valley	770	2.7	4.4	0.3	0.6
	East Central Texas Plains	2,129	3.8	41.3	1.4	1.9
	Blue Ridge	561	1.2	47.7	2.7	8.5
	Northern Allegheny Plateau	4,679	10.1	99.1	7.0	2.1
	Ozark Highlands	1,958	1.8	275.0	9.5	14.0
	Boston Mountains	8	0.1	0.1	-	0.8
	Wasatch and Uinta Mountains	631	1.4	31.8	3.8	5.0
	Columbia Plateau	31,914	38.4	741.5	54.1	2.3
	Acadian Plains and Hills	1,197	2.6	23.7	3.7	2.0
	High Plains	117,293	40.7	1,826.0	46.1	1.6
	Southwestern Tablelands	13,143	6.6	236.3	9.4	1.8
	Sierra Nevada	11	0.0	0.8	0.1	6.6
	South Central Plains	3,120	2.1	8.6	0.5	0.3
	Chihuahuan Deserts	3,835	2.3	20.2	1.1	0.5
	Eastern Great Lakes Lowlands	8,190	20.3	131.3	30.2	1.6

Table 2.5. Area, distribution and proportions of eroded phase soils on cultivated lands by ecoregion and ecoregion type. [1]U.S. EPA; [2]SSURGO Database (USDA-NRCS, 2014).

		Cultivated Lands				
Type	Ecoregion	Area (km^2)[3]	% of Total Area[1,3]	On Eroded Phase (km^2)[2,3]	% of Total Eroded Cultivated[2,3]	% on Eroded Phase[1,2]
Type I Ecoregions: < 85th %tile Eroded, < 85th %tile Cultivated	Madrean Archipelago	1,625	4.1	15.1	4.0	0.9
	Coast Range	75	0.1	1.8	0.5	2.4
	Central Appalachians	615	1.0	11.2	2.7	1.8
	Central Basin and Range	6,768	2.2	116.5	5.7	1.7
	Arizona/New Mexico Mountains	28	0.0	-	-	-
	Atlantic Coastal Pine Barrens	1,463	10.2	14.8	18.2	1.0
	Klamath Mtns/CA Coast Range	150	0.3	-	-	-
	Nebraska Sand Hills	3,367	5.7	118.6	44.2	3.5
	Middle Atlantic Coastal Plain	17,477	22.3	128.0	42.4	0.7
	Snake River Plain	14,688	27.4	27.6	13.9	0.2
	Northeastern Coastal Zone	1,617	3.8	1.3	1.0	0.1
	Ouachita Mountains	13	0.0	0.1	0.1	0.8
	Arizona/New Mexico Plateau	2,163	1.5	0.1	-	-
	Mojave Basin and Range	230	0.2	3.5	1.1	1.5
	Northern Lakes and Forests	8,352	4.4	178.2	40.2	2.1
	Northern Basin and Range	3,596	2.6	1.1	0.3	-
	Eastern Cascades Slopes & Fthills	2,013	3.8	1.0	0.8	0.1
	Colorado Plateaus	3,166	2.3	29.2	9.7	0.9
	Sonoran Basin and Range	8,255	7.0	6.1	2.8	0.1
	Northwestern Glaciated Plains	67,836	38.8	67.3	21.0	0.1
	Western Gulf Coastal Plain	20,359	27.0	14.0	10.3	0.1
	North Cascades	58	0.2	0.8	1.6	1.3
	Northwestern Great Plains	42,501	11.9	30.3	6.0	0.1
	Southern Rockies	345	0.2	-	-	-
	Southern Texas Plains	3,045	5.7	1.2	1.8	-
	Northern Rockies	2,328	2.8	24.2	22.8	1.0
	North Central Appalachians	233	0.9	1.0	3.0	0.4
	Edwards Plateau	778	1.0	4.0	4.5	0.5
	Middle Rockies	3,386	2.1	6.3	3.7	0.2
	Southern Coastal Plain	7,944	5.6	20.2	18.0	0.3
	Northeastern Highlands	1,643	1.3	3.6	4.8	0.2
	Cascades	54	0.1	-	-	-
	Blue Mountains	1,540	2.2	4.2	16.3	0.3
	Willamette Valley	2,230	15.0	0.5	16.2	-
	Wyoming Basin	2,284	1.7	0.3	2.1	-
	Idaho Batholith	73	0.1	-	-	-
	Southern Florida Coastal Plain	2,819	12.5	-	-	-
	Northern Minnesota Wetlands	1,092	4.8	-	-	-
	Puget Lowland	553	3.3	-	-	-
	Canadian Rockies	2	0.0	-	-	-
	Type I Total	**546,865**	**9.1**	**14,944.8**	**11.2**	**2.7**
	Continental U.S.	**1,339,006**	**17.2**	**125,769**	**27.2**	**9.4**

Table 2.5 (Cont). Area, distribution and proportions of eroded phase soils on cultivated lands by ecoregion and ecoregion type. [1]U.S. EPA; [2]SSURGO Database (USDA-NRCS, 2014).

Soil Series	County/State	Selected Etalon Morphology	Eroded Morphology	Survey Edition	Eroded Phase	Key Morphological designators
Zanesville	Vanderburgh (IN)	26-34in - Bx	20 - 24 in - Bx	1976	Severely Eroded	Depth to fragipan 6-10 inches shallower
Pawnee (3-7% slopes)	Nemaha (KS)	0-7 in - A: CL 7-12 in - AB: CL 12-41in - Bt: C	0-6 in - A: C 6-39 in - Bt: C	2005	Eroded	A horizon is C, eroded into original Bt/BC
Palouse (25-40% slopes)	Whitman (WA)	0-(10-12) in - A	0-(3-6) in - A	1980	Eroded	A horizon 6-9 inches thinner
Renshaw (6-12% slopes)	Pope (MN)	0-(6-12) in - A (10YR 2/1)	0-(2-8) in - A (10YR 2/1 mixed w/ 10YR 3/3)	1972	Eroded	A 4-10 inches shallower, recognizable B material mixed
Marlton (10-15% slopes)	Gloucester (NJ)	0-10 in - Ap/A: (2.5Y 4/2, 10YR 5/6), SL 10 + in - Bt: (5Y 4/4), C	0-7 in - Ap: (5Y 4/4), C	1962	Severely Eroded	A horizon is C, eroded into original Bt
Grina	Lander (NV)	0-5 in A: GRL 0-5% CB/ST, 30-45% pebbles	0-3 in A: VGRL, 0-5% CB/ST, 55-70% pebbles	1992	Eroded	Significantly higher proportion of coarse fragments in top horizon
Clarion (2-5% slopes)	Hamilton (IA)	0-7 in - Ap: (10YR 2/1) 7-18 in - A: (10YR 2/2, 10YR 3/3) 18-36 in - Bw: (10YR 4/4) 36-60 in - Ck: (10YR 5/6)	0-8 - Ap: (10YR 3/2, mixed streaks and pockets of 10YR 4/3, 10YR 5/3) 8-28 in - Bw 28-60 in - Ck	1986	Moderately Eroded	A horizon lighter, mixed with B horizon, depth to Ck 8in shallower
Mexico (1-3% slopes)	Boone (MO)	0-7 in - Ap: SiL 7-10 in - E: SiL 10-13 in - BE: SiCL 13-27 in - Btg: SiC 27-60 in - 2Btg: SiCL	0-7 in - Ap: SiL 7-22 in - Btg1: SiC 22-41 in - Btg2: SiCL 41-60 in - 2BC 41-60, SiL	2001	Eroded	No E or BE Upper Bt directly below surface horizon
Blanchard (12-35% slopes)	Upper Flathead Valley Area (MT)	0-7 in - Ap: non-calcareous 7-18 in - C1: slightly calcareous 18-30 - C2: calcareous, strong effervescence	0-7 in - Ap: calcareous	1960	Wind Eroded	Calcareous material (normally 7-18 inches deep is exposed at surface
Mapleton (8-15% slopes)	Aroostook (ME)	0-7 in - Ap: (10YR 4/3), SiL 24-30 - R	0-7 in - Ap: (mixed 10YR 4/3 and 10YR 5/6 18-24 - R	1958	Eroded	Ap mixed with original B horizon, DTB 6-12 inches shallower
Tama (5-9% slopes)	Tama (IL)	0-6 in - Ap 6-14 in - A: (10YR 2/2), SiCL 14-18in - BA (10YR 3/2, 4/3) 18-32 - Bt: (10YR 4/3), SiCL 32-45 in- BC (10YR 4/4), SiCL	0-6 in - Ap (10YR 4/3 mixed w streaks of 10YR 2/2) 6-33 in - Bt/BC	1995	Severely Eroded	No A below Ap, directly to Bt/BC, bottom of BC 12 in shallower
Downs (2-6% slopes)	Buffalo (WI)	0-(8-12)in - Ap/A	0-(4-8) in Ap/A	1962	Moderately Eroded	Ap/A 4-8 inches shallower
Pentz (9-16% slopes)	Amador Area (CA)	0-10 in - A 10-19 in - Bw 19+ in Cr	0-(0-8) in - A 14+ in - Cr	1965	Eroded	A horizon shallower, depth to rhyolite Cr 5-10 inches shallower.

Table 2.6. Selected examples of key morphologies differentiating etalon and eroded phase soils in published county-level soil surveys across the U.S.

	Classification (Joel, 1937)	State				All	
		TX	OK	CO	KS	Total	Proportion
SSURGO ERODED PHASE	**None**	-	2,318	569	-	2,887	0.9
	Removal - Wind Only	-	1,390	6,897	254	8,542	2.7
	Removal - Water	-	-	1,021	-	1,021	0.3
	Removal - Wind and Water	-	17,306	4,794	109	22,209	7.1
	Removal Only Total	-	18,696	12,713	363	31,771	10.2
	Both - Predominantly Removal	-	317	3,603	52	3,972	1.3
	Both - Predominantly Accumulation	-	174,774	51,786	40,181	266,742	85.8
	Accumulation Only	-	-	5,073	456	5,529	1.8
	Total	**-**	**196,105**	**73,743**	**41,052**	**310,900**	**100.0**
	Proportion (%)	**-**	**63.1**	**23.7**	**13.2**	**100.0**	
1936-1937 SURVEY (Joel, 1937)	**None**	219,014	82,216	180,806	29,680	511,716	3.1
	Removal - Wind Only	590,520	44,008	502,846	40,596	1,177,969	7.2
	Removal - Water	756,316	16,375	276,326	-	1,049,017	6.4
	Removal - Wind and Water	136,457	456,450	436,664	79,828	1,109,399	6.8
	Removal Only	1,483,293	516,833	1,215,836	120,424	3,336,385	20.5
	Both - Predominantly Removal	95,861	13,646	111,554	8,870	229,931	1.4
	Both - Predominantly Accumulation	4,079,396	3,040,273	2,118,844	2,611,796	11,850,309	72.8
	Accumulation Only	289,972	-	46,737	13,305	350,013	2.2
	Total	**6,167,537**	**3,652,967**	**3,673,776**	**2,784,074**	**16,278,354**	**100.0**
	Proportion (%)	**37.9**	**22.4**	**22.6**	**17.1**	**100.0**	

Table 2.7. Area and proportions of erosion categories in the 20 county Dust Bowl region surveyed by Joel (1937), and with respect to the distribution of eroded phase soils from the SSURGO database, grouped as described in methods. Digitized spatial data for Joel (1937) from Cunfer et al. (2011).

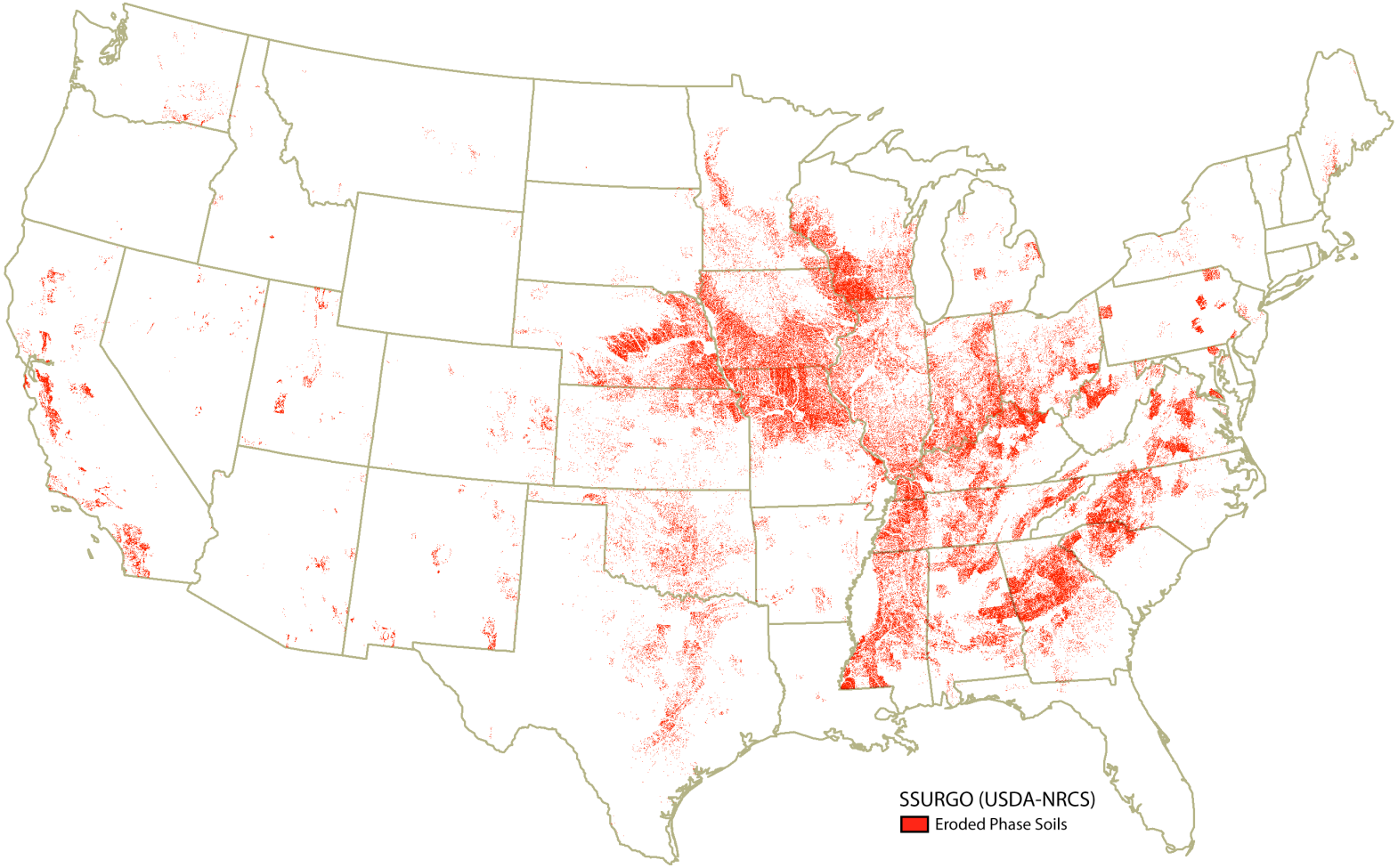

Figure 2.1. Distribution of eroded phase soils in the continental U.S.

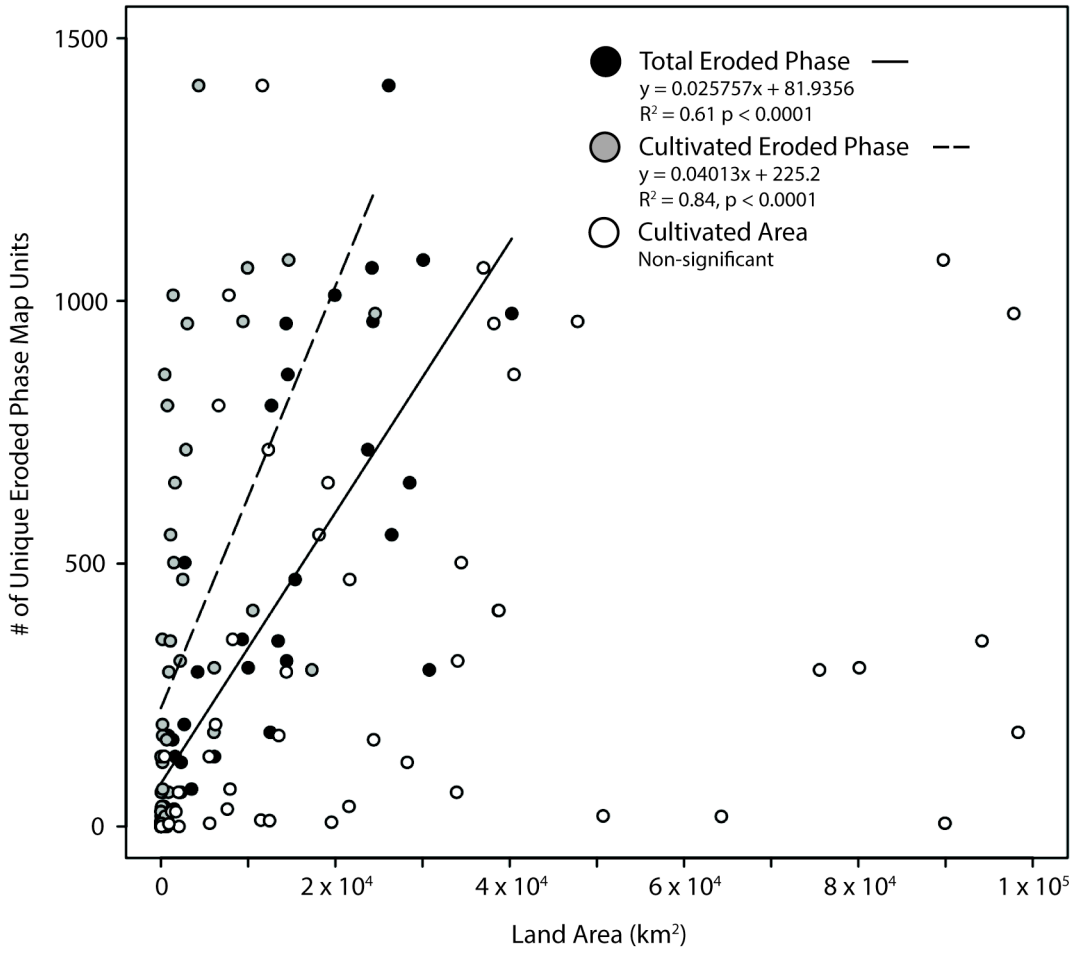

Figure 2.2. Relationship of total unique eroded phase map units with total area mapped as eroded phase, area of cultivated lands on eroded phase soils, and cultivated area by state.

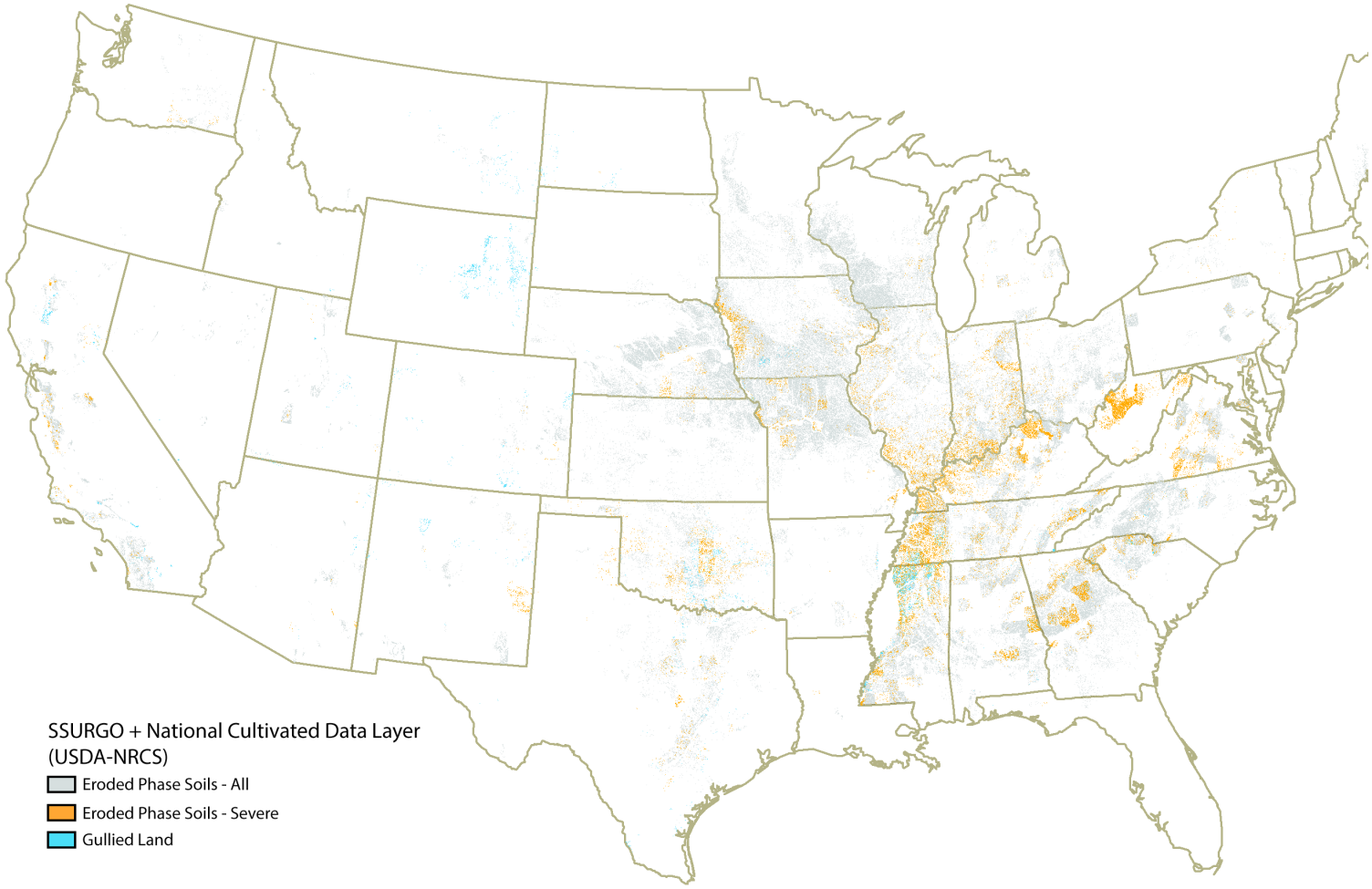

Figure 2.3. Distribution of severely eroded soils, gullied complexes, and eroded soils in the continental U.S.

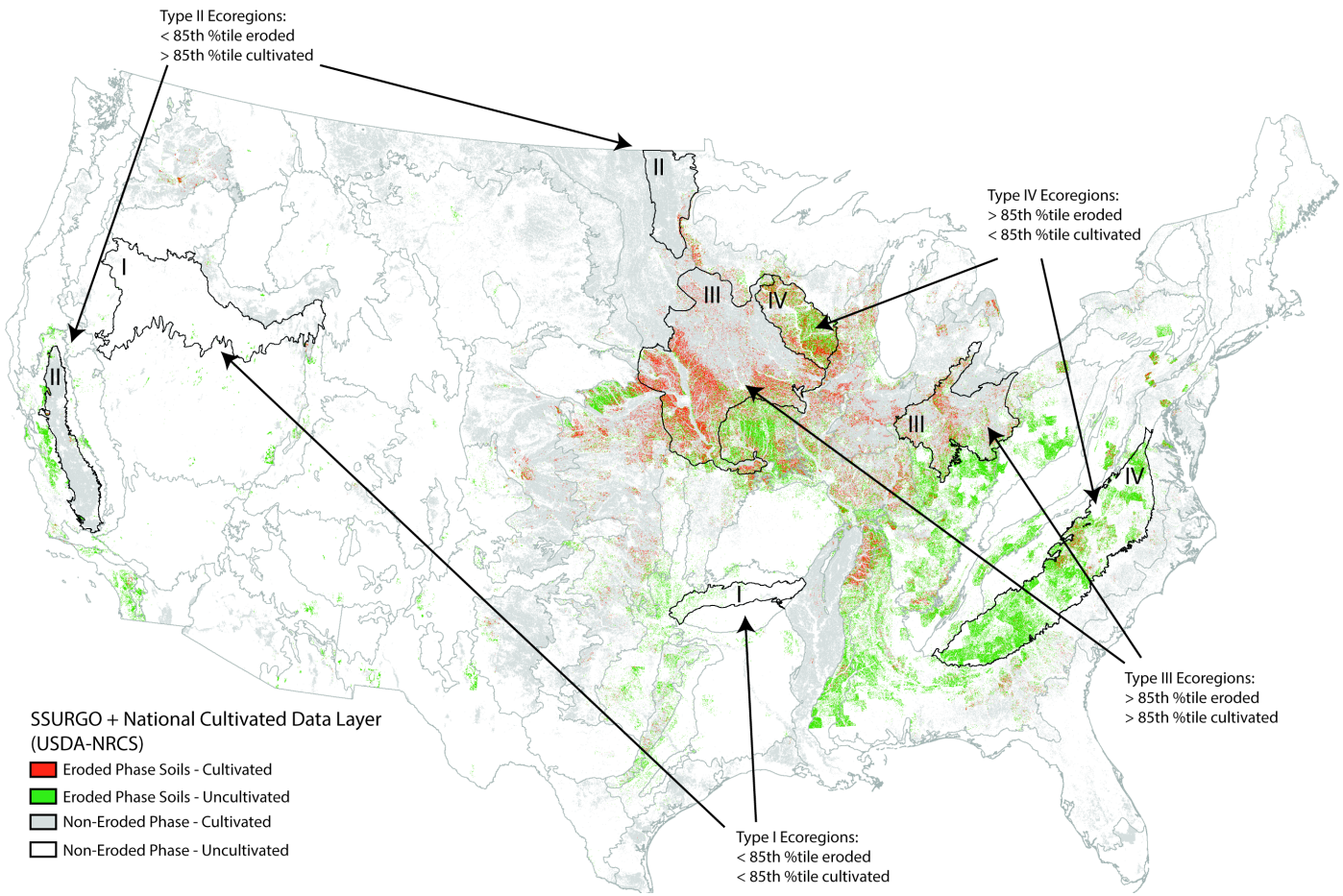

Figure 2.4. Distribution of cultivated lands and eroded phase soils in the continental U.S. Example Highlighted Type I Ecoregions: Northern Basin and Range; Arkansas Valley. Type II: Lake Agassiz Plain, Centreal CA Valley. Type III: Western and Eastern Corn Belt Plains. Type IV: Driftless Area; Piedmont.

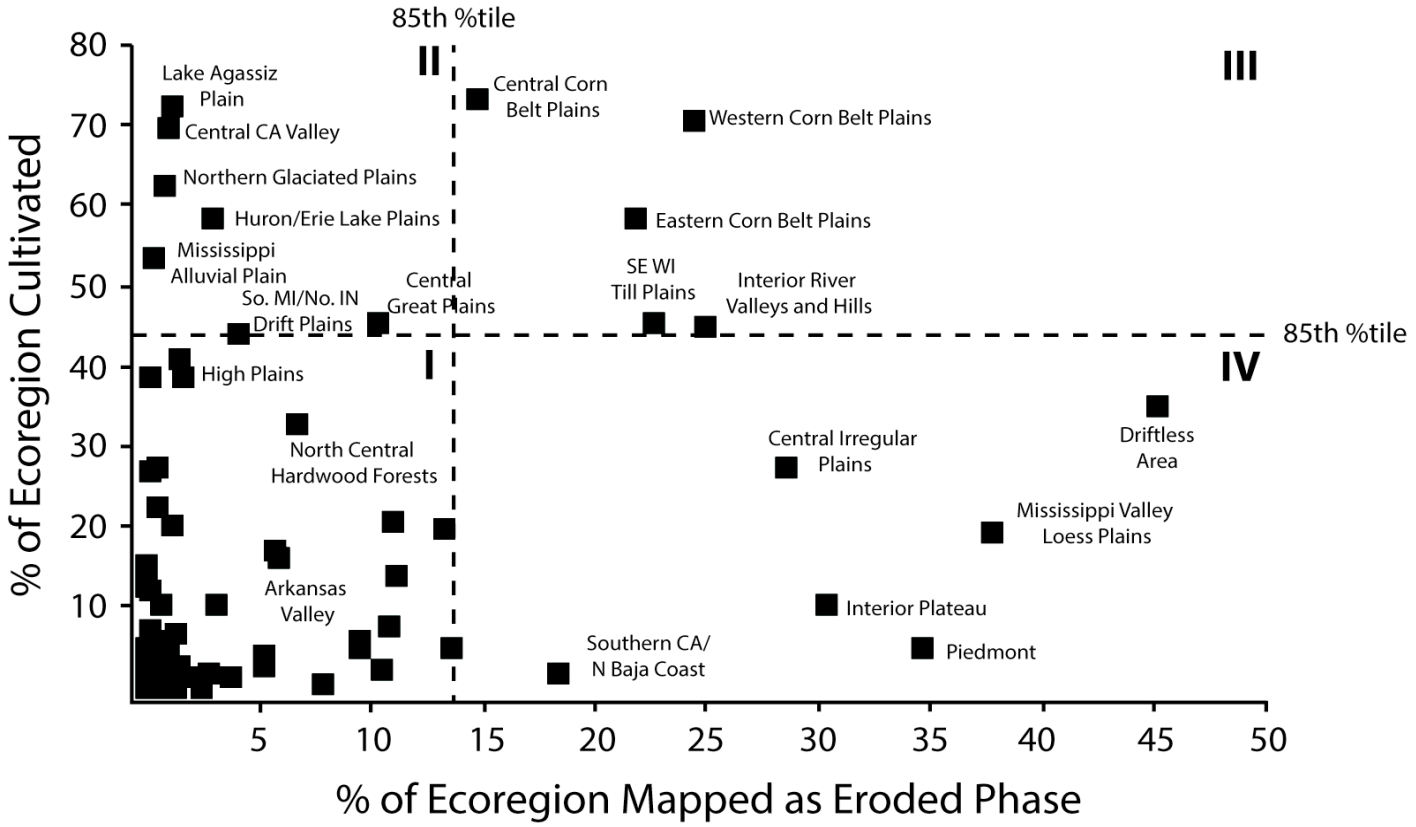

Figure 2.5. Proportion of cultivated land vs. proportion of land mapped as eroded phase by EPA Level III Ecoregion, showing division into ecoregion types by quadrant.

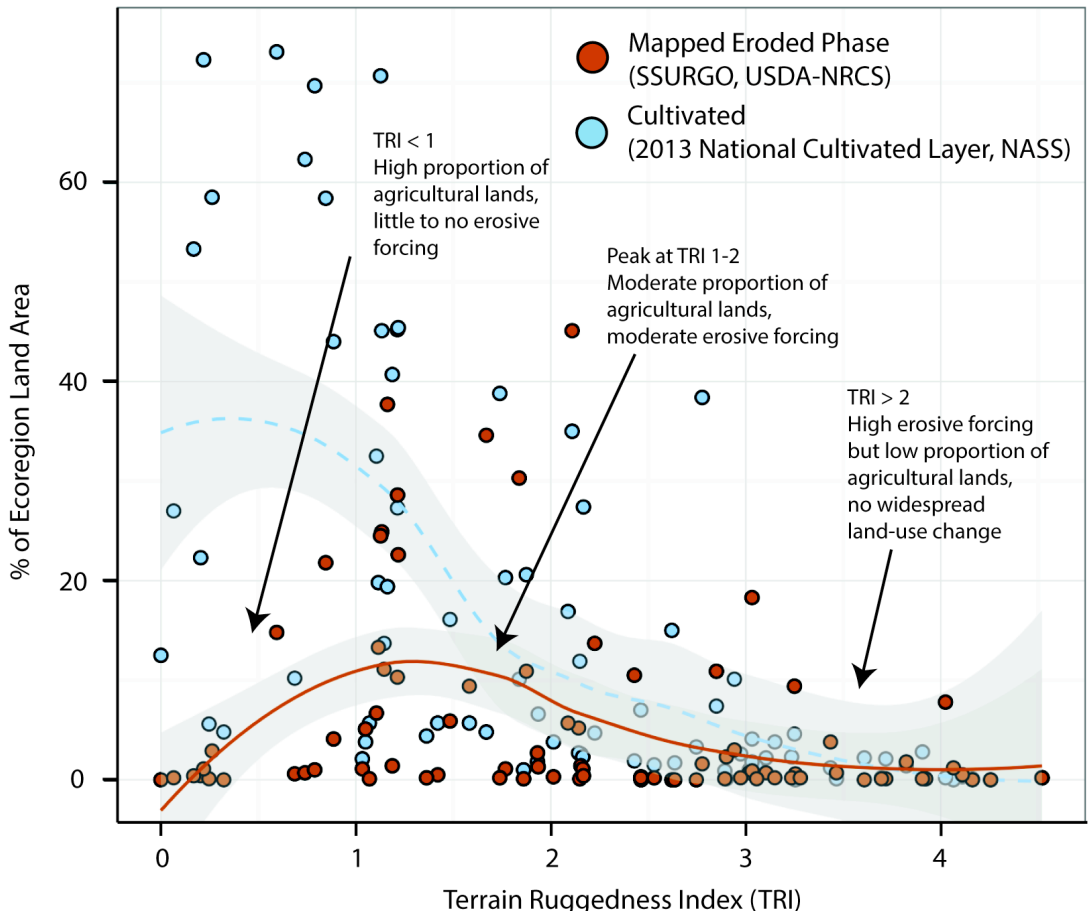

Figure 2.6. Proportion of total ecoregion land area cultivated and mapped as eroded phase by ecoregion average Terrain Ruggedness Index (TRI). TRI data from Gruber (2012). Trend lines and shaded confidence intervals are Locally Weighted Least Squares Regression (LOESS) fits; Span = 0.75, C.I. = 95%, fitted in R using the "loess" function.

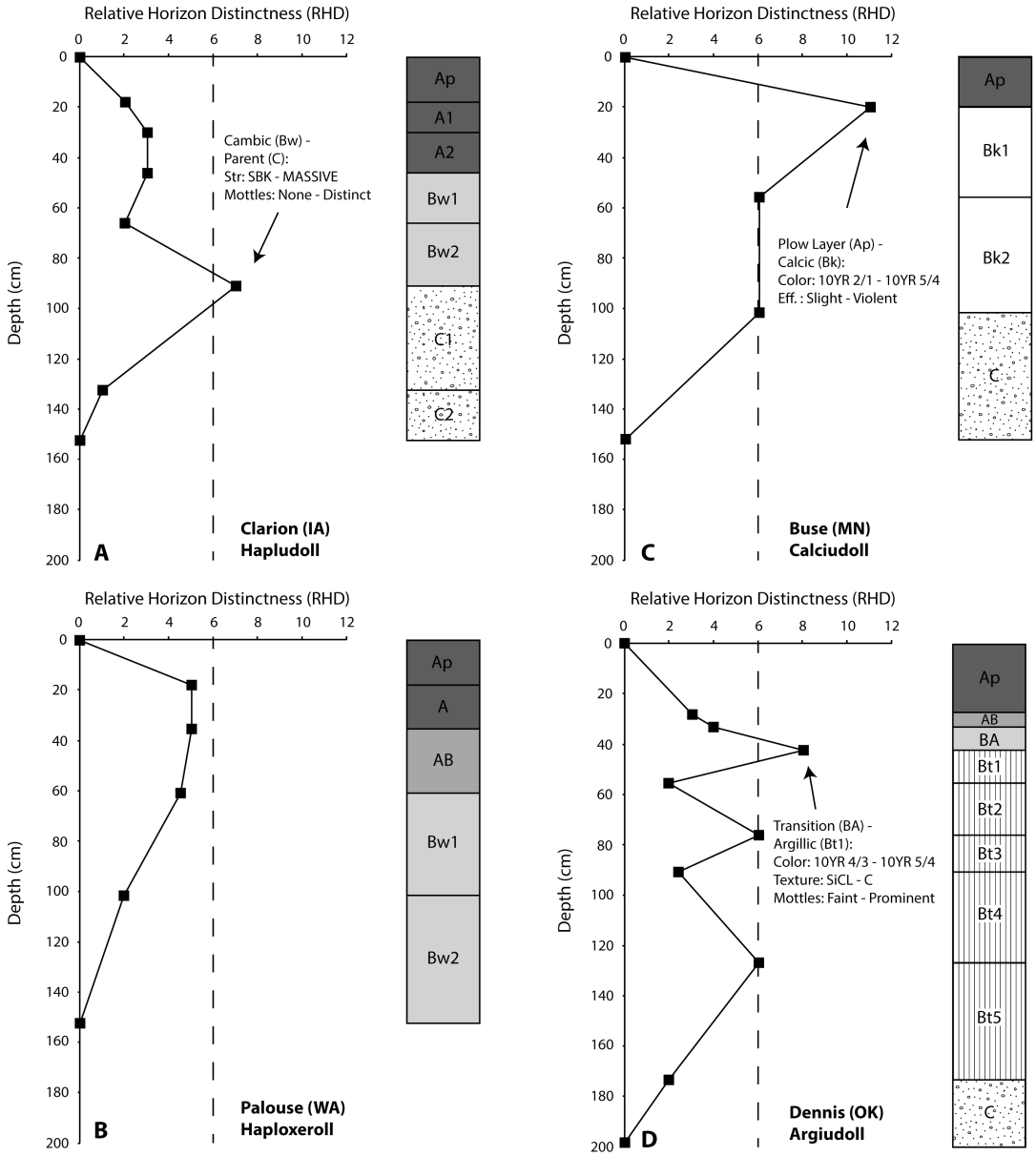

Figure 2.7. Example RHD depth profiles and horizons for selected Mollisol Official Series Descriptions (OSDs) descriptions. Data from Soil Survey Staff (2014b).

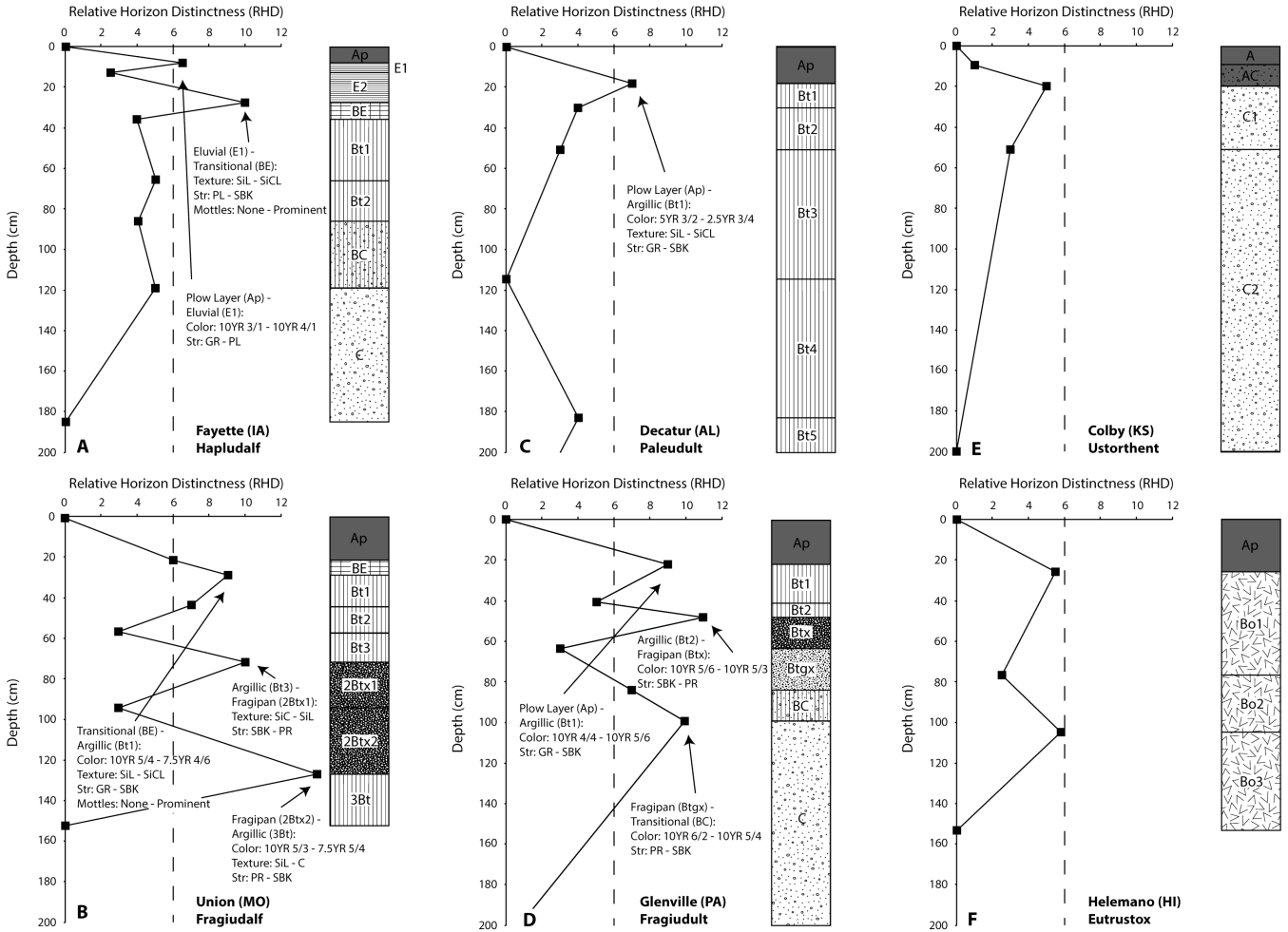

Figure 8. Example RHD depth profiles for selected Alfisol, Ultisol, Entisol and Oxisol profiles. Data from Survey Staff (2014b).

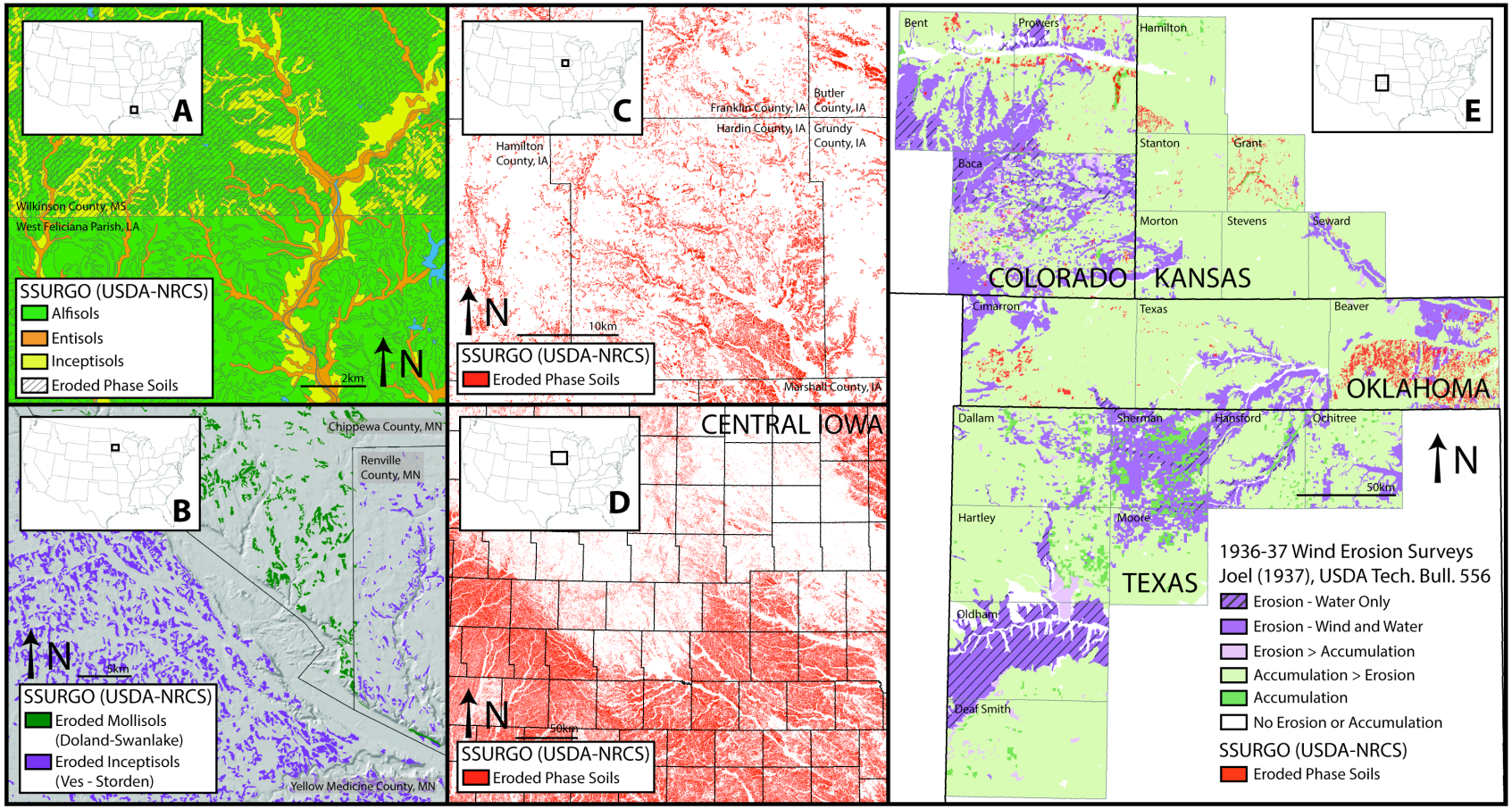

Figure 2.9. Case studies of eroded phase soil distribution and classification.

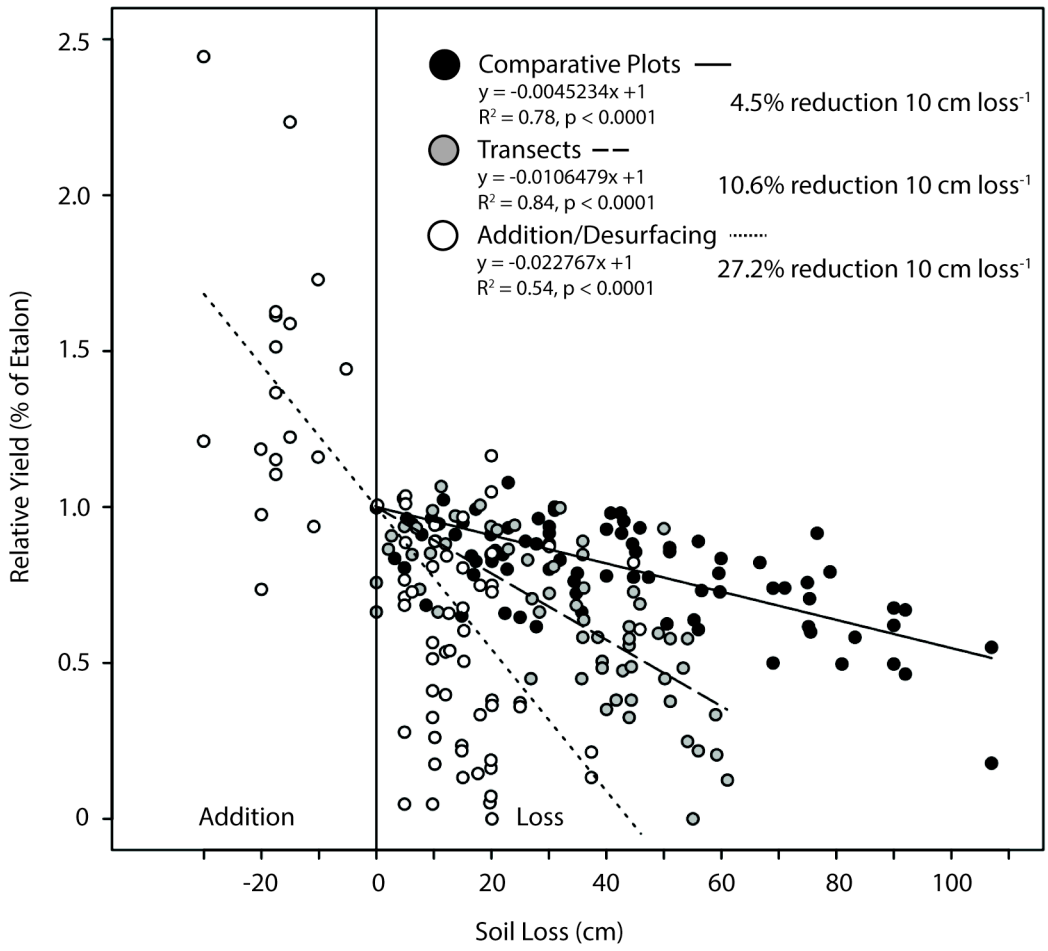

Figure 2.10. Meta-analysis of normalized yield-erosion depth relationships by experimental type. Figure adapted from Bakker et al., 2004 – with the addition of Papiernik et al., 2009, Graveel et al., 2002; Jagadamma, 2009 and Andraski and Lowery, 1992.

Page Left Intentionally Blank

CHAPTER 3

Meteoric Beryllium-10 as a tracer of cumulative erosion due to post-settlement land use in west-central Minnesota, USA.

Submitted to the Journal of Geophysical Research-Earth Surface as:

Jelinski, N.A., J.K. Willenbring, T.E. Schumacher, S. Li, D.A. Lobb, S.K. Papiernik, and K. Yoo: "Meteoric Beryllium-10 as a tracer of cumulative erosion due to post-settlement land use in west-central Minnesota, USA." [Paper #2014JF003340]

Submitted: 16SEP2014

Accepted w/ Revisions: 05NOV2014; Revision deadline: 19JAN2015

With Jane K. Willenbring (University of Pennsylvania – Contribution: ^{10}Be guidance), Tom E. Schumacher (South Dakota State University – Contribution: Field site, sample selection and background data), Sheng Li (Agriculture and Agri-Food Canada – Contribution: ^{137}Cs data), David A. Lobb (University of Manitoba – Contribution: Field site, background data and sample selection), Sharon K. Papiernik (USDA-ARS – Contribution: Field site, sample selection and background data), and Kyungsoo Yoo (University of Minnesota).

Abstract

Soil sustainability in agricultural landscapes is highly dependent upon the pattern and intensity of wind, water, and tillage erosion, and is closely related to carbon cycling, nutrient status, and crop productivity. Radioisotope tracers such as ^{137}Cs have long been used to study soil erosion due to land-use on timescales from days to decades. In contrast, meteoric Beryllium-10 (^{10}Be) has been under-utilized in anthropogenic landscapes as a tracer of erosion and soil truncation despite its ability to provide insights into erosion and landscape change on timescales of centuries to millennia. In this study, we present meteoric ^{10}Be data from paired uncultivated and cultivated sites in west-central Minnesota, USA, and determine the relationship of ^{10}Be to soil organic carbon (SOC), soil inorganic carbon (SIC) and ^{137}Cs data across land-uses. Meteoric ^{10}Be concentrations were highly correlated to SIC but not ^{137}Cs activities. We apply conversion models to ^{10}Be data in order to estimate pre- and post-European settlement erosion rates across the cultivated transect. Results suggest that pre-settlement erosion rates on the cultivated transect averaged 0.38 ± 0.16 Mg ha^{-1} y^{-1}, whereas total post-settlement erosion rates average 31 ± 20 Mg ha^{-1} y^{-1}. The rates derived from ^{10}Be are comparable to those derived from ^{137}Cs and previously simulated water and tillage erosion rates based on topography driven models (WATEM). Meteoric Beryllium-10 is an important tool for anthropogenic systems, which, when used in conjunction with shorter-lived isotopes, models, and geospatial data, can provide novel insights into the evolution and long-term sustainability of agricultural landscapes.

Index Terms and Keywords

Meteoric Beryllium-10, Cesium-137, conversion models, post-settlement erosion, pre-settlement erosion.

Acknowledgements

The authors would like to thank Joseph A. Schumacher, Research Engineer for assistance in setting up transects, georeferencing, detailed mapping, and field collection; Doug D. Malo for assistance in soil profile description and sampling; University of Minnesota Grant-in-Aid #22239 to K. Yoo; and an NSF Graduate Research Fellowship to N. A. Jelinski.

3.1. Introduction

Understanding landscape change in regions dominated by agricultural land-use is a critical component in predicting the future sustainability of soils for agronomic and environmental benefits (Lal, 2012). The tools for estimating cumulative soil profile truncation and landscape change under anthropogenic forcings were initially based on descriptive data (depth to diagnostic subsurface horizons) and expert opinion (Trimble, 1974; Daniels, 1987), but more quantitative estimates through the development of radionuclide tracers (Ritchie and McHenry, 1990; Matisoff and Whiting, 2011; Kaste and Baskaran, 2011) and spatially explicit erosion models (Li et al., 2007; Li et al., 2008) have now become indispensible for studying landscape change due to agricultural land-use.

Cesium-137 (^{137}Cs), with a half-life of 30 years, has commonly been used as a tracer in studies of agricultural erosion over decadal timescales (Ritchie and McHenry, 1990; Matisoff and Whiting, 2011). Through conversion models, ^{137}Cs inventories can provide erosion rate and soil loss estimates by comparing a reference site to sites under a particular land-use or erosion regime of interest (Walling and He, 1999). Because these estimates are on decadal scales, land-use histories are often well constrained and changes in reference site activities due to natural, long-term soil movement are minimal.

In contrast, Beryllium-10 (^{10}Be) is a cosmogenic radionuclide with a half-life of 1.39 million years (Niishizumi et al., 2007; Chmeleff et al., 2009; Korschinek et al., 2009) that is produced in the atmosphere and in solid matrices when high-energy solar particles strike oxygen (and other) atoms, resulting in spallation reactions (Dunai, 2010).

Beryllium-10 produced through spallation reactions in solid substances at the earth's surface, commonly referred to as *in-situ* ^{10}Be ($^{10}Be_{in\text{-}situ}$), occupies sites in mineral matrices in soil and rocks which must be weathered to released this ^{10}Be into adsorbed phase or soil solution. Conversely, the ^{10}Be produced through spallation reactions in the atmosphere, commonly referred to as *meteoric* Beryllium-10 ($^{10}Be_{met}$) is rapidly adsorbed onto aerosols following production and falls out to the earth's surface in wet and dry deposition (Niishizumi et al., 2007; Willenbring and von Blanckenburg, 2010). $^{10}Be_{met}$, due to its widespread distribution and long half-life, has been used to quantify long-term erosion and soil production rates under natural vegetation on steady-state landscapes (Pavich et al., 1986; Monaghan et al., 1992), global rates of mineral weathering (Willenbring and von Blanckenburg, 2010), loess accumulation rates (Harden et al., 2002) and the fate of regolith and saprolite under the influence of glacial processes (Balco, 2004; Ebert et al., 2012). Although the use of both forms of ^{10}Be as tracers of erosion and landscape change due to agricultural land-use has been suggested (Lal et al, 1991; Harden et al., 2002), the utility of $^{10}Be_{met}$ in these contexts has only been cursorily explored (Harden et al., 2002, Graly et al., 2010).

Due to its long half-life, $^{10}Be_{met}$ can record histories of long-term soil movement and material deposition in addition to changes in erosive mechanisms from land-use change. In the U.S. Corn Belt, where the conversion of natural vegetation to agricultural lands occurred largely 100-140 years ago, estimating these differences is a critical component of applying this isotope as a tracer of total post-settlement erosion. Selecting and applying conversion models for $^{10}Be_{met}$ data thus requires the additional steps of

modeling expected distributions of $^{10}Be_{met}$ due to natural processes alone, and subsequently due to anthropogenic forcing. We therefore discuss two rates of physical denudation, and clarify our use of terms here. We estimate natural erosion rates since de-glaciation and term these "*pre-settlement*" erosion rates (E_{pre}) – erosion rates that represent the long-term (millennial-scale) average Holocene physical denudation rates across the landscape under native vegetation and climate forcings, prior to conversion of the landscape to agriculture at the time of European settlement. Second, we derive *post-settlement* erosion rate estimates (E_{post}), which represent estimated erosion rates since the time of agricultural conversion of the landscape (~ 110 years at the time of sampling).

A significant amount of foundational work is available to inform our use of various conversion models for $^{10}Be_{met}$ distributions. $^{10}Be_{met}$ distributions in soil profiles have typically been described by empirical relationships that decline exponentially with depth (Willenbring and von Blanckenburg, 2010). Process based models for near-surface $^{10}Be_{met}$ depth distributions have seldom been implemented, but with knowledge of cation behavior and adsorption characteristics in soils, numerical models for short-lived isotopes (e.g. Olsen et al., 1981; Kaste et al. 2007) can be adapted for $^{10}Be_{met}$. Linking these models of profile-scale $^{10}Be_{met}$ depth distributions with geomorphic and landscape evolution models will provide a foundation for utilizing $^{10}Be_{met}$ as a quantitative tracer of erosion due to land-use change.

We apply three different conversion models that utilize observations of $^{10}Be_{met}$ to derive E_{pre} and E_{post}. We compare the results of these models to results from ^{137}Cs observations and the WATEM model (Van Oost et al., 2000), derived for these same

locations, and investigate the relationships between $^{10}Be_{met}$, ^{137}Cs, soil organic carbon (SOC), and soil inorganic carbon (SIC). Lastly, we discuss other consequences and challenges facing the use of ^{10}Be in agricultural settings and at our study site in west-central Minnesota, USA.

3.2. Background and Methods

3.2.1. Study Area

The study site has been described extensively in previous publications (DeAlba et al., 2004; Papiernik et al., 2005; Papiernik et al., 2007; Li et al., 2007; Li et al., 2008). Briefly, the site lies on the margins of the Alexandria moraine complex of central Minnesota, approximately 3km north of the town of Cyrus (-95.74W, 45.67N, Fig 3.1A, inset), a landscape which was initially formed by the Wadena Lobe and eventually overridden (at least in part) by the Des Moines Lobe during its southeasterly advance in the later stages of the Wisconsinan glaciation (Wright, 1962). Surficial sediments in the study area are comprised of glacial till of the Goose River formation on the uplands, with Quaternary and Holocene alluvial sediments in the river valleys (Harris, 2003). Goose River group sediments are loamy textured carbonate-rich Wisconsinan-age glacial tills of the Des Moines lobe (Harris, 2003), with pH values ranging from 6.9-7.9 (Papiernik et al., 2005). Original estimates for Goose Lake till suggested that it was deposited 11800 – 13000 y.b.p. (Harris, 2003). More detailed analyses of buried organic sediments and OSL on quartz grains has confirmed these initial age estimates on a series of recessional ages in the area to ~ 11,800 – 13,900 y.B.P. (Lepper et al., 2007). We therefore consider an

average age of 13,000 y.B.P. as the age of deposition of the glacial till associated with the study site.

The site consists of paired sampling areas along an uncultivated, grassed hillslope and a cultivated field of ~ 2.7 ha, both on Goose Lake till (Fig 3.1A; Harris, 2003). The uncultivated hillslope used in this study is too steep to have been plowed but was likely grazed for at least 50 years. These assumptions are confirmed by local historical knowledge and are consistent with the earliest available aerial photography of the study site. In June, 2007, samples were taken with a hydraulic corer as part of a larger gridded sampling scheme, described, air-dried, hand-pulverized and homogenized by genetic horizon. A subset of five profiles along the uncultivated hillslope (Fig 3.1D), encompassing all hillslope positions, and five profiles on the cultivated hillslope (Fig 3.1B) was selected for $^{10}Be_{met}$ extraction and analysis.

The uncultivated hillslope is characterized by significantly steeper slopes (10.3 ± 3.0°, slope tangents of 0.18 ± 0.05) than the cultivated field (1.9 ± 1.3°, slope tangents of 0.03 ± 0.02) and does not have a stable summit position, but does have an intermediate summit/shoulder, which has been previously used as the most stable point on the hillslope (De Alba et al., 2004). The uppermost summit position of the hillslope is currently located in a cultivated field at the top of an interfluve (Fig 3.1A,D; Harris, 2003). The situation presented by these paired study sites is common throughout the Corn Belt, where uncultivated sites are rare and, if they do exist, often have remained uncultivated because they were too steep, too dry, or too wet to be easily cultivated (Corbett and Anderson, 2006). Although this presents several challenges in interpretation, sampling

across the uncultivated hillslope provides valuable information for deriving both pre- and post-settlement erosion rates in cultivated systems with $^{10}Be_{met}$ data.

Sample names used in this manuscript follow conventions from previous publications (De Alba et al., 2004; Papiernik et al., 2005), with the uncultivated hillslope termed the "2H" transect (with sample point 1 at the top and sample point 5 at the bottom of the hillslope (Fig. 3.1D). Cultivated transect samples form a portion of a previously investigated East -West transect across a hillslope, termed transect "5". The profiles chosen for $^{10}Be_{met}$ analysis along the transect are on summit (5-7, 5-8), shoulder (5-9, 5-10), backslope (5-12) and footslope positions (5-14) (Fig 3.1B and 3.1C). In 2007, at the time of sampling, the field had been under cultivation for ~ 110 years and under a conventional tillage management regime (annual moldboard plow and secondary tillage) for at least 40 years (Papiernik et al., 2005; Papiernik et al., 2007). Cultivated transect positions and eroding positions on the uncultivated hillslope have pH values from 6.0-7.9 for all depth increments, while depositional positions on the uncultivated hillslope have pH values to 5.5 in upper horizons due to increased leaching of carbonates and higher concentrations of organic matter (Papiernik et al., 2007). Previous research at this site has utilized the uncultivated hillslope as a reference for organic carbon, ^{137}Cs, and the expected distribution of inorganic carbon across the landscape with topography (De Alba et al., 2004; Papiernik et al., 2007).

3.2.2 Soil Characterization – SOC, SIC, ^{137}Cs and Clay

Gridded samples have been extensively characterized for bulk density, organic carbon,

inorganic carbon and ^{137}Cs, following methods described in Papiernik et al. (2005, 2007) and Li et al. (2007). ^{137}Cs activities were determined on germanium detectors in the University of Manitoba's Environmental Radiochemistry Laboratory, following previously described calibration and determination procedures (Li et al., 2008). Clay % was determined on samples shaken and dispersed in sodium hexa-metaphosphate for 12 hours and run in duplicate on a laser particle size analyzer (Horiba, by laser particle size diffraction with a silt-clay size class cutoff of 8um for comparison with particle size classes by sedimentation (Konert and Vandenberghe, 1997).

3.2.3 Meteoric ^{10}Be extraction and measurement

^{10}Be adsorbed to mineral grains and bound to organic materials was removed through a series of acidification steps and ion exchange chromatography prior to being oxidized and analyzed by accelerator mass spectrometry (AMS). The methodology used here is modified from Ebert et al. (2012). 0.5 g of air-dried, homogenized, and sieved (2mm) soil was digested in Teflon vessels with 0.5 M HCl and 250 ug of spiked ^{9}Be carrier at 110° C for 3 hours, after which time the sediment was removed via centrifugation. 4ml of HF was added to the cation solution in two steps to bind excess Ca and Mg. After each HF addition step, 2ml of ultrapure H_2O_2 was added to remove organics. The ultrapure water containing Be and other cations was removed from the fluoride cake via centrifugation and pipetting. Ion exchange chromatography (both anion and cation removal steps) was used to purify Be cations from the bulk cation solution. Be-hydroxides were precipitated from the purified cation solution by titration to pH 9 through the addition of ammonia.

The supernatant was decanted and the precipitate was washed several times with ultrapure water and dried overnight at 100 deg C in low-boron quartz vials. The dry precipitate was flame-oxidized at > 850° C to form BeO powder and pressed into cathodes with niobium powder for AMS analysis at PRIME Lab, Purdue University, USA. A process blank was run with each batch of 9 samples.

3.2.4 Calculation of Meteoric ^{10}Be concentrations

We calculated total $^{10}Be_{met}$ concentrations (atoms g soil^{-1}) through the application of equation (22) to measured $^{10}Be/^{9}Be$ ratios from AMS (Table 3.1):

$$\frac{{}^{9}Be_{carrier}(g)\left(\frac{{}^{10}Be}{{}^{9}Be}(sample)-\frac{{}^{10}Be}{{}^{9}Be}(blank_{ave})\right)N_A}{M({}^{10}Be)g_{sample}} \quad (22)$$

Where $^{9}Be_{carrier}(g)$ is the total amount of Be carrier added to the sample, $^{10}Be/^{9}Be(sample)$ and $^{10}Be/^{9}Be(blank_{ave})$ are the $^{10}Be/^{9}Be$ ratios of the sample and of all blanks (averaged), N_A is Avogadro's number, $M(^{10}Be)$ is the molar mass of ^{10}Be, and g_{sample} is the amount of sample added.

Although our protocol was designed to extract only $^{10}Be_{met}$ from our soil samples (that ^{10}Be which was deposited from the atmosphere and adsorbed to mineral grain surfaces or bound to organic materials), there is the potential that our HF treatment could have etched some mineral grains and released the *in-situ* ^{10}Be present in those grains. We ignore this source of error as *in-situ* ^{10}Be concentrations are typically 2 orders of

magnitude lower than $^{10}Be_{met}$ concentrations, particularly in deposited materials that have already accumulated significant concentrations (~ 1 x 10^7 atoms g^{-1}) of meteoric ^{10}Be (Jungers et al., 2009).

Second, we consider the effect of native ^9Be present in the parent material that has been weathered out of minerals and remains adsorbed to mineral surfaces or bound to organic materials. Significant amounts of native adsorbed ^9Be can result in calculated apparent $^{10}Be_{met}$ concentrations that are less than actual concentrations (Eqn 22). Native ^9Be concentrations in mineral soils and tills near the study area are in the 0.5 – 1.5 ppm range (Lively and Thorleifson, 2009). Because these soils are young and relatively unweathered, it is likely that only a small percentage of this Be is in the adsorbed phase, as a highly weathered Ultisol on a stable landscape position in South Carolina which has undergone 1-3 My of soil development and weathering had a maximum of ~ 50% of its total ^9Be in the adsorbed phase (Bacon et al., 2012). However, as an upper bound on error, if we assume that all of this Be is in the adsorbed phase, 1.5 ppm of native ^9Be adsorbed results in 5 x 10^{15} atoms of native ^9Be present in the sample during processing. Adding 250 mg of ^9Be carrier with a concentration of 1000mg L^{-1} results in the addition of 1.67x10^{19} atoms ^9Be. Therefore, even if all of the native ^9Be contained in these soils is in the adsorbed phase and released to solution during sample processing, it results in a negligible addition to total ^9Be that would affect the apparent $^{10}Be_{met}$ concentration by < 0.1%, well within AMS measurement errors (Table 3.1).

3.2.5 Calculation of ^{10}Be Inventories and Landscape Age

Measurements of total meteoric ^{10}Be concentrations ($^{10}Be_{met,T}$ atoms g^{-1}) include the inherited meteoric ^{10}Be present in the soil parent material (till) when it was deposited ($^{10}Be_{met,I}$ atoms g^{-1}) and the ^{10}Be accumulated during the period of soil formation since the land surface was ice free ($^{10}Be_{met,A}$ atoms g^{-1}). Values of $^{10}Be_{met,I}$ are important for comparisons of soil parent materials, material age, and provenance (Balco, 2004; Willenbring and von Blanckenburg, 2010), but do not contain information relevant to erosion due to post-settlement land-use change. When $^{10}Be_{met,T}$, $^{10}Be_{met,I}$ or $^{10}Be_{met,A}$ are discussed, they are explicitly identified in text and with the corresponding abbreviations. Criteria used to determine the average concentration of inherited ^{10}Be ($^{10}Be_{met,I,ave}$) from parent material are as follows. The average $^{10}Be_{met,T}$ concentration from the bottom depth increment of all profiles (ranging from 87cm – 150cm), was subtracted from all observed $^{10}Be_{met,T}$ concentrations. Any resulting depth increment concentrations that were negative or less than the average were considered to contain only $^{10}Be_{met,I}$.

For each measured depth increment (i), the inventory of $^{10}Be_{met,A}$ is the excess of $^{10}Be_{met,T}$ over $^{10}Be_{met,I}$ (Eqn 23), where $^{10}Be_{met,I,ave}$ is the average inherited $^{10}Be_{met}$ concentration across all samples, from above:

$$^{10}Be_{met,A,i} = {}^{10}Be_{met,T,i} - {}^{10}Be_{met,I_{ave}} \quad (23)$$

If, by equation 23, $^{10}Be_{met\,A,i} < 0$, then $^{10}Be_{met,T,i}$ is assumed = $^{10}Be_{met,I,i}$, and $^{10}Be_{met,A,i}$ is set to 0.

The total accumulated, non-inherited ^{10}Be inventory (I_A atoms m^{-2}) for each

profile is then:

$$I_A = \sum_{i=1}^{n} {}^{10}Be_{met,A,i}\rho_s(z_{bot,i} - z_{top,i}) \quad (24)$$

where ρ_s is the increment bulk density (kg m^{-3}) and $z_{bot,i}$, $z_{top,i}$ are the bottom and top depths (m) of the sampled increment, respectively, and i=1 is the top (surficial) depth increment, and i=n is the bottom depth increment. Inventories of $^{10}Be_{met,T}$, $^{10}Be_{met,I}$, $^{10}Be_{met,A}$, SOC, SIC, and ^{137}Cs were calculated to 1.5 m (depth of deepest observation in dataset) for all profiles by extending observed values of the lowest depth increment to 1.5 m if it did not extend that far. This resulted in a maximum of 28cm of gap-filling for profile 2H3, but in all cases the contribution of the gap-filled portion was < 5% of the inventory. All inventories for other soil constituents discussed in this study were calculated as in equation 24, above.

Because the non-inherited ^{10}Be inventory (I_A) is related to the development time of the soil, the total inventory of a stable landform provides a measure of landscape age or time since soil development began on a deposited parent material [*Pavich* et al., 1984; *Graly* et al., 2010]. An estimate of this age is provided by the total inventory (I_A) of a stable landform, excluding the radioactive decay of ^{10}Be (which is reasonable on timescales of < 100,000 years due to the long half-life (~ 1.4 My) of ^{10}Be:

$$t = \frac{I_A}{P_{Be}} \tag{25}$$

where t is time since parent material deposition (y) or exposure at the surface (related to time since the beginning of soil development), and P_{Be} is the long-term average wet and dry deposition of $^{10}Be_{met}$ (atoms cm^{-2} y^{-1}). We utilize 1.3 x 10^6 atoms cm^{-2} y^{-1} , which is similar to the long-term global average reported in other studies and the value used for published studies of ^{10}Be distributions in soils for other parts of Minnesota and Iowa (Harden et al., 2002; Balco, 2004). This value is highly congruent with that for the study site based on a modern precipitation-normalized sigmoidal fit to measured global latitudinal trends in meteoric ^{10}Be flux (Graly et al., 2011).

3.2.6. ^{137}Cs conversion models for calculating 47-year average erosion rates

Two different models were used to convert observed ^{137}Cs inventories to 47-year average erosion rates for each profile and both require a reference inventory of ^{137}Cs from an undisturbed site. The first is the linear model of de Jong et al. (1983), applied by Lobb et al. (1999):

$$E_{47,ave} = \left(\frac{\rho_s D(^{137}Cs^0 - {}^{137}Cs^j)}{t(^{137}Cs^0)} \right) \tag{26}$$

Where $E_{47,ave}$ is the 47-year average erosion rate assuming all ^{137}Cs inventory was deposited to the study site as a pulse event in the year 1960, ρ_s is the average soil bulk

density, and D is the depth of soil through which ^{137}Cs is distributed, $^{137}Cs^0$ is the reference inventory (atoms m^{-2}), $^{137}Cs^j$ is the profile inventory (atoms m^{-2}) at sampling point j, and t is the time period from 1960 to the time of sampling (47 years).

The second conversion model is the power method, developed by Kachanoski (1987), applied by Lobb et al. (1999):

$$E_{47,ave} = \left(\frac{\rho_s D \left(1 - \frac{^{137}Cs^j}{^{137}Cs^0} \right)^{\frac{1}{t}}}{\eta} \right) \quad (27)$$

Where variables are as described above and η is an enrichment ratio, generally assumed to be 1.0.

The reference ^{137}Cs inventory used for model input was 2099 Bq m^{-2}, which is the average of three estimates of reference inventories at the study site (2224 Bq m^{-2} (Li et al., 2008), 2093 Bq m^{-2} (Li et al., 2007), and 1893 Bq m^{-2} (Li and Lobb, unpublished)).

3.2.7. $^{10}Be_{met}$ conversion models for estimating E_{post} and E_{pre}

We utilize three different conversion algorithms to estimate post-settlement (E_{post}) erosion rates, two of which allow us to derive natural (E_{pre}) erosion rates at the cultivated sampling points (Models 2 and 3).

Conversion Model 1. Conversion Model 1 is a proportional, linear conversion model equivalent to the linear model for ^{137}Cs (de Jong et al., 1983; Walling and He,

1999) which assumes the independence of sampling points and calculates apparent erosion rates based solely on the normalized difference in ^{10}Be inventories at each sampling point. For short-lived radioisotopes such as ^{137}Cs, a reference is a single reference inventory, however in our analysis of $^{10}Be_{met}$, we utilize the uncultivated hillslope average inventory as the reference considering the entire hillslope as a box which contains all $^{10}Be_{met,A}$ deposited since the landscape has been ice-free :

$$E_{post} = \left(\frac{\rho_s D(I_A^0 - I_A^j}{tI_A^0} \right) \tag{28}$$

where E_{post} is the post-settlement erosion rate (Mg ha^{-1} y^{-1}), ρ_s is the average soil bulk density, and D is the depth of soil through which 10Be is distributed, I_A^0 is the reference inventory (atoms m^{-2}), I_A^j is the profile inventory (atoms m^{-2}) at sampling point j, and t is the time period since the start of cultivation (y). Key assumptions in this model are 1) the independence of sampling points from eachother and from the landscape and 2) the uncultivated hillslope average inventory provides a reasonable reference value.

Conversion Model 2. Conversion Model 2 consists of two parts - a numerical model of the long-term diffusion of radionuclides into soils following Olsen et al. (1981) to estimate pre-settlement $^{10}Be_{met}$ distribution and inventory, followed by a simplified version of models applied by Kachanoski and DeJong (1984) and Li et al (2010) to estimate erosion rates under annual tillage while taking into account the vertical mixing and dispersion of ^{137}Cs poor subsoil into the plow layer (Kachanoski and

De Jong, 1984). Unlike short-lived radioisotopes, which have been deposited under conditions of cultivation, $^{10}Be_{met,A}$ inventories were established under natural conditions and thus necessitate additional modeling to estimate pre-settlement inventories.

For the pre-settlement portion, briefly, the soil profile is subdivided into layers of equal thickness. A mixing coefficient is determined for the boundary between each layer at depth z (cm) that is based off of an exponential curve which is dependent on the surficial diffusion parameter (D_b, $cm^2\ y^{-1}$) and characterized by a half-thickness depth - the depth at which D_i is one-half the surface value (H, cm):

$$D_i = D_b \exp\left(\frac{-0.693}{H / z}\right) \tag{29}$$

These diffusion coefficients are then applied to a soil profile divided into 1 cm increments which has $^{10}Be_{met}$ deposited at the surface during each timestep according to the long-term average (1.3×10^6 atoms $cm^{-2}\ y^{-1}$) as derived above. The profile is diffusively mixed (Eqn 30) to establish a new profile distribution of $^{10}Be_{met}$ and is subsequently eroded by a specified increment (E_{pre}) value completing each timestep:

$$\frac{\partial C}{\partial t} = \frac{\partial}{\partial z}\left(D_i \frac{\partial C}{\partial z}\right) \tag{30}$$

We differ from the approach of Olsen et al. (1981) because we exclude radioactive decay (negligible due to the long half-life of ^{10}Be and short-timespan under

consideration). We also exclude an advection term because the high pH of these soils, lack of clay illuviation and precipitation range of the study site means that the majority of the $^{10}Be_{met}$ deposited on the soil surface is not likely to be mobilized by leaching (Willenbring and von Blanckenburg, 2010). This numerical model is run for the length of landscape development in 1 year timesteps to 13,000 years.

We iteratively solve the model for a best fit solution for D_b, H and E_{pre} and choose the model that minimizes root mean square error (RMSE) for the soil loss positions on the uncultivated hillslope, 2H1 and 2H2. The parameters are then applied in an additional model run to estimate the pre-settlement $^{10}Be_{met}$ profile distribution at each eroding cultivated transect position (5-7, 5-8, 5-9, 5-10, 5-12) with the magnitude of gross soil loss (E_{pre} for this model) scaled relative to the slope of the uncultivated hillslope positions (Eqn 31):

$$E_{pre,j} = E_{pre,uncult} \frac{S_j}{S_{uncult}} \tag{31}$$

This model is reasonable because even though the uncultivated site has steeper slopes than the cultivated site (Fig 3.1C,E), all of these slopes are still well within the range where colluvial soil transport scales linearly with curvature (Roering et al., 1999), and hence with slope where only colluvial mass flux away from the point of interest is considered.

This estimated pre-settlement ^{10}Be profile is then run through a series of agricultural erosion scenarios where the plow layer is completely homogenized and

eroded on 1 year timesteps in a simplified version of models applied by Kachanoski and DeJong (1984) and Li et al (2010). When time since initial cultivation and plow layer $^{10}Be_{met}$ concentrations are constrained, a single solution for E_{post} is possible based on a log-linear regression of the numerical modeling results for a range of erosion rates, with parametrical uncertainty evaluated by 1000 Monte Carlo simulations.

Therefore, Conversion Model 2 requires the following steps:

1. Iteratively solve numerical diffusion model for best-fit values of D_b, H and E_{pre} (natural erosion rate) at soil-loss positions on the uncultivated hillslope (2H1 and 2H2).
2. Apply these parameters to model the expected pre-settlement depth distribution of $^{10}Be_{met}$ at soil-loss positions at the cultivated site (5-7, 5-8, 5-9, 5-10, 5-12), with E_{pre} (natural erosion rate) linearly scaled to slope.
3. Fully mix the plow layer (0-25 cm), erode and mix again on annual timesteps for 110 years. Evaluate at multiple values of E_{post} to obtain regression equation, solve regression equation with plow layer input for unique value of E_{post} (average post-settlement erosion rate).

Key assumptions in this model: 1) This model considers only soil loss (gross mass flux out) and not net soil loss and 2) the derived diffusion parameters from uncultivated profiles 2H1 and 2H2 are representative across the landscape.

Conversion Model 3. Conversion Model 3 utilizes the same numerical modeling approach as conversion model 2, but instead of first solving for a best-fit solution and scaling according to slope, we solve for the landscape diffusivity parameter k (cm^3 cm^{-1}

y^{-1}) based on uncultivated hillslope $^{10}Be_{met}$ inventories and the assumption of linear dependence of soil volume creep on slope gradient and in downslope plug flow from a summit position (McKean et al., 1993):

$$k(x) = \frac{P_{Be} x}{\rho_s C_{Be}(x) S(x)} \tag{32}$$

Where P_{Be} is the average annual deposition of $^{10}Be_{met}$ (atoms cm^{-2} y^{-1}), x is the distance from the summit (cm), ρ_s is the average surface soil bulk density (g cm^{-3}), $C_{Be}(x)$ is the average soil $^{10}Be_{met}$ concentration (atoms g^{-1}), and $S(x)$ is the tangent of the slope at distance x cm from the summit.

We make a steady-state assumption as in McKean et al (1993) to estimate E_{pre} under uncultivated conditions for each sampling point, where we use the slope 10m above and 10m below each point perpendicular to the contour line to calculate long-term erosion rates:

$$E_{pre} = \left(\frac{\partial(\rho_s k_{ave} S(x))}{\partial x} \right) \tag{33}$$

Where E_{pre} (Mg ha^{-1} y^{-1}) is the long-term erosion rate at point x, ρ_s is the average bulk density of the soil (Mg m^{-3}), and k_{ave} is the average landscape diffusivity (m^2 y^{-1}) derived from the uncultivated hillslope, above. E_{post} is solved by applying logarithmic regressions to unique numerical solutions of plow layer $^{10}Be_{met}$ observations for 1000 Monte Carlo

runs as in conversion Model 2.

Key assumptions: Although this model considers net soil mass flux, it assumes that $^{10}Be_{met}$ flux in is equal to $^{10}Be_{met}$ flux away from the sample point under consideration. It also makes a steady-state assumption in order to derive the landscape diffusivity parameter (k) from observed uncultivated hillslope inventories [*McKean* et al., 1993].

The assumption of independence in Models 1 and 2 and assuming only soil loss (Model 2) or steady-state ^{10}Be (Model 3) have the advantage of simplifying conversion algorithms, but the disadvantage of ignoring landscape setting and soil accumulation as well as loss. Therefore, except for the proportional method (Model 1) we restrict our analyses to cultivated sampling points on eroding (convex or nearly linear – positive curvature). Depositional settings are inappropriate settings in which to apply these models (except for the completely independent Model 1) and require more extensive algorithms that are beyond the scope of this analysis.

Conversion Model Error Analysis. Three sources of uncertainty (measurement, structural and parametrical) in our model analysis were evaluated. Measurement uncertainty due to ^{10}Be AMS errors and bulk density variability was included in all erosion rate estimates. Where unmeasured parameters were critical for erosion estimates (models 2 and 3), model parametrical uncertainty was evaluated through Monte Carlo simulations in which models were run 1000 times over a range of randomized input variables. For Models 2 and 3, all parameters for the Monte Carlo simulations were run over a range of $\pm$ 20% of the best estimated parameter. This range encompassed all

reasonable values of input parameters as determined from the literature and previous studies. Model structural uncertainty (systemic error due to model structure) was evaluated by inter-comparison with results obtained from the models suite as well as results from the same sampling points using the WAter and Tillage Erosion Model (WATEM - Van Oost et al. (2000)), as reported in Papiernik et al. (2005).

3.3. Results

3.3.1. Meteoric Beryllium-10 Concentrations and Relationships

$^{10}Be_{met,T}$ concentrations were significantly affected by depth ($p < 0.001$), land-use ($p = 0.02$) and hillslope position ($p = 0.02$). Concentrations of $^{10}Be_{met,T}$ across the study area ranged from 0.63×10^7 atoms g^{-1} in subsoils to 26.8×10^7 atoms g^{-1} in topsoils at depositional sites (Table 3.1). Concentrations of $^{10}Be_{met,T}$ in the lowest sampling increment of each profile averaged 1.85×10^7 atoms g^{-1}. Only one soil profile (2H4) had no $^{10}Be_{met,T}$ concentrations that met the criteria for inheritance and thus that entire profile was excluded from the calculation of $^{10}Be_{met,I\ ave}$. The resulting $^{10}Be_{met,I}$ average for the study site per our algorithm (Eqns 22-24) was $1.07 \times 10^7 \pm 0.29 \times 10^7$ (SD) atoms g^{-1}. When this average value was applied to all cultivated increments to determine $^{10}Be_{met,A}$ inventories, only the depositional position of the cultivated transect had $^{10}Be_{met,A}$ below the plow layer (Table 3.1). All other cultivated profiles had $^{10}Be_{met,A}$ remaining only in the plow layer. Uncultivated upper hillslope positions 2H1 and 2H2 had $^{10}Be_{met,A}$ from to 24-32 cm depth, while the uncultivated backslope, and footslope positions had $^{10}Be_{met,A}$ to 67-144 cm (Table 3.1).

In accordance with expectations of largely unsorted, loamy-textured glacial tills, clay percentage was not affected by land-use, depth or hillslope position ($p > 0.5$ in all cases). We conclude that grain size effects on $^{10}Be_{met}$ concentrations can be safely ignored in the studied soil profiles and that observed concentration differences are not due to differential sorting of materials during erosive processes.

The surficial $^{10}Be_{met,T}$ concentrations of sampled profiles ranged from a minimum of 3.16×10^7 atoms g^{-1} on the highly eroded cultivated backslope position (5-12) to a maximum of 26.8×10^7 atoms g^{-1} in a depositional position (2H4) on the uncultivated hillslope (Table 3.1). Importantly, surficial concentrations of $^{10}Be_{met,T}$ across the uncultivated hillslope were not always greater than surficial concentrations of $^{10}Be_{met,T}$ at the cultivated site. Surficial concentrations at uncultivated summit and shoulder positions 2H1 and 2H2 (12.4×10^7 atoms g^{-1} and 11.0×10^7 atoms g^{-1}, respectively) were less than surficial $^{10}Be_{met}$ concentrations at profile 5-8 on the relatively flat summit of the cultivated site (15.8×10^7 atoms g^{-1}, Table 3.1).

SOC concentrations were significantly affected by depth and land-use ($p < 0.001$ in both cases). SOC concentrations ranged from 0.1 – 5.0% across all samples, with averages of 0.6 ± 0.5 and 1.5 ± 1.5 % for cultivated and uncultivated samples, respectively. Surficial concentrations of SOC ranged from 0.96 – 4.96% across all samples, with averages of 1.2 ± 0.2 and 4.2 ± 0.5 % for cultivated and uncultivated samples, respectively (Table 3.1).

Across all samples, SIC concentrations were significantly affected by land-use and hillslope position ($p < 0.001$ in both cases). Surficial concentrations of SIC ranged

from 0.0 – 2.5% across all samples, with averages of 1.7 ± 0.9 and 0.3 ± 0.4 % for cultivated and uncultivated samples, respectively (Table 3.1).

^{137}Cs activities (including subsoil increments) were significantly affected by depth ($p < 0.001$) and marginally affected by land-use ($p = 0.04$). ^{137}Cs activities ranged from 0.0 – 12.5 Bq kg^{-1} across all samples, with averages of 0.7 ± 1.3 and 2.3 ± 3.9 Bq kg^{-1} for cultivated and uncultivated samples, respectively. Surficial activities of ^{137}Cs ranged from 1.3 – 12.5 Bq kg^{-1} across all samples, with averages of 2.8 ± 0.9 and 9.2 ± 2.4 Bq kg^{-1} for cultivated and uncultivated samples, respectively (Table 3.1).

When all samples are considered, $^{10}Be_{met,T}$ concentrations are correlated with SIC, and SOC concentrations, but not ^{137}Cs activities (Fig 3.2A-D). SIC concentrations were negatively correlated to $^{10}Be_{met,T}$ concentrations, while SOC concentrations were positively correlated to $^{10}Be_{met,T}$ concentrations (Fig 3.2A-D). Clay percentages were not significantly correlated to $^{10}Be_{met,T}$ concentrations across all samples ($p > 0.7$). When only the surficial values of these samples are considered, SIC is an excellent predictor of surficial increment $^{10}Be_{met,T}$ concentrations, while ^{137}Cs and SOC are not significantly correlated with $^{10}Be_{met,T}$ concentrations (Fig 3.2). Specifically, SIC has the highest R^2 for all predictors of surficial $^{10}Be_{met,T}$ ($R^2=0.81$, $p < 0.001$). In contrast to the poor correlation between $^{10}Be_{met,T}$ and SOC, ^{137}Cs activities were highly correlated to SOC concentrations when all samples and surficial samples were considered ($R^2=0.89$, $p < 0.001$ and $R^2=0.87$, $p < 0.001$, respectively).

3.3.2. Meteoric Beryllium-10 Depth Distributions, Inventories, and Relationships

The shape of $^{10}Be_{met}$ concentration depth profiles is highly dependent upon landscape position. Summit and shoulder positions for complete profiles of both the uncultivated (2H1, 2H2) and cultivated (5-8, 5-9, 5-10) sites as well as a backslope position at the cultivated site (5-12) exhibit exponential decreases in $^{10}Be_{met,T}$ concentrations with depth,(Fig 3.3 and 3.4), typical of stable or eroding landscape positions in young landscapes where diffusion and not advection is the dominant process of the downward movement of $^{10}Be_{met}$ in the soil profile (Willenbring and von Blanckenburg, 2010; Graly et al., 2010). In contrast, the uncultivated backslope (2H3) and all footslope positions (5-14, 2H4, 2H5) were cumulative in profile (Fig 3.3 and 3.4), and look similar to plug flow accumulation or other sedimentary or depositional environments of $^{10}Be_{met}$ (McKean et al., 1993; Harden et al., 2002).

Inventories of $^{10}Be_{met,T}$ varied according to hillslope position and land-use. On average, $^{10}Be_{met,T}$ inventories on the cultivated transect were significantly less than those on the uncultivated hillslope ($7.04 \times 10^{13} \pm 0.70 \times 10^{13}$ atoms m^{-2}, n=6 and $14.0 \times 10^{13} \pm 1.17 \times 10^{13}$ atoms m^2, n=5, respectively), however important differences within land-uses existed as well (Table 3.2). Along the cultivated transect, $^{10}Be_{met,T}$ inventories varied systematically with landscape position, with the exception of profile 2H5, which, although at the lowest elevation along the hillslope, had a lower inventory ($14.8 \times 10^{13} \pm 1.5 \times 10^{13}$ atoms m^{-2}) than 2H4, the profile above it (30.9×10^{13} atoms $m^{-2} \pm 2.3 \times 10^{13}$ atoms m^{-2}) (Table 3.2). We assume, based on all other observations of cultivated profiles on summit, shoulder or backslope positions, that the plow layer inventory of $^{10}Be_{met}$,T at profile 5-7 also represents the total profile inventory ($4.6 \times 10^{13} \pm 0.5 \times 10^{13}$ atoms m^{-2}).

Maximum concentrations of $^{10}Be_{met,T}$ (which occurred in the surficial increment except for profiles 2H4 and 5-14) were log-linearly correlated to total inventories ($R^2 = 0.86$, $p < 1 \times 10^{-4}$, Fig 3.5A), with a tighter relationship between the two variables at lower values of maximum concentrations ($< 20 \times 10^7$ atoms g^{-1}) than at higher maximum concentrations ($> 20 \times 10^7$ atoms g^{-1}) (Fig 3.5).

Calculated inventories of $^{10}Be_{met,I}$ to 1.5m averaged $2.1 \times 10^{13} \pm 0.16 \times 10^{13}$ atoms m^{-2} and did not differ between hillslope positions or land-use. Because $^{10}Be_{met}$,I does not differ between sampled profiles, $^{10}Be_{met,A}$ inventories are highly correlated to $^{10}Be_{met}$,T inventories and were significantly less on the cultivated transect than uncultivated hillslope ($8.14 \times 10^{13} \pm 0.83 \times 10^{13}$ atoms m^{-2}, n=6 and $11.8 \times 10^{13} \pm 1.08 \times 10^{13}$ atoms m^2, n=5, respectively). The resulting average uncultivated $^{10}Be_{met,A}$ inventory ($11.8 \pm 1.1 \times 10^{13}$ atoms m^{-2}, Fig 3.5), results in landscape age estimates of 8,300 - 9,900 years (Eqn 25), assuming long-term average $^{10}Be_{met}$ deposition of 1.3×10^{10} atoms m^{-2} y^{-1}.
On the uncultivated hillslope, total inventories of SOC and ^{137}Cs did not vary by more than 30% from the hillslope average, while $^{10}Be_{met,T}$ inventories varied as much as 100% from the average (Fig 3.3). In contrast, SOC, ^{137}Cs and $^{10}Be_{met,T}$ varied by greater than 150%, 200% and 400%, respectively on the cultivated transect (Fig 3.4), with most of the variability occurring at the footslope position (5-14).

SOC inventories were significantly different between land-uses (19.2 ± 1.8 kg m^{-2} and 9.4 ± 2.5 kg m^{-2}, $p < 0.01$, uncultivated and cultivated profiles, respectively). $^{10}Be_{met,I}$ and SIC inventories were not significantly different between cultivated and uncultivated profiles ($p > 0.05$, Welch's two-sample t-test). $^{10}Be_{met,T}$ inventories and SIC inventories

were highly correlated ($R^2 = 0.85$, $p < 0.001$). ^{137}Cs inventories also differed significantly between land-uses (2186 ± 395 and 876 ± 519 Bq m^{-2}, uncultivated and cultivated, respectively). Surficial ^{137}Cs activities (maximum ^{137}Cs activities, in all cases) were correlated to total ^{137}Cs inventories (Fig 3.5B) but the shape of the relationship contrasted strongly with that of the maximum $^{10}Be_{met,T}$ concentration to inventory relationship (Fig 3.5), with inventories saturating but activities increasing. The relationship between maximum $^{10}Be_{met,T}$ concentration and total $^{10}Be_{met,T}$ inventory contrasts sharply with the relationship between surficial (or maximum, in all cases) ^{137}Cs activity and total ^{137}Cs inventory. Maximum concentrations of $^{10}Be_{met,T}$ appear to saturate ~ 2.5 x 10^8 atoms g^{-1}, while profiles continue to collect inventory, while (because of the finite deposition of ^{137}Cs) ^{137}Cs inventories asymptote at ~ 2000-2500 Bq kg^{-1} but surficial activities can continue to increase with less disturbance to the surface layer (Fig 3.5).

3.3.3. 47-year average erosion rate estimates: ^{137}Cs Conversion Models

The linear conversion model using observed ^{137}Cs inventories as inputs resulted in soil loss estimates of 31 - 42 Mg ha^{-1} y^{-1} at summit, shoulder and backslope positions and a deposition rate of +3 Mg ha^{-1} y^{-1} at the cultivated toeslope position (5-14) for the linear model. The power model resulted in lower erosion estimates ($p = 0.03$) than the linear model, with soil loss estimates ranging from 22 - 30 Mg ha^{-1} y^{-1} at summit, shoulder and backslope positions and a deposition rate of +110 Mg ha^{-1} y^{-1} at the toeslope position.

3.3.4. Total post-settlement erosion rate estimates: ^{10}Be Conversion Model 1

We utilized the uncultivated hillslope average $^{10}Be_{met,A}$ inventory (11.8 x 10^{13} atoms m^{-2}) as the reference inventory for erosion rate calculations based on linear methods through equation (8). This linear, slope independent model resulted in post-settlement erosion rates ranging from 16-24 Mg ha^{-1} y^{-1} on eroding landscape positions (5-7, 5-8, 5-9, 5-10, 5-12) of the cultivated site (Table 3.3). Accordingly, cultivated point 5-12 (backslope), which has the lowest measured $^{10}Be_{met,A}$ inventory also had the largest erosion rate estimate (-24 Mg ha^{-1} y^{-1}). In contrast, the footslope position on the cultivated transect had the largest $^{10}Be_{met}$ inventory, resulting in a deposition rate estimate of +79 Mg ha^{-1} y^{-1} (Table 3.3).

3.3.5. Pre-settlement (E_{pre}) and total post-settlement (E_{post}) erosion rate estimates: ^{10}Be Conversion Model 2

The best iterative fit solution of the parameters to the observed $^{10}Be_{met,A}$ profile at uncultivated position 2H1 was H=5, D_b=0.08, and E_{pre} = 0.1 mm y^{-1} (Fig 3.3B, Table 3.3), and the best iterative fit solution to the observed $^{10}Be_{met}$ profile at uncultivated position 2H2 was H=5, D_b=0.06, and E_{pre} = 0.1 mm y^{-1} (Fig 3.3C, Table 3.3). Therefore, best fit parameters used for modeling pre-settlement distributions on the cultivated transect were H=5, D_b=0.07 (average of D_b=0.06 and D_b=0.08) and E_{pre} scaled to slope based on an E_{pre} of 0.1 mm y^{-1} for slope tangents of 0.21 – 0.22 (Eqn 31).

E_{pre} derived from our numerical model with input parameters from 2H1 and scaled by slope (Eqn 31) for points 5-7 to 5-12 ranged from 0.35 – 0.61 Mg ha^{-1} y^{-1} (0.028 – 0.049 mm y^{-1}, (Table 3.3)). This resulted in expected pre-settlement $^{10}Be_{met,T}$

inventories of 5.2– 8.6 x 10^{13} atoms m^{-2}, while observed inventories ranged from 2.3 - 6.7 x 10^{13} atoms m^{-2} (Table 3.2). Regression equations from 1000 Monte Carlo runs of our numerical loss-only model were utilized to determine Epost estimates from observed plow layer $^{10}Be_{met}$ inventories (Fig 3.6). Estimated E_{post} at profiles 5-7, 5-8, 5-9, 5-10 and 5-12 resulted in erosion estimates ranging from 15 – 50 Mg ha^{-1} y^{-1} (1.17 – 4.09 mm y^{-1}, (Table 3.3)), with an average E_{post} of 33 ± 17 Mg ha^{-1} y^{-1}. E_{post} at shoulder and backslope positions (5-9, 5-10, 5-12) is more than twice those at the summit positions (5-7 and 5-8, Table 3.3). Similar to conversion Model 1, the backslope position (5-12) has the highest estimate of E_{post}.

3.3.6. Pre-settlement (E_{pre}) and total post-settlement (E_{post}) erosion rate estimates: ^{10}Be Conversion Model 3

The average landscape diffusivity value (k, cm^2 y^{-1}) was estimated from observed inventories across a linear portion of the uncultivated hillslope (profiles 2H2, 2H3, and 2H4) which comes closest to representing linear, plug-flow like accumulation necessary to apply steady-state models and derive estimates of long-term average erosion rates (McKean et al., 1993). The average value of k estimated from these $^{10}Be_{met}$ inventories (Eqn 32) is ~ 93 cm^2 y^{-1} (Table 3.4). Applying this average diffusivity value under steady-state assumptions and slope-dependent transport for the cultivated site, we arrive at independently derived estimates of natural erosion for the uncultivated site at points 5-7, 5-8, 5-9, 5-10, and 5-12 (Table 3.3).

The values of E_{pre} derived independently from uncultivated hillslope k and

curvature are 0.0009 – 0.44 Mg ha^{-1} y^{-1} (0.001 – 0.035 mm y^{-1}, Table 3.3). Corresponding estimated pre-settlement $^{10}Be_{met}$ inventories are 9.6 – 16.2 x 10^{14} atoms m^{-2}. E_{post} estimates, determined by applying regression equations over a range of unique solutions for E_{post} and plow layer $^{10}Be_{met}$ inventories resulted in E_{post} estimates ranging from 31-68 Mg ha^{-1} y^{-1} (0.235 – 0.526 mm y^{-1}, (Table 3.3)), with an average of 46 ± 17 Mg ha^{-1} y^{-1}. Similar to conversion other models, the highest erosion rate estimate for conversion Model 3 is at the backslope position (5-12).

3.3.7. Model suite inter-comparison

To facilitate the evaluation of structural errors in models, we also utilized previous published WATEM estimates for these sampling points in our model inter-comparison (Papiernik et al., 2005; Table 3.3). We tested for systematic differences between model estimates through paired t-tests of result sets (Table 3.5). Although important differences existed between summit (5-7, 5-8) and shoulder/backslope positions (5-9, 5-10, 5-12) for ^{10}Be conversion Models 1,2 and 3 (Table 3.3), there was no significant difference between all paired ^{10}Be conversion Model estimates of E_{post} (Table 3.5). ^{10}Be conversion model 1 resulted in the lowest average E_{post} estimates and smallest differences (20 ± 4 Mg ha^{-1} y^{-1}) for all ^{10}Be models and other models considered (including WATEM and ^{137}Cs), while ^{10}Be conversion model 3 resulted in the highest average E_{post} estimates and largest differences (41 ± 29 Mg ha^{-1} y^{-1}) for all ^{10}Be models (Table 3.3). Paired results from ^{10}Be conversion model 3 were not significantly different from WATEM or ^{137}Cs estimates of E_{post} (Table 3.5). E_{post} estimates at the sampling

points from WATEM (Papiernik et al., 2005) were greater than all other paired estimates except ^{10}Be conversion model 3 (Table 3.5).

3.4. Discussion

3.4.1. Relationship of $^{10}Be_{met}$ observations to previous studies of $^{10}Be_{met}$ and erosion in U.S. Midwestern and agricultural landscapes

Topsoil $^{10}Be_{met,T}$ concentrations at upper hillslope positions of both the uncultivated and cultivated portions of this study site are well below the range of previously reported values for surficial soils in the region, suggesting that the landscape at the margins of the Alexandria moraine is geomorphically dynamic under anthropogenic agricultural regimes, relative to the lower-relief areas surrounding the Minnesota River Valley investigated in previous studies (Balco, 2004, Belmont et al., 2011). The average of surficial depth increment concentrations of $^{10}Be_{met,T}$ in these previous studies in Minnesota and Iowa (n=11) is 24.6 x 10^7 atoms g^{-1}, with an average of 20.7 x 10^7 atoms g^{-1} in agricultural systems (n=8) and 21.2 x 10^7 atoms g^{-1} in natural (n=3, forest and prairie) systems. In contrast, the surficial values of $^{10}Be_{metT}$ at this study site are 10.1 x 10^7 atoms g^{-1} (SD = 6.8 x 10^7) for cultivated points (n=6) and 19.1 x 10^7 (SD = 7.0 x 10^7) for uncultivated points (n=5).

Values of $^{10}Be_{met,I}$ at our study site, which ranged from 0.88 x 107 atoms g^{-1} to 1.97 x 10^7 atoms g^{-1} are very similar to meteoric ^{10}Be concentrations from the banks of the Minnesota River (0.8 x 10^7 atoms g^{-1}), which represent deep deposits of unweathered Des Moines lobe till (Belmont et al., 2011), and inherited values from below 1m (1.9 x

10^7 atoms g^{-1} in Des Moines lobe till on a roadcut near Henderson, Minnesota (Balco, 2004).

Our average measured topsoil concentrations at the cultivated site were generally 50% of those measured in the grassland site despite the large differences in slope, demonstrating that the erosive forcing of ~ 100 years of tillage-intensive annual cropping systems is greater than that of 13,000 years of landscape evolution under natural regimes. This further supports meta-analyses that have shown that human-driven soil disturbance now accounts for the majority of global soil movement and sedimentation, even in relatively low-relief landscapes (Wilkinson and McElroy, 2007; Montgomery, 2007).

Because topsoil $^{10}Be_{met}$ concentrations are related to hillslope position, surficial concentrations of $^{10}Be_{met}$ are significantly correlated with whole-profile $^{10}Be_{met}$ inventories, as has been identified on a global scale in previous meta-analyses (Graly et al., 2010). The existence of high (> 20 x 10^7 atoms g^{-1}) $^{10}Be_{met}$ concentrations to 1m depth on the uncultivated hillslope demonstrates the ability of $^{10}Be_{met}$ to provide information on geomorphic change across long timescales. SOC inventories vary by 25% or less across the uncultivated hillslope and are not related to hillslope position, suggesting that the soil movement characterized by $^{10}Be_{met}$ is related to long-term diffusive soil movement and not recent or episodic deposition events. If agricultural activities post-settlement had significantly altered soil movement along the uncultivated hillslope, we would expect to see a significant increase in the variability of SOC inventories across the hillslope associated with post-settlement soil erosion and deposition (Papiernik et al., 2005; Quine and Van Oost, 2007). This is in strong contrast

to $^{10}Be_{met}$ and SIC inventories, which exceed 150 and 200% variation around the average across the uncultivated hillslope.

3.4.2. Soil profile truncation and depth of erosion

The strong relationship between surficial $^{10}Be_{met}$ concentrations and inventories to surficial SIC concentrations and inventories demonstrates a critical link between soil morphology, classification and changes in dynamic soil properties over timescales of centuries and beyond, which has been conceptually explored in previous studies (De Alba et al., 2004). The exposure or incorporation of subsoil carbonate-rich horizons with high concentrations of inorganic carbon has been shown to provide a reliable proxy for total post-settlement erosion and depth of soil profile truncation (Papiernik et al., 2007). Our use of direct observations of a tracer that provides evidence of total post-settlement soil truncation provides a critical link between morphologic and modeling studies (De Alba et al., 2004, Papiernik et al., 2005, Papiernik et al., 2007) and quantifiable long-term erosion rates. This link holds promise, if explored at multiple scales, to provide a quantitative basis for long-term erosion rate estimates from SIC concentrations and profile morphology alone. In contrast, SOC and ^{137}Cs activities were weak or non-significant predictors of surficial $^{10}Be_{met}$ concentrations due to the difference in timescales over which they operate. While SOC can reach steady-state over timescales of decades to centuries and ^{137}Cs was deposited and decays over decadal scales, the accumulation of $^{10}Be_{met}$ and the time it takes to reach steady-state is on the order of tens of thousands to millions of years (Willenbring and von Blanckenburg, 2010).

When erosion rates are converted into total post-settlement profile truncation depths (assuming 110 years of cultivation), the upper hillslope positions of the cultivated site have been truncated to an average depth of 26 ± 17 cm, which is into the original subsurface carbonate –rich subsoil horizons at many of the landscape positions, evidenced by high SIC concentrations in the cultivated Ap horizons. These estimates are consistent with results from soil properties alone (Papiernik et al., 2007).

3.4.3. Erosion estimates, conversion model and tracer comparisons

Our estimates of E_{pre} on the uncultivated hillslope for slope tangents of 0.21 and 0.22 (2H1 and 2H2, respectively) from Model 2 converged at 1 Mg ha^{-1} y^{-1} (0.1 mm y^{-1}). This erosion rate is well within the global mean of natural erosion rates for soil-mantled landscapes (Montgomery, 2007) and so represents a reasonable estimate based solely on model fit alone. Estimates of E_{pre} on the cultivated transect from Models 2 and 3 had a mean of 0.38 ± 0.16 Mg ha^{-1} y^{-1}, also well within the global mean of natural erosion rates for soil-mantled landscapes (Montgomery, 2007). Average estimates of E_{post} for ^{10}Be (31 ± 20 Mg ha^{-1} y^{-1}) suggest that erosion rates have increased 2 orders of magnitude across the hillslope since the time of European settlement.

The derived surficial diffusion parameter (D_b = 0.07 cm^2 y^{-1}) is lower than previous estimates across a range of natural ecosystems (0.2 – 2.4 cm^2 y^{-1}, Kaste et al, (2007), however these previous estimates were derived on stable landscape positions with short-lived radioisotopes and were heavily bioturbated. Under these parameters, assuming constant diffusion values across the landscape, $^{10}Be_{met}$ would have been largely

absent below 30cm on stable landscape positions or landscape positions experiencing soil loss. This is reasonable at our study site because $^{10}Be_{met}$ is likely to be largely immobile (due to high pH) and therefore largely transported downward through bioturbation by fossorial mammals. No $^{10}Be_{met,A}$ was observed below 30cm in soil loss profiles (5-7,5-8, 5-9, 5-10, 5-12, 2H1, 2H2), regardless of land-use. In other related landscapes where advective or sedimentation-like processes such as clay illuviation or loess accumulation become more important, $^{10}Be_{met,A}$ can be found below 50cm even on stable or eroding landscape positions (Harden et al., 2002; Balco, 2004).

Choice of conversion model (an evaluation of structural error) has a strong effect on $^{10}Be_{met}$ erosion rate estimates. The application of three different conversion models for the estimation of E_{post} using $^{10}Be_{met}$ observations resulted in differing point estimates. ^{10}Be conversion Models 1, 2 and 3 resulted in very similar estimates at summit positions (5-7, 5-8), but diverged at the shoulder (5-9, 5-10) and backslope (5-12). The erosion rates derived from conversion model 3 were higher than all model 1 and 2 estimates (Table 3.4). The erosion rates near the summit from $^{10}Be_{met}$ models are all significantly lower than estimates from other models (Table 3.3). These point estimates of erosion rates, when combined with ^{137}Cs inventories and erosion rates from conversion models as well as previous work at the study site (Li et al., 2007; Li et al 2008) provide an important context for observations of near-term (<50 year) erosion rates by extending the timeframe of agricultural erosion rate estimation to century timescales.

Differences between ^{10}Be, ^{137}Cs and WATEM models at the cultivated sampling points may be due to actual differences in tracers or due to structural differences in

models. It is clear from our paired comparisons (Table 3.5) that ^{10}Be conversion Model 1 presents a lower boundary of E_{post} across all cultivated profiles as the estimates it produced are significantly less than those from WATEM and 137Cs (Table 3.5). It also produced the most narrow range of estimates (16-24 Mg ha^{-1} y^{-1}) demonstrating the insensitivity of the model to landscape parameters as it assumes complete independence. In contrast, ^{10}Be conversion model 3 resulted in E_{post} estimates that were not significantly different from those derived from ^{137}Cs or WATEM. Because ^{10}Be conversion Model 3 is the most detailed ^{10}Be model presented in this study (taking into account soil mass balance through hillslope evolution), it is likely that these estimates are the best E_{post} estimates derived from our $^{10}Be_{met}$ data. The similarities in these estimates and ^{137}Cs and WATEM estimates support the hypothesis that current erosion rates at the cultivated site have not changed significantly since the time of settlement. In this case, E_{post} estimates from ^{10}Be Models 1 & 2, which are independent of geomorphic setting (Model 1) or take into account only soil loss (Model 2) should be viewed as conservative boundaries on E_{post}, particularly on shoulder and backslope positions (5-9, 5-10, 5-12).

However, we cannot rule out that these model estimates reflect a real difference in century vs. decadal scale erosion rates, particularly at summit positions (5-7, 5-8). This could result even under similar tillage regimes if implement velocities were less frequent and slower at the time of settlement (due to use of animal power), both of which would result in lower rates of tillage erosion pre-mechanization. In this scenario, we would expect (if tillage regime has been fairly consistent) that long-term estimates from ^{10}Be would be less than estimates from ^{137}Cs but similar to those from models driven by

topography alone (WATEM). Conversely, if conservation practices have improved, we may expect decadal-scale erosion rates to be less than long-term rates. We find no evidence in our model estimates to suggest this third scenario.

Interestingly, ^{137}Cs derived erosion estimates at the cultivated footslope profile (5-14) resulted in a net soil accumulation estimate of 3 Mg ha^{-1} y^{-1} (linear model). The results of a linear model applied to $^{10}Be_{met}$ data at the same location resulted in estimates of soil accumulation of almost 80 Mg ha^{-1} y^{-1}. Therefore, although ^{137}Cs and ^{10}Be erosion estimates are convergent on soil loss positions, the results at 5-14 demonstrate that there may be a strong dependency of landscape position on the convergence of these tracers.

All models have erred on the side of conservative estimation at every step of parameter estimation and application. Even the basis of our erosion rate estimates (the uncultivated $^{10}Be_{met}$ observations) are conservatively applied due to the nature of slope differences on our paired cultivated and uncultivated study sites. Because the uncultivated study site acts as a reference through the application of our conversion models, steeper reference sites (which have higher rates of E_{pre}) should lead to more conservative estimates of E_{post}. It is best, then, to view the $^{10}Be_{met}$ erosion rate estimates as minimum total post-settlement erosion rates. It is likely that under some scenarios total post-settlement erosion rates greatly exceed those estimated here.

One other study has attempted to utilize observations of $^{10}Be_{met}$ on paired cultivated and uncultivated hillslopes and found similar convergence between values of long-term erosion estimated from $^{10}Be_{met}$ and ^{137}Cs at a single sampling point (27 Mg ha^{-1} y^{-1} and 20-60 Mg ha^{-1} y^{-1}, respectively, (Harden et al., 2002)). Harden et al. (2002) and a

revisit of the ^{10}Be data contained therein (Graly et al., 2010) utilized space-for-time direct comparisons of hillslope positions to derive erosion rates and total post-settlement soil truncation. Our study is the first to apply numerical models of depth profile evolution of $^{10}Be_{met}$ through accumulation during landscape evolution and subsequent erosive losses from agricultural land-use. The convergence of these results from independent numerical models with those of traditional approaches is encouraging and suggests that $^{10}Be_{met}$ is useful in other settings for constraining agricultural erosion beyond the timeframe of other tracers.

These numerical methods likely work best in a study site such as the one presented here, where the landscape is relatively young (< 20,000 years), with only moderate precipitation and neutral natural pH. This allows simplifying assumptions regarding the relative importance of diffusive and advective movement, however these limitations have not been fully explored and could be overcome with further development of the numerical modeling approach presented here and integration with complex landscape evolution models.

3.5. Conclusions and Implications

The results of this study show that $^{10}Be_{met}$ can be used as a powerful tracer of erosion rates (both pre-and post- settlement) in agricultural systems that cannot be replicated by other direct lines evidence apart from morphology. $^{10}Be_{met}$ therefore provides the first supporting observations of long-term average erosion point estimates from WATEM models (Papiernik et al., 2005) and suggests that erosion rates have

increased by at least 2 orders of magnitude over pre-settlement rates. Post-settlement erosion rate estimates derived from some ^{10}Be conversion models at this site in west-central Minnesota are similar but lower, on average, to those derived from ^{137}Cs and topography-driven models. This suggests the need for further research on the development of $^{10}Be_{met}$ as a tracer of erosion due to land-use change in settings where these models would be expected to yield highly diverging estimates. In this study:

- Meteoric ^{10}Be revealed millennial scale soil movement across an uncultivated hillslope that was not revealed in carbon or ^{137}Cs inventories.
- $^{10}Be_{met}$-derived estimates of pre-settlement erosion across the cultivated sampling points ranged from 0.009 – 0.61 Mg ha^{-1} y^{-1}.
- $^{10}Be_{met}$-derived 110-year average post-settlement erosion rates across a cultivated transect at our study site ranged from 10 - 85 Mg ha^{-1} y^{-1}.
- Meteoric ^{10}Be inventories are negatively correlated to SIC inventories and erosion rates scaled to total post-settlement truncation (9-77 cm) closely match morphological data and observed depths to calcic horizons.
- Integrated models of long-term landscape evolution and diffusive/advective models of $^{10}Be_{met}$ in soil profiles should be built and tested under various geomorphic and land-use scenarios.

Sample Location	Depth Increment (cm)	Genetic Horizon[a]	Bulk Density (g cm^{-3})	$^{10}Be_{met}$ concentration, 10^7 atoms g^{-1}, Total[b]	$^{10}Be_{met}$ concentration, 10^7 atoms g^{-1}, Accumulated[c]	Soil Organic Carbon (g $100g^{-1}$)[d]	Soil Inorganic Carbon (g $100g^{-1}$)[d]	^{137}Cs activity (Bq kg^{-1})
				Cultivated				
5-7[e]	0-18	Ap	1.27	12.6 ± 0.7	11.5 ± 0.8	1.4 ± 0.2	1.4 ± 0.4	3.4 ± 0.4
5-8	0 – 23	Ap	1.31	15.8 ± 0.3	14.7 ± 0.3	1.4 ± 0.2	0.9 ± 0.2	3.0 ± 0.2
5-8	23 – 47	Bk1	1.53	1.18 ± 0.03[f]*	-	0.7 ± 0.1	2.1 ± 0.6	-
5-8	47 – 67	Bk2	1.31	0.97 ± 0.06*	-	0.3 ± 0.1	2.2 ± 0.6	-
5-8	67 – 92	BC	1.60	0.99 ± 0.04*	-	0.2 ± 0.1	2.2 ± 0.6	-
5-8	92 – 145	C	1.33	1.09 ± 0.02*	-	0.1 ± 0.1	2.2 ± 0.6	-
5-9	0 – 19	Ap	1.50	5.18 ± 0.08	4.11 ±0.09	1.0 ± 0.2	2.5 ± 0.7	2.8 ± 0.3
5-9	19 – 48	Bk	1.40	0.82 ± 0.02*	-	0.4 ± 0.1	3.0 ± 0.8	-
5-9	48 – 92	C1	1.43	0.63 ± 0.03*	-	0.3 ± 0.1	2.7 ± 0.7	-
5-9	92 – 130	C2	1.40	0.63 ± 0.02*	-	0.2 ± 0.1	2.2 ± 0.6	-
5-10	0 – 21	Ap	1.38	4.16 ± 0.08	3.08 ± 0.09	1.0 ± 0.2	2.2 ± 0.6	2.4 ± 0.2
5-10	21-75	Bk	1.19	1.20 ± 0.03*	-	0.2 ± 0.1	2.2 ± 0.6	-
5-10	75 – 115	C1	1.48	0.846 ± 0.04*	-	0.2 ± 0.1	2.4 ± 0.7	-
5-10	115 -147	C2	1.47	0.904 ± 0.03*	-	0.3 ± 0.1	2.4 ± 0.7	-
5-12	0 – 18	Ap	1.22	3.16 ± 0.06	2.09 ± 0.08	1.2 ± 0.2	2.4 ± 0.7	1.3 ± 0.2
5-12	18-60	Bk	0.68	1.48 ± 0.04*	-	0.6 ± 0.1	4.7 ± 1.3	-
5-12	60-100	BC	1.09	1.31 ± 0.06*	-	0.8 ± 0.1	3.8 ± 1.0	-
5-12	100- 130	C	1.29	0.873 ± 0.04*	-	0.6 ± 0.1	2.8 ± 0.8	-
5-14	0 – 22	Ap	1.48	19.2 ± 0.3	18.1 ± 0.3	1.4 ± 0.2	0.5 ± 0.1	3.9 ± 0.3
5-14	22 – 55	AB	1.38	24.8 ± 0.3	23.8 ± 0.4	1.2 ± 0.2	0.1 ± 0.1	1.3 ± 0.2
5-14	55 – 82	Bw1	1.35	12.0 ± 0.2	10.9 ± 0.2	0.5 ± 0.1	-	-
5-14	82 – 122	2Bw2	1.34	1.26 ± 0.03*	-	0.2 ± 0.1	-	-
5-14	122- 146	2Bk	1.37	0.782 ± 0.02*	-	0.1 ± 0.1	0.9 ± 0.2	-
				Uncultivated				
2H1	0 – 16	A	1.00	12.4 ± 0.4	11.3 ± 0.4	5.0 ± 0.8	1.0 ± 0.3	12.5 ± 0.4
2H1	16 - 24	AB	1.51	5.20 ± 0.04	4.12 ± 0.1	2.3 ± 0.3	2.5 ± 0.7	3.1 ± 0.3
2H1	24 – 48	Bk1	1.47	1.49 ± 0.04*	-	1.2 ± 0.2	3.0 ± 0.8	-

2H1	48 – 84	Bk2	1.35	1.30 ± 0.05*	-	0.5 ± 0.1	2.7 ± 0.7	-
2H1	84 – 135	C	1.39	1.07 ± 0.04*	-	0.3 ± 0.1	2.3 ± 0.6	-
2H2	0 -16	A	1.09	11.0 ± 0.1	9.98 ± 0.1	3.9 ± 0.6	0.3 ± 0.1	8.4 ± 0.3
2H2	16-32	AB	1.30	3.38 ± 0.07	2.31 ± 0.08	2.4 ± 0.3	2.3 ± 0.6	5.4 ± 0.7
2H2	32 – 60	Bk1	1.15	1.09 ± 0.03*	-	1.0 ± 0.2	3.4 ± 0.9	-
2H2	60 – 87	Bk2	1.51	0.986 ± 0.05*	-	0.4 ± 0.1	2.5 ± 0.7	-
2H2	87 – 131	C	1.41	0.947 ± 0.04*	-	0.4 ± 0.1	2.1 ± 0.6	-
2H3	0 – 22	A	0.91	23.1 ± 0.5	18.1 ± 0.5	4.4 ± 0.7	-	9.4 ± 0.4
2H3	22 – 40	AB	1.10	21.6 ± 0.6	20.5 ± 0.6	1.5 ± 0.2	-	0.8 ± 0.2
2H3	40 – 70	Bw1	1.24	13.6 ± 0.2	12.6 ± 0.2	0.7 ± 0.1	-	-
2H3	70 – 122	Bw2	1.11	1.97 ± 0.06*	-	0.3 ± 0.1	0.2 ± 0.1	-
2H4	0 – 24	A1	1.00	22.1 ± 0.2	21.0 ± 0.2	3.9 ± 0.6	-	9.7 ± 0.6
2H4	24 – 58	A2	1.19	16.7 ± 0.2	15.6 ± 0.2	1.2 ± 0.2	-	0.2 ± 0.1
2H4	58 – 86	AB	1.53	19.0 ± 0.3	17.9 ± 0.3	0.8 ± 0.1	-	-
2H4	86 – 107	Bw1	1.30	23.1 ± 0.3	22.0 ± 0.3	0.7 ± 0.1	-	-
2H4	107- 144	Bw2	1.34	8.74 ± 0.1	7.66 ± 0.1	0.3 ± 0.1	-	-
2H5	0 – 23	A	1.16	26.8 ± 0.3	25.8 ± 0.3	4.0 ± 0.6	-	5.9 ± 0.2
2H5	23-47	AB	1.36	17.0 ± 0.6	16.0 ± 0.2	1.2 ± 0.2	-	-
2H5	47 – 67	Bw1	1.38	3.53 ± 0.08	2.46 ± 0.09	0.4 ± 0.1	0.5 ± 0.1	-
2H5	67 – 98	Bk1	1.25	1.18 ± 0.08*	-	0.4 ± 0.1	2.0 ± 0.5	-
2H5	98-125	Bk2	1.31	0.881 ± 0.03*	-	0.5 ± 0.1	2.2 ± 0.6	-
2H5	125-150	C	1.63	0.866 ± 0.03*	-	0.1 ± 0.1	2.2 ± 0.6	-

Table 3.1. Meteoric ^{10}Be, soil organic carbon (SOC), soil inorganic carbon (SIC) concentrations and ^{137}Cs distributions.

[a]Genetic soil horizon designations from Schoeneberger et al. 2012.

[b]Total $^{10}Be_{met}$ concentration ($^{10}Be_{met,T}$ - 07KNSTD standard used for normalization (10Be/9Be ratio of 2.85 x 10^{-12}), uncertainty reported represents 1 standard deviation from the mean AMS measurement.

[c]Accumulated $^{10}Be_{met}$ concentration ($^{10}Be_{met,A}$) = $^{10}Be_{met,T}$ – $^{10}Be_{met,Iave}$ ($^{10}Be_{met,Iave}$ = average inherited $^{10}Be_{met}$: 1.07 ± 0.04 x 10^7 atoms g^{-1})

[d]Uncertainty reported represents the analytical uncertainty (1σ) evaluated from 21 duplicate samples.

[e]Due to sampling limitations, 5-7 is characterized solely by the surficial (plow layer) increment, which, based on all other observations across the cultivated site is assumed to contain all profile accumulated ^{10}Be ($^{10}Be_{met,A}$).

[f]Measurements with an asterisk (*) meet the criteria for inclusion in calculation of average parent material values and ^{10}Be inheritance.

Profile	Hillslope Position	Slope[a]	Curvature[b]	$^{10}Be_{met}$ 10^{13} atoms m^{-2}, Total[c]	$^{10}Be_{met}$ 10^{13} atoms m^{-2}, Accum.[d]	SOC[e] kg m^{-2}	SIC[f] kg m^{-2}	^{137}Cs[g] Bq m^{-2}
				Cultivated				
5-7	Summit	0.06	+0.04	4.6 ± 0.5	2.6 ± 0.5	8.9 ± 1.7	44 ± 10	771 ± 153
5-8	Summit	0.06	+0.04	6.7 ± 0.8	4.4 ± 0.7	8.9 ± 1.7	41 ± 10	894 ± 161
5-9	Shoulder	0.07	+0.04	2.8 ± 0.3	1.2 ± 0.2	7.8 ± 1.5	55 ± 13	792 ± 158
5-10	Shoulder	0.10	+0.04	2.9 ± 0.3	0.9 ± 0.2	6.6 ± 1.3	47 ± 11	680 ± 129
5-12	Backslope	0.11	0.0	2.3 ± 0.2	0.5 ± 0.1	10.6 ± 2.0	53 ± 12	280 ± 65
5-14	Footslope	0.08	-0.01	22.9 ± 2.2	20.7 ± 2.1	13.8 ± 2.6	5.5 ± 1.3	1843 ± 353
				Uncultivated				
2H1	Sum./Shld.	0.21	+0.06	4.7 ± 0.4	2.3 ± 0.3	19.8 ± 3.9	49 ± 12	2359 ± 420
2H2	Shoulder	0.22	+0.05	4.2 ± 0.4	2.2 ± 0.3	19.4 ± 3.7	45 ± 11	2584 ± 484
2H3	U. Backslope	0.17	0.0	15.5 ± 1.3	13.1 ± 1.2	16.2 ± 3.1	1.5 ± 0.3	2035 ± 360
2H4	L. Backslope	0.16	-0.01	30.9 ± 2.3	28.8 ± 2.1	21.2 ± 4.0	0.01 ± 0.01	2380 ± 434
2H5	Footslope	0.15	-0.02	14.8 ± 1.5	12.8 ± 1.4	19.5 ± 3.7	26 ± 6	1571 ± 260

Table 3.2. Land use, geomorphic parameters and inventories at cultivated and uncultivated sampling points.
[a]Slope tangent from USGS 10m DEM.
[b]Curvature from USGS 10m DEM.
[c]Total $^{10}Be_{met}$ inventory, uncertainty reported represents the standard combined uncertainty (1σ). Inventories calculated to 150cm extending lowest increment observations to 150cm if shallower.
[d]Accumulated $^{10}Be_{met}$ inventory ($^{10}Be_{met,\,A}$) = $^{10}Be_{met,T} - {}^{10}Be_{met,Iave}$, uncertainty reported represents the standard combined uncertainty (1σ).
[e]Soil Organic Carbon inventory, uncertainty reported represents the standard combined uncertainty (1σ).
[f]Soil Inorganic Carbon inventory, uncertainty reported represents the standard combined uncertainty (1σ).
[g]^{137}Cs inventory, uncertainty reported represents the standard combined uncertainty (1σ).

Profile	Hillslope Position	E_{pre} (Model 2) Mg ha^{-1} yr^{-1} (mm yr^{-1})[a]	E_{pre} (Model 3) Mg ha^{-1} yr^{-1} (mm yr^{-1})[b]	E_{post} (^{10}Be Model 1) Mg ha^{-1} yr^{-1} (mm yr^{-1})[c]	E_{post} (^{10}Be Model 2) Mg ha^{-1} yr^{-1} (mm yr^{-1})[d]	E_{post} (^{10}Be Model 3) Mg ha^{-1} yr^{-1} (mm yr^{-1})[d]	E_{post} (^{137}Cs Linear Model) Mg ha^{-1} yr^{-1} (mm yr^{-1})[c]	E_{post} (^{137}Cs Power Model) Mg ha^{-1} yr^{-1} (mm yr^{-1})[c]	E_{post} (WATEM, Papiernik et al., 2005) Mg ha^{-1} yr^{-1} (mm yr^{-1})[e]
5-7	Summit	0.35 (0.028)	0.28 (0.022)	16 ± 4 (1.26 ± 0.31)	15 ± 6 (1.21 ± 0.51)	19 ± 8 (1.57 ± 0.66)	31 ± 10 (2.44 ± 0.79)	23 ± 4 (1.81 ± 0.31)	43 (3.46)
5-8	Summit	0.35 (0.028)	0.39 (0.031)	17 ± 5 (1.30 ± 0.38)	15 ± 6 (1.17 ± 0.49)	10 ± 4 (0.79 ± 0.33)	36 ± 12 (2.75 ± 0.92)	30 ± 5 (2.29 ± 0.38)	37 (2.98)
5-9	Shoulder	0.40 (0.032)	0.44 (0.035)	23 ± 5 (1.53 ± 0.33)	43 ± 9 (2.89 ± 0.57)	42 ± 8 (2.79 ± 0.55)	38 ± 12 (3.53 ± 0.80)	28 ± 5 (1.87 ± 0.33)	50 (4.03)
5-10	Shoulder	0.55 (0.044)	0.43 (0.034)	24 ± 6 (1.74 ± 0.43)	44 ± 9 (3.21 ± 0.62)	50 ± 10 (3.64 ± 0.70)	42 ± 13 (3.04 ± 0.94)	29 ± 5 (2.10 ± 0.36)	63 (5.08)
5-12	Backslope	0.61 (0.049)	0.009 (0.001)	19 ± 4 (1.56 ± 0.33)	50 ± 8 (4.09 ± 0.67)	85 ± 14 (7.01 ± 1.15)	41 ± 12 (3.36 ± 0.98)	22 ± 4 (1.80 ± 0.33)	50 (4.03)
5-14	Footslope	-	-	+79[f] ± 26 (+5 ± 2)	-	-	+3 ± 45 (+0.2 ± 3)	+110 ± 17 (+7 ± 1)	+20 (+1.35)

Table 3.3. Erosion estimates at cultivated sampling points for suite of conversion models.

[a]Minimum RMSE solution for average pre-settlement erosion rate (E_{pre}) from numerical model. All estimates presented in both Mg ha^{-1} yr^{-1} and mm yr^{-1} to facilitate model comparison. Unit conversions utilize observed bulk density values.

[b]Estimated pre-settlement erosion rate (E_{pre}) estimated from derived landscape diffusivity value (K = 93 cm^2 yr^{-1}) and elevation differences along normal to contour lines across sampling point from USGS 10m DEM.

[c]Estimated post-settlement erosion rate (E_{post}), reported uncertainty represents standard combined uncertainty (1σ).

[d]Estimated post-settlement erosion rate (E_{post}), reported uncertainty represents lower and upper boundaries of 10th and 90th percentiles of 1000 Monte Carlo simulations.

[e]Estimated post-settlement erosion rate (Epost) from WATEM model in Papiernik et al. (2005)

[f]Positive values (+) represent accumulation rate estimates at footslope position (5-14). Numerical models are invalid at accumulation positions.

Uncultivated Sampling Point	Distance from crest (cm)	Depth averaged $^{10}Be_{met}$ Concentration[a] (10^7 atoms g^{-1})	Depth averaged soil bulk density[b] (g cm^{-3})	Slope tangent[c]	Diffusivity K (cm^2 yr^{-1})[d]
2H1	0	8.91	1.30	0.21	-
2H2	1100	6.15	1.15	0.22	91.9
2H3	2400	17.6	1.31	0.17	79.6
2H4	3300	15.9	1.47	0.17	108
2H5	4400	15.3	1.32	0.15	-
				Average	93

Table 3.4. Estimation of average landscape diffusivity (K cm^2 yr^{-1}) from uncultivated $^{10}Be_{met}$ observations

[a]Weighted depth-average of total 10Bemet ($^{10}Be_{met,T}$)concentrations for all profile depth increments containing accumulated (non-inherited) $^{10}Be_{met}$ ($^{10}Be_{met,A}$).

[b]Weighted depth-average bulk density for all profile depth increments containing accumulated (non-inherited) $^{10}Be_{met}$ ($^{10}Be_{met,A}$).

[c]Slope tangent from USGS 10m DEM.

[d]Diffusivity estimates utilize 1.3 x 10^6 atoms cm^{-2} yr^{-1} as the estimated long-term average $^{10}Be_{met}$ deposition rate.

Model	^{10}Be –Model 1[a]	^{10}Be – Model 2	^{10}Be –Model 3	WATEM[b]	^{137}Cs – Linear	^{137}Cs – Power
^{10}Be – Model 1	-					
^{10}Be – Model 2	NS[c]	-				
^{10}Be – Model 3	> , p=0.02[d]	>, p=0.02	-			
WATEM	>, p<0.001	>, p=0.04	NS	-		
^{137}Cs – Linear	>, p<0.001	NS	NS	<, p=0.03	-	
^{137}Cs – Power	>, p=0.02	NS	NS	<, p<0.01	<, p<0.01	-

Table 3.5. Comparison of modeled post-settlement (E_{post}) erosion rates.

[a]Model names refer to text descriptions for ^{10}Be and ^{137}Cs conversion models.

[b]Results from Water and Tillage Erosion (WATEM) model (Van Oost et al., 2000), reported for sampling points in Papiernik et al., 2005).

[c]Results of paired t-tests (with Bonferroni correction) for all cultivated sampling position estimates, NS = not significant at $\alpha = 0.05$.

[d]Results of paired t-tests (with Bonferroni correction) for all cultivated sampling position estimates, >/< refer to the row – column comparison (i.e. >, p = 0.02 means that the post-settlement erosion estimates (E_{post}) from the row model were greater than the E_{post} from the column model with p = 0.02).

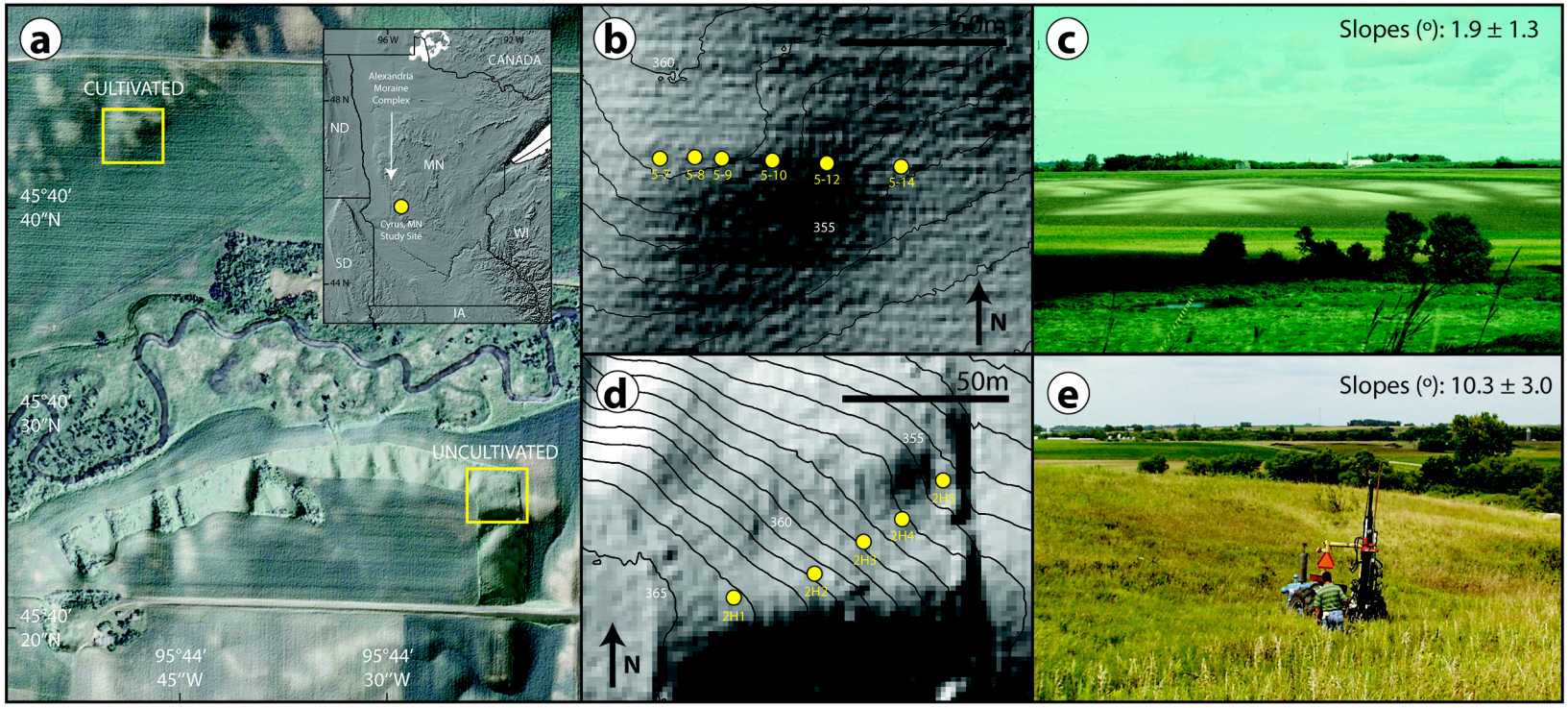

Figure 3.1. Study site landscape setting and hillslope transects. (a) Regional setting (inset), orthophoto and hillshade of study site showing location of cultivated and uncultivated sampling areas. (b) 1-m DEM (LIDAR) showing sampling points and elevation contours (m) for cultivated transect. (c) Landscape photo of cultivated transect with eroded summit, shoulder and backslopes (light-colored, exposed sub-surface material), Photo Credit: S. K. Papiernik. (d) 1-m DEM (LIDAR) showing sampling points and elevation contours (m) for uncultivated hillslope. (e) Landscape photo of uncultivated hillslope, Photo Credit: T.E. Schumacher.

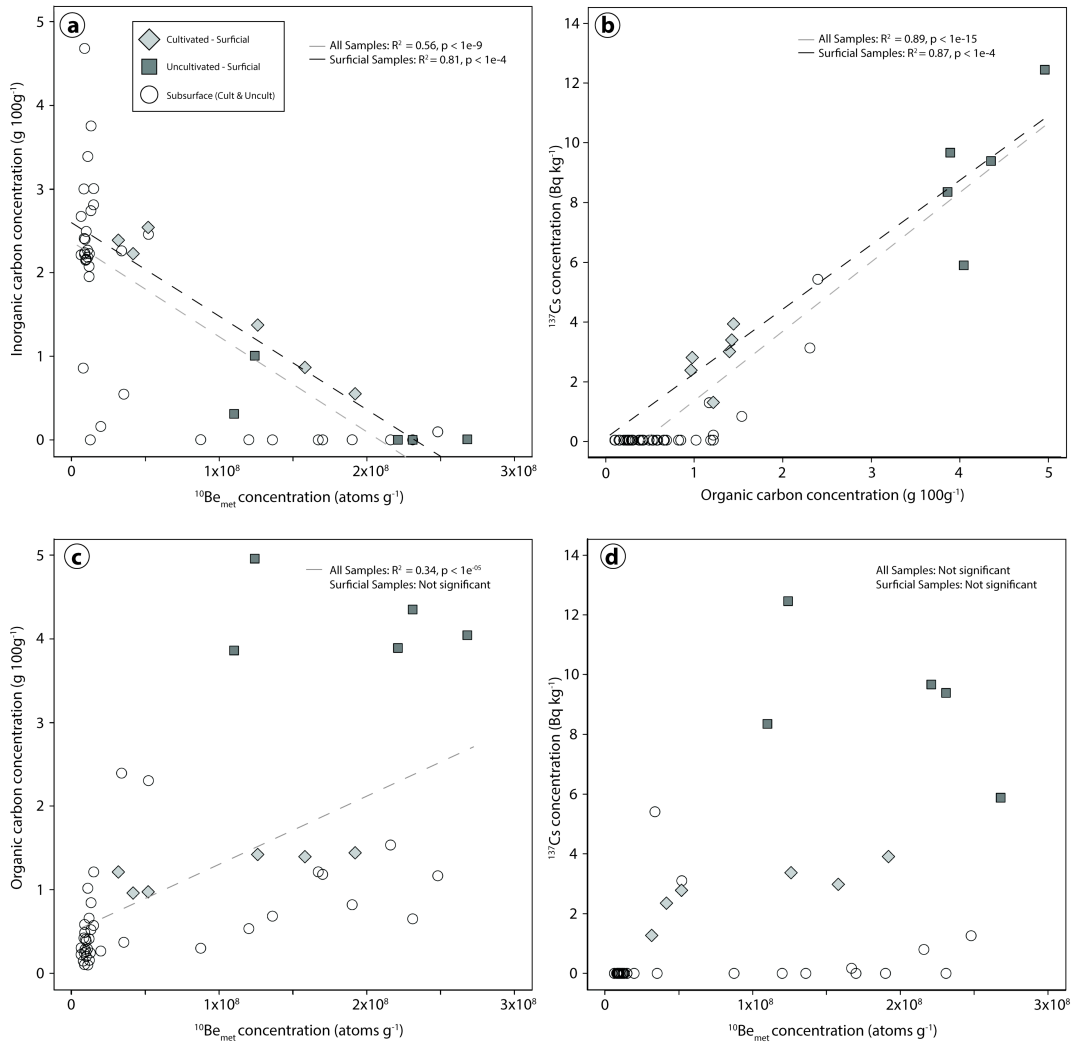

Figure 3.2. Relationship of (a) $^{10}Be_{met}$ concentrations and soil inorganic carbon, (b) Soil organic carbon and ^{137}Cs activities and soil organic carbon, (c) $^{10}Be_{met}$ concentrations and soil organic carbon, and (d) $^{10}Be_{met}$ concentrations and ^{137}Cs activities.

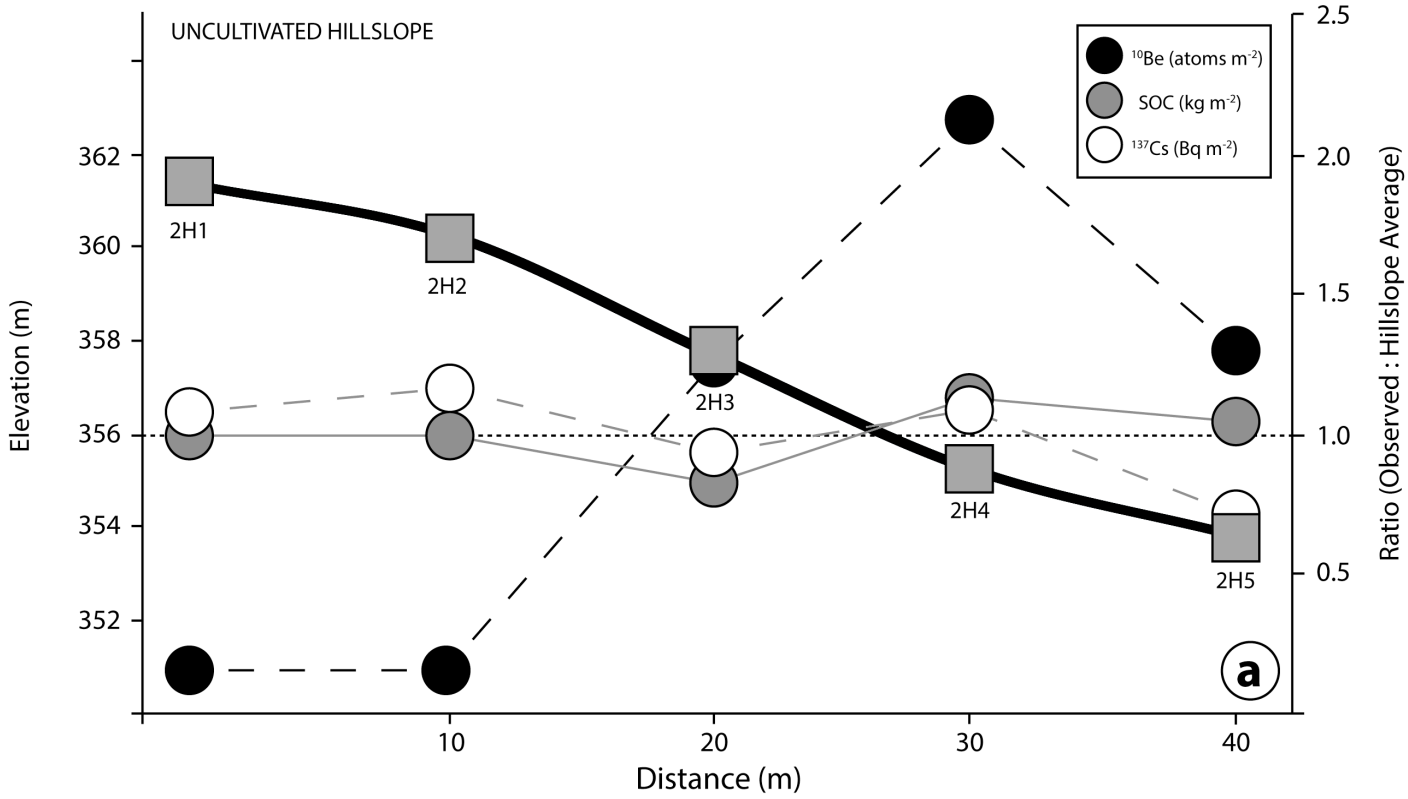

Figure 3.3. (a) Variation in $^{10}Be_{met,T}$, soil organic carbon (SOC) and ^{137}Cs across uncultivated hillslope and $^{10}Be_{met,T}$ profile inventories at (b) 2H1, (c) 2H2, (d) 2H3, (e) 2H4, (f) 2H5. Dotted lines in panels b and c are the best-fit (minimum RMSE) profiles of $^{10}Be_{met,T}$ from numerical model 2 (Eqn 29 and 30), where H = depth of half maximum (cm), Db = surficial diffusion parameter (cm^2 y^{-1}), E_{pre} = long-term average erosion rate. Note logarithmic scale and units (g cm^{-3}) for $^{10}Be_{met,T}$ inventories in panels b-f. Error bars on $^{10}Be_{met,T}$ increment inventories (g cm^{-3}) represent the standard combined uncertainty (1σ), including $^{10}Be_{met}$ and bulk density measurement error. Abbreviations next to increments are genetic horizon nomenclature following (Schoeneberger et al. 2012).

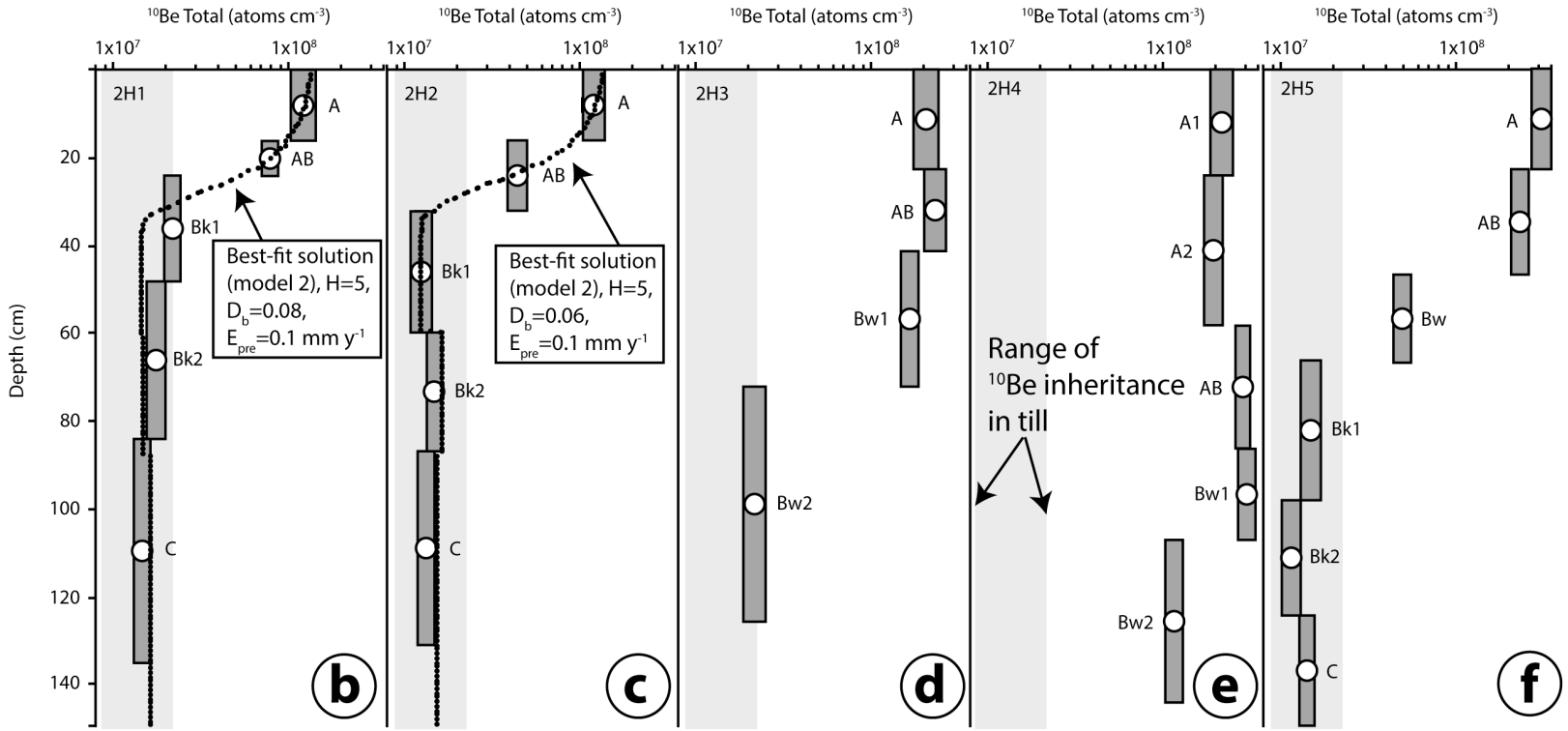

Figure 3.3 (Cont). (a) Variation in $^{10}Be_{met,T}$, soil organic carbon (SOC) and ^{137}Cs across uncultivated hillslope and $^{10}Be_{met,T}$ profile inventories at (b) 2H1, (c) 2H2, (d) 2H3, (e) 2H4, (f) 2H5. Dotted lines in panels b and c are the best-fit (minimum RMSE) profiles of $^{10}Be_{met,T}$ from numerical model 2 (Eqn 29 and 30), where H = depth of half maximum (cm), Db = surficial diffusion parameter ($cm^2\ y^{-1}$), E_{pre} = long-term average erosion rate. Note logarithmic scale and units (g cm^{-3}) for $^{10}Be_{met,T}$ inventories in panels b-f. Error bars on $^{10}Be_{met,T}$ increment inventories (g cm^{-3}) represent the standard combined uncertainty (1σ), including $^{10}Be_{met}$ and bulk density measurement error. Abbreviations next to increments are genetic horizon nomenclature following (Schoeneberger et al. 2012).

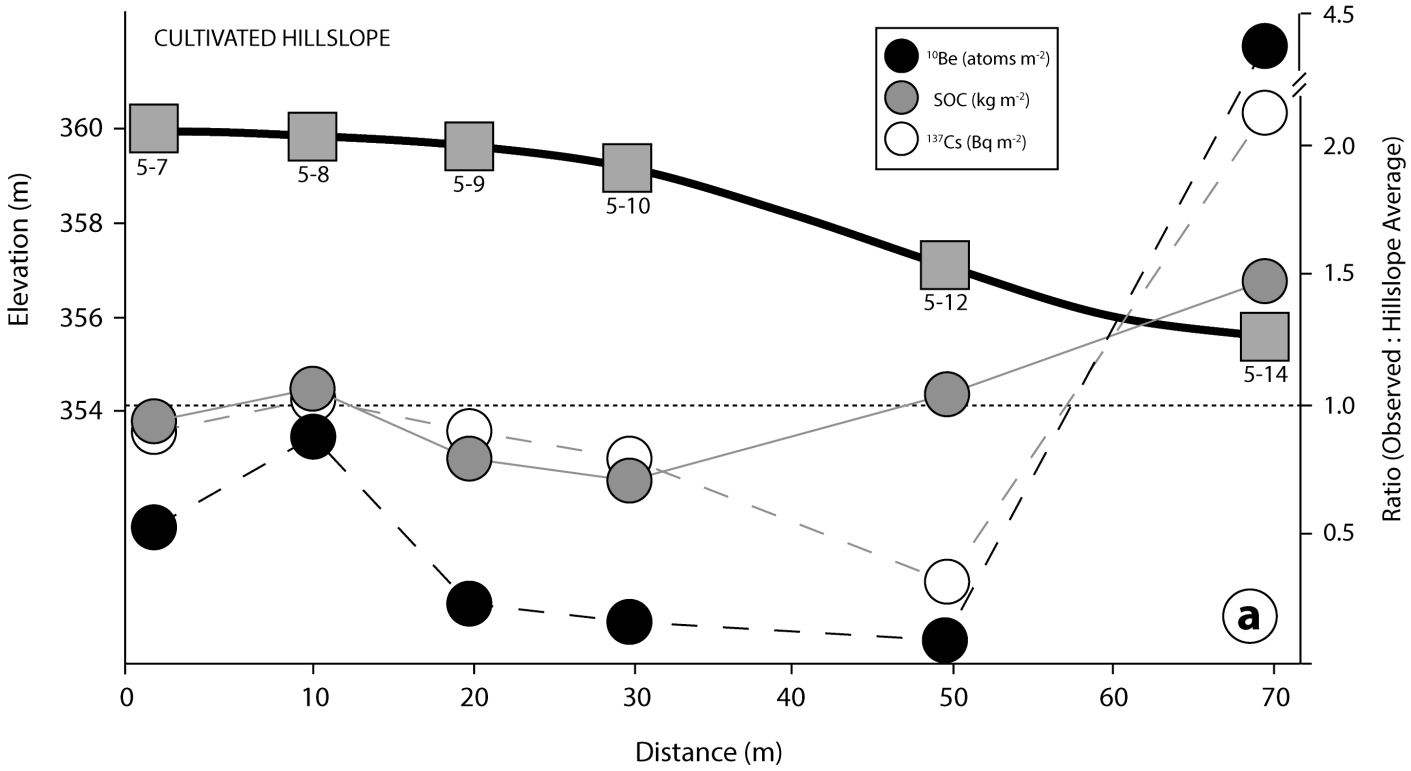

Figure 3.4. Variation in (a) $^{10}Be_{met,T}$, soil organic carbon (SOC) and ^{137}Cs across cultivated transect and $^{10}Be_{met,T}$ profile inventories at (b) 5-7, (c) 5-8, (d) 5-9, (e) 5-10, (f) 5-12 and (g) 5-14. Black dotted lines in panels b-g are the best estimate pre-settlement profiles of $^{10}Be_{met,T}$ from numerical model 2, where E_{pre} = average pre-settlement erosion rate and Epost = average post-settlement erosion rate. Grey dotted lines in panels b-g are increment-averaged values of best estimate pre-settlement inventories (black dotted lines). Note logarithmic scale and units (g cm^{-3}) for $^{10}Be_{met,T}$ inventories in panels b-g. Error bars on $^{10}Be_{met,T}$ increment inventories (g cm^{-3}) represent the standard combined uncertainty (1σ), including $^{10}Be_{met}$ and bulk density measurement error. Abbreviations next to increments are genetic horizon nomenclature following (Schoeneberger et al. 2012).

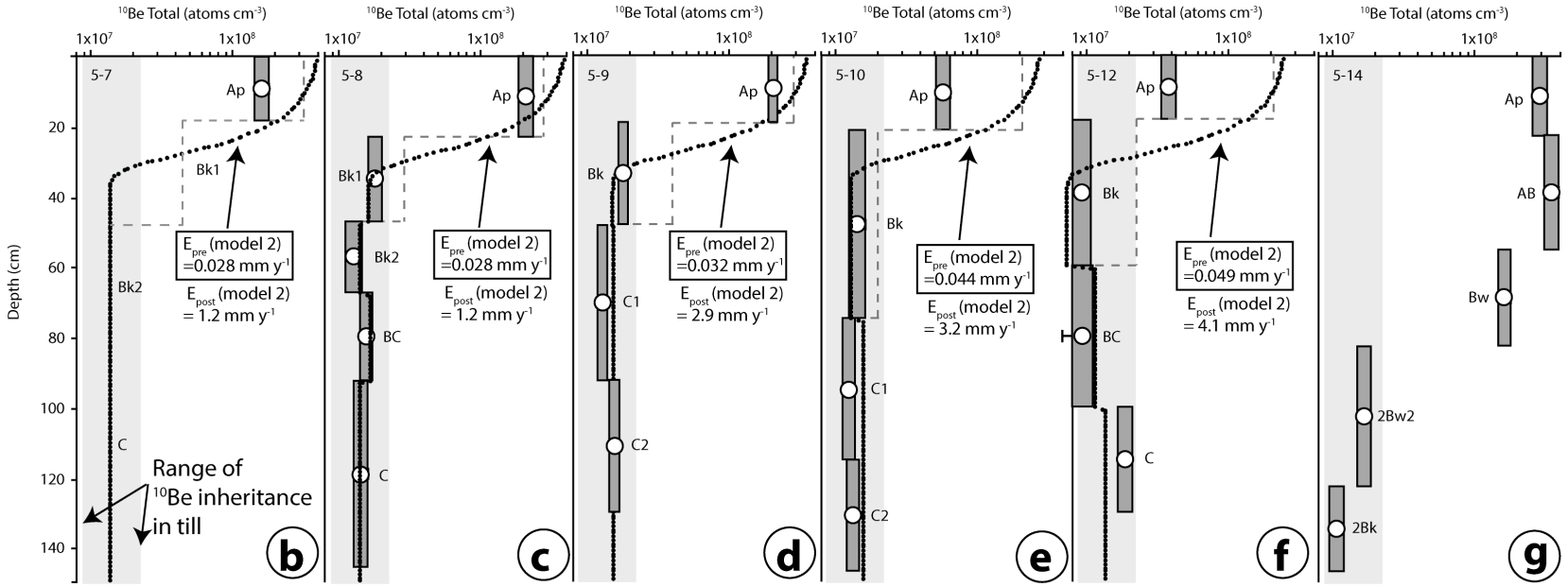

Figure 3.4 (Cont). Variation in (a) $^{10}Be_{met,T}$, soil organic carbon (SOC) and ^{137}Cs across cultivated transect and $^{10}Be_{met,T}$ profile inventories at (b) 5-7, (c) 5-8, (d) 5-9, (e) 5-10, (f) 5-12 and (g) 5-14. Black dotted lines in panels b-g are the best estimate pre-settlement profiles of $^{10}Be_{met,T}$ from numerical model 2, where E_{pre} = average pre-settlement erosion rate and Epost = average post-settlement erosion rate. Grey dotted lines in panels b-g are increment-averaged values of best estimate pre-settlement inventories (black dotted lines). Note logarithmic scale and units (g cm^{-3}) for $^{10}Be_{met,T}$ inventories in panels b-g. Error bars on $^{10}Be_{met,T}$ increment inventories (g cm^{-3}) represent the standard combined uncertainty (1σ), including $^{10}Be_{met}$ and bulk density measurement error. Abbreviations next to increments are genetic horizon nomenclature following (Schoeneberger et al. 2012).

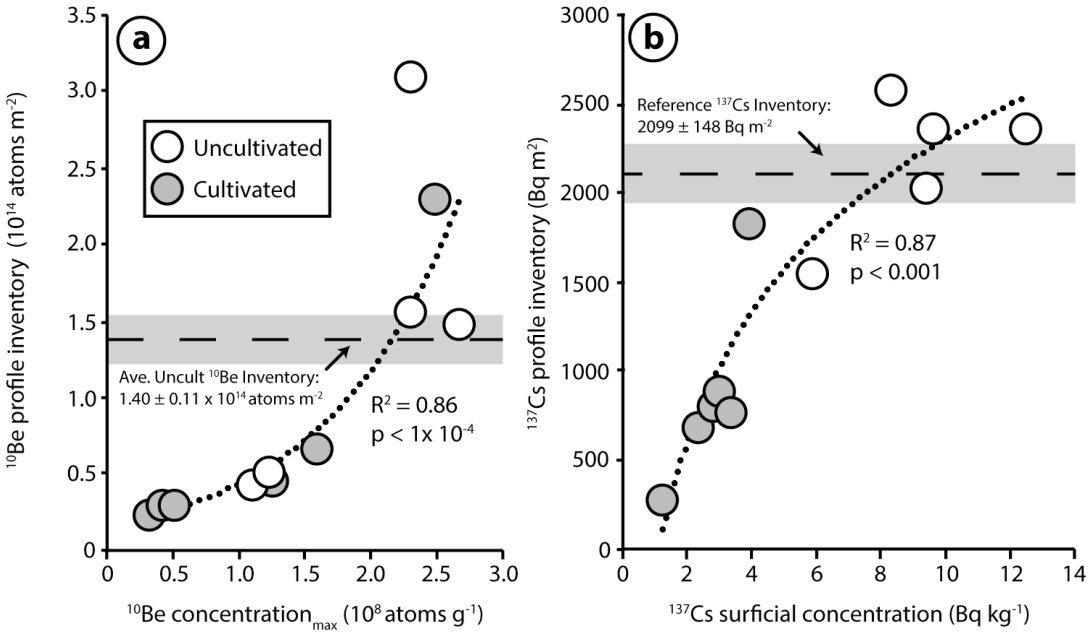

Figure 3.5. Relationship of (a) maximum profile $^{10}Be_{met}$ concentrations to total $^{10}Be_{met}$ inventories (150cm) – regression line is a log-linear transformation plotted on standard scale: ln($^{10}Be_{met,T}$ atoms m^{-2}) = 9.934 x 10-9*($^{10}Be_{met,T,max}$ atoms g^{-1}) + 30.41. (b) ^{137}Cs surficial activities to total ^{137}Cs profile inventories – trendline is best-fit non-linear least squares for logarithmic relationship: ^{137}Cs Inventory (Bq m^{-2}) = 1062 * ln(^{137}Cs, surficial, Bq kg^{-1}) – 142.8.

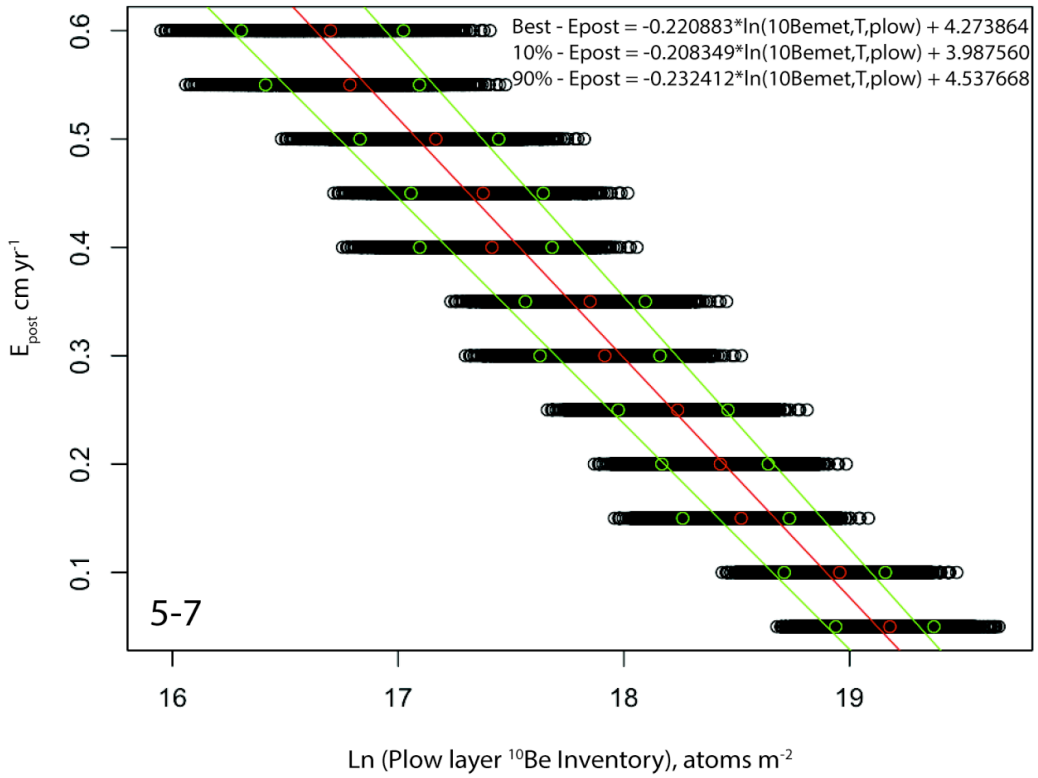

Figure 3.6. Example results of Monte Carlo simulations (n=1000) and regression equations for erosion estimates at cultivated transect point 5-7 to estimate parametrical uncertainty for ^{10}Be conversion model 2. Red line is the best-estimate regression for Epost from the natural logarithm of plow layer ^{10}Be inventories. Green lines are regressions for the 10% and 90% quantiles from Monte Carlo simulations.

December 15th, 2014

Nic,

Permission is granted to reprint the following article in your dissertation:

Jelinski, N.A. 2013. Cryoturbation in the Central Brooks Range, Alaska. *Cover Article - Soil Horizons 54(5): 01-007.

Permission is always granted for dissertation use.

Thanks and good luck.

Lisa Al-Amoodi
Managing Editor, Soil Horizons
5585 Guilford Road,
Madison, WI 53711-5801
(t) 608-268-4971
(f) 608-273-2021
(email) lalamoodi@sciencesocieties.org

CHAPTER 4

Cryoturbation in the Central Brooks Range, Alaska

Abstract

Cryoturbation in permafrost-affected soils is important to many Arctic biogeochemical processes and critical to the appropriate classification of Gelisols. Standardized methodologies for describing the soils formed from these processes and knowledge regarding the timescales at which they operate continue to evolve. Twenty-six profiles were described across a transect in the Midas Lake region of the Central Brooks Range of Alaska using a modified version of the standard USDA and Turbel description protocol that is appropriate for work in wilderness areas. Profile descriptions and associated field data were aggregated and generalized to reveal major trends and relationships in horizonation between cryoturbated and non-cryoturbated soils on the transect. A conceptual model for the geomorphic relationships of cryoturbated and non-cryoturbated soils on this landscape was developed. In addition to a landscape-scale perspective, individual profiles were described on patterned ground features at a location where cryoturbated horizons were strongly expressed. Samples from these profiles were analyzed for Cesium-137 (^{137}Cs) activity, and it was found that the surficial activity of this fallout radioisotope varied strongly by position on the patterned ground microtopography and material type. These differences suggest that the use of fallout isotopes such as ^{137}Cs, when combined with quantitative profile descriptions and a standardized description protocol, may significantly improve our understanding of the spatial distribution and mechanisms of cryoturbation.

Keywords

Cryoturbation, Gelisols, Brooks Range, Cesium-137, Arctic, non-sorted circles

Abbreviations

^{137}Cs, Cesium-137; MAAT, Mean Annual Air Temperature; MAST, Mean Annual Soil Temperature.

Acknowledgments

My special thanks to Dr. Dave Swanson of the National Park Service's Arctic Research Coordination Network for guidance and interpretations provided in the conception and review of this manuscript, and to Fleur Nicklen and Marta Roser for their assistance in the field and laboratory. Many thanks to Dr. Kyungsoo Yoo for providing gamma spectrometer time and to Dr. Ed Nater, Dr. Brent Dalzell, and Dr. Terry Cooper of the University of Minnesota Department of Soil, Water and Climate for their critiques on initial drafts. Lastly, I thank two anonymous reviewers for providing critical perspectives that have significantly improved this manuscript. This work was supported in part by NSF Graduate Research Fellowship # 2011122508 to N.A. Jelinski.

4.1. Introduction

Cryoturbation plays a critical role in the formation of Arctic soils through ground patterning, the sequestration of organic matter below the soil surface, and alterations to the physical structure of soil materials (Bockheim and Hinkel, 2007; Kaiser et al., 2007; Ping, 2013). Additionally, the Turbel suborder and Turbic subgroups of other suborders are defined by the presence of cryoturbated horizons and gelic materials, which "are manifested by involuted, irregular, or broken horizons, organic matter near or within the permafrost table, oriented rock fragments and silt enriched layers" (Bockheim et al., 1997; Soil Survey Staff, 2010). Thus the accurate mapping of Arctic soils and quantification of carbon in Arctic landscapes is dependent upon our understanding of cryoturbation and related permafrost processes (Ping et al., 2013).

Large-scale latitudinal gradients and regional to local scale patterns of cryoturbation have been well characterized by U.S., Canadian, and Russian scientists (Zoltai et al., 1981; Kokelj et al., 2007; Walker et al., 2008). Conceptual and quantitative models have been constructed that can adequately represent cryoturbation in some environments (Vandenberghe, 1992; Swanson et al., 1999; Peterson et al., 2003; Nicolsky et al., 2008), but best practices for the description of these soils and knowledge regarding the rates at which these processes operate remain an evolving area of research (Bockheim, 2007; Ping et al., 2013). Cryoturbation can produce highly complex soil profiles and therefore standardizing the description of these soils warrants supplemental procedures and methodologies (Ping et al., 2013). These methodologies require an inherent understanding of the multi-scale variations in surficial patterns produced by

cryoturbative processes as well as the landscape settings under which these processes should be expected to occur (Ping, 2013).

Additionally, quantifying the magnitude and timescales over which cryoturbation operates are critical to questions of Arctic soil genesis and predictions of future response to climate change (Bockheim, 2007). Although radiocarbon (^{14}C) and the fallout radioisotope Lead-210 (^{210}Pb) have been used to constrain the age of individual buried organic horizons (Kaiser et al., 2007; Becher et al., 2013), radioisotope tools remain underutilized in studies of cryoturbation. Cesium-137 (^{137}Cs), has long been used to infer the movement and mixing of soil materials at a landscape and profile scale (Ritchie and McHenry, 1989; Kaste et al., 2007). Both wet and dry ^{137}Cs deposition occurred following atmospheric testing of thermonuclear weapons in the 1950's and 1960's (Aoyama et al., 2006). Under most environmental conditions, this fallout ^{137}Cs adsorbs strongly to soil minerals and organic matter, and can be used to track soil movement over decadal timescales through spatial differences in measured activities (Matisoff and Whiting, 2011).

The objectives of this study were to utilize pedon descriptions across a transect in the Central Brooks Range of Alaska to demonstrate how this information can be used to produce a generalized view of the differences between cryoturbated and non-cryoturbated soils and their relationships to landscape parameters. Additionally, I explore the qualitative use of ^{137}Cs as a potential tracer of soil movement due to cryoturbation across patterned ground and advocate for the future use of quantitative, spatially-explicit sampling schemes for utilizing a suite of radioisotope tracers to further improve our

knowledge of cryoturbation processes in Arctic soils.

4.2. Materials and Methods

Data and samples were collected in late July, 2012 as part of long-term monitoring work across the Arctic National Park network. The Midas Lake region of the Noatak River valley (67° 48' N, 156° 15' W) is located north of the Schwatka Mountains and approximately 40 km downstream of the headwaters of the Noatak River, in the western portion of Gates of the Arctic National Park, central Brooks Range, Alaska (Fig. 4.1). Although no direct temperature or precipitation observations are available for this area, modeling results predict mean annual air temperatures (MAAT) of -8° C and 450-500 mm of precipitation (PRISM Climate Group, 2012). Because mean annual soil temperatures (MAST) are typically 2° C higher than MAAT in Arctic and Subarctic regions (Smith et al., 1998), this site likely has an average MAST of ~ -6° C, which places the location within the gelic soil temperature regime. Modern alluvium and alluvial terrace deposits of Holocene age dominate the parent materials of the Noatak floodplain (elevation 500m, 0-2% slopes), while glacial drift of Itkillik II Age (Late Pleistocene) and colluvium occupy the low moraines (2-5% slopes) and bedrock controlled foothills (10-20% slopes) of the surrounding mountains (Hamilton and Labay, 2011). At elevations to 1200m, depth to schist bedrock is shallow (< 20 cm) and most unconsolidated material is colluvial in nature.

Twenty-six soil profiles were described across a 4-km transect from the valley floor (500 m elevation) to an elevation of 700 m (Fig. 4.1). Vegetation ecotypes across the

transect were characterized by Lowland Sedge-Dryas Meadow and Riverine Birch, Alder and Low Willow Shrub tundra in the floodplain of the Noatak River; Upland Dwarf Birch-Tussock Shrub and Lowland Alder Tall Shrub tundra at mid elevations and south- and west-facing slopes; and Alpine Dryas Dwarf Shrub and Upland Birch-Ericaceous-Willow Low Shrub tundra at high elevations and north- and east-facing slopes (National Park Service, 2009).

Standard USDA description techniques (Soil Survey Staff, 2002) and the supplementary Turbel description protocol of Ping et al. (2013) were adapted to meet critical time, equipment, and sampling constraints in place due to work in a remote, National Park wilderness area. The organic and mineral components of gelic materials in cryoturbated horizons were described independently, with percentages of each material estimated over the entire horizon interval. Pit excavation was limited to the depth of hand tool refusal by frozen or lithic material or maximum depth of the implement (typically 40 - 135 cm), because power tools were not permitted in the wilderness area. Excavated pit size was limited to 40cm x 40cm in order to accommodate archeological considerations. Evidence of irregular or broken boundaries, the presence of gelic materials, and surficial microtopography were used to identify cryoturbated horizons, in instances where pit dimensions prohibited the observation of involutions. A pH testing kit (La Motte Model ST-M) was used to record approximate pHs of individual horizon components on soil slurries in the field. To demonstrate broad soil-landscape relationships, soils were classified into subgroups from field descriptions (Soil Survey Staff, 2010) and generalized across the transect. The R-based package Algorithms for Quantitative

Pedology (AQP, Beaudette et al., 2013) was used to visualize horizon information and properties from field descriptions as well as to conduct data aggregation and generalization. Statistical analyses were conducted using native algorithms in R 3.0 (R Development Core Team, 2011).

Restrictions on pit size did not allow the sampling of full cycles of patterned ground as recommended by Ping et al. (2013), so three individual profiles were excavated across a single cycle at one location with strong patterned ground expression (Fig. 4.3, #2) to provide a complete "snapshot" of variability. Five to six samples were taken from each profile at average depths of 5, 10, 20, 30 and 40 cm (Fig. 4.4). These samples were sieved to remove coarse fragments and roots > 2mm, and analyzed for ^{137}Cs activity by gamma spectrometry. Samples for gamma spectrometry were packed into glass vials and counted for 24hrs on a high-purity Germanium crystal well detector (Canberra, Inc.). Final activities and uncertainties were calculated by applying energy and efficiency calibrations to the gamma spectrum with reference to the ^{137}Cs characteristic 661.5 keV peak. Uncertainties in ^{137}Cs activities were generally around 10% of measured values.

Although the Fukushima Daiichi nuclear incident occurred prior to the sampling of these soils, the estimated deposition of ^{137}Cs due to the Fukushima incident in this region of the Brooks Range is 10 - 100 Bq/m2 (Christoudias and Lelieveld, 2012; Stohl et al., 2012). This is still about an order of magnitude lower than the ^{137}Cs activity expected to remain on the land surface in the Central Brooks Range from atmospheric weapons testing in the mid 1960s (3,000-4,000 Bq m^2 by Jan. 1970 (Aoyama et al., 2006), and 1100 - 1900 Bq m^2 at time of sampling in late Jul. 2012), so likely has had minimal

impact on these results. Furthermore, it is likely that ^{137}Cs fallout from Fukushima Daiichi would be uniformly distributed across landscape elements; potentially influencing total activity but not changing the qualitative interpretation of the relative activities of surficial materials.

4.3. Results

4.3.1. General Soil Characteristics and Horizonation

Generalizing profile descriptions and field pH measurements by groups based on the presence of cryoturbated soil horizons and landscape positions revealed important trends in the data (Fig. 4.2). The average depth of observation for non-cryoturbated soils along the transect was 44cm. Observation depth was restricted by consolidated (non-cryoturbated upland soils) or frozen materials (non-cryoturbated lowland soils) (Fig. 4.2B and 4.2C). All non-cryoturbated profiles had organic materials at the surface (Fig. 4.2B and 4.2C). Non-cryoturbated profiles in lowland landscape positions were characterized by the thickest surficial organic layers (an average of 26 cm), while non-cryoturbated soils on uplands had an average depth of organic layer to 9 cm and shallow depth to schist bedrock (33cm).

In contrast, less than half of all cryoturbated profiles had a continuous organic layer at the surface. Instead, cryoturbated horizons containing gleyed subsoil were exposed in almost half of all observed profiles (Fig. 4.2A). Horizon generalization across cryoturbated profile descriptions revealed a peak probability of cyroturbated horizon identification ~ 30cm, consistent with evidence of organic material being subducted to

the top of the permafrost table (Nicolsky et al., 2008). For those cryoturbated soils which had frozen layers that were encountered in excavation, the frozen layer was present at an average of 47 cm and represents a reasonable assumption of permafrost depth in these soils given that they were sampled in late July. Importantly, five of the sixteen cryoturbated profiles were unfrozen to a depth of at least 135cm (maximum depth of implement penetration).

The presence of subsoil material and patchy or broken organic horizons at the surface in many of the cryoturbated soils was reflected in the observed field pH differences between cryoturbated (n=16) and non cryoturbated (n=11) profiles (Fig. 4.2D). These differences were highly significant both when pH observations were aggregated throughout the entire profile depth (6.85 and 6.01 , $p<0.001$ for cryoturbated and non-cryoturbated soils, respectively, Welch's two sample T-Test) and when only the top 44 cm (the average depth of observation for non-cryoturbated profiles) was considered (6.69 and 6.01, $p < 0.001$ for cryoturbated and non-cryoturbated soils, respectively, , Welch's two sample T-Test).

4.3.2. Soil-Landscape Relationships

Across the lowest portions of the landscape, on the floodplain of the Noatak River (Fig. 4.3, #1), weakly expressed low-center polygons dominated the ground pattern. Extended periods of saturation have led to the development of Typic Fibristels, with thick organic mats composed of fibric materials that provide efficient insulation for the underlying frozen layer, further promoting epi-saturation due to strong limitations on infiltration.

Because only the surficial organic materials in these soils thaw during the growing season, they are relatively static under current climate regimes. The exception to this was on the high polygon boundaries (making up < 1% of this portion of the landscape), where the combination of surface heave due to the presence of ice wedges and elevation above the water table produced cryoturbated organic materials (Ping et al., 2013). Although no formal description was completed on these polygon boundaries, informal observations matched those described in similar conditions by Ping et al., 2013.

Across the low moraine composed of glacial drift (Fig. 4.3, #2), soils were high enough above the water table to permit aquic conditions without permanent saturation, and ground pattern was dominated by non-sorted circles, one of the most typical surficial patterns indicative of cryoturbative processes (Nicolsky et al., 2008). These non-sorted circles were only slightly vegetated (< 20% cover) and profiles were well mixed. In addition to non-sorted circles on this landform, inter-circle areas and earth hummocks were part of the full cycle of patterned ground (Fig. 4.4D). Because non-sorted circles were highly expressed at this location, profiles representative of all patterned ground features were described (Fig. 4.3, Fig. 4.4). The two profile descriptions below illustrate the variability between individual profiles on separate microforms at this location (Fig. 4.4A and 4.4C):

Moraine Profile A (Fig. 4.4A)

Oi: 0-8 cm (14% of profile to 53 cm depth): black (7.5YR 2/1) and brown (7.5YR 4/4) peat; many very fine, fine and common medium roots; abrupt boundary.

Oajj: 7-32 cm (28% of profile to 53 cm depth): black (7.5YR 2/1) muck, common very fine, fine and medium roots; abrupt broken boundary.

Bg/Oajj: 7-42 cm: (33% of profile to 53 cm depth): grey (5Y 5/1) and greyish olive (5Y 4/2) gravelly fine sandy loam; 20% brownish black (10YR 3/2) medium blocks of highly decomposed muck; weak fine to moderate subangular blocky structure and weak thin platy structure; friable; non-sticky and non-plastic; few very fine to fine roots; abrupt broken boundary.

Oa/Bgjj: 30-42 cm (22% of profile to 53 cm depth): black (7.5YR 2/1) muck; 15% grey (5Y 5/1) coarse blocks of firm very gravelly fine sandy loam; common very fine, fine and medium roots; abrupt broken boundary.

Oaf: 42-44 cm (3% of profile to 53 cm depth): black (7.5YR 2/1) muck; extremely firm.

Moraine Profile C (Fig. 4.4C)

Oejj: 0-12 cm (1% of profile to 140 cm depth): black (7.5YR 2.5/1) mucky peat; many very fine, fine, and few medium roots; abrupt broken boundary.

Oajj: 8-54 cm (3% of profile to 140 cm depth): black (7.5YR 2/1) muck; common very fine, fine, and medium roots; abrupt broken boundary.

Bg1jj: 0-82 cm (37% of profile to 140 cm depth): gray (5Y 4/1) and grayish olive (5Y 4/2) very gravelly fine sandy loam; moderate fine to coarse subangular blocky structure and moderate thin platy structure; friable; non-sticky and non-plastic; few very fine and medium roots; clear broken boundary.

Bg2jj: 12-95 cm (28% of profile to 140 cm depth): gray (5Y 5/1) very gravelly fine sandy loam; Fe concentrations (2.5Y 4/4) as distinct coarse masses; moderate medium subangular blocky structure and weak thin platy structure; friable, non-sticky and non-plastic; clear broken boundary.

Bg3jj: 52-140 cm (31% of profile to 140 cm depth): grayish olive (5Y 4/2) very gravelly fine sandy loam; 10% brownish black (10YR 3/2) coarse blocks of highly decomposed muck; moderate fine to coarse medium subangular blocky structure; friable; non-sticky and non-plastic.

To the east of Midas Lake, a low-relief plain underlain by glacial drift with highly saturated soils was dominated by *Carex* tussocks (Fig. 4.3,#3). Much like the Noatak River floodplain with thick, insulating organic materials at the surface, cryoturbated horizons were not observed at this location. Instead, soils were classified as Typic Historthels, with a thick, saturated mat of fibric material over mineral soil. Only on the upper toeslopes and lower backslopes of the adjacent, drift mantled hill (Fig. 4.3, #4)

were drainage conditions appropriate for cryoturbation to be manifested in soil profiles. Here, again, ground pattern was dominated by non-sorted circles. Although strong evidence of cryoturbation was apparent, soils also showed evidence of colluvial influence due to hillslope position. This was apparent from the presence of an A/Bgjj surficial horizon, which contained much more homogeneous and mixed organic material than the O/Bgjj horizons on the moraine.

Above these landscape positions, with increasing slopes, colluvial processes (solifluction lobes and colluvial deposits) overwhelmed any signal from cryoturbation; therefore, on the upper backslope, shoulder and summit positions (Fig. 4.3, #5), soils were shallow and poorly developed Lithic Dystrogelepts. The classification of these soils as Inceptisols in a gelic soil temperature regime may seem surprising, but the classification is based on the best available evidence from the field and is not an uncommon phenomenon (Ping, 2013). First, these soils are shallow to schist bedrock and have relatively thin insulating organic layers. This means that the thawing front likely advances at least a meter into the bedrock on most years, as has been observed in other sites at similar latitudes (Smith et al., 2010). Further, some cryoturbated soils just 100-150m in elevation below these soils were not frozen to depths of at least 135 cm, suggesting that if the thawing front penetrated deeply into unconsolidated materials at this site it would penetrate at least as deep into consolidated materials due to higher thermal conductivities (Guglielmin et al., 2011).

At the small basin saddle position (Fig. 4.3, #6) weak non-sorted circle patterns were observed and were indicative of the underlying cryoturbated soils, which were

classified as Ruptic-Histic Aquiturbels. At the highest elevations (Fig. 4.3, #7, #8), Lithic Dystrogelepts dominated where depths to underlying consolidated materials were deeper than 20cm and Lithic Udifolists where depths to bedrock were very shallow and organic materials overlie weathered bedrock. Paralithic materials were present as partially weathered (frost-shattered) and weakly cemented schist - these materials are described as Cr horizons at transect locations 5, 7 and 8 (Fig. 4.3). As elevation increased beyond point B, little to no unconsolidated materials were present and exposed, frost-shattered bedrock and tors dominated the landscape.

4.3.3. Quantifying patterned ground movement using ^{137}Cs as a tracer

The results of the small-scale sampling at location #2 (Fig. 4.4) along the transect showed that surficial ^{137}Cs activities can be highly heterogeneous across very short spatial scales on patterned ground features (Fig. 4.4A-C). Most strikingly, samples collected from non-vegetated Bgjj material at the surface and small, isolated patches of Oe material in the circle center show significant differences in activities (Fig. 4.4C). While no ^{137}Cs could be detected in the Bgjj material, 17 Bq/kg was detected in the adjacent Oe. It is not surprising that no ^{137}Cs was detected in subsurface horizons, because the profiles were sampled in the center and edge of the non-sorted circle to characterize maximum variability. The most recently subducted material should be expected to lie somewhere just in from the circle edge, which would only be captured with extensive grid sampling. Nevertheless, these results demonstrate the potential of ^{137}Cs to track the movement of soil materials at small scales on cryoturbated landforms.

Ceisum-137 was not detected below 15 cm in these samples, so it is likely that these soils adsorb and retain most of the ^{137}Cs fallout inventory without leaching to underlying horizons. Material with measurable ^{137}Cs was therefore likely present at at or near the soil surface when the majority of atmospheric fallout occurred between 1958 and 1971 (Aoyama et al., 2006) while the absence of ^{137}Cs indicates the material was buried around the same time period and subsequently exhumed. This independently confirms the upward movement of subsoil materials in the non-sorted circle center on at least decadal timescales. This is not surprising as these non-sorted circles remain largely vegetation free (or at least sparsely vegetated, even at lower latitudes sites such as this study area). Additionally, the lower activities in the inter-circle areas relative to the organic rich earth hummock (Fig. 4.4A-C) could suggest that there has been a mechanism of loss of ^{137}Cs from the surface of the inter-circle areas. One potential mechanism for this reduced activity is the subduction of surficial organic matter below the surface on time scales of 40 years or less.

Alternative explanations for the lack of ^{137}Cs activity in the surficial Bgjj material at the circle center may include the differential deposition of ^{137}Cs across microtopography or small-scale wind erosion from the exposed circle center. Additionally, the mineral soil may have lower infiltration rates compared to surrounding organic materials when accumulated snow is melting in the spring and early summer. This may lead to runoff away from the higher elevation circle centers. If any of these were true, however, we would expect the highest ^{137}Cs activities in the low elevation inter-circle areas. Instead, the highest activities were present in the organic materials of

the earth hummock, the highest elevation microtopographic element of the ground pattern (Fig. 4.4D).

4.4. Discussion and Conclusions

This work shows that in remote areas with significant sampling constraints, modifications of existing protocols can still produce relevant information that can be utilized to characterized cryoturbated and non-cryoturbated soils at the profile and landscape scale. The aggregation of field data through the use of quantitative analysis such as the algorithms provided in the AQP package holds significant promise for generalizing profile descriptions from highly complex cryoturbated soils. Analysis of field pH measurements demonstrated that cryoturbation not only influences profile physical properties and horizonation, but also master environmental variables such as pH through the movement of surficial materials.

The identification of areas dominated by cryoturbated soils from surficial characteristics and the quantitative description of these soils through standardized methodologies is critical for advancing our knowledge of the distribution and global importance of these soils (Ping et al., 2013). Through this case-study and the use of a modified version of a new standardized Turbel description protocol (Ping et al., 2013), the descriptions show that cryoturbated soils can be expected to occur in distinct positions on high-relief landscapes, where moisture regime is appropriate, unconsolidated materials are available, and disturbance from other processes such as colluvial transport do not overwhelm any signal from cryoturbative movement. This is in agreement with a

qualitative soil description and classification previously undertaken by the National Park Service in Arctic Parklands (National Park Service, 2009) and with research on the spatial distribution of cryoturbated soils in other regions (Luoto and Hjort, 2004; Feuillet, 2011).

The application of ^{137}Cs and other radionuclides to track soil movement in landscapes such as this is a promising approach to quantify processes that have occurred over the past 50 years. Understanding the rates at which cryoturbative processes operate is critical for understanding how these soils will respond to future changes in climate. The results presented show that naturally-occurring fallout radionuclides (in this case ^{137}Cs) have the potential to constrain rates and processes of movement in cryoturbated soils. Further work which characterizes a suite of radionuclides (i.e. ^{137}Cs, ^{210}Pb and ^{14}C) using a horizontally and vertically gridded sampling scheme across multiple cycles of patterned ground would have an opportunity to demonstrate the power of this approach.

Significant progress has now been made in standardizing these descriptions and linking them explicitly to sampling protocols. It is anticipated that future investigations will be able to utilize these approaches to improve upon and advance our knowledge of how cryoturbation is distributed across diverse Arctic landscapes as well as how it functions to produce these dynamic and unique soils.

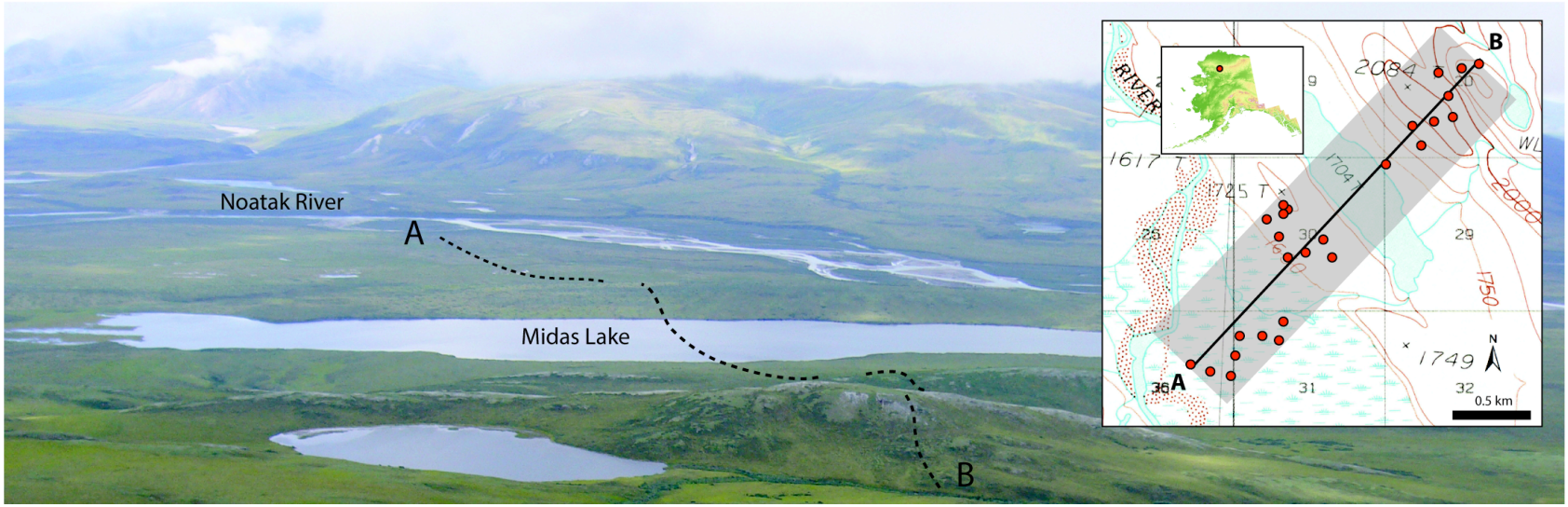

Figure 4.1. Geographic location and landscape setting of Midas Lake transect, central Brooks Range, Alaska. Soil profiles were described across the transect within the grey bar. Inset topographic map: USGS Ambler River Quadrangle, 1990 (elevations in feet).

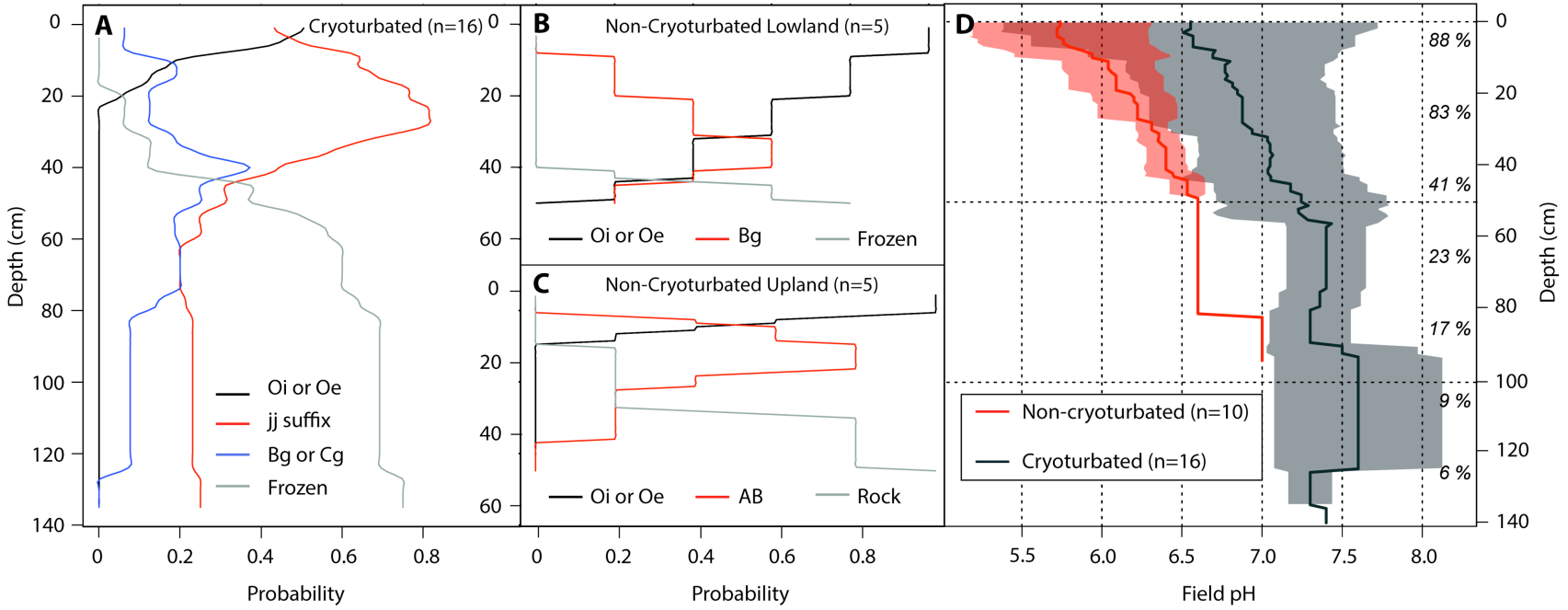

Figure 4.2. Aggregated and generalized horizonation for soils across the Midas Lake transect. Probability distributions with depth as a fraction of total profiles for cryoturbated soils (A), non-cryoturbated lowland soils (B), and non-cryoturbated upland soils (C). Frozen and rock layers noted in the field were assumed to extend with depth for visualization purposes only. Field pH values with depth for cryoturbated and non-cryoturbated soils (D); group means are represented by the solid lines, shaded range represents 25th and 75th percentiles. Percentages on right (D) are percent of total profiles contributing values with depth. All analyses conducted in AQP (Beaudette et al., 2013).

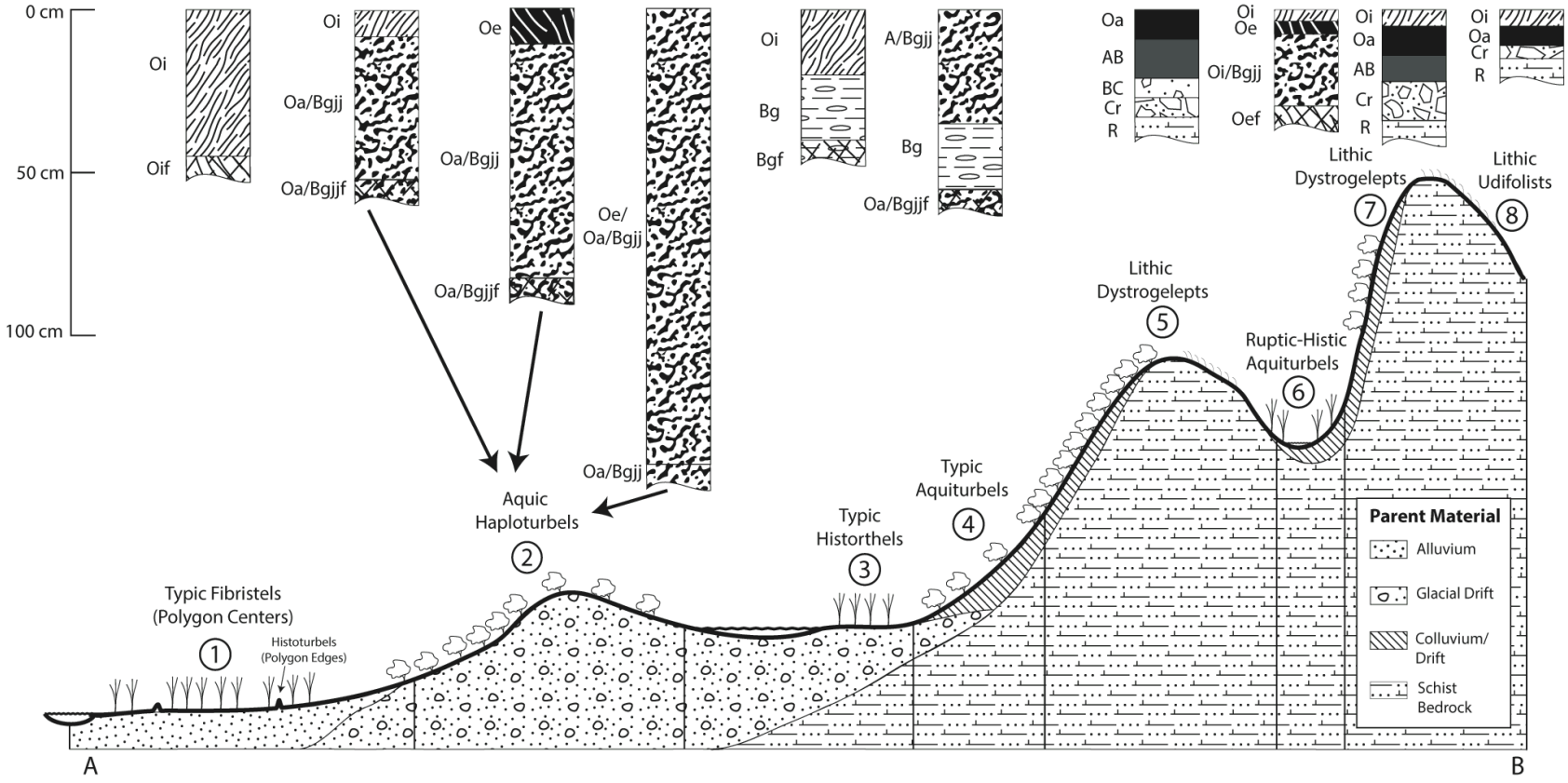

Figure 4.3. Generalized soil-landscape relationships across the Midas Lake transect. Points A and B at bottom of bar refer to the same points in Figure 1. Vertical elevations are exaggerated.

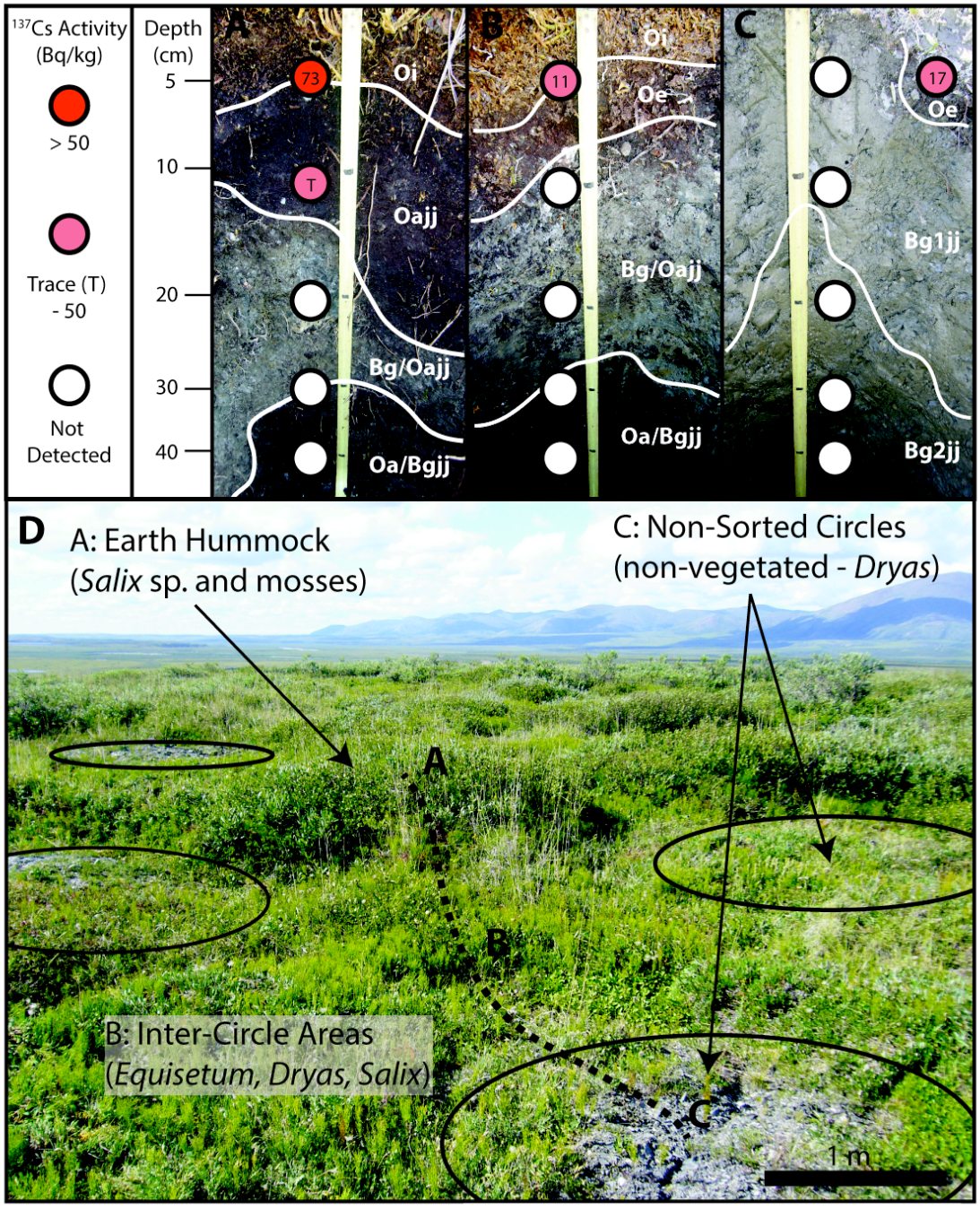

Figure 4.4. Overview of patterned ground microtopography, cryoturbated soil profiles and observed activities of ^{137}Cs on transect location #2 (moraine). Letters above soil profile pictures refer to letters of surficial features in overview photograph. Numbers inside shaded circles denoting ^{137}Cs activity range indicate measured values.

CHAPTER 5

Utilizing suites of isotopic and elemental tracers to constrain cryoturbation rates and patterns in a non-sorted circle (Abisko, SE)

With Jonatan Klaminder (Umea University – Contribution: Field site, sampling, ^{210}Pb, Hg, and background data) and Kyungsoo Yoo (University of Minnesota).

5.1. Introduction

Cryoturbation is a globally important process of pedoturbation that takes place in permafrost-affected regions and plays a central role in the distribution of carbon and nutrients, water movement, and surface ground patterning in Arctic ecosystems (Bockheim, 2007, Walker et al., 2004, Kaiser et al., 2007). Although significant progress has been made in the characterization, distribution and ecological effects of cryoturbation in the past two decades (Walker et al., 2008), the quantification of rates and patterns of material movement in soils affected by cryoturbative processes has lagged far behind (Bockheim, 2007, Jelinski et al., 2013).

5.1.1 Physical soil movement and Arctic soil carbon

Many studies have investigated the quality and temperature sensitivity of soil organic carbon (SOC) contained in Arctic soils, relating these to quantitative biochemical factors (i.e. Davidson and Janssens, 2006, Biasi et al., 2005, Waldrop et al., 2010). However, these strictly biochemical models do not address the differential depth distributions of soil organic matter brought about by cryoturbation (Bockheim, 2007 Kaiser et al., 2007, Koven et al., 2009) and the effects that these physical processes have on the stabilization of SOC (much more so than other forms of mixing in temperate and tropical areas) due to the strong temperature gradients in permafrost soils and extreme inhibition of microbial activity at depth (Washburn, 1980, Waldrop et al., 2010). Recently, global and regional scale models of soil carbon accumulation in permafrost-affected soils have been constructed that explicitly represent cryoturbation and the insulation of the mineral soil

surface by organic materials (Koven et al., 2009). These models have suggested that the effects of these two processes alone can result in 30% higher stocks of SOC in the top meter, with additional increases down to three meters (Koven et al., 2009). Additional evidence suggests that the rapid freezing and burial of some cryoturbated organic matter in some permafrost-affected soils may result in different long-term behavior with regard to decomposition and lability (Ping et al., 2014). Lastly, the most recent estimates of permafrost SOC stocks to 3m depth places SOC in cryoturbated soils at close to 37% of the total circumpolar permafrost SOC pool (Tarnocai et al., 2009). These new revelations make understanding the rates of the physical movement of soil materials due to cryoturbation a critical new frontier in Arctic soil science.

5.1.2 Equilibrium cell model of cryoturbation in non-sorted circles (NSCs)

The three currently accepted models of cryoturbative processes include the cryostatic, diapiric, and differential frost-heave/equilibrium cell (henceforth 'equilibrium cell') models (Vandenberghe, 1992, Swanson et al., 1999, Peterson et al., 2003, Nicolsky et al., 2008). The cryostatic and diapiric models of cryoturbation are stochastic processes that may not be expressed in surface patterns (Swanson, 1996). In contrast, the equilibrium cell model mechanistically describes the movement of organic materials and minerals in non-sorted circles (NSCs) or 'frost-boil' microforms, so called because they give the appearance of subsurface material "boiling" up in the centers of repeating circular patterns of mineral material surrounded by inter-circle areas with thick surficial organic layers (Walker et al., 2004). NSCs dominate high-latitude tundra environments (Ping et

al., 2008) across Arctic ecosystems, and in contrast to the unreliable surface evidence for cryostatic and diapiric processes, NSC landscapes are characterized by regular, spatially repeatable microforms which can be identified by aerial photography and satellite imagery (Walker et al., 2008), making them amenable to scaling. The equilibrium cell model of NSCs therefore provides a critical starting point for constraining rates of cryoturbation processes because frost-boils 1) are active features, 2) dominate tundra environments, 3) occur in spatially regular patterns, and 4) exhibit well defined morphologies and patterning with regard to vertical and horizontal distributions of SOC, depth to permafrost table, and temperature gradients (Nicolsky et al., 2008).

The equilibrium cell model of NSC material cycling has developed from field descriptions of frost-boil cross sections, which, regardless of variations due to climate, exhibit strikingly similar general morphologies (Nicolsky et al., 2008, Fig 5.1). Typically, frost-boil cross-sections have a bowl-shaped depression in the permafrost table directly below the raised circle microform, which is non-vegetated (or lightly vegetated) and has no overlying organic material (Fig 5.1). The NSC center is characterized by well-mixed mineral materials and the inter-circle areas are characterized by a thick organic mat and a relatively shallow permafrost table (Fig 5.1). Lastly, organic-rich material overlies the permafrost table in nearly all cases - an observation which has provided the major impetus for the development of the equilibrium cell model (Nicolsky et al., 2008, Bockheim, 2007). For ease of reference, the non-vegetated or slightly vegetated circular area with exposed mineral soil materials that participates in equilibrium cell circulation is termed the “Inner Domain” (Fig 5.1), while the inter-circle areas characterized by thick,

well developed mats of surficial organic materials and a shallower permafrost table are termed the "Outer Domain" (Harris, 1998, Makoto and Klaminder, 2012, Fig 5.1).

Three major mechanisms occur to create cell-like circulation of materials in the equilibrium cell model (Fig 5.1): 1) differential frost heave due to accelerated movement of the freezing front through the non-vegetated center leads to the formation of ice lenses and further reinforcement of micro-high topography; 2) colluvial movement of material from the NSC center towards the edges, and 3) the subduction of large, intact parcels of surface organic material downward towards (and eventually along) the permafrost table. The net movement of materials in the NSC microform is therefore a pseudo-circular pattern (depending on actual geometry of the ground surface) (Fig 5.1, Nicolsky et al., 2008). The most critical factor in the development of circulatory movement in these features is differential frost-heave, which creates and maintains micro-topographic gradients (Peterson et al., 2003). Briefly, the mineral surface material in the non-vegetated center conducts heat an order of magnitude faster (1.0 - 2.0 W m^{-1} K^{-1}) than the vegetated boil-edges with thick mats of organic material (0.15 - 0.20 W m^{-1} K^{-1}) (Washburn, 1980, Rinke et al., 2008). This leads to the accelerated formation of segregation ice and ice lens growth in frost-boil centers through unfrozen water migration from adjacent areas during freeze-back (Walker et al., 2008).

5.1.3 Previous approaches to rates of material movement/cell circulation in NSCs

Significant work has been done in estimating the rates of short and long-term material movement by tracking positioning changes in physical markers in NSCs and other related

patterned ground in periglacial environments around the world (Egginton and Shilts, 1978, Selkirk, 1998, Smith, 1986, Ballantyne, 1996, Sawyer, 2007). Rates of lateral movement have also been quantified through repeated micro-scale laser altimetry of NSCs (Kaab et al., 2013), and more recently, through the use and application of the short-lived radioisotope ^{210}Pb (Hagedorn et al., 2008, Klaminder et al., 2014). Most of these studies have focused on quantifying rates of surficial movement across the NSC inner domain (Fig 5.1, arrow #2), with only a few estimates of the patterns or rates of subduction (Becher et al., 2013, Harris, 1998) and subsurface movement (Dyke and Zoltai, 1980) in NSCs, which remains poorly constrained.

5.1.4 Geochemical tracer suites for constraining material movement in NSCs

In our work, we explore a novel suite of elemental (C, N, Na, Mg, K, Ca, S, P, Pb, Cl) stable isotope (^{13}C) and radioisotope (^{137}Cs, ^{210}Pb, ^{14}C, ^{10}Be) tracers to constrain the rates and patterns of soil material movements in NSCs over a range of timescales. Elemental tracers have addition and loss rates that are dependent on the environmental conditions they are currently experiencing, however in some well constrained cases (notably Pb and Hg), may be amenable to rate quantification. In contrast, radioisotopes decay at a constant, well-characterized rate independent of environment, an important factor in their use as rate estimators. Therefore, elemental tracers are amenable to understanding cryoturbation patterns by providing qualitative information on material provenance (surface or subsurface) and other environmental processes and conditions affected by the physical movement of soil materials in NSCs, while radioisotope tracers can be used to

both understand both patterns and quantify rates.

5.1.5. Elemental and stable isotope tracers (C, N, Na, Mg, K, Ca, S, P, Pb, Cl, Hg, ^{13}C)

The elemental tracers differ in their modes of accumulation and loss in soils, as well as their environmental behavior (Table 5.1). Although many of these elements have multiple sources of origin, three distinct groups of elemental tracers can be defined from their predominant modes of deposition in the Arctic environment: 1) those that are predominantly controlled by parent material composition and/or mineral weathering, 2) those predominantly controlled by primary production processes, and 3) those primarily controlled by atmospheric deposition.

Elements controlled by parent material composition and/or weathering processes: Na, Ca, Mg, K, P and Pb. The base cations Na, Mg, K and Ca all share similar origins and fates in the environment. On a global scale, the major source of these elements to terrestrial soils is mineral weathering, with minor sources from dust deposition and sea spray aerosols. Sites located within ~ 100 km from estuarine and marine environments are within the range of influence of sea spray aerosols on deposition chemistry (Gustafsson and Franzen, 2000, Benassai et al., 2005), but this process would be expected to have a minor influence on concentrations relative to weathering because background levels of the base cations in most soils ~ 8000 – 16,000 ppm, are ~ 2 orders of magnitude higher than what we would expect from sea spray deposition (Gustaffsson and Janzen, 2000)

The primary source of P to soils on a global basis is geogenic, through the

weathering of minerals (primarily apatite) in soil parent materials (Fillipelli, 2002). In many soil environments, P bound to Fe and Al oxides is unavailable for plant uptake (Cross and Schlesinger, 1995). This P is then accumulated in soil organic matter through aggressive scavenging and uptake by plants and micorrhizae (Weintraub, 2011). In environments where significant organic matter accumulation occurs such as Arctic tundra environments, a significant proportion of the total P pool may be in organic form and controlled primarily by decomposition processes, which also tend to be slow in permafrost-affected soils, leading to P limitation (Weintraub , 2011).

Geogenic sources of Pb to soils through the weathering of Pb-containing primary minerals are highly significant for establishing background levels of Pb in soils (Bindler et al., 2008), however anthropogenic influences on atmospheric Pb deposition drive the regional distribution of Pb (Klaminder et al., 2011). These sources can be highly significant and orders of magnitude greater than natural sources in localized areas close large anthropogenic point sources such as smelters, but even in remote Arctic environments, the accumulation of Pb in surface organic horizons can be 3-5 times greater than the geogenic background (Bindler et al., 2008). This has been attributed primarily to deposition from anthropogenic processes, not bioaccumulation or mixing, although those may also play roles (Klaminder et al., 2011).

Elements controlled by primary production: C and N. Carbon and nitrogen are accumulated in organic matter through primary production and fixation of atmospheric CO_2 and N_2 (Shaver and Jonasson, 2001; Christensen et al., 2007), as well as atmospheric pollutant deposition in the form of NO_3^- for N (Lee and Malmer, 1988, Malmer, 1988).

Even in remote Arctic environments, increasing nitrogen concentrations in vegetation due to elevated nitrate deposition have been observed (Barsdate and Alexander, 1975, Malmer, 1990) but in most Arctic environments, the vast majority of the total nitrogen pool is from atmospheric nitrogen fixation by legumes and mosses (Bordeleau and Prevost, 1994).

Elements controlled by atmospheric deposition: Hg, S and Cl. Hg has a very strong affinity for reduced sulfur (thiol) groups in soil organic matter (Skyllberg et al., 2000), resulting in strong correlations between the distributions of SOC, S and Hg in soils and the tight coupling of dissolved organic carbon to the hydrologic export of Hg from terrestrial soils (Kolka et al., 2001). Both Hg and S have similar natural and anthropogenic sources leading to atmospheric deposition (Zdanowicz et al., 2014). Geogenic sources of mercury can be significant in some areas, and vary strongly even on regional scales (Nater and Grigal, 1992). Cl is predominantly controlled by atmospheric deposition of sea spray aerosols, and these can reach far inland (Gustaffsson and Franzen, 2000, Oberg, 2002).

Depth-dependent depletion and enrichment of ^{13}C. The depth dependent variation of $^{13}C/^{12}C$ ratios in soils is a well-documented phenomenon conditioned by multiple drivers (Wynn et al., 2006; Alewell et al., 2011). In most well drained soils that have not been severely affected by erosion, bulk SOC becomes increasing enriched in ^{13}C ($\delta^{13}C$ less negative) with depth, which can be due to the mixing of different sources of SOC, the preferential decomposition of different components of SOC, or fractionation during decomposition processes (Wynn et al., 2006). In anoxic systems where anaerobic

decomposition is the dominant process, the depth trends of these processes can result in the opposite phenomena – that is a trend of increasing depletion ($\delta^{13}C$ more negative) with depth (Alewell et al., 2011). In either case, if the soil materials under consideration have formed under similar sets of environmental processes, $\delta^{13}C$ can provide information on material provenance and isotopic changes of bulk SOC through maturation processes in soil environments.

5.1.6. Radioisotope Tracers (^{137}Cs, ^{210}Pb, ^{14}C, ^{10}Be).

Cesium-137. ^{137}Cs is a radioactive isotope of Cesium (atomic mass 133) with a half-life of 30.08 years, which undergoes beta-decay (100%) to its daughter isotope Barium-137 (National Nuclear Data Center, 2011). ^{137}Cs is the best known and most frequently applied radioisotope tracer in studies of soil erosion and deposition (Matisoff and Whiting, 2011), is a reactive cation which is readily adsorbed to mineral grains and exchange sites on organic macromolecules once it reaches the soil surface. ^{137}Cs distribution in the Arctic is primarily derived of fallout from atmospheric nuclear weapons testing between 1955 and 1965 (Wright et al., 1999), with additional small amounts of fall-out from the nuclear accidents of Chernobyl (Strandberg, 1997) and Fukushima (Thakur et al., 2012). Close to 57% of the total ^{137}Cs fallout in the Northern Hemisphere was due to concentrated atmospheric nuclear weapons testing in the years 1961 and 1962 alone, and in general, except for small local effects of the incidents mentioned above has generally ceased completely (Wright et al., 1999). Therefore, ^{137}Cs can generally be considered a “pulse” radionuclide tracer, which fell out and was

conservatively adsorbed by soil minerals and organic matter, effectively labeling soil materials that were at or near the surface during the fallout period (Table 5.1).

Lead-210. ^{210}Pb is a radioisotope of Lead (atomic mass 207) with a half-life of 22.2 years, which undergoes beta-decay (~ 100%) and alpha decay (< 0.001%) to its daughter isotopes ^{206}Hg and ^{210}Bi, respectively (National Nuclear Data Center, 2011). ^{210}Pb is a product of the decay chain of ^{238}U that occurs naturally in geologic materials. During this decay process, a daughter nuclide - ^{226}Ra - decays to ^{222}Rn (a gas with a half-life of 3.8 days), which can diffuse out of the soil and proceed through a series of brief decays to the ^{210}Pb daughter isotope (Faure and Mensing, 2005). ^{210}Pb, like ^{137}Cs, is a cation that is preferentially adsorbed to aerosols and falls out to the earth's surface through both precipitation and dry deposition (Appleby and Oldfield, 1992). ^{210}Pb activity resulting from fallout is termed excess ^{210}Pb ($^{210}Pb_{ex}$), in contrast to ^{210}Pb remaining in the soil from ^{222}Rn that was unable to diffuse completely from the soil, resulting in a *in-situ* soil pool (supported ^{210}Pb). Excess ^{210}Pb ($^{210}Pb_{ex}$) falls-out to the soil surface similar to ^{137}Cs, effectively labelling surface materials as it is also preferentially sorbed to soil minerals and organic matter (Matisoff and Whiting, 2011). Unlike ^{137}Cs however, the long-term production and deposition rates of ^{210}Pb are largely constant because the strength of its production depends solely on local variations of geologic materials. This difference in production source and long-term production patterns between ^{210}Pb and ^{137}Cs can be leveraged to provide further constraints on the movement of soil materials (Matisoff et al., 2002) (Table 5.1).

Beryllium-10. ^{10}Be is a long-lived radioisotope of Beryllium (atomic mass 9) with a

half-life of 1.39 x 10^6 years (Dunai, 2009), which undergoes beta decay (100%) to its daughter isotope ^{10}B (National Nuclear Data Center, 2011). ^{10}Be is produced in the atmosphere when high-energy neutrons from cosmogenic radiation collide with molecular nitrogen and oxygen (Dunai, 2009). The spallation reactions that result from this collision break up the target nucleus, producing ^{10}Be and a number of other lighter particles (Willenbring and von Blanckenburg, 2010). The production of ^{10}Be in the atmosphere depends primarily on 1) the strength of cosmic ray production, which varies in conjunction with metrics of solar activity and 2) the intensity of the earth's geomagnetic field, which selectively blocks lower energy cosmic radiation (Lal and Peters, 1967, Willenbring and von Blankenburg, 2010). Because these factors vary predictably, global models of atmospheric ^{10}Be production have successfully reproduced these patterns (Field et al., 2006, Masarik and Beer, 2009). Like ^{137}Cs and ^{210}Pb, atmospheric ^{10}Be is sorbed strongly onto aerosols in the atmosphere and eventually falls out as both wet and dry deposition (Graham et al., 2003, Lal, 2007). The delivery rate of ^{10}Be to the Earth's surface is therefore also a function of precipitation and dust deposition patterns (Heikkila et al., 2008). The ^{10}Be that falls out from the atmosphere (termed "meteoric" ^{10}Be) is preferentially sorbed onto the exchange sites of soil minerals (as Be^{2+} for low pH values < 6 or as Beryllium hydroxide at higher pH values) or organic materials (as a Be-humate complex in a large pH range between 3 - 10) (Takahashi et al., 1999). Meteoric ^{10}Be can be leached from soils under conditions of high acidity, however understanding of the environmental boundaries characterizing these conditions has improved significantly (Willenbring and von Blanckenburg, 2010). ^{10}Be retention by soil

materials under most environmental conditions is high, and therefore due to its long half-life (~ 1.4 Ma), meteoric ^{10}Be accumulates in soils with increasing soil age (Graly, 2010, Willenbring and von Blanckenburg, 2010) (Table 5.1).

Carbon-14. ^{14}C is a radioisotope of Carbon (atomic mass 12) with a half-life of 5,730 years, which undergoes beta decay (100%) to its daughter isotope ^{14}N (National Nuclear Data Center, 2011). ^{14}C is produced cosmogenically in the atmosphere through spallation reactions similar to those of ^{10}Be as discussed above (Dunai, 2009), however it has also been produced anthropogenically through atmospheric nuclear weapons testing, similar to ^{137}Cs (Trumbore, 2000). ^{14}C differs fundamentally from the three fallout radionuclides discussed above because it is not deposited directly on the Earth's surface. Instead, ^{14}C is incorporated into plant materials during photosynthesis as atmospheric CO_2 is converted to organic carbon compounds, with ratios of ^{14}C:^{12}C in the resulting organic material related to atmospheric ^{14}C:^{12}C ratios at the time of photosynthesis (Trumbore, 2009). Hence, for organic materials that have been closed to exchange with external carbon pools, the carbon-dating technique uses decay calculations to relate the observed ratio of ^{14}C:^{12}C to date the time since the material last exchanged carbon with the atmosphere (Torn et al., 2009). The situation for soil organic matter is considerably more complex, as SOC is an open pool, exchanging carbon with external pools through decomposition and humification processes (Wang et al., 1996, Trumbore, 2009). However, the mean residence time of bulk soil organic matter (or its fractionated components) can be determined from ^{14}C concentrations, providing a primary constraint on SOC dynamics. If organic matter pools have been largely separated from surface

inputs and decomposition has been negligible (such as in deposits of organic matter in permafrost- affected soils or deeply buried materials), the apparent ^{14}C age can be used as an indicator of burial date - with applicable caveats as described above (Kaiser et al., 2007, Bockheim, 2007) (Table 5.1).

5.1.7. Objectives

The objectives of this study were to utilize our elemental and isotopic suite for soil profiles on a radial transect across an NSC near Abisko, Sweden to (i) determine what elemental or isotopic tracers show promise for elucidating rates and patterns of cryoturbation in NSCs, (ii) quantify the rates and patterns of both surficial and sub-surficial movement rates in NSCs using radioisotopes (^{137}Cs, ^{210}Pb, ^{14}C, ^{10}Be), and (iii) use space for time substitutions to examine the temporal changes (physical and chemical) that occur in subducted surficial materials (^{14}C, ^{13}C and elemental tracers).

5.2. Materials and Methods

5.2.1 Site Description and Soil Sampling

Our study site is located in a non-sorted circle (frost-boil) field, 20km south of the village of Abisko, Sweden (68° 18'N, 19° 10'E) located on the north slope of Mt. Suorooaivi at an altitude of approximately 700 m a.s.l. This site has been utilized for investigations into NSC dynamics previously and has been intensively described in those works (Makoto and Klaminder, 2012; Klaus et al., 2013, Becher et al., 2013). Briefly, the site lies in the zone of discontinuous permafrost, the active layer can be up to 2m thick and data

suggests that rapid degradation of the permafrost table has taken place over the past 4 decades (Becher et al., 2013). Despite this, active soil movement in NSC mircoforms continues to be documented at this site (Klaminder et al., 2014) and seasonal elevation differences indicative of differential frost-heave processes that initiate and maintain NSCs continue to be observed (Klaus et al., 2013, Klaminder et al., 2014).

Soil profiles were sampled in 5 locations (at 0, 83, 145, 180, and 260 cm) along a 2.6m radial transect in the hypothesized direction of surficial soil movement, from the NSC circle center to inter-circle areas, using an 8cm diameter auger and spade excavation. Sampling location 1 (at 0 cm) was termed the mineral center and abbreviated CM. Location 2 (at 83 cm) is termed the inner profile and abbreviated IN. Location 3 (at 145 cm) is termed the Mixing Transition and abbreviated MT. Together, locations CM, IN, and MT constitute the Inner Domain, that is, the part of the transect that is actually included in the NSC morphology (Fig 5.2). Location 4 (180 cm) is termed outer domain 1 and abbreviated OD1, and location 5 (260 cm) is termed outer domain 2 and abbreviated OD2. Together, OD1 and OD2 make up the outer domain, that is, the inter-circle areas that do not participate in material movement in the equilibrium cell (Fig 5.2). Profiles were sampled until bedrock was reached (Fig 5.2).

5.2.2 Soil property and elemental characterization

Soil pH was determined on a 1:1 soil – water slurry. Soil organic carbon and total nitrogen were determined on a Elementar varioMax CN analyzer, with combustion at 1000° C. Texture was determined by the micropipette method (Miller and Miller, 1987),

with quality control samples determined by the hydrometer method (Gee and Or, 2002). The concentration of major elements (Na, Mg, K, Ca, P) was determined by Lithium Borate Fusion and ICP-AES, and S was determined by Leco furnace combustion, Cl by KOH fusion and ion chromatography, Pb by four-acid digestion and ICP-AES, and Hg by Aqua Regia digestion and ICP-MS. Hg_{ex}, or atmospherically-derived Hg was calculated by subtracting average Hg concentrations of soils and sediments overlying bedrock across the Abisko study site ("inherited Hg") from total Hg concentrations.

5.2.3 Measurements of Stable (^{13}C) and Radioiostopes (^{14}C, ^{137}Cs, ^{210}Pb, ^{10}Be)

^{13}C:^{12}C ratios of bulk soil samples were determined at the UC Davis Stable Iotope Facility (SIF, Davis, CA). Briefly, samples were combusted at 1000° C using an Elementar EL or Micro Cube elemental analyzer (Elementar, Hanau, Germany) interfaced to a PDZ Europa 20-20 isotope ratio mass spectrometer (Sercon Ltd., Cheshire, UK). The final δ values (per mil, ‰), are expressed relative to international standards V-PDB (Vienna PeeDee Belemnite) carbon.

^{12}C:^{14}C ratios of bulk soil samples was determined by AMS analysis on graphite from converted CO_2 produced upon complete sample combustion on acid washed pre-treatments of soil samples at Beta Analytic (Miami, FL), using NIST Oxalic Acid I as the modern reference standard.

^{137}Cs was determined by gamma spectrometry on a high-purity Germanium (HPGe) crystal well detector (Canberra, Inc.) at the University of Minnesota-Twin Cities. Samples were counted for 48 hours to an uncertainty of 5% of the predicted value. ^{210}Pb

activities were determined using alpha spectrometer that measured the activities of its granddaughter ^{210}Po in equilibrium. ^{210}Po analyses were carried out by the complete dissolution of the aliquot samples (between 150 and 250 mg) by microwave digestion and its deposition on silver discs using ^{209}Po as an internal tracer to determine yield. Po sources were measured using an EG & G Ortec ULTRA-AS Ion-Implanted-Silicon Charged-Particle Detector (model U-020-450-AS) at Umea University, Abisko, SE. ^{10}Be adsorbed to mineral grains and bound to organic materials was removed through a series of acidification steps and ion exchange chromatography prior to being oxidized and analyzed by accelerator mass spectrometry (AMS). The methodology used here is modified from Ebert et al. (2012). Briefly, 0.5 g of air-dried, homogenized, and sieved (2mm) soil was digested in Teflon vessels with 0.5 M HCl and 250 ug of spiked ^{9}Be carrier at 110° C for 3 hours, after which time the sediment was removed via centrifugation. 4ml of HF was added to the cation solution in two steps to bind excess Ca and Mg. After each HF addition step, 2ml of ultrapure H_2O_2 was added to remove organics. The ultrapure water containing Be and other cations was removed from the fluoride cake via centrifugation and pipetting. Ion exchange chromatography (both anion and cation removal steps) was used to purify Be cations from the bulk cation solution. Be-hydroxides were precipitated from the purified cation solution by titration to pH 9 through the addition of ammonia. The supernatant was decanted and the precipitate was washed several times with ultrapure water and dried overnight at 100 deg C in low-boron quartz vials. The dry precipitate was flame-oxidized at > 850 deg C to form BeO powder and pressed into cathodes with niobium powder for AMS analysis at PRIME Lab, Purdue

University, USA. A process blank was run with each batch of 9 samples.

5.2.4 Calculation of Inventories and Inventory Ratios

Inventories were calculated by cumulative mass, utilizing the mass of each sampling increment to determine the total increment inventory and, by sum, the total profile inventory. For radioisotopes (^{137}Cs, ^{210}Pb, ^{10}Be):

$$I_{\alpha,j} = \sum_{n=1}^{N} \alpha_n BD_n l_n \qquad (34)$$

where $I_{\alpha,j}$ is the inventory of radionuclide α at sampling location j (atoms m^{-2}), N is the total number of samples layers in the profile, α_n is the radionuclide concentration (atoms kg^{-1}), BD_n is the bulk density of increment n (kg m^{-3}), and l is the increment length (m).

For elemental analytes (SOC, TN, Na, Mg, K, Ca, S, P, Cl, Pb, Hg):

$$I_{\beta,j} = \sum_{n=1}^{N} \beta_n BD_n l_n \qquad (35)$$

where Iβ,j is the inventory of element β at sampling location j (kg m^{-2}), N is the total number of samples layers in the profile, β_n is the radionuclide concentration (kg kg^{-1}), BD_n is the bulk density of increment n (kg m^{-3}), and l is the increment length (m).

In a system where depth to bedrock limits sampling depth, total profile depth affects the absolute inventory of all constituents that are present below the depth of the

shallowest profile (in this case the depth of CM – 56cm). Therefore, we calculate profile mass ratios (and 1-sigma mass ratio uncertainties) normalized by the cumulative mass of profile CM for profiles IN and MT and normalized by MT for profiles OD1 and OD2:

$$\Omega_{M,j} = \frac{M_j}{M_{ref}} \quad (36)$$

where $\Omega_{M,j}$ is the ratio of cumulative profile mass at profile j to the profile mass at the reference profile, and cumulative profile mass was calculated as:

$$M_j = \sum_{n=1}^{N} BD_n l_n \quad (37)$$

where M_j is the cumulative profile mass at profile j (kg m^{-2}), BD_n is the bulk density of increment n (kg m^{-3}), and l is the increment length (m).

We then calculated similar ratios for the inventories of isotopic tracers, normalized by the cumulative mass of profile CM for profiles IN and MT and normalized by MT for profiles OD1 and OD2:

$$\Omega_{I\alpha,j} = \frac{I_{\alpha,j}}{I_{\alpha,ref}} \quad (38a)$$

where $\Omega_{I\alpha,j}$ is the normalized inventory of radionuclide α at profile j (atoms m^{-2}).

And in the case of elemental tracers:

$$\Omega_{I\beta,j} = \frac{I_{\beta,j}}{I_{\beta,ref}} \qquad (38b)$$

where $\Omega_{I\beta,j}$ is the normalized inventory of element β at profile j (kg m^{-2}).

Finally, to detect differences in profile inventories of isotopic and elemental analytes that were not due to cumulative mass changes along the radial transect alone, we compared increases or decreases in inventories between sampling points to the 1-sigma range of increases or decreases in cumulative profile mass ratios (Eqn 36). Changes in inventory ratios (Eqns 38a and 38b) outside of the 1-sigma uncertainty in the mass ratio (Eqn 36) were considered to be significant differences that warrant further consideration. Changes in inventory ratios lying within the 1-sigma uncertainty of this profile mass ratio were considered to be predominantly due to differences in depth to bedrock or total profile mass.

5.2.5 Material Movement Models: Surficial movement from short-lived radionuclide tracers - Analytical model

Klaminder et al (2014) developed an analytical solution for estimating the rate of surficial movement from radial transect points along the surface of a frost boil using $^{210}Pb_{ex}$ inventories. This model assumes piston-type flow of the soil matrix across the frost-boil surface, where $^{210}Pb_{ex}$ is continuously deposited at the surface. Therefore, gains of $^{210}Pb_{ex}$ to the soil matrix are atmospherically derived and losses are through radioactive

decay. This mass balance can be described as:

$$\frac{dI}{dx} = \frac{D}{V_{surf}} - \frac{\lambda}{V_{surf}} I \qquad (39)$$

where I is the total profile inventory $^{210}Pb_{ex}$ (atoms m^{-2}), x is the distance from the center of the frost-boil (m), D is the atmospheric deposition rate of $^{210}Pb_{ex}$ (atoms m^{-2} yr^{-1}), V_{surf} is the apparent piston flow velocity (m yr^{-1}) and λ is the radionuclide decay constant (equal to $\ln(2)/t_{1/2}$, with units of yr^{-1}), where $t_{1/2}$ is the radionuclide half-life (yr).

The atmospheric deposition rate of $^{210}Pb_{ex}$ can be estimated by assuming steady-state inventories. Where significant material movement occurs relative to the half-life of $^{210}Pb_{ex}$ such as in systems like NSCs, one of two strategies must be taken to derive estimates of D (atoms m^{-2}) from observed inventories (because a single profile in the inner domain cannot be assumed to represent steady-state conditions). Either the entire NSC inventory can be calculated (along with NSC area) to estimate the steady state inventory, or the outer domain inventories, which do not theoretically participate in material movement, can be taken as steady state inventories. In either case, once the steady-state inventory reference is chosen, (atoms m^{-2}), then, assuming steady-state, D (atoms m^{-2} yr^{-1}) is equal to the annual amount of inventory loss by decay. Therefore at steady state:

$$D = \frac{I_{ss} - I_{ss} e^{-\lambda t}}{t} \qquad (40)$$

where D is the atmospheric deposition rate of $^{210}Pb_{ex}$ (atoms m^{-2} yr^{-1}), I_{ss} is the chosen steady-state reference inventory of $^{210}Pb_{ex}$ (atoms m^{-2}), and t is the time period under consideration (yr), generally evaluated at t=1.

Rearranging equation 39 we can derive an apparent surficial flow velocity:

$$V_{surf} = \frac{(D - \lambda I)}{dI / dx} \qquad (41)$$

5.2.6. Material Movement Models: Surficial movement from short-lived radionuclide tracers - Numerical model

Analytical solutions only exist when the assumption of steady state is reasonable. This is reasonable for $^{210}Pb_{ex}$ because given fallout and radioactive decay (occurring over decadal timescales), steady-state inventories can be reached within centuries. For tracers that can be considered pulse tracers (non-continuous fallout, such as ^{137}Cs) a steady state condition does not exist, so no analytical mass balance model can be derived. Therefore, numerical modeling is required to yield apparent movement rates. In our numerical model, the NSC is assumed to be a circle of radius r and is discretized into K increments of radial length ι. The area of each increment is therefore:

$$A_k = \pi r_{k(o)}^2 - \pi r_{k(i)}^2 \qquad (42)$$

where A_k is the area of increment k (m), $r_{k(o)}$ is the outer radius (m) and $r_{k(i)}$ is the inner radius (m) of increment k. The numerical model is run for yearly timesteps where material is assumed to move radially outward as plug flow so that:

$$I_{k(t+1)} = (I_{k-\frac{v}{l}t_s(t)} + Dt_s)e^{-\lambda t_s} \quad (43)$$

where $I_{k(t+1)}$ is the inventory of increment k at the next timestep (atoms m^{-2}), v is the velocity of plug flow (m yr^{-1}), D and λ are as defined above, l is the increment radial length $r_{k(o)} - r_{k(i)}$, (m) and t_s is the timestep length (yr; equal to 1 yr in these model runs).

Boundary conditions are set so that:

$$I_k = 0 \text{ for } k < 0 \text{ and } t \geq 0 \quad (44)$$

and:

$$I_{K(t+1)} = \left[\sum_{k=K-\frac{v}{l}t_s(t)}^{K} I_k + Dt_s \right] e^{-\lambda t_s} \quad (45)$$

where I_K is the inventory of the outermost increment and other variables are defined as in equations 42 and 43 above.

Models are then run until steady-state is achieved (for $^{210}Pb_{ex}$ ~ 300 years-1000

years, depending on D) or the time since assumed pule deposition is reached (^{137}Cs). For ^{137}Cs, we assume pulse deposition in 1963. This does not account for any deposition from the Chernobyl incient, which did have a minimal influence on radionuclide inventories in Arctic Sweden (Barrie et al., 1992). Therefore, this should be considered a minimum velocity estimate for ^{137}Cs tracer. The inventories at t=0 are:

$$I_{k(t=0)} = 0 \text{ for } {}^{210}\text{Pb}_{ex} \qquad (46a)$$

which assumes that we develop steady state inventories across the NSC with time on transported till materials which have been ice-shielded prior to deglaciation with no ^{210}Pb$_{ex}$ concentration – this assumes instantaneous NSC development, but over the timescales considered, the assumption is negligible, as steady state inventories are achieved within centuries depending on D (Eqn 40). For ^{137}Cs, the t=0 inventories are:

$$I_{k(t=0)} = \frac{I_{OD,ave}}{e^{-\lambda(t_{samp}-1963)}} \text{ for } {}^{137}\text{Cs} \qquad (46b)$$

where $I_{OD,ave}$ is the average ^{137}Cs (atoms m^{-2}) inventory of the outer domain profiles (OD1 and OD2), and t_{samp} is the year (A.D.) of sampling.

Once the model was run through all of the required timesteps, 10cm segments of the NSC (starting with the outermost portion) were summed to generate total expected radionuclide inventories (and subsequently activity inventories per unit ground area) for

specific values of v (m yr^{-1}). The predictions for the model (apparent rates) were taken as the best estimate and range of results from numerical runs that lay inside of the reported 1-sigma uncertainty in the observed inventories at each point.

5.2.7 Material Movement Models: Subsurface movement from ^{14}C - Numerical model

To estimate subsurface rates of material movement, 2-sigma uncertainties (Y.B.P.) from ^{14}C in parcels of soils were taken to represent the time since subduction. Then, a straight-line path was drawn from the previous marker of material movement (minimum path length) and along the sides of a right triangle (maximum path length) between the two points. The apparent subsurface movement rate is then:

$$V_{sub} = \frac{p}{Y_2 - Y_1} \qquad (47)$$

where V_{sub} is the movement velocity (cm yr^{-1}), Y_1 is the apparent radiocarbon age of bulk SOC at the point of origin, Y_2 is the apparent radiocarbon age of bulk SOC at the end point, and p is the path length (cm). ^{14}C age of surficial bulk SOC between MT and OD1 (the hypothesized origin of subducted organic material in the equilibrium cell model) is assumed to be 0 (or 100% modern C).

5.2.8 Material Movement Models: Former surficial residence time of cryoturbated materials

Meteoric ^{10}Be and Hg_{ex} can provide a measure of the surface exposure time when

atmospheric deposition rates are constrained. We utilize three different long-term atmospheric deposition rates for ^{10}Be in this study: 0.8 x 10^{10} atoms m^{-2} yr^{-1} (Willenbring and von Blanckenburg, 2010), 0.35 x 10^{10} atoms m-2 yr^{-1} (Finkel et al., 1997), and the D_{atm} derived from the equation below, when t is constrained by deglaciation chronologies of 9,000 years (Lundqvist, 2004):

$$D_{atm} = \frac{I_{^{10}Be,ave}}{t_{glac}} \qquad (48)$$

where D_{atm} is the long-term average deposition rate of meteoric ^{10}Be (atoms m^{-2} yr^{-1}), $I_{10Be,ave}$ is the average ^{10}Be inventory across all profiles (atoms m^{-2}), and t_{glac} is the time since deglaciation (yr).

In this model, the exposure time of a subducted parcel is equal to the inventory of excess ^{10}Be in a soil parcel or profile section divided by the atmospheric deposition rate:

$$t_{res} = \frac{I_{excess,n}}{D_{atm}} \qquad (49)$$

where t_{res} is the surficial residence time (the cumulative time of atmospheric exposure (yr)), $I_{excess,n}$ is the excess ^{10}Be inventory - defined below - (atoms m^{-2}) of cyroturbated parcel n, and D_{atm} is the atmospheric deposition rate (atoms m^{-2} yr^{-1}). For the purposes of this model, the excess ^{10}Be inventory of cryoturbated parcels was calculated as:

$$I_{excess,n} = (\alpha_n BD_n - \alpha_{n-1} BD_{n-1}) l_n \quad (50)$$

where $I_{excess,n}$ is the excess ^{10}Be inventory of cryoturbated parcel n (atoms m^{-2}), α_n is the radionuclide concentration (atoms kg^{-1}) of increment n, α_{n-1} is the radionuclide concentration (atoms kg^{-1}) of increment n-1, BD_n is the bulk density of increment n (kg m^{-3}), BD_{n-1} is the bulk density of increment n-1 (kg m^{-3})and l is the increment length of increment n (m).

Hg_{ex} is estimated as the difference between the total Hg concentration and the geogenic Hg estimated as the average Hg concentration (kg m^{-3}) of the lowest sampling increments for each profile, a strategy used in other studies of Hg that estimate geogenic sources (Nater and Grigal, 1992):

$$Hg_{ex,n,j} = Hg_{tot,n,j} - \frac{\sum_{j=1}^{J} Hg_{tot,N}}{J} \quad (51)$$

where $Hg_{ex,n}$ is the Hg_{ex} concentration (mg kg^{-1}) of increment n in profile j, $Hg_{tot,n}$ is the total Hg concentration (mg kg^{-1}) of increment n in profile j, $Hg_{tot,N}$ is the total Hg concentration (mg kg^{-1}) of the lowest depth increment (N) in profile j, and J is the total number of profiles.

Surficial exposure times of the same cryoturbated parcels were estimated with Hg_{ex} observations as:

$$t_{res} = \frac{I_{excess,n}}{D_{atm}} \quad (52)$$

where t_{res} is the surficial residence time (the cumulative time of atmospheric exposure (yr)), $I_{excess,n}$ is the excess Hg_{ex} inventory - defined below - (mg m^{-2}) of cyroturbated parcel n, and D_{atm} is the atmospheric deposition rate (mg m^{-2} yr^{-1}). For Hg_{ex} D_{atm}, we use three different long-term atmospheric deposition rates for Hg_{ex} of 0.5 x 10^{-3}, 1.0 x 10^{-3} and 2.0 x 10^{-3} mg m^{-2} yr^{-1} (Bindler, 2003)), except $I_{excess,n}$ represents the excess Hg_{ex} inventory, calculated as:

$$I_{excess,n} = (\beta_n BD_n - \beta_{n-1} BD_{n-1}) l_n \quad (53)$$

where $I_{excess,n}$ is the excess Hg_{ex} inventory of cryoturbated parcel n (mg m^{-2}), β_n is the Hg_{ex} concentration (mg kg^{-1}) of increment n, β_{n-1} is the Hg_{ex} concentration (mg kg^{-1}) of increment n-1, BD_n is the bulk density of increment n (kg m^{-3}), BD_{n-1} is the bulk density of increment n-1 (kg m^{-3})and l is the increment length of increment n (m).

5.3. Results

5.3.1. Morphological aspects of sampled profiles

Sampling locations in the mineral center (CM, 0cm), Inner Domain (IN, 83cm), Mixing Transition (MT, 145cm) and Outer Domains (OD1 and OD2, 180 and 260cm, respectively) had distinct profile morphologies (Fig 5.2). Profiles at sampling locations

CM and IN had no surficial organic horizon (0 cm depth), while Profiles at MT, OD1 and OD2 had surficial organic horizons with thicknesses of 4cm, 6cm and 8cm, respectively (Fig 5.2). Additionally, profile IN had a morphologically distinct organic-rich layer at a depth of 36-42 cm (Fig 5.2). Depth to bedrock also co-varied with distance from the mineral center, with observed bedrock depths at 56, 59, 71, 76 and 81cm, respectively, for sampling locations CM, IN, MT, OD1 and OD2. Although this trend does not reflect typical NSC observations (Fig 5.1), we note that the morphology and functionality (Klaus et al., 2013) of these NSCs are highly congruent with observations at other sites. Total variation in bedrock depth from the center to the outer domain was 25 cm, 45% of the center profile depth. Measurements of surficial elevation differences between sampling location MT and OD1 were 5cm, while the elevation gradient between CM and OD2 was measured at 14 cm in the summer and 21 cm in the winter (a seasonal difference of 7cm) (Fig 5.2).

5.3.2 Sample characterization, elemental concentrations and radioisotope activities

Trends in surficial pH across the frost-boil transect closely follow those of O horizon morphology and hypothesized material movement. A trend of decreasing surficial pH from 5.4-3.6 occurs (Fig 5.2) from CM to OD2. Deep mineral soil increments have a maximal pHs of 5.2-5.4, while organic materials have an average pH of 3.6 (Table 5.2).

Clay concentrations ranged between 5-25% across all sampling increments with no observable trends (except for the extremely low clay contents of surficial organic horizons and organic-rich subsurface materials) with depth or location on the NSC (Table

5.2). SOC concentrations ranged from 0.2-41.8% across all samples, and exhibited a numerically increasing trend across the outward radial transect associated with the change from surficial mineral materials to surficial organic materials from IN to MT. The average SOC concentrations for mineral depth increments (n=35) were 1.6 ± 2.6 g $100g^{-1}$, while average SOC concentrations for surficial organic materials (from MT, OD1 and OD2; n=3) were 39.0 ± 3.4 g $100g^{-1}$ soil. Bulk soil total nitrogen concentrations varied from 0.1 – 1.4 g $100g^{-1}$ and closely followed trends in SOC concentrations for mineral depth increments (0.1 ± 0.2 g $100g^{-1}$) and surficial organic materials (0.9 ± 0.7 g $100g^{-1}$). C:N ratios are wider for surficial organic samples (32.8 ± 3.5) than mineral sampling increments (21.2 ± 8.3).

S and Hg concentrations also closely followed SOC, with average S concentrations across all sampling increments of 387 ± 549 ppm, and averages of 1966 ± 680 ppm and 255 ± 263 ppm for organic and mineral materials, respectively. Total Hg spanned four orders of magnitude across all sampling increments (0.1 – 358 ng g-1), and showed pronounced differences in surficial concentrations across the radial outward transect, consistent with observed trends of organic layer thickness and SOC content. Geogenic concentrations of Hg, calculated as the average of the Hg concentration of the bottom depth increment for each profile were estimated at 4.4 ± 0.8 ng g^{-1}. Averages of Hg_{ex} for organic and mineral sampling increments, respectively, were 257 ± 90 ng g^{-1} and 10 ± 22 ng g^{-1}, respectively (Table 5.3).

Concentrations (μg g^{-1}) of the base cations Na, Mg, K and Ca were all significantly lower in organic materials (2596 ± 1874, 3482 ± 1656, 5718 ± 2515 and 8671 788 μg g^{-1},

respectively) than in mineral soil materials (7925 ± 954, 12295 ± 2017, 11635 ± 1082, and 14409 ± 2524 μg g^{-1} respectively). Conversely, concentrations of P, Pb and Cl were greater in organic materials than mineral soil materials. P concentrations averaged 729 ± 239 μg g^{-1} across all sampling increments, with averages of 1259 ± 218 μg g^{-1} in organic materials and 684 ± 183 μg g^{-1} in mineral materials (Table 5.3). Concentrations of Pb averaged 12.6 ± 8.2 μg g^{-1} across all samples, with averages of 38.3 ± 10.3 μg g^{-1} in organic materials and 10.4 ± 2.3 μg g^{-1} in mineral materials (Table 5.3). Concentrations of Cl averaged 162 ± 51 μg g^{-1} across all samples with averages of 297 ± 80 μg g^{-1} in organic samples and 151 ± 29 μg g^{-1} in mineral samples (Table 5.3).

Elements in addition to Hg which have significant background concentrations include Na, Mg, Ca , K, P, Pb, Cl, and meteoric ^{10}Be (inherited ^{10}Be). Similar to Hg, we estimate background concentrations through the averages of the bottom depth increments. Base cation background concentrations were 8498 ± 291, 11999 ± 477, 13397 ± 984 and 16336 ± 371 μg g^{-1} for Na, K, Mg, and Ca, respectively. Background concentrations for P, Pb and Cl were 663 ± 37, 10.7 ± 1.0, and 144 ± 16 μg g^{-1}, respectively.
δ^{13}C values averaged -25.9 ± 0.7 per mil across all sampling increments, -27.2 ± 0.5 per mil for organic materials and -25.7 ± 0.6 per mil for mineral sampling increments. There were no apparent radial outward trends in profile-averaged ^{13}C maximum, minimum or mean values.

Activities of $^{210}Pb_{ex}$ across all depth increments ranged from 0 (below detection limit) to 311 Bq kg^{-1}, and except for a decline within analytical error from CM to IN, showed increasing trends from 38 Bq kg^{-1} to 311 Bq kg^{-1} for surficial sampling

increments across the NSC radial transect. In all cases, the surficial depth increment had the highest activity of $^{210}Pb_{ex}$ (Table 5.2). ^{137}Cs activities ranged from 0 to 108 Bq kg^{-1} across all sampling increments and in contrast to $^{210}Pb_{ex}$ did not always have the highest activities in the surficial depth increment of each profile (Table 5.2). For profiles MT and OD2, the highest ^{137}Cs activities were measured in the 4-7 cm and 8-15 cm depth increments, respectively. Despite this, the maximum profile ^{137}Cs activity increased in an outward direction along the radial transect. Therefore, $^{210}Pb_{ex}$ was consistently detected in the top 15-20cm of all profiles (Table 5.2), while the depth of ^{137}Cs detection varied significantly. No ^{137}Cs was detected at location CM, while ^{137}Cs was detected to depths of 2, 12, 10 and 50 cm at locations IN, MT, OD1 and OD2, respectively (Table 5.2). ^{10}Be concentrations were generally much more similar in whole material averages 4.12 ± 2.45 x 10^7 atoms g^{-1} across all sampling increments (n = 38) and 3.98 ± 2.52 x 10^7 atoms g^{-1} and 5.13 ± 1.98 x 10^7 atoms g^{-1} for mineral and organic materials, respectively) with a total range from 0.7 – 13.6 x 10^7 atoms g^{-1} and were more normally distributed than the other radioisotope tracers (Fig 5.4). Meteoric ^{10}Be background concentrations calculated from the average of the bottom depth increments for each sampling point resulted in 2.85 ± 0.20 x 10^7 atoms g^{-1}.

Two sampling increments were analyzed for ^{14}C:^{12}C and estimated radiocarbon dates for bulk soil organic carbon. The 37-42 cm depth increment at sampling location IN (indentified as potentially cryoturbated, organic-rich material in morphological sampling) has an SOC content of 8.4 ± 0.9 g $100g^{-1}$, a ^{14}C pmC (% modern) of 80.4 ± 0.4%, and a 2-sigma uncertainty of radiocarbon age of 1860-1990 Y.B.P. The 22-32 cm depth

increment at sampling location CM has an SOC content of 1.4 ± 0.2 g $100g^{-1}$, a ^{14}C pmC (% modern) of 74.2 ± 0.4%, and 2-sigma uncertainty in radiocarbon age of 2350-2680 Y.B.P.

5.3.3. Relationships between tracers

Elemental concentrations closely related in origin and deposition mode were significantly correlated (Table 5.4). In particular, SOC was significantly and positively correlated with TN, S, Cl and Hg (Kendall's tau-b, with Bonferonni correction, $\alpha = 0.05$, Table 5.4), which were all significantly correlated with eachother. The base cations Na, K, Ca and Mg were generally negatively correlated with the SOC and atmospheric-associated tracers. Na and Ca were negatively correlated with SOC, TN, S, Cl and Hg, while Mg and K were not significantly negatively correlated with those tracers, but were significantly correlated with eachother. ^{13}C:^{12}C ratios were significantly correlated with SOC (log transformation) on linear regression ($R^2 = 0.44$, $p < 0.0001$, Fig 5.8).

The highest correlation coefficients across all relationships for the non base cations (Kendall's tau-b, with Bonferonni correction, $\alpha = 0.05$, Table 5.4) were S and Hg_{ex} (0.81), S and Cl (0.78), SOC and S (0.76), SOC and TN (0.75), S and TN (0.70), and SOC and Hg_{ex} (0.67). As a three element group, SOC, S and Hg_{ex} were the most closely related (average of 0.75). These 3 tracers showed highly skewed distributions due to a few large values for organic sampling increments (and just below) at MT, OD1 and OD2 that were significantly greater than the bulk of the measurements (Fig 5.3). Log-log transformation of the variables resulted in significant improvement in normality of

distributions (Fig 5.3). Linear regressions of log-log transformations of these 3 variables were highly significant (R^2 = 0.73, 0.81 and 0.80, respectively, for SOC-Hg_{ex}, SOC-S, and Hg_{ex}-S, respectively, $p < 0.0001$, Fig. 5.3).

In contrast. relationships between the radioisotope markers (^{137}Cs, $^{210}Pb_{ex}$ and ^{10}Be, not including 14C) and SOC were non-significant, with the exception of SOC-$^{210}Pb_{ex}$, which showed weak correlations (R^2 = 0.37, $p = 0.004$, Fig 5.4). Similar to the elemental tracers associated with surface materials and atmospheric deposition, $^{210}Pb_{ex}$ and ^{137}Cs have highly skewed distributions due to both the large numbers of sample increments in which they could not be detected and surficial increments which had high activities. In contrast, meteoric ^{10}Be distributions were fairly normally distributed.

5.3.4 Within and between profile trends in elemental and isotopic tracers

Single tracer profiles. Depth profiles of elemental and isotopic tracers exhibited distinct morphologies across sampling locations and tracer type. We distinguish between 5 different depth profile morphologies: spiked, inverse-spiked, decreasing, increasing and irregular. Spiked-type profile are defined as depth profiles which have a single, definite subsurface increase with decreases on either side, while inverse-spiked profiles have a single, definite decrease with increases on either side. Irregular profiles have more than one increase or decreases with depth, while decreasing or increasing profiles show continuous increases or decreases with depth (within analytical error). For profiles that did not fit these criteria exactly, we utilize two terms to describe them, with the primary shape first.

At sampling point CM, spiked or inverse-spiked profiles were apparent for all tracers except P, Mg, K, $^{210}Pb_{ex}$, ^{137}Cs and Pb (Fig 5.5-5.7). At sampling point IN, spiked or inverse-spiked profiles were apparent for all tracers except $^{210}Pb_{ex}$, ^{137}Cs, and Pb (Fig 5.5-5.7). At sampling point MT, tracers exhibited either decreasing (SOC, $^{210}Pb_{ex}$, ^{10}Be, Pb, Hg, S, Cl), spiked-decreasing (with a spike in the depth increment just under the surface (TN, ^{137}Cs), irregular-decreasing (P), or irregular-increasing distributions (Na, Ca, Mg, K, ^{13}C). For outer domain profiles, the base cations and ^{13}C exhibited increasing or irregular-increasing profiles, while TN, P, SOC, $^{210}Pb_{ex}$, Pb, Hg, S and Cl exhibited decreasing or irregular-decreasing profiles. OD1 and OD2 tracer profiles differed most significantly for ^{137}Cs and ^{10}Be, which were decreasing in OD1 and irregular-decreasing (^{137}Cs) or irregular-increasing (^{10}Be) at OD2.

^{13}C SOC down-profile trends. Down-profile trends of $\delta^{13}C$ and SOC (log transformed) were different between inner domain profiles CM and IN containing cryoturbated materials and those not containing cryoturbated materials. Figure 5.8B shows down-profiles trends of $\delta^{13}C$ and SOC (log transformed) for MT, OD1 and OD2, which do not contain cryoturbated materials. These profiles show a consistent trend of lower SOC concentrations and more positive $\delta^{13}C$ values as one moves downward in the profile (Fig 5.8B). In contrast, profiles containing cryoturbated materials (CM and IN) show much more irregular down-profile patterns (Fig 5.8C), as $\delta^{13}C$ values for subsurface materials change due to the presence of cryoturbated materials.

Coincidence of tracer peaks. The tracers most closely associated with the surficial exposure of soil materials are SOC, Hg, ^{13}C, ^{137}Cs and $^{210}Pb_{ex}$ and ^{10}Be. However, if a

material parcel has been buried for longer than ~ 100 years, ^{137}Cs and $^{210}Pb_{ex}$ will likely be below detectable limits, leaving SOC, Hg, ^{13}C and ^{10}Be as the most conservative long-term tracers of surficial origin. Therefore, in the evaluation of sampling increments which have been buried for some time but show evidence of a surficial origin, these 4 tracers should show convergent peaks in the subsurface (Fig 5.9A and 5.9B). Although the increment from 22-32 cm in profile CM was not identified in morphological sampling, these tracers share convergent peaks at that depth increment for CM, suggesting strong evidence of previous surficial origin.

5.3.5 Inventories

Constituent inventories can be grouped into two categories – those that show a substantial variation across the radial transect (range to mean ratio > 0.5), and those that showed little variation in inventory across the transect (range to mean ratio < 0.5). This first category includes SOC, TN, S, Hg, ^{137}Cs and $^{210}Pb_{ex}$. The second category contains Na, Mg, K, Ca, P, Cl, Pb, and ^{10}Be.

Large inventory variation. SOC, TN, S, Hg, ^{137}Cs, $^{210}Pb_{ex}$. Inventories of SOC had a range-mean ratio (range of observed inventory values for each tracer across all sampling points divided by the mean inventory across all sampling points) of 1.2 and varied from 2.6 kg m^{-2} to 13.4 kg m^{-2} (Table 5.5) across the radial transect, with an average of 9.0 ± 4.7 kg m^{-2} over all profiles (Table 5.5) and averages of 7 kg m^{-2} in the inner domain and 12 kg m^{-2} in the outer domain (Table 5.5). A weighted-average SOC inventory across the radial transect can be derived by extending each observed profile

inventory to in between observed sampling points. Calculating a total SOC transect inventory average in this way results in a value of 8.7 kg m^{-2}.

TN inventories had a range-mean ratio of 1.5 and ranged from 0.11 kg m^{-2} to 0.83 kg m^{-2} (Table 5.5), with an average of 0.49 ± 0.25 kg m^{-2} across all profiles, 0.46 kg m^{-2} in the inner domain and 0.52 kg m-2 in the outer domain. S inventories varied from 69 g m^{-2} to 153 g m^{-2} (Table 5.5), with an overall average of 115 g m^{-2}, an inner domain average of 111 g m^{-2}, an outer domain average of 123 g m^{-2}, and a range to mean ratio of 0.72. Hg_{ex} inventories varied from 0.9 to 12.6 mg m^{-2}, with an overall average of 5.3 mg m^{-2}, an inner domain average of 3.8 mg m^{-2}, and outer domain average of 7.5 mg m^{-2}, and a range to mean ratio of 1.8. ^{137}Cs inventories varied from 0 to 1625 Bq m^{-2}, with an overall average of 987 Bq m^{-2}, an inner domain average of 714 Bq m^{-2}, an outer domain average of 1397 Bq m^{-2}, and a range to mean ratio of 1.8. Lastly, $^{210}Pb_{ex}$ varied from 1840 to 4939 Bq m^{-2}, with an overall average of 2964 Bq m^{-2}, an inner domain average of 2533 Bq m^{-2}, an outer domain average of 3611 Bq m^{-2}, and a range to mean ratio of 1.0.

Little to no inventory variation. Na, Mg, K, Ca, P, Cl, Pb, ^{10}Be. For the tracers that did not show high variability across the radial transect, only ^{10}Be, Pb and Cl are predominantly atmospherically derived. Overall profile inventory averages for Na, Mg, K, Ca were 4.0, 6.2, 5.8, 7.3 kg m^{-2}, respectively. Overall averages for P, Cl and Pb were 332, 73.2, and 5.3 g m^{-2}, respectively. The transect inventory average for ^{10}Be was 1.78 x 10^{13} atoms m^{-2} (Table 5.5).

Normalized trends in inventories along the radial transect. Depth to bedrock co-varies with distance along the radial transect (Fig 5.2), so a true comparison of

inventories must take into account inventory ratios normalized for cumulative profile mass (Eqns 36-38). Therefore, for comparative purposes, changes in cumulative profile mass were normalized to the center (CM) profile for inner domain profiles IN and MT, and to MT for the outer domain profiles OD1 and OD2 (Fig 5.10). This provides a comparative picture of normalized stocks relative to the center along the direction of soil movement in the inner domain (Fig 5.10A), and also relative to the mixing transition for the outer domain profiles (Fig 5.10B). The reason for this is that the mixing transition represents a cumulative location (receiving material) and normalization of outer domain to this sampling point allows us to assess the stability of the outer domain profiles. At sampling point IN, the range of 1 sigma normalized ratios were 0.88 – 1.04. The range of 1 sigma normalized ratios for MT (relative to CM) was 0.84 – 1.22. For the outer domain sampling points, the 1 sigma normalized ratios (relative to MT) were 0.84 – 1.13 and 0.87 – 1.02 for OD1 and OD2, respectively.

For the inner domain, (CM, IN, MT), normalized inventories of Hg (IN-CM: 3.66; MT-CM: 7.59), TN (IN-CM: 3.67, MT-CM: 6.92), OC (IN-CM: 2.09; MT-CM: 5.25), and $^{210}Pb_{ex}$ (IN-CM: 1.36; MT-CM: 1.77) all lay outside of the 1 sigma expected space if inventory increases were due solely to changes in profile depth alone. ^{137}Cs would also fall into this group but normalized inventories cannot be calculated because the inventory at CM is 0 Bq m^{-2}, so ^{137}Cs is omitted from these results but understood to show exceedingly strong variation in the inner domain. Cl inventories were outside of the expected 1 sigma space for MT only (MT-CM: 1.33) and not IN (IN-CM: 1.16). All other tracers did not exhibit inventory increases in excess of that expected from increases in

profile depth alone.

In the outer domain comparisons (MT, OD1, OD2), inventories of TN (OD1-MT: 0.60; OD2-MT: 0.65) showed significant decreases relative to MT, while inventories of ^{137}Cs (OD1-MT: 0.67; OD2-MT: 0.93), SOC (OD1-MT: 0.82; OD2-MT: 0.94) and S (OD1-MT: 0.67; OD2-MT: 1.08) showed significant decreases relative to MT at OD1, but no significant change relative to MT at OD2 (Fig 5.10B). $^{210}Pb_{ex}$ (OD1-MT: 0.70; OD2-MT: 1.51) and Hg (OD1-MT: 0.64; OD2-MT: 1.50) showed significant decreases relative to MT at OD1 and significant increases relative to MT at OD2 (Fig 5.10B). Lastly, Ca (OD1-MT: 1.19, OD2-MT: 1.17) showed a significant increase relative to MT at OD1 and no significant change relative to MT at OD2. All other tracers did not exhibit inventory increases in excess of that expected from increases in profile depth alone.

5.3.6 Material movement rate estimates

Apparent rates were strongly convergent among model and movement types considered but differed between domain sections and surficial/subsurficial movement rates. Apparent rates of surficial movement were 2.6 and 0 cm yr^{-1} for the analytical solution $^{210}Pb_{ex}$ model between CM-IN and IN-MT, respectively, for an inner domain numerical rate average of 1.3 cm yr^{-1} (Eqn 41, Table 5.6). Numerical models for $^{210}Pb_{ex}$ (Eqns 42-46) resulted in apparent rates of 0-1.0 for the CM-IN and 0-0.1 for the IN-MT increments, resulting in an average of 0.22 cm yr^{-1}. Calculating averages for both analytical and numerical models results in an apparent average rate across the inner domain of 0.76 cm yr^{-1}. Averages of numerical models (Eqns 42-46) applied to observed ^{137}Cs inventories

were 1.2 and 0.1 cm yr^{-1} for CM-IN and IN-MT increments, respectively, for a entire inner domain average of 0.65 cm yr^{-1}. Overall apparent rate averages for both ^{137}Cs and $^{210}Pb_{ex}$ across all models were 1.4 cm yr^{-1} for CM-IN, 0.05 cm yr^{-1} for IN-MT and 0.7 cm yr^{-1} across the whole inner domain.

Apparent rates for subsurface movement from observations of ^{14}C in subsurface cryoturbated parcels were calculated based on assumptions of (i) ongoing movement and (ii) linear minimum and maximum path lengths (with the assumed starting spatial location in between MT and OD1 (Fig 5.2). These resulted in apparent rate averages of 0.05 cm yr^{-1} for the MT-IN increment and 0.18 cm yr^{-1} for the IN-CM increment (Eqn 47, Table 5.6). Overall averages for all increments and path lengths were 0.11 cm yr^{-1} for subsurface movement.

Average of maximum exposure years for the cryoturbated parcels based on excess ^{10}Be inventory (Eqns 48-50) are 1032 and 759 years for IN 37-42 cm and CM 22-32 cm, respectively. Average maximum exposure years based on Hg_{ex} inventory (Eqns 51-53) are 2298 and 555 years for IN 37-42 cm and CM 22-32 cm, respectively (Table 5.6).

5.4. Discussion

In our interpretations, we focus on the context of the tracer depth distributions and inventories, identify the tracers in our suite that show the most promise for future studies, set our derived rates in context to previous work in NSCs, and pose a set of unresolved questions related to cryoturbation rates and suggest the methodologies that may solve them.

5.4.1. Inventories and utility of elemental tracers

Inventories of C in the studied profiles are on the low end of SOC and TN inventories measured in permafrost-affected soils and Arctic patterned ground. For example, the most current database for pedon information in Arctic Alaska calculated an average of 47 kg SOC m^{-2} and 2.7 kg TN m^{-2} to 100cm for Arctic soils (Michaelson et al., 2013). Hugelius et al. (2010) reported C inventories for cryoturbated soils in central Canada of 28 – 37 kg m^{-2}, while Bockheim (2007) reported inventories ranging from 17-120 kg m^{-2} for cryoturbated soils in Arctic Alaska. This is likely due to the shallow depths (56-81 cm) to lithic contact across the NSC, as our estimated transect SOC inventory of 8.7 kg m^{-2} and TN inventory of 0.5 kg m^{-2} is more closely aligned to high Arctic (76° N) SOC inventories in cryoturbated soils (9.4 kg m^{-2}; Horwath et al., 2008).

Our reported concentrations and depth distributions of Pb and Hg are similar to those previously reported at sites near Abisko, Sweden. Background concentrations of Pb in our NSC profiles (8-12 mg kg^{-1}) were similar to those reported in previous studies near Abisko, Sweden; 2-20 mg kg^{-1} (Klaminder et al., 2011), and we observed higher concentrations of Pb in organic surface horizons (27-47 mg kg^{-1}) than those reported previously in the area (8-27 mg kg^{-1}, Klaminder et al., 2011). However, even these concentrations are still orders of magnitude below soils close to localized pollution sources in other parts of Sweden (Klaminder et al., 2008). Weighted average whole-transect inventory of Hg_{ex} was 5.1 mg Hg m^{-2}, which close to the range (5.6-7.8 mg Hg m^{-2}) of previously observed inventories in regional soils on a tundra peat hummock

landscape (Klaminder et al., 2008).

An important difference in Pb and Hg is that Hg is a conservative tracer of cryoturbated materials that were exposed to the surface 1000-2000 Y.B.P., while Pb is not. No subsurface spikes were observed in Pb concentrations associated with cryoturbated parcels (Fig 5.7). Pb deposition reconstructed for the Boreal and Sub-Arctic zones of Sweden shows a pronounced large increase in deposition rates around the first half of the 20th century, before which levels were 1-2 orders of magnitude below peak deposition rates (Jaworski et al., 1987, Klaminder et al., 2006). This is consistent with our observation of no elevated Pb levels in cryoturbated parcels (22-32cm in CM and 37-42 cm in IN), with carbon dates suggesting subduction of these materials occurred some time between the 7th century B.C. and the 2nd century A.D. Because natural deposition rates of Pb are much lower relative to soil inventories derived from geogenic sources (Klaminder et al., 2011) compared to natural Hg deposition rates and inventories (Bindler, 2003), the pre-industrial atmospheric signal is not apparent for Pb. Similar to other global observations, recent depositional histories for Hg in southern Sweden exhibit a peak at least 1-2 orders of magnitude higher than background rates in the 1950s-1970s followed by a decline over the following 3 decades (Bindler, 2003).

Cl shows significant retention in cryoturbated parcels and decreasing depth profiles (Fig 5.7), in strong contrast to the base cations, which are not retained in organic materials and show increasing depth profile indicative of leaching (Fig 5.5). Although classical interpretations of Cl maintained that it is a non-conservative element in soils, more recent work has collected many lines of evidence that suggest in organic rich soils,

particularly those in arctic environments, Cl can form stable complexes with organic matter and be relatively conservative (Leri and Myneni, 2010). Our estimates of Cl inventories across the NSC transect of 73 ± 8 g m^{-2} are much higher than those previously estimated for a site in southern Sweden (~ 13 g m^{-2}, Oberg, 2002). Several reasons could account for this; first, our Abisko study site lies closer (70-100 km) to the oceanic sources of aerosols than the catchment in that study (120-140 km), and there is a non-linear relationship between distance from the coast and marine aerosol deposition in Sweden (Gustafsson and Franzen, 2000). Additionally, the difference in leaching regime and decomposition rates of organic matter (a key release of organic-bound Cl in organic – rich systems (Oberg et al., 2002)) is likely much slower in Arctic Sweden than in Boreal systems near the coast. Lastly, the leaching regime is much more intense in the forested, boreal vegetation of the Ober (2002) study, so Cl is much more likely to be lost through leaching. Although Cl inventories did not vary significantly across the transect, depth distributions of Cl demonstrated that a significant amount of organic-bound Cl was retained in cryoturbated parcels, even after 1500-2000 years of subsurface movement (Table 5.3, Fig 5.7). In any event, the higher concentrations of Cl observed at the surface of all profiles is indicative of ongoing atmospheric deposition and soil retention.

Na, Mg, K, Ca. Unlike Cl, depth distributions of these elements in the low pH outer domain all exhibited leached profiles with generally increasing concentrations with depth. Inner domain depth distributions of these elements were highly irregular in form, exhibiting no consistent patterns except for an inverse-spiked distribution in Ca at CM and N1 associated with cryoturbated surficial materials. For these reasons, the base

cations are the least useful of all the tracers we explored for quantifying the rates and patterns of cryoturbation in NSCs.

5.4.2 Distribution and inventories of isotopic tracers

^{137}Cs and $^{210}Pb_{ex}$. The fact that no ^{137}Cs or $^{210}Pb_{ex}$ was detected below 15 cm in the inner domain and that all profiles showed decreasing ($^{210}Pb_{ex}$) or shallow subsurface peaks (^{137}Cs) provides a primary constraint on cryoturbated soil movement in this NSC. That is, the subduction and movement of soil materials at the mixing transition and mineral center cannot be occurring at rates faster than it takes for ^{137}Cs and $^{210}Pb_{ex}$ to decay (half lives 20-30 years). Therefore, given the material movement rates occurring in this particular NSC, these isotopes are decayed beyond detection limits by the time the surficial material originally containing them is subducted at the NSC edge and moved along the base of the permafrost table. These patterns agree with previous studies in both the Swedish and Alaskan Arctic (Klaminder et al., 2014, Jelinski, 2013) which found no detectable ^{137}Cs in the mineral materials at NSC centers and no deep subsurface ^{137}Cs or $^{210}Pb_{ex}$ activities, but significant inventories at the far edges of the inner domain and in the outer domain.

Two other studies have examined ^{210}Pb distributions and inventories with the intent to quantify the rates and patterns of material movement in NSCs. Hagedorn et al., (2008) observed the spatial pattern of ^{210}Pb activities across an NSC cross-section, which are consistent with the qualitative direction of material movement reported here. Klaminder et al. (2014) used $^{210}Pb_{ex}$ to quantify rates of lateral soil creep along the NSC inner

domain surface. In all of these studies, ^{210}Pb activities and inventories increased with increasing distance from the NSC center to the mixing transition (MT).

^{14}C. The radiocarbon dates reported for subducted organic material in this study (1860-1990 and 2350-2680 Y.B.P.) are highly convergent with radiocarbon dates from other subducted materials in NSCs on a global basis. In another study at Abisko, Becher et al. (2013) measured radiocarbon contents of 12 buried organic horizons in NSCs and found a range of radiocarbon dates from 0 – 1960 Y.B.P. Bockheim (2007) compiled radiocarbon dates from organic inclusions beneath patterned ground and found a range from 240 – 10,000 Y.B.P. However, both of those studies concluded that the radiocarbon dates of buried organic materials at least loosely coincided with periods of climatic warming, and hypothesized that under some scenarios some warming may actually increase cryoturbative activity. The radiocarbon date of our cryoturbated parcel at CM (22-32 cm) does roughly coincide with an inferred warming period near Abisko based on reconstructions of glacial advances (Becher et al., 2013).

^{13}C:^{12}C. Using space-for-time substitutions from the inferred subsurface movement of organic materials allows us to infer the timing and direction of ^{13}C enrichment and depletion as material moves around the equilibrium cell (Fig 5.8D). Material begins at the surface (between MT and OD1) as organic material (~ 37% SOC) which is depleted in ^{13}C (~ -27‰). Over the course of the 1925 years (the difference in best estimate bulk SOC radiocarbon dates from an assumed radiocarbon age of 0 years to a radiocarbon age of 1960 for the cryoturbated parcel at IN) that it takes to move from the surface to IN, the material undergoes an enrichment of ^{13}C to ~ 26.75 ‰ or $1.3x10^{-4}$ ‰ enrichment per

year. Bulk carbon, however, is reduced to 8% a decrease in concentration of ~ 1.5% per 100 years, likely due to decomposition, physical compression, mixing and diapirism with surrounding depth increments (this is may be evidenced by elevated inventories and activities of tracers above and below the cryoturbated parcel (Tables 5.2 and 5.3)). Over a period of ~ 540 years (the difference in best estimate bulk SOC radiocarbon dates from a radiocarbon age of 1960 years for the cyroturbated parcel at IN to a radiocarbon age of 2400 Y.B.P. for the cryoturbated parcel at CM), the material undergoes further change with enrichment of bulk SOC to ~ -26.4‰, a 5.9 x 10^{-4}‰ enrichment per year. Bulk carbon is reduced to 1.4%, a decrease in concentration of 1% per 100 years. In surficial transit, bulk SOC does not change significantly from that at the surface at CM, however once organic materials begin accumulating at the surface due to stabilization of the surface, rapid ^{13}C enrichment and carbon accumulation occurs.

Our study is the first to examine the distribution and inventories of meteoric ^{10}Be across small-scale patterned ground features such as NSCs. No other study has reported on densely investigated ^{10}Be profiles within a 3m horizontal distance, and the variation revealed due to physical and chemical processes is striking. Two other studies have reported single profile ^{10}Be concentrations in permafrost-affected soils – one in a non-glaciated region of northern Alaska (Bierman et al., 2014), which exhibited a hump-like depth distribution due to leaching and observed ^{10}Be concentrations 1-2 orders of magnitude higher than those reported here. A second study (Ebert et al., 2012) investigated ^{10}Be profiles in saprolite underlying glacial deposits in northern Sweden, and also found much higher concentrations of ^{10}Be. However, we expect our ^{10}Be

concentrations to be relatively low compared to these other studies because the NSC has developed in relatively recent (~ 9,000 year-old) glacial deposits.

Methodologies for the calculation of ^{10}Be inheritance are complicated in NSC systems due to the diversity in ^{10}Be profile shapes over short distances. However, total inventories can give an estimate of the long-term atmospheric deposition of ^{10}Be at the site. Deglaciation chronologies suggest that glacial retreat occurred ~ 9,000 YBP at Abisko (Lundqvist, 2004). This value results in an apparent long-term deposition rate (using the average profile integrated meteoric ^{10}Be inventory of $1.8 \pm 0.2 \times 10^9$ atoms cm^{-2}) of $0.2 \pm 0.02 \times 10^6$ atoms cm^{-2} yr^{-1} with no inheritance. Long-term average 10Be deposition is poorly constrained in high-latitude regions, however this value is lower than those reported or predicted previously (0.8×10^{10} atoms m^{-2} yr^{-1} (Willenbring and von Blanckenburg, 2010), 0.35×10^{10} atoms m^{-2} yr^{-1} (Finkel et al., 1997)), but of similar magnitude, and likely reflects differences in precipitation patterns or other environmental variables. This should therefore be viewed as the maximal long-term deposition rate based on the measured inventories at this study site. With previous inheritance, the long-term deposition rate would be lower.

5.4.3 Convergent markers for determining material provenance and surface history

SOC, Hg, ^{13}C, and ^{10}Be are strong indicators of the surficial origin of samples, and together can be used to confirm the surficial origin of cryoturbated parcels, despite extensive physical changes. For example, our original morphological sampling did not identify the parcel from 22-32 cm at CM as a cryoturbated parcel, and SOC is only

slightly elevated (1.4%) and similar to surficial values at CM. The convergence of peaks in SOC, $\delta^{13}C$, Hg and ^{10}Be, however, clearly establish the original surficial origin of this sample (Fig 5.9) and allowed the prioritization of ^{14}C analysis of the sample to estimate subsurface movement rates from IN to CM. In contrast, apparent peaks in any single one or two of these tracers in outer domain profiles are not convergent, and can be attributed to leaching or differential retention processes.

5.4.4 Derived rates and patterns of material movement – relationship to previous work

We compare the rates derived from radionuclide and elemental tracers in this study to those derived in previous work with reference to movement types described in Fig 5.1. Center upward movement due to ice lens formation and heave (Fig 5.1 #1) is not directly quantified in the scope of our work, but previously studies have estimated upward movement in the NSC center from 0 – 1.5 cm yr^{-1} (Table 5.7). Because the extent and magnitude of differential frost heave (Peterson et al., 2003) drives the net upward motion in individual NSCs, and is highly dependent on many environmental factors such as vegetation, hydrologic conditions and material, it is expected that these rates would vary significantly between sites. Nonetheless, rates derived from physical and short-lived radioisotope tracers and across NSCs from Canada and Sweden are convergent in magnitude (Table 5.7).

Lateral surficial creep (Fig 5.1 #2) has been the most extensively studied and quantified form of material movement in NSCs, due to the relative ease of measuring rates of surface movement, which make quantifying this movement type amenable to

multiple approaches, compared to subsurface movement which is much more difficult to directly observe or measure. Temporal changes in micro-scale digital elevation models (Kaab et al., 2013), physical tags (Egginton and Shilts, 1978, Sawyer, 2007) and $^{210}Pb_{ex}$ have resulted in similar magnitudes of lateral creep rate estimates, again, across NSC in different environments (Canada, Norway and Sweden) of 0 – 4.5 cm yr^{-1} (Table 5.7). If rates are quantified for multiple sections of the NSC inner domain, lateral creep rates nearest to the center of the NSC are typically 2-5x greater than those rates estimated in the outer portions of the inner domain. The use of analytical and numerical models resulted in similar estimated magnitudes and patterns of lateral creep rates. Rates in our NSC derived from $^{210}Pb_{ex}$ and ^{137}Cs for the proximal part of the inner domain ranged from 0 – 2.6 cm yr^{-1}, while rates for the distal portion of the inner domain ranged from 0 – 0.2 cm yr^{-1} (Table 5.6).

Subduction and subsurface creep rates (Fig 5.1, #3) have previously been estimated primarily by $^{210}Pb_{ex}$, ^{14}C and in a single study using telescoping probes (Harris, 1998, Table 5.7). These previously derived rates of subduction and subsurface movement are typically an order of magnitude lower than rates of lateral creep (Table 5.7). In this study, we provide two time points with evidence of previous surficial subduction (CM 22-32 cm and IN 36-42 cm). The difference in ^{14}C age between these timepoints allows us to place first order constraints on the movement rate of subducted materials in the subsurface along the path of hypothesized movement, which appears to be an order of magnitude lower than apparent rates of surficial movement (Table 5.6), in consensus with previous studies (Table 5.7). It also appears that the rate of movement is faster nearer to the center

of the frost boil, as subsurface movements from the MT/OD1 surface to 37-42 cm at IN are 0.04 – 0.06 cm yr^{-1}, while subsurface movements from IN/CM are 0.10-0.27 cm yr^{-1}. Physical markers in the center of a newly developing NSC in Canada showed evidence of 0.4 – 1.2 cm yr^{-1} of upward displacement in the area where ice lens growth is strongest (Harris, 1998). These two estimates show a trend of increasing rates of material movement as the parcels get closer to the NSC center, where they will presumably be transported upward in response to ice lens formation and frost-heave processes (Nicolsky et al., 2008). Therefore, under standard rates of movement, the surficial movement at the center of the NSC should be the fastest rates of subsurface movement, whereas the subduction process at the frost-boil edge may be the slowest movement in the process (Table 5.7).

No other studies have estimated the surface residence time of cryoturbated materials, but our analysis of ^{10}Be and Hg accumulation allowed us to provide primary, independent constraints on these time periods. The time periods estimated from these independent tracers are highly convergent for the parcel at CM 22-32 cm (313-1250 years (^{10}Be) and 238-952 years (Hg_{ex})), but the Hg_{ex} tracer results in ~ 2x longer estimates of residence time at IN 37-42 cm (425-1700 (^{10}Be) and 986 – 3940 (Hg_{ex})). The large difference in excess ^{10}Be and Hg inventory in CM and IN parcels suggests a non-continuous or stochastic mechanism of subduction that is congruent with previous hypotheses related to cryoturbative mechanisms in frost-boils and climatic triggers (Bockheim, 2007, Becher et al., 2013).

5.4.5. Unresolved questions.

Although our elemental and isotope tracer suite was able to produce primary, comprehensive constraints on the rates and patterns of cryoturbation in this particular NSC, many questions remain unresolved. Two specific questions of interest to the larger implications of the response of Arctic carbon to climate change are:

1. Is material subduction at the inner domain edge a continuous or stochastic process? Clear indications of stochasticity would include wide variations in ^{10}Be inventories along the direction of subducted material movement, but a more continuous sampling of subducted material such as that which could be achieved in gridded sampling would be necessary to fully evaluate this mechanism.
2. If material movement rates are different by an order of magnitude between the surface and subsurface, but upward movement rates near the top of the profile in the NSC center are similar to lateral creep rates, where is the additional volume of material coming? Our approach may be able to address this by clearly defining material provenance by the convergence of tracer distributions.
3. Do cryoturbation rates in NSCs vary consistently with climate? This could be evaluated by conducting similar analyses across climatic gradients and comparing the derived rates. NSCs end themselves particularly well for this type of study because they can be found throughout the Arctic in a wide variety of temperature and moisture regimes.

We suggest that detailed, gridded sampling of NSC cross-sections combined with detailed morphologies and application of a subset of this tracer suite could resolve many

of these questions in the future.

5.4.6. Conclusions

This study is the first to utilize a large, powerful suite of geochemical tracers to analyze patterns and rates of material movement in NSCs. Our results show that a subset of tracers in this suite (SOC, Hg, ^{13}C, ^{137}Cs, ^{210}Pb, ^{14}C and ^{10}Be) provide most of the inferred information and should be considered for use moving forward. By applying analytical and numerical models to our observed tracer distributions and inventories, we provide the first complete report of primary constraints on long-term NSC dynamics at a single site. We expect that this approach, when combined with detailed morphological and gridded sampling to better define small scale changes in distributions will be able to answer many of the remaining unresolved questions related to material movement and the climate sensitivity of equilibrium cell circulation in Arctic patterned ground.

Tracer	Primary Mechanism of Accumulation	Secondary Mechanisms of Accumulation	Mechanisms of loss or change	Significant Direct Anthropogenic Influence
Ca	Primary Minerals	Atmospheric - Seaspray	Leaching/Erosion	No
Mg	Primary Minerals	Atmospheric - Seaspray	Leaching/Erosion	No
K	Primary Minerals	Atmospheric - Seaspray	Leaching/Erosion	No
P	Primary Minerals	-	Leaching/Erosion	No
Na	Primary Minerals	Atmospheric - Seaspray	Leaching	No
C	Primary Production	-	Decomposition/Erosion	No
N	Primary Production	Atmospheric Deposition – Anthropogenic Nitrates	Denitrification/Leaching	Yes
S	Atmospheric Deposition – Natural and Anthro.	-	Leaching, Volatilization	Yes
Hg	Atmospheric Deposition – Natural and Anthro.	Primary Minerals	Volatilization	Yes
Cl	Atmospheric Deposition - Seaspray	-	Leaching	Yes
Pb	Atmospheric Deposition – Natural and Anthro	Primary Minerals	Leaching/Erosion	Yes

Isotope	Half-life (yrs)	Current Estimated Annual Accumulation Rate	Accumulation Type	Constraint type
^{10}Be	1.39×10^{6}	$0.1 – 0.8 \times 10^{6}$ atoms m^{-2} yr^{-1}	Continuous	Surface Residence Time
^{14}C	5,730	Dependent on Primary Production	Continuous/Pulse	Subsurface (Fig 5.1 #3)
^{137}Cs	30.08	0 Bq m^{-2} yr^{-1}	Pulse	Lateral Creep (Fig 5.1 #2)
^{210}Pb	22.20	40-100 Bq m^{-2} yr^{-1}	Continuous	Lateral Creep (Fig 5.1 #2)

Table 5.1. Isotope and elemental suite and tracer properties.

Location	Material Type	Depth (cm)	pH	Clay (%)	SOC (%)	$\delta^{13}C$ (‰)	^{14}C (f. Modern)	^{137}Cs (Bq kg^{-1})	$^{210}Pb_{ex}$ (Bq kg^{-1})	^{10}Be (10^7 atoms g^{-1})
Center (CM)	Mineral	0-2	5.4	14 ± 5	1.7 ± 0.19	-26.4 ± 0.20	-	0	38 ± 5.7	2.65 ± 0.09
	Mineral	2-7	5.4	-	0.6 ± 0.06	-25.2 ± 0.19	-	0	12 ± 1.7	-
	Mineral	7-15	5.2	20 ± 8	0.6 ± 0.06	-25.2 ± 0.19	-	0	12 ± 1.7	3.36 ± 0.11
	Mineral	15-22	5.1	16 ± 7	0.2 ± 0.02	-25.1 ± 0.19	-	0	0	-
	Mineral	22-32	5.2	16 ± 7	1.4 ± 0.15	-26.4 ± 0.20	0.7417 (2400)	0	0	7.01 ± 0.21
	Mineral	32-42	5.0	17 ± 8	0.6 ± 0.07	-25.7 ± 0.20	-	0	0	-
	Mineral	42-56	5.3	15 ± 7	0.2 ± 0.02	-25.0 ± 0.19	-	0	0	2.64 ± 0.08
Inner (IN)	Mineral	0-2	5.0	12 ± 6	1.9 ± 0.21	-25.8 ± 0.20	-	19 ± 1.1	33 ± 4.9	-
	Mineral	2-7	5.0	11 ± 5	0.6 ± 0.07	-24.9 ± 0.19	-	0	10 ± 1.4	2.07 ± 0.05
	Mineral	7-15	5.2	14 ± 6	0.6 ± 0.07	-24.3 ± 0.19	-	0	10 ± 1.4	-
	Mineral	15-22	5.2	15 ± 7	0.5 ± 0.06	-25.8 ± 0.20	-	0	14 ± 2.1	3.51 ± 0.08
	Mineral	22-32	5.0	13 ± 6	0.5 ± 0.06	-26.0 ± 0.20	-	0	0	-
	Mineral	32-37	4.8	5 ± 2	0.7 ± 0.08	-27.1 ± 0.20	-	0	0	4.01 ± 0.14
	Organic	37-42	4.0	-	8.4 ± 0.93	-26.7 ± 0.21	0.8040 (1960)	0	0	13.6 ± 0.17
	Mineral	42-59	4.9	13 ± 6	0.4 ± 0.04	-25.6 ± 0.20	-	0	0	3.04 ± 0.09
Mixing Transition (MT)	Organic	0-4	3.8	-	35.2 ± 3.91	-27.6 ± 0.21	-	26 ± 1.5	94 ± 14	5.80 ± 0.18
	Mineral	4-7	4.0	-	2.7 ± 0.30	-26.4 ± 0.20	-	48 ± 3.1	9 ± 1.4	4.69 ± 0.14
	Mineral	7-12	3.9	11 ± 5	2.7 ± 0.30	-26.0 ± 0.20	-	1.5 ± 1.0	9 ± 1.4	-
	Mineral	12-20	4.2	21 ± 9	2.3 ± 0.26	-26.5 ± 0.20	-	0	8 ± 1.3	5.07 ± 0.16
	Mineral	20-29	4.6	20 ± 9	1.1 ± 0.12	-26.1 ± 0.20	-	0	0	-
	Mineral	29-39	5.0	20 ± 9	0.6 ± 0.07	-26.7 ± 0.21	-	0	0	-
	Mineral	39-60	5.1	19 ± 9	0.6 ± 0.07	-25.6 ± 0.20	-	0	0	2.65 ± 0.08
	Mineral	60-71	5.2	19 ± 9	0.3 ± 0.03	-25.6 ± 0.20	-	0	0	-

Table 5.2. pH, texture and concentrations of isotopic markers by depth and location.

Location	Material Type	Depth (cm)	pH	Clay (%)	SOC (%)	$\delta^{13}C$ (‰)	^{14}C (f. Modern)	^{137}Cs (Bq kg^{-1})	$^{210}Pb_{ex}$ (Bq kg^{-1})	^{10}Be (10^7 atoms g^{-1})
Outer Domain 1 (OD1)	Organic	0-6	3.6	-	40.1 ± 4.44	-26.7 ± 0.21	-	105 ± 4.8	128 ± 19	6.69 ± 0.16
	Mineral	6-10	4.0	12 ± 5	5.1 ± 0.57	-25.9 ± 0.20	-	2 ± 0.7	14 ± 2	4.62 ± 0.13
	Mineral	10-20	4.0	13 ± 6	5.0 ± 0.56	-25.9 ± 0.20	-	0	7 ± 1	3.88 ± 0.08
	Mineral	20-30	4.4	15 ± 6	0.5 ± 0.06	-25.9 ± 0.20	-	0	0	-
	Mineral	30-40	4.7	13 ± 6	0.3 ± 0.04	-25.2 ± 0.19	-	0	0	2.98 ± 0.11
	Mineral	40-50	5.1	15 ± 7	0.3 ± 0.04	-25.5 ± 0.20	-	0	0	-
	Mineral	50-71	5.2	14 ± 6	0.3 ± 0.03	-25.8 ± 0.20	-	0	0	2.86 ± 0.07
Outer Domain 2 (OD2)	Organic	0-8	3.6	-	41.8 ± 4.63	-27.4 ± 0.21	-	16 ± 4.5	311 ± 47	2.90 ± 0.09
	Mineral	8-15	3.5	12 ± 5	13.2 ± 1.46	-26.1 ± 0.20	-	108 ± 6.3	6 ± 1	0.70 ± 0.02
	Mineral	15-30	4.3	25 ± 11	0.7 ± 0.07	-26.5 ± 0.20	-	69 ± 5.0	0	4.56 ± 0.09
	Mineral	30-40	5.3	-	0.4 ± 0.05	-25.7 ± 0.20	-	74 ± 2.5	0	2.10 ± 0.05
	Mineral	40-50	5.0	11 ± 5	0.2 ± 0.02	-25.8 ± 0.20	-	4 ± 1	0	-
	Mineral	50-60	5.1	13 ± 6	0.2 ± 0.02	-25.6 ± 0.20	-	0	0	4.39 ± 0.11
	Mineral	60-70	5.1	14 ± 6	0.8 ± 0.08	-25.6 ± 0.20	-	0	0	4.39 ± 0.11
	Mineral	70-81	5.1	14 ± 6	0.3 ± 0.03	-25.6 ± 0.20	-	0	0	-

Table 5.2 (Cont). pH, texture and concentrations of isotopic markers by depth and location.

Location	Depth (cm)	Na (ppm)	Mg (ppm)	K (ppm)	Ca (ppm)	P (ppm)	S (ppm)	Cl (ppm)	Pb (ppm)	Hg_{ex} (ng g^{-1})
Center (CM)	0-2	7100 ± 120	13722 ± 247	12850 ± 160	11448 ± 250	646 ± 39	400 ± 120	238 ± 12	11 ± 1	24 ± 0.9
	2-15	8900 ± 150	11723 ± 211	11269 ± 141	16538 ± 361	671 ± 41	100 ± 30	125 ± 6	16 ± 2	0 ± 0
	15-22	8600 ± 140	13570 ± 244	12119 ± 152	15485 ± 338	597 ± 36	100 ± 30	132 ± 7	14 ± 1	0.94 ± 0.03
	22-32	7600 ± 120	13377 ± 240	12111 ± 151	11763 ± 257	555 ± 34	300 ± 90	160 ± 8	9 ± 1	6.8 ± 0.3
	32-42	7800 ± 130	14001 ± 252	13077 ± 164	13548 ± 296	547 ± 33	200 ± 60	143 ± 7	9 ± 1	0 ± 0
	42-56	8700 ± 140	13281 ± 239	12140 ± 152	16480 ± 360	682 ± 41	100 ± 90	128 ± 6	12 ± 1	0.03 ± 0.01
Inner (IN)	0-2	7287 ± 119	12265 ± 221	11366 ± 142	13443 ± 293	735 ± 45	400 ± 120	210 ± 10	9 ± 1	15 ± 0.6
	2-15	8018 ± 131	13640 ± 242	12289 ± 154	15473 ± 338	666 ± 40	200 ± 60	133 ± 7	11 ± 1	1.37 ± 0.05
	15-22	8292 ± 135	12362 ± 223	12117 ± 152	15077 ± 329	626 ± 38	100 ± 30	135 ± 7	10 ± 1	0 ± 0
	22-32	7607 ± 124	13630 ± 245	12396 ± 155	12738 ± 278	535 ± 33	200 ± 60	146 ± 7	11 ± 1	4.9 ± 0.2
	32-37	7526 ± 123	12110 ± 218	11831 ± 148	12066 ± 263	679 ± 41	300 ± 90	170 ± 9	10 ± 1	12.6 ± 0.5
	37-42	5309 ± 87	6014 ± 108	8615 ± 108	8336 ± 182	1566 ± 95	1100 ± 340	203 ± 10	11 ± 1	56 ± 2
	42-59	8771 ± 143	12022 ± 216	11231 ± 140	16038 ± 350	650 ± 40	200 ± 60	169 ± 8	10 ± 1	2 ± 0.08
Mixing Trans. (MT)	0-4	4759 ± 78	5386 ± 97	8623 ± 108	9204 ± 201	1153 ± 70	1200 ± 370	206 ± 10	27 ± 3	176 ± 7
	4-12	6836 ± 111	13519 ± 243	12309 ± 154	11537 ± 252	658 ± 40	400 ± 120	185 ± 9	9 ± 1	20.4 ± 0.8
	12-20	8227 ± 134	11535 ± 207	11303 ± 141	14199 ± 310	593 ± 36	300 ± 90	152 ± 8	8 ± 1	6.9 ± 0.3
	20-29	8130 ± 132	13139 ± 236	12288 ± 154	14404 ± 314	589 ± 36	200 ± 60	137 ± 7	11 ± 1	3.1 ± 0.1
	29-60	7612 ± 124	12770 ± 230	12756 ± 160	12578 ± 274	544 ± 33	200 ± 60	146 ± 7	9 ± 1	5.3 ± 0.2
	60-71	8485 ± 138	13155 ± 237	11970 ± 150	16629 ± 363	712 ± 43	100 ± 30	138 ± 7	10 ± 1	0.70 ± 0.03
Outer Dom. 1 (OD1)	0-6	1588 ± 26	2686 ± 48	4267 ± 53	7766 ± 169	1115 ± 68	2200 ± 670	325 ± 16	41 ± 4	240 ± 9
	6-10	6265 ± 102	8713 ± 157	9639 ± 121	10209 ± 223	940 ± 57	800 ± 240	178 ± 9	11 ± 1	54 ± 2
	10-20	8771 ± 143	12080 ± 217	11034 ± 138	16667 ± 364	622 ± 38	100 ± 30	132 ± 7	9 ± 1	3.1 ± 0.1
	20-30	8631 ± 141	12363 ± 223	11228 ± 140	16659 ± 364	623 ± 38	100 ± 30	127 ± 6	11 ± 1	1.67 ± 0.06
	30-40	8890 ± 139	12119 ± 218	11696 ± 146	16360 ± 357	647 ± 39	100 ± 30	131 ± 7	8 ± 1	0.13 ± 0.01
	40-50	8497 ± 139	13128 ± 236	12003 ± 150	16258 ± 355	623 ± 38	100 ± 30	132 ± 7	9 ± 1	0.33 ± 0.01
	50-71	8442 ± 138	13815 ± 249	12121 ± 152	16682 ± 364	662 ± 40	100 ± 30	136 ± 7	10 ± 1	0.04 ± 0.01

Table 5.3. Elemental concentrations by depth and location.

Location	Depth (cm)	Na (ppm)	Mg (ppm)	K (ppm)	Ca (ppm)	P (ppm)	S (ppm)	Cl (ppm)	Pb (ppm)	Hg_{ex} (ng g^{-1})
Outer Dom. 2 (OD2)	0-8	1443 ± 24	2373 ± 43	4266 ± 53	9043 ± 197	1511 ± 92	2500 ± 770	359 ± 18	47 ± 5	355 ± 14
	8-15	4991 ± 81	4668 ± 84	7881 ± 99	7928 ± 173	1100 ± 67	1200 ± 370	219 ± 11	18 ± 2	112 ± 4
	15-30	7649 ± 125	11287 ± 203	11340 ± 142	14414 ± 315	644 ± 39	300 ± 90	144 ± 7	10 ± 1	11.2 ± 0.4
	30-40	9023 ± 147	12052 ± 217	11113 ± 139	17295 ± 377	671 ± 41	100 ± 30	125 ± 6	8 ± 1	2.7 ± 0.1
	40-60	8530 ± 139	12072 ± 217	10960 ± 137	16783 ± 366	705 ± 43	100 ± 30	129 ± 6	8 ± 1	0 ± 0
	60-70	8341 ± 136	12604 ± 227	11579 ± 145	16247 ± 355	651 ± 40	100 ± 30	130 ± 6	10 ± 1	0.67 ± 0.02
	70 - 81	8050 ± 131	14716 ± 265	12534 ± 157	15851 ± 345	612 ± 37	100 ± 30	148 ± 7	12 ± 1	0.33 ± 0.01

Table 5.3 (Cont). Elemental concentrations by depth and location.

	SOC	TN	Na	K	Ca	Mg	S	Cl	Hg_{ex}
SOC	1								
TN	**0.75**	1							
Na	**-0.57**	**-0.54**	1						
K	-0.22	-0.21	-0.05	1					
Ca	**-0.62**	**-0.58**	**0.76**	-0.06	1				
Mg	-0.33	-0.32	0.06	**0.71**	0.13	1			
S	**0.76**	**0.70**	**-0.79**	-0.11	-0.80	-0.27	1		
Cl	**0.51**	**0.49**	**-0.75**	-0.01	**-0.71**	-0.08	**0.78**	1	
Hg_{ex}	**0.67**	**0.63**	**-0.64**	-0.16	**-0.68**	-0.27	**0.81**	**0.67**	1

Table 5.4. Tracer correlation matrix – Kendall's tau-b w/ Bonferroni correction for multiple comparisons. Numbers in bold are significant to an alpha < 0.05.

Location	SOC kg m^{-2}	TN kg m^{-2}	Na kg m^{-2}	Mg kg m^{-2}	K kg m^{-2}	Ca kg m^{-2}	S g m^{-2}	P g m^{-2}	Cl g m^{-2}	Pb g m^{-2}	Hg_{ex} mg m^{-2}	^{137}Cs Bq m^{-2}	$^{210}Pb_{ex}$ Bq m^{-2}	$^{10}Be_{met}$ (10^{13} atoms g^{-1})
CM	2.6 ± 0.5	0.11 ± 0.02	3.6 ± 0.6	5.7 ± 0.9	5.3 ± 0.8	6.5 ± 1.0	69 ± 11	271 ± 93	61 ± 10	5 ± 1	0.9 ± 0.1	0 ± 0	1840 ± 331	1.71 ± 0.26
IN	5.3 ± 1.0	0.44 ± 0.08	3.6 ± 0.5	5.5 ± 0.8	5.3 ± 0.8	6.5 ± 1.0	122 ± 42	321 ± 52	71 ± 11	5 ± 1	3.4 ± 0.5	405 ± 65	2499 ± 450	1.76 ± 0.27
MT	13.4 ± 2.5	0.83 ± 0.15	4.1 ± 0.6	6.6 ± 1.0	6.5 ± 1.0	7.1 ± 1.1	141 ± 48	329 ± 53	81 ± 13	5 ± 1	7.0 ± 1.1	1739 ± 322	3262 ± 588	2.06 ± 0.31
OD1	10.9 ± 2.0	0.51 ± 0.10	4.4 ± 0.7	6.6 ± 1.0	6.1 ± 0.9	8.5 ± 1.3	94 ± 32	352 ± 57	74 ± 11	5 ± 1	4.5 ± 0.7	1169 ± 189	2284 ± 411	1.81 ± 0.28
OD2	12.6 ± 2.4	0.54 ± 0.10	4.3 ± 0.6	6.3 ± 1.0	6.0 ± 0.9	8.3 ± 1.3	153 ± 52	388 ± 63	80 ± 13	6 ± 1	11 ± 1.6	1625 ± 270	4064 ± 798	1.79 ± 0.27

Table 5.5. Profile integrated inventories by location.

Marker	Movement Type	Model	Location	Fallout Rate ($Bq\ cm^{-2}\ yr$)	Inventory Difference ($Bq\ m^{-2}$)	Apparent Rate ($cm\ yr^{-1}$)
$^{210}Pb_{ex}$	Surficial	Analytical (Klaminder et al., 2014)	CM – IN	101 ± 14	659 ± 559	2.55 ± 0.4
			IN – MT		763 ± 740	0 ± 2.6
		Numerical (This study)	CM – IN	101 ± 14	659 ± 559	0 – 1.0
			IN – MT		763 ± 740	0 – 0.1

Marker	Movement Type	Model	Location	Original Inventory ($Bq\ m^{-2}$)	Inventory Difference ($Bq\ m^{-2}$)	Apparent Rate ($cm\ yr^{-1}$)
^{137}Cs	Surficial	Numerical	CM – IN	4306 ± 508	405 ± 65	1.1 – 1.3
			IN – MT		1334 ± 328	0 – 0.2

Marker	Movement Type	Model	Location	Path Length (cm)	Difference 95% 2 sigma age (yr)	Apparent Rate ($cm\ yr^{-1}$)
^{14}C	Subsurface	Linear Minimum Path	MT – IN	88	1860 – 1990	0.04 – 0.05
			IN – CM	84	360 – 820	0.10 – 0.23
		Linear Maximum Path	MT – IN	117	1860 – 1990	0.06 – 0.06
			IN – CM	96	360 – 820	0.12 – 0.27

Marker	Movement Type	Model	Location	Fallout Rates (10^6 atms $cm^{-2}\ yr^{-1}$)	Parcel Inventory (excess atoms cm^{-2})	Maximum Exposure Years
$^{10}Be_{met}$	Parcel Surface Residence Time	Atmospheric Accumulation	IN 38 – 42 cm	0.8 (Ebert et al. 2012) 0.35 (Finkel et al. 1997) 0.2 (This study)	$3.4 \pm 0.7 \times 10^8$	425 ± 87 971 ± 200 1700 ± 350
			CM 22 – 32cm	0.8 (Ebert et al. 2012) 0.35 (Finkel et al. 1997) 0.2 (This study)	$2.5 \pm 0.8 \times 10^8$	313 ± 100 714 ± 229 1250 ± 400

Table 5.6. Material movement rates and types inferred for various models and locations.

Marker	Movement Type	Model	Location	Deposition Rate ($mg\ m^{-2}\ yr^{-1}$)	Parcel Inventory ($Hg_{ex}\ mg\ m^{-2}$)	Maximum Exposure Years
Hg_{ex}	Parcel Surface Residence Time	Atmospheric Accumulation	IN	0.002 (Munthe et al, 2007)	1.97 ± 0.30	986 ± 148
			38 – 42 cm	0.001 (Bindler, 2003)		1970 ± 296
				0.0005 (Bindler, 2003)		3940 ± 591
			CM	0.002 (Munthe et al, 2007)	0.48 ± 0.07	238 ± 35
			22 – 32cm	0.001 (Bindler, 2003)		476 ± 71
				0.0005 (Bindler, 2003)		952 ± 143

Table 5.6 (Cont). Material movement rates and types inferred for various models and locations.

Movement Type	Method	Apparent Rates	Reference
Center Upward (Fig 1, #1)	^{210}Pb	0.2 – 0.7 cm yr-1	Klaminder et al., 2014
	Telescoping Probes	0.4 – 1.2 cm yr-1	Harris, 1998
	Tube Intrusion	0 – 1.5 cm yr-1	Egginton and Shilts, 1978
Surficial Lateral Creep (Fig 1, #2)	Laser Altimetry	0.3 – 2.0 cm yr-1	Kaab et al., 2013
	Physical Tags	< 1.0 – 3.0 cm yr-1	Sawyer, 2007
	Physical Tags	0 – 3.8 cm yr-1	Egginton and Shilts, 1978
	^{210}Pb	3.1 – 4.5 cm yr-1	Klaminder et al., 2014
	^{137}Cs	0 – 1.3 cm yr-1	*This study*
	^{210}Pb	0 – 2.55 cm yr-1	*This study*
Subduction and Subsurface (Fig 1, #3)	^{210}Pb – ^{14}C	0.01 – 0.012 cm yr-1	Becher et al., 2013
	^{14}C	0.03 – 0.1 cm yr-1	Dyke and Zoltai, 1980
	^{210}Pb	0.3 – 1.2 cm yr-1	Klaminder et al., 2014
	Telescoping Probes	0.8 – 1.2 cm yr-1	Harris, 1998
	^{14}C	0.04 – 0.27 cm yr-1	*This study*
Parcel Surface Residence Time (Fig 1, Inner/Outer Transition)	$^{10}Be_{met}$	313 – 1700 yr	*This study*
	Hg_{ex}	238 – 3940 yr	*This study*

Table 5.7. Compilation of rate estimates in non-sorted circles for 4 movement types across studies using different tracers.

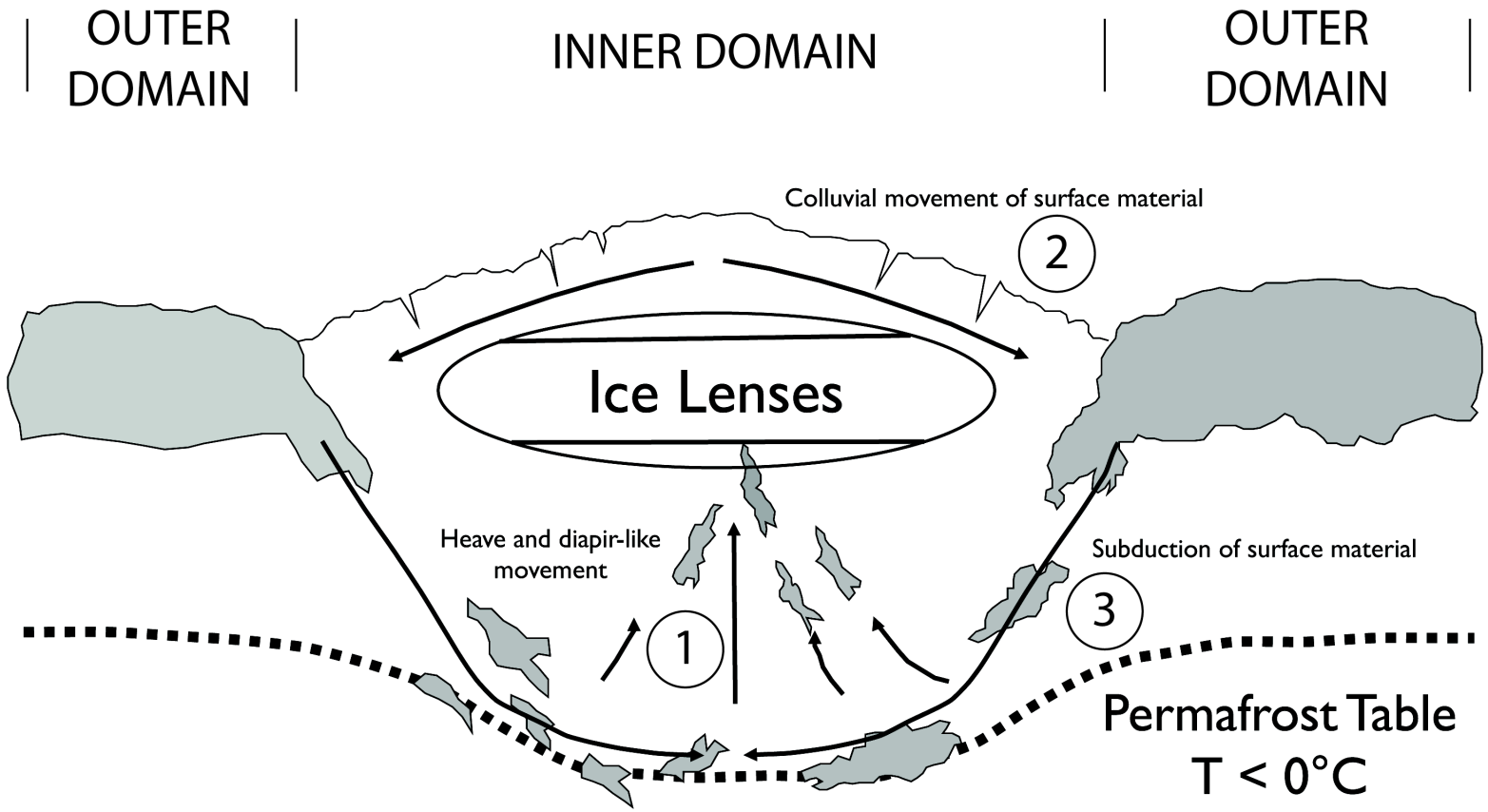

Figure 5.1. Idealized depiction of frost-boil (non-sorted circle), showing spatial relationship of organic (grey) and mineral (white) materials, permafrost table, domain terminology, physical movement processes, and hypothesized directions of soil movement. Adapted from Nicolsky et al. (2008).

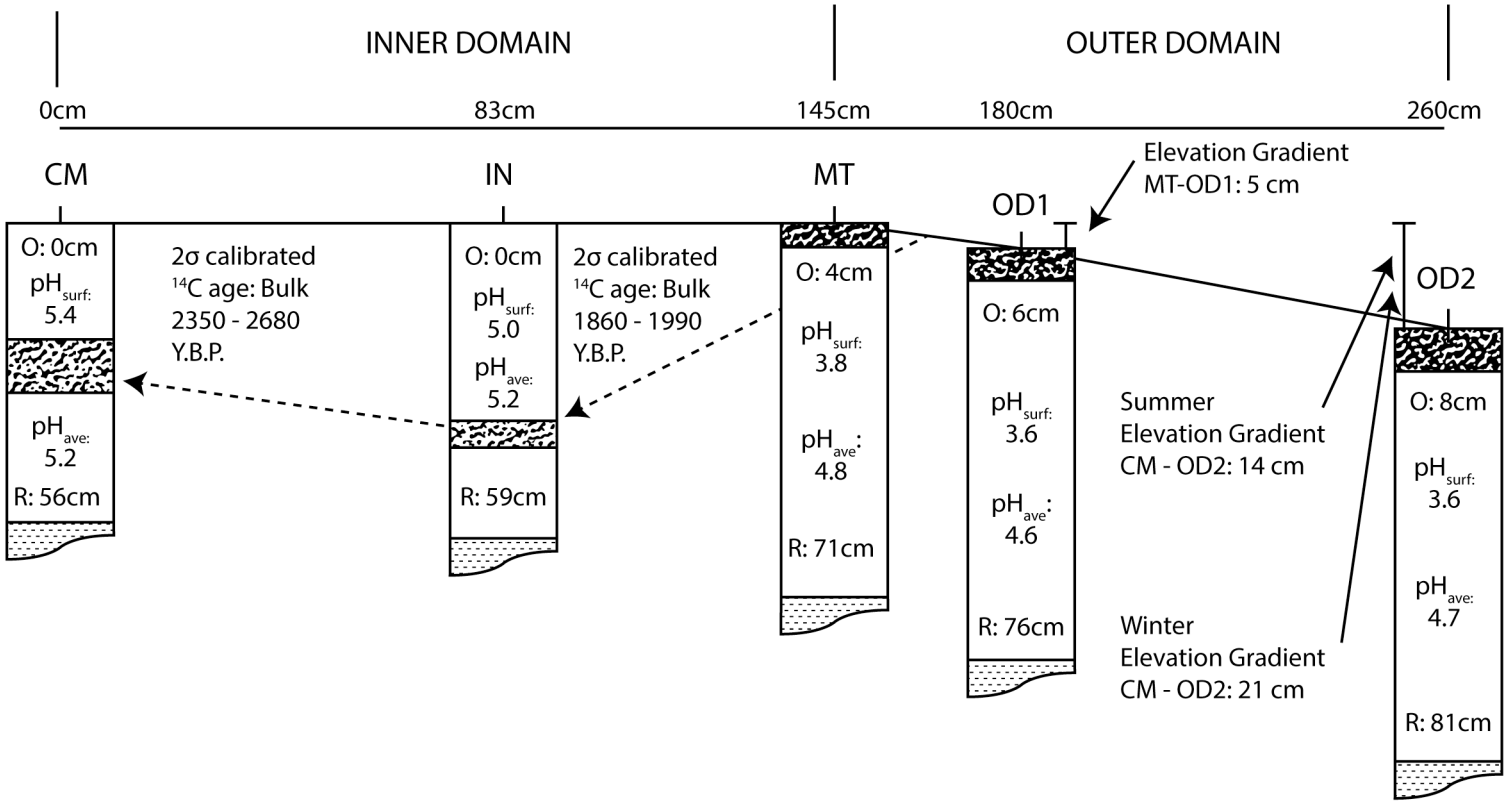

Figure 5.2. Morphology, environmental characteristics, and hypothesized direction of subsurface inner domain material movement (dashed arrows), Abisko, SE non-sorted circle. O = organic layer thickness, R = depth to bedrock.

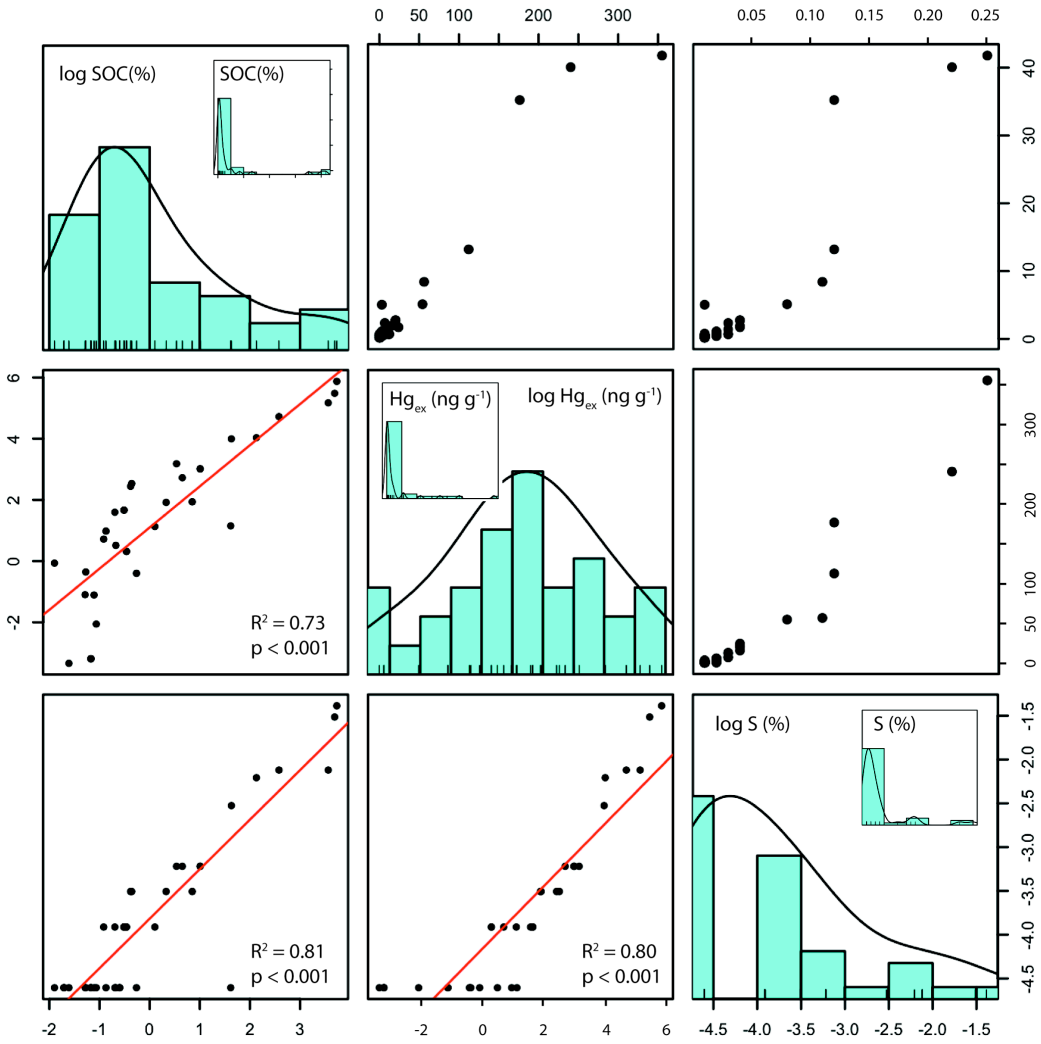

Figure 5.3. Relationships between soil organic carbon (SOC), Hg, and S for all samples, Abisko, SE non-sorted circle. Boxes below diagonal show log-log relationships, boxes above diagonal show untransformed relationships. Diagonal boxes show untransformed variable distributions (inset) and transformed variable distributions.

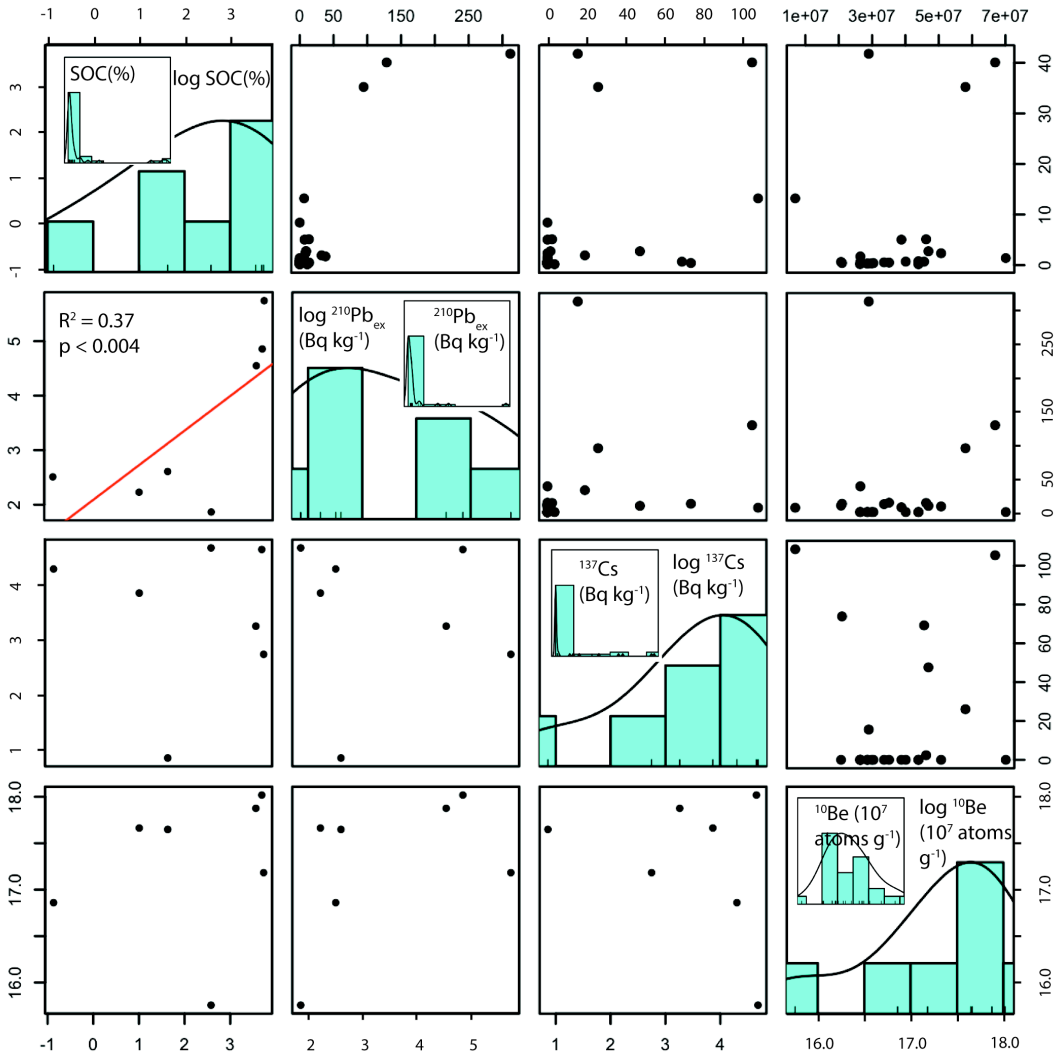

Figure 5.4. Relationships between soil organic carbon (SOC), $^{210}Pb_{ex}$, ^{137}Cs, and ^{10}Be for all samples, Abisko, SE non-sorted circle. Boxes below diagonal show log-log relationships, boxes above diagonal show untransformed relationships. Diagonal boxes show untransformed variable distributions (inset) and transformed variable distributions.

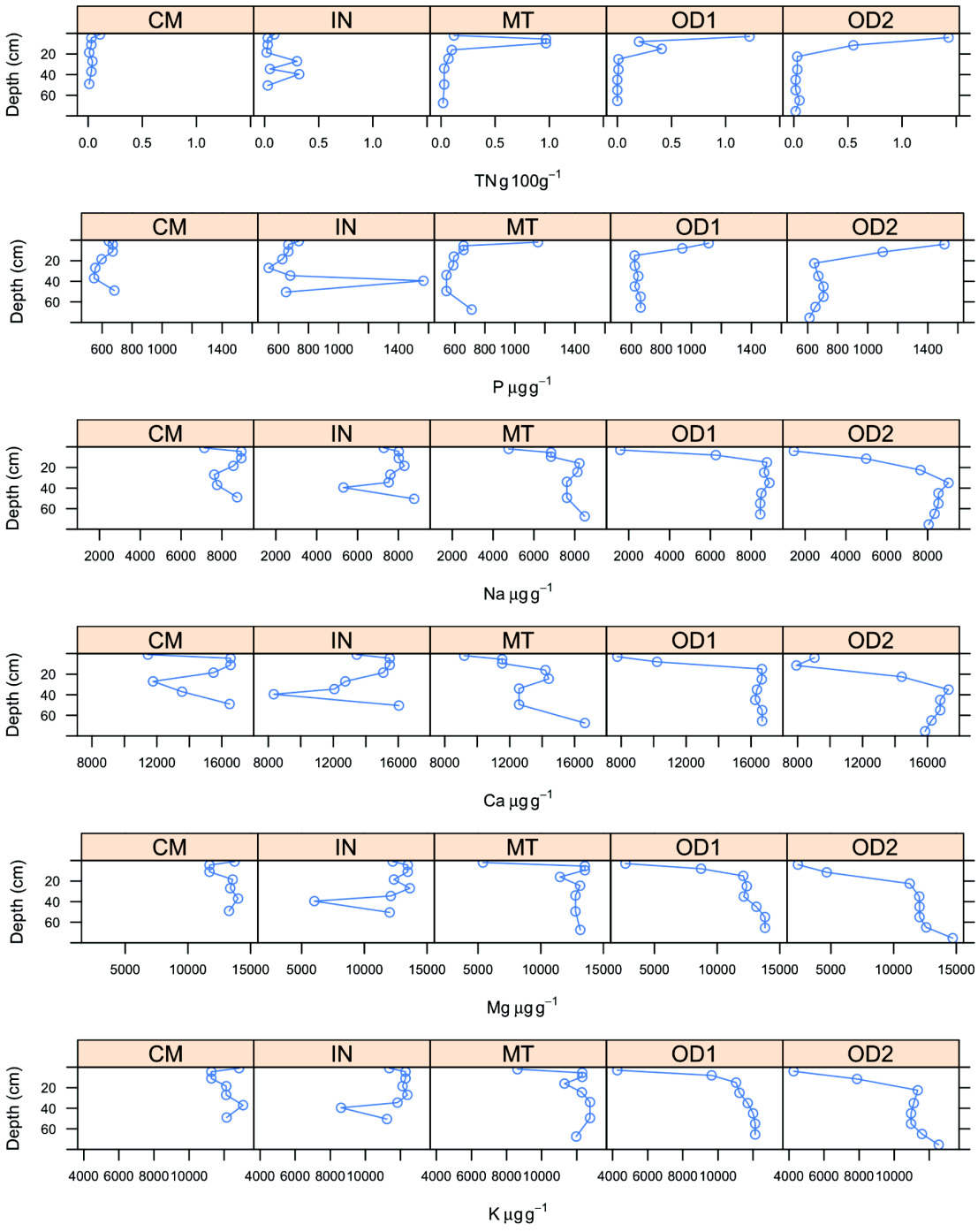

Figure 5.5. Profile depth distributions for total nitrogen (TN), phosphorous (P), sodium (Na), calcium (Ca), magnesium (Mg) and potassium (K).

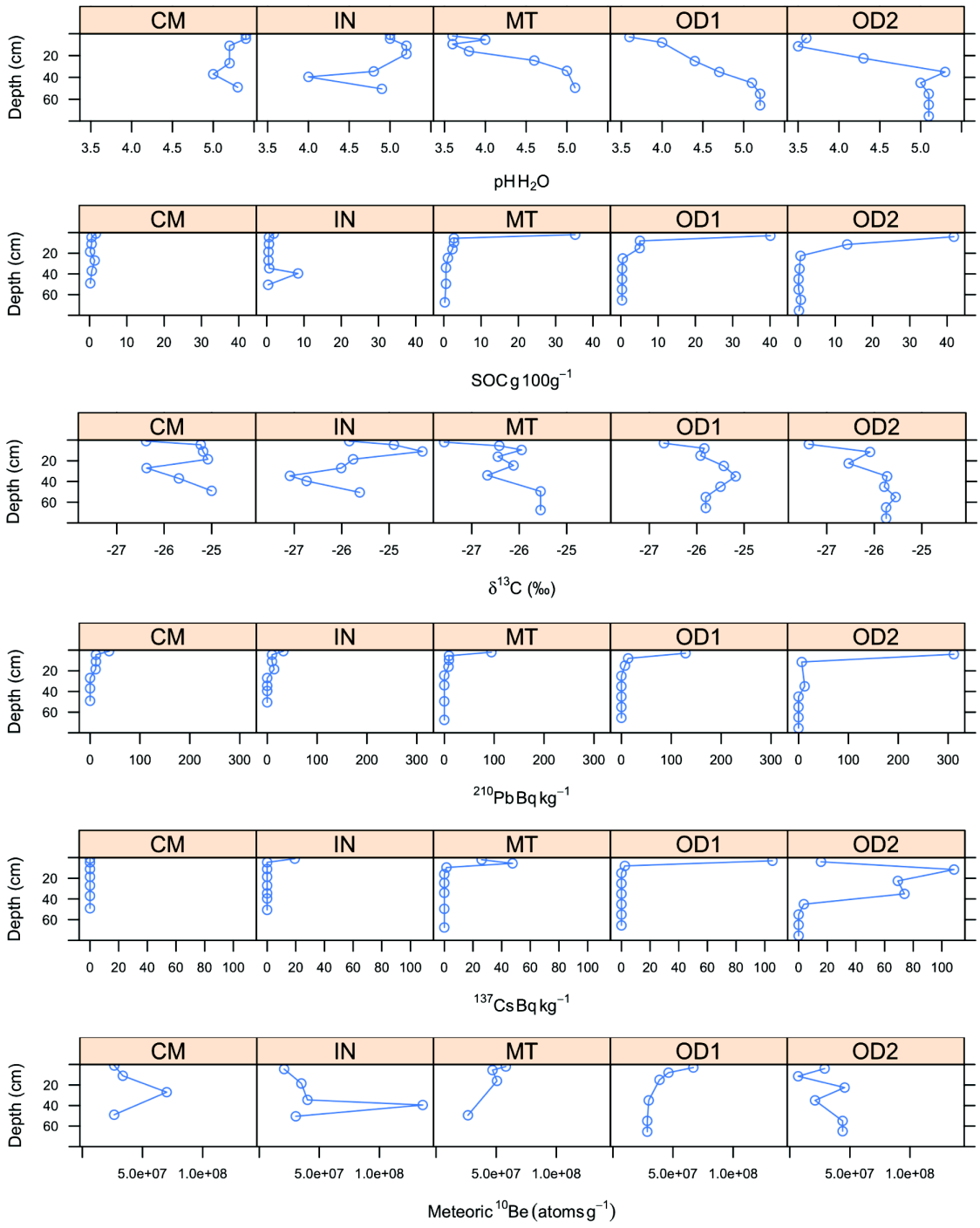

Figure 5.6. Profile depth distributions for pH, soil organic carbon (SOC), $\delta^{13}C$, lead-210 (^{210}Pb), cesium-137 (^{137}Cs), and meteoric beryllium-10 (^{10}Be).

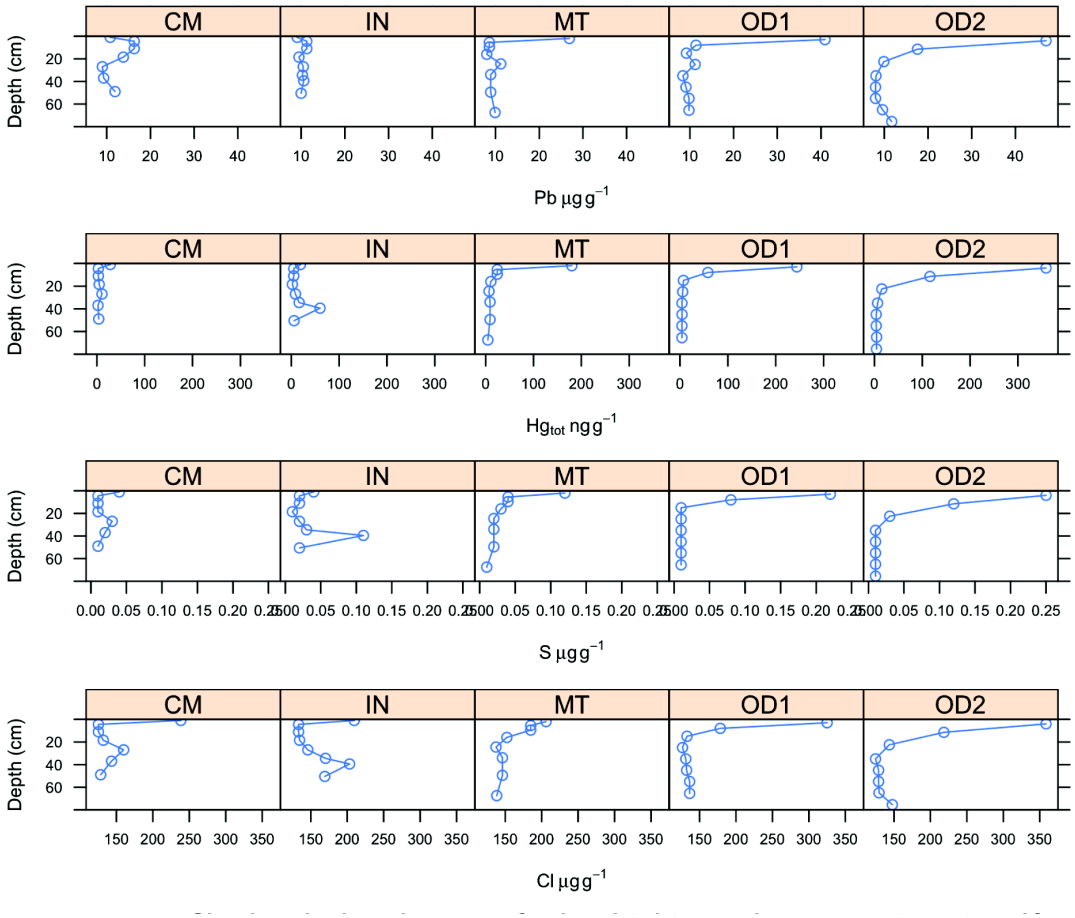

Figure 5.7. Profile depth distributions for lead (Pb), mercury (Hg), sulfur (S) and chlorine (Cl).

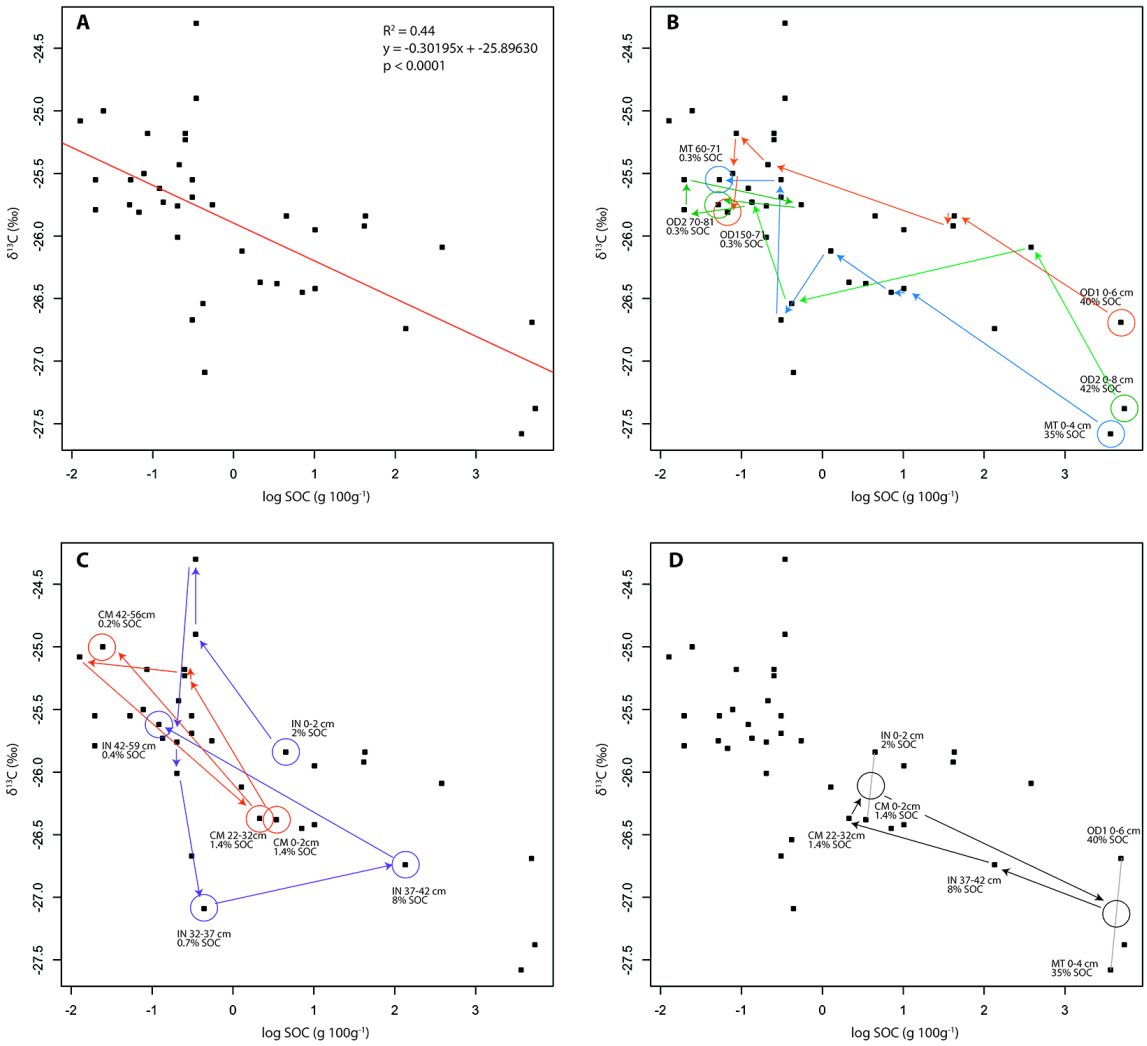

Figure 5.8. (A) Relationship between $\delta^{13}C$ and soil organic carbon (SOC, log normalized) for all samples. (B) Down-profile trajectories of $\delta^{13}C$ and SOC for non-cryoturbated sampling locations (MT, OD1 and OD2). (C) Down-profile trajectories of $\delta^{13}C$ and SOC for cryoturbated sampling locations (CM and IN). (D) Trajectories of $\delta^{13}C$ and SOC for hypothesized direction of subsurface movement and surficial return.

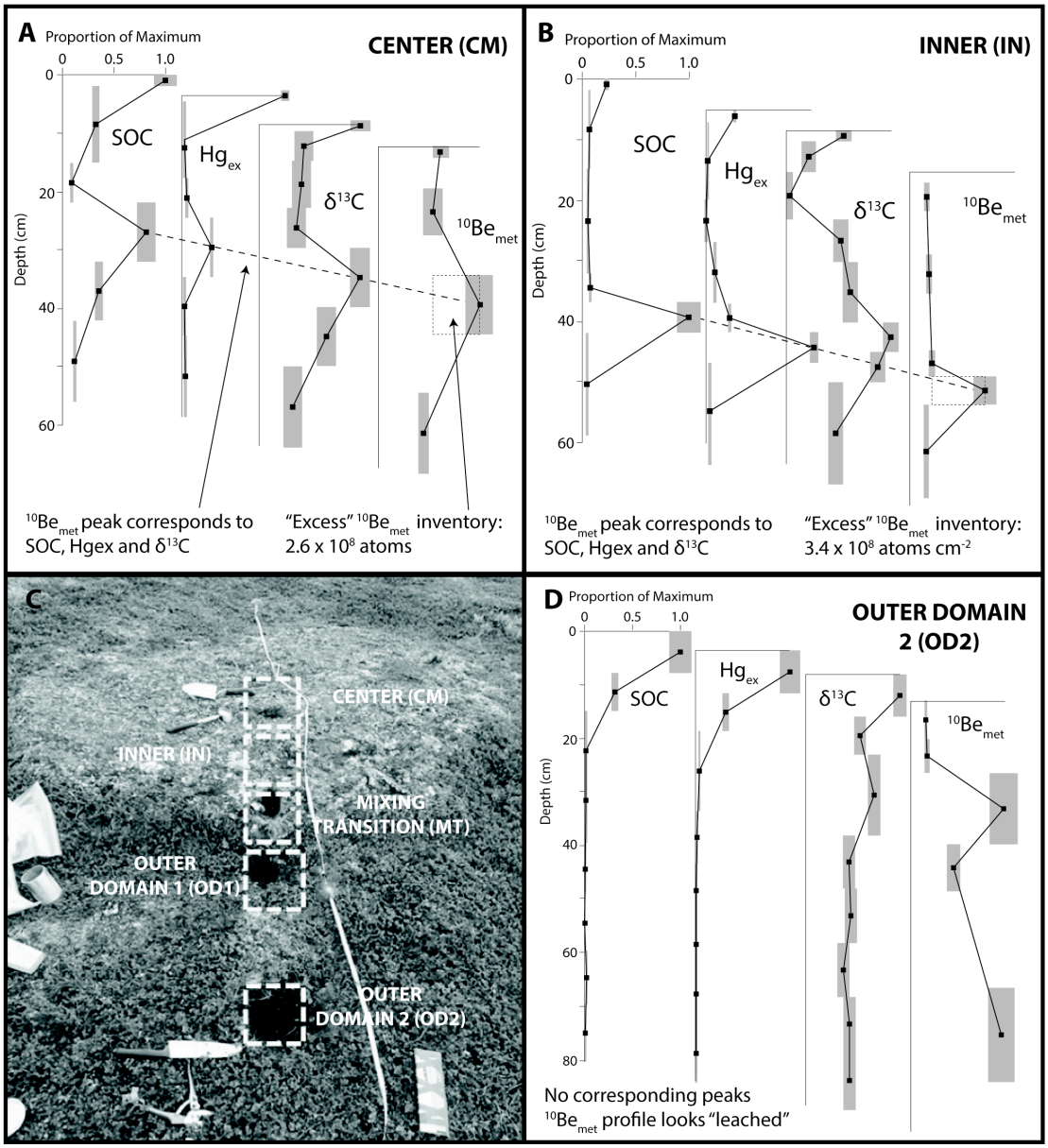

Figure 5.9. Normalized (to profile maximum) soil organic carbon (SOC), Hg_{ex}, $\delta^{13}C$ and ^{10}Be concentrations for selected sampling points across Abisko, SE non-sorted circle. Center (CM) and Inner Domain (IN) sampling points (panels A and B, respectively) show convergence of tracer peaks indicating subducted material, while Outer Domain 2 (OD2 – panel D), shows no subsurface peak convergence and apparent leaching of ^{10}Be. Picture in panel C is adapted from Kalminder et al. (2012).

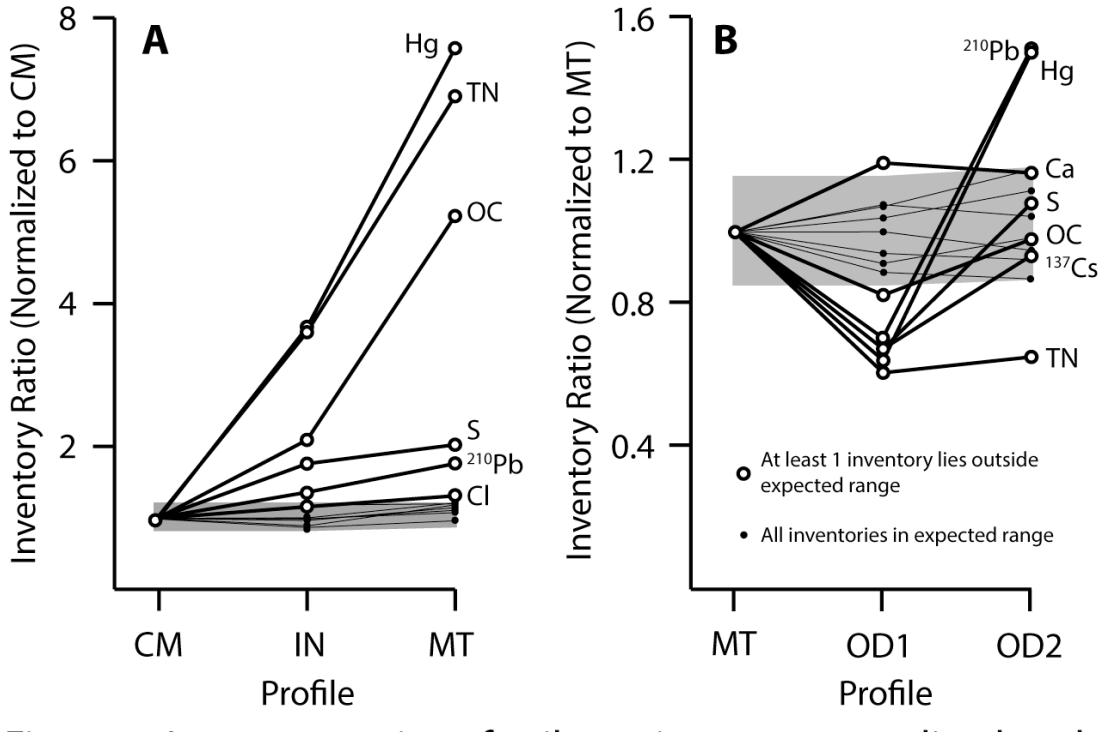

Figure 5.10. Inventory ratios of soil constituents normalized to the respective inventory of profile CM (panel A) and MT (panel B). Shaded regions represent 1-sigma variation in cumulative profile mass, so that constituents with variability outside of the shaded region are interpreted as having inventories that are significantly different due to concentrations of constituents and not due to differences in cumulative profile mass alone. Labelled constiuents with open circles have at least one sampling point that is outside of the expected range due to cumulative mass alone, while those with closed circles (unlabeled) have no sampling points that lie outside of the 1-sigma expected range

Bibliography

Aikins, S.H.M., J.J. Afuakwa. 2012. Effect of four different tillage practices on soil physical properties under cowpea. Agriculture and Biology Journal of North America. 3(1): 17-24.

Alewell, C., R. Giesler, J. Klaminder, J. Leifield, M. Rollog. 2011. Stable carbon isotopes as indicators for environmental change in palsa peats. Biogeosciences 8: 1769-1778.

Alexander, E.B. 1985. Rates of soil formation from bedrock or consolidated sediments. Physical Geography 6(1): 25-42.

Alexander, E.B. 1988. Rates of soil formation: Implications for soil-loss tolerance. Soil Science 145(1): 37-45.

Andraski, B.J., B. Lowery. 1992. Erosion effects on soil water storage, plant water uptake, and corn growth. Soil Science Society of America Journal 56:1911 – 1919.

Aoyama, M., K. Hirose, and Y. Igarashi. 2006. Re-construction and updating our understanding on the global weapons tests ^{137}Cs fallout. Journal of Environmental Monitoring 8: 431-438.

Appleby, P.G., and F. Oldfield. 1992. Application of lead-210 to sedimentation studies. In: Ivanovich, M. and R.S. Harmon (Eds.), Uranium-Series Disequilibria; Applications to Earth, Marine and Environmental Sciences. 2nd Ed. Clarendon, Oxford, UK.

Bacon, A.R., D.deB. Richter, P.R. Bierman, and D.H. Rood. 2012. Coupling meteoric 10Be with pedogenic losses of ^{9}Be to improve soil residence time estimates on an ancient North American interfluve. Geology published online 29 June 2012; doi: 10.1130/G33449.1.

Bakker, M.M., G. Govers, M.D.A. Rounsevell. 2004. The crop productivity-erosion relationship: an analysis based on experimental work. Catena 57: 55-76.

Ballantyne, Colin K. 1996. Formation of miniature sorted patterns by shallow ground freezing: A field experiment. *Permafrost and Periglacial Processes* 7, no. 4: 406- 24.

Balco, G.A. 2004. The sedimentary record of subglacial erosion beneath the Laurentide Ice Sheet. Ph.D. Dissertation, University of Washington.

Barrie, L.A., D. Gregor, B. Hargrave, R. Lake, D. Muir, R. Shearer, B. Tracey, T. Bidleman. 1992. Arctic contaminants: sources, occurrence and pathways. The Science of the Total Environment 122: 1-74.

Barsdate, R.J., V. Alexander. 1975. The nitrogen balance of Arctic tundra: Pathways, rates and environmental implications. Journal of Environmental Quality 4(1): 111-117.

Beaudette, D.E., P. Roudier, A.T. O'Geen. 2013. Algorithms for quantitative pedology: A toolkit for soil scientists. Computers and Geosciences 52: 258-268.

Becher, M., C. Olid and J. Klaminder. 2013. Buried soil organic inclusions in non-sorted circles fields in northern Sweden: Age and Paleoclimatic context. Journal of Geophysical Research: Biogeosciences 118: 104-111.

Belmont, P., K.B. Gran, S.P. Schottler, P.R. Wilcock, S.S. Day, C. Jennings, J.W. Lauer, E. Viparelli, J.K. Willenbring, D.R. Engstrom, and G. Parker. 2011. Large shift in source of fine sediment in the upper Mississippi river. Environmental Science and Technology 45: 8804-8810.

Benassai, S., S. Becagli, R. Gragnani, O. Magand, M. Proposito, I. Fattori, R. Traversi, R. Udisti. 2005. Sea-spray deposition in Antarctic coastal and plateau areas from ITASE traverses. Annals of Glaciology 41: 32-40.

Bennett, H.H. 1939. Soil Conservation. McGraw-Hill Book Co., New York.

Bilzi, A.F. and E.J. Ciolkosz. 1977a. A field morphology rating scale for evaluating pedological development. Soil Science 124(1): 45-48.

Biasi, C., O. Rusalimova, H. Meyer, C. Kaiser, W. Wanek, P. Barsukov, H. Junger, A Richter. 2005. Temperature-dependent shift from labile to recalcitrant carbon sources of arctic heterotrophs. Rapid Communications in Mass Spectrometry 19: 1401 - 1408.

Bierman, P.R., L.B. Corbett, J.A. Graly, T.A. Neumann, A. Lini, B.T. Crosby, D. H. Rood. 2014. Preservation of a preglacial landscape under the center of the Greenland ice sheet. Science 344(6182): 402-405.

Bilzi, A.F. and E.J. Ciolkosz. 1977b. Time as a factor in the genesis of soils developed in recent alluvium. Soil Science Society of America Journal 41: 122-127.

Bindler, R. 2003. Estimating the natural background atmospheric deposition rate of mercury utilizing ombrotrophic bogs in southern Sweden. Environmental Science and Technology 37: 40-46.

Bindler, R., I. Renberg, J. Klaminder. 2008. Bridging the gap between ancient metal pollution and contemporary biogeochemistry. Journal of Paleolimnology 40: 755-770.

Blanco-Canqui, H. and R. Lal. 2008. Principles of Soil Conservation and Management. Springer. New York, NY. 616 pp.

Bockheim, J.G., C. Tarnocai, J.M. Kimble, C.A.S. Smith. 1997. The concept of gelic materials in the new gelisol order for permafrost-affected soils. Soil Science 162(12): 927-939.

Bockheim, J.G. 2007. Importance of cryoturbation in redistributing organic carbon in permafrost-affected soils. Soil Science Society of America Journal 71(1): 1335-1342.

Bockheim, J.G., and K.M. Hinkel. 2007. The importance of "deep" organic carbon in permafrost-affected soil of Arctic Alaska. Soil Science Society of America Journal 71(6): 1889-1892.

Borldeleau, L.M., D. Prevost. 1994. Nodulation and nitrogen fixation in extreme environments. Plant and Soil 161: 115-125.

Bui, E.N., G.J. Hancock, S.N. Wilkinson. 2011. 'Tolerable' hillslope soil erosion rates in Australia: Linking science and policy. Agriculture, Ecosystems and Environment 144: 136-149.

Chesworth, W. 2008. Encyclopedia of Soil Science. Springer, Inc. New York, NY.

Chmeleff, J., F. vonBlanckenburg, K. Kossert, and D. Jakob. 2010. Determination of the 10Be half-life by multicollector ICP-MS and liquid scintillation counting. - Nuclear Instruments and Methods in Physics Research / B, 263, 2, 192-199.

Christensen, T.R., T. Johansson, M. Olsrud, L. Strom, A. Lindroth, M. Mastepanov, N. Malmer, T. Friborg, P. Crill and T.V. Callaghan. 2007. A catchment-scale carbon and greenhouse gas budget of a subarctic landscape. Philisophical Transactions of the Royal Society A 365: 1643-1656.

Christoudias, T., J. Lelieveld. 2012. Modelling the global atmospheric transport and deposition of radionuclides from the Fukushima Dai-ichi nuclear accident. Atmospheric Chemistry and Physics Discussions 12: 24531-24555.

Corbett, E. and R.C. Anderson. 2006. Landscape analysis of Illinois and Wisconsin Remnant Prairies. Journal of the Torrey Botanical Society 133(2): 267–279.

Craven, A.O. 2006. Soil exhaustion as a factor in the agricultural history of Virginia and Maryland, 1606 – 1860. (First published, 1925, University of Illinois Press). University of South Carolina Press, Columbia, SC.

Cross, A.F., W.H. Schlesinger. 1995. A literature review and evaluation of the Hedley fractionation: Applications to the biogeochemical cycle of soil phodphrus in natural ecosystems. Geoderma 64: 197-214.

Cunfer, G. 2011. The southern Great Plains Wind Erosion Maps of 1936-1937. Agricultural History 85(4): 540-559.

Daniels, R.B. 1987. Soil erosion and degradation in the southern Piedmont of the USA. Chapter 12 in: M.G. Wolman and F.G.A. Fournier (Eds.), Land Transformation in Agriculture. John Wiley and Sons, Ltd., Hoboken, NJ.

Davidson, E.A., I.A. Janssens. 2006. Temperature sensitivity of soil carbon decomposition and feedbacks to climate change. Nature 440: 165 - 173.

De Alba, S. M. Lindstrom, T.E. Schumacher, D.D. Malo. 2004. Soil landscape evolution due to soil redistribution by tillage: a new conceptual model of soil catena evolution in agricultural landscapes. Catena 58: 77-100.

De Jong, E., C.B.M. Begg, and R.G. Kachanoski. 1983. Estimates of soil erosion and deposition for some Saskatchewan soils. Canadian Journal of Soil Science 63: 607-617.

Dixon, J.L., F. von Blanckenburg. 2012. Soils as pacemakers and limiters of global silicate weathering. C.R. Geoscience 344: 597-609.

Dunai, T.J. 2010. Cosmogenic Nuclides: Principles, Concept and Applications in the Earth Surface Sciences. Cambridge University Press, New York, NY.

Ebert, K., J.K. Willenbring, K.P. Norton, A. Hall, and C. Hattestrand. 2012. Meteoric 10Be concentrations from saprolite and till in northern Sweden: Implications for glacial erosion and age. Quaternary Geochronology 12:11-22.

Ellert, B.H. and J.R. Bettany. 1995. Calculation of organic matter and nutrients stored in soils under contrasting management regimes. Candian Journal of Soil Science 529-538.

Faure, G., T.M. Mensing. 2005. Isotopes: Principles and Applications. John Wiley and Sons, Inc., Hoboken, NJ.

Feuillet, T. 2011. Statistical analyses of active patterned ground occurrence in the Taillon Massif (Pyrenees, France/Spain). Permafrost and Periglacial Processes 22: 228-238.

Field, C.V., G.A. Schmidt, D. Koch, C. Salyk. 2006. Modeling production and climate-related impacts on 10Be concentration in ice cores. Journal of Geophysical Research 111: D15107.

Fillippelli, G.M. 2002. The Global Phosphorous Cycle. Reviews in Mineralogy and Geochemistry 48(1): 391-425.

Foster, G.R., R.A. Young, M.J.M. Romkens, C.A. Onstad. 1985. Chapter 9 (pp. 137-162) in: Follett, R.F. and B.A. Stewart (Eds.): Soil Erosion and Crop Productivity, American Society of Agronomy, Madison, WI

Gee, G. W., D. Or. 2002. The solid phase. Chapter 2 in: J.H. Dane and G.C. Topp (Eds.). Methods of soil analyses: part 4 - physical methods. Soil Science Society of America, Madison, Wisconsin, USA. pp. 210-414.

Graedel, T.E. and W.C. Keene. 1996. The budget and cycle of Earth's natural chlorine. Pure and Applied Chemistry 68(9): 1689 – 1697.

Graham, I., R. Ditchburn, B. Barry. 2003. Atmospheric deposition of 7Be and 10Be in New Zealand rain (1996-98). Geochimica et Cosmochimica Acta 67: 361 - 373.

Graly, J.A., P.R. Bierman, L.J. Ruesser, and M.J. Pavich. 2010. Meteoric 10Be in soil profiles – A global meta-analysis. Geochimica et Cosmochimica Acta 74: 6814-6829.

Graly, J.A., L.J. Reusser, and P.R. Bierman. 2011. Short and long-term delivery rates of meteoric 10Be to terrestrial soils. Earth and Planetary Science Letters 302: 329-336.

Graveel, J.G., D.D. Tyler, J.R. Jones, W.W. McFee. 2002 Crop yield and rooting as affected by fragipan depth in loess soils in the southeast USA. Soil and Tillage Research 68: 153-161.

Gruber, S. 2012. Derivation and analysis of a high-resolution estimate of global permafrost zonation. The Cryosphere 6: 221-233.

Guglielmin, M., M.R. Balks, L.S. Adlam, F. Baio. 2011. Permafrost thermal regime from two 30-m deep boreholes in southern Victoria Land, Antarctica. Permafrost and Periglacial Processes 22: 129-139.

Gustafsson, M. E.R. and L.G. Franzen. 2000. Inland transport of marine aerosols in southern Sweden. Atmospheric Environment 34: 313-325.

Hall, G.F., R.B. Daniels, J.E. Foss. 1982. Rate of soil formation and renewal in the USA. Chapter 3 in: Chapter 9 in D.M. Kral (Ed): Determinants of Soil Loss Tolerance. ASA Publication 45. Soil Science Society of America, Madison, WI.

Hamilton, T.D., and Labay, K.A., 2011, Surficial geologic map of the Gates of the Arctic National Park and Preserve, Alaska: U.S. Geological Survey Scientific Investigations Map 3125, pamphlet 19 p., scale 1:300,000, available at http://pubs.usgs.gov/sim/3125/.

Harden, J.W., J.M. Sharpe, W.J. Parton, D.S. Ojima, T.L. Fries, T.G. Huntington, and S.M. Dabney. 1999. Dynamic replacement and loss of soil carbon on eroding cropland. Global Biogeochemical Cycles 13(4): 885-901.

Harden J. W., Fries T. L. and Pavich M. J.. 2002. Cycling of Beryllium and carbon through hillslope soils in Iowa. Biogeochemistry 60: 317–336.

Harris, S.A. 1998. Nonsorted circles on plateau mountain, S.W. Alberta, Canada. Proceedings of the 7th International Conference on Permafrost, pp. 441-448. Yellowknife, CA.

Harris, K.L. 2003. Geologic atlas of Pope County, Minnesota. Minnesota Geological Survey, Minneapolis, MN.

Heikkila, U., J. Beer, V. Afimov. 2008. Beryllium-10 and Beryllium-7 in precipitation in Dubendorf (440 m) and at Jungfraujoch (3580 m), Switzerland (1998-2005). Journal of Geophysical Research 113: D11104.

Heimsath, A.M., Dietrich, W.E., Nishiizumi, K., Finkel, R.C. 1997. The soil production function and landscape equilibrium. Nature 388: 358-361.

Heimsath, A.M., J. Chappell, W.E. Dietrich, K. Niishizumi, R.C. Finkel. 2000. Soil production on a retreating escarpment in southeastern Australia. Geology 28: 787-790.

Heimsath, A.M., R. A. DiBiase, K.X. Whipple. 2012. Soil production limits and the transition to bedrock-dominated landscapes. Nature Geoscience 5: 210-214.

Heimsath, A.M. 2014. Limits of soil production? Science 343: 617.

Hilgard, E.W. 1860. Report on the Geology and Agriculture of the State of Mississippi. Mississippi State Printer, Oxford, MS.

Holtz, R.D., W.D. Kovacs, T.C. Sheahan. 2010. An Introduction to Geotechnical Engineering. Prentice Hall, Inc. Upper Saddle River, NJ.

Horwath, J.L., R.S. Sletten, B. Hagedorn, and B. Hallet. 2008. Spatial and temporal distribution of soil organic carbon in nonsorted striped patterned ground of the High Arctic. Journal of Geophysical Research 113: G03S07.

Hudson, B.D. 1994. Soil organic matter and available water capacity. Journal of Soil and Water Conservation 49(2): 189-194.

Hugelius, G., P. Kuhry, C. Tarnocai, T. Virtanen. 2010. Soil organic carbon pools in a periglacial landscape: a case study from the central Canadian arctic. Permafrost and Periglacial Processes 21: 16-29.

Jagadamma, S., R. Lal, and B.K. Rimal. 2009. Effects of topsoil depth and soil amendments on corn yield and properties of two Alfisols in central Ohio. Journal of Soil and Water Conservation 64(1): 70-80.

Jankauskas, B., G. Jankauskiene, M.A. Fullen. 2007. Relationships between soil organic matter content and soil erosion severity in Albeluvisols of the Zemaiciai Uplands. Ekologija 53(1): 21-28.

Jaworski, J.F., J. Nriagu, P. Denny, B.T. Hart, M.R. Lasheen, V. Subramanian, M. H. Wong. 1987. Group Report: Lead. Chapter 1 in: Lead, Mercury, Cadmium and Arsenic in the environment (T.C. Hutchinson and K.M. Meema, Eds.). John Wiley and Sons, Ltd.

Jelinski, N.A. 2013. Cryoturbation in the Central Brooks Range, Alaska. Soil Horizons 54(5): 01-007.

Jelinski, N.A. and C.J. Kucharik. 2009. Land-use effects on soil carbon and nitrogen on a U.S. Midwestern floodplain. Soil Science Society of America Journal 73(1): 217-225.

Joel, A.H. 1937. Soil conservation reconnaissance survey of the southern Great Plains wind-erosion area. Technical Bulletin No. 556, United States Department of Agriculture, Washington, D.C.

Johnson, D.L. 1968. Lunar Soil: Should this term be used? Science 160: p.

Johnson, D.L., E.A. Keller, T.K. Rockwell. 1990. Dynamic pedogenesis: New views on some key concepts, and a model for interpreting quaternary soils. Quaternary Research 33: 306-319.

Johnson, D.L., D.L. Johnson. 2010. A holistic and universal view of soil. Proceedings of the 19th World Conference of Soil Science, Brisbane, Australia.

Jungers, M.C., P.R. Bierman, A. Matmon, K. Nichols, J. Larsen, and R. Finkel. 2009. Tracing hillslope sediment production and transport with in-situ and meteoric 10Be. Journal of Geophysical Research 114: F04020.

Kaab, A., L. Girod, I. Berthling. 2013. Surface kinematics of periglacial sorted circles using Structure-from-Motion technology. The Cryosphere Discussions 7: 6043-6074.

Kachanoski, R.G. 1987. Comparison of measured Cesium-137 losses and erosion rates. Canadian Journal of Soil Science 67(1): 199-203.

Kachanoski, R.G. and E. DeJong. 1984. Predicting the temporal relationship between soil cesium-137 and erosion rate. Journal of Environmental Quality 13:301-304.

Kaiser, C., H. Meyer, C. Biasi, O. Rusalimova, P. Barsukov, and A. Richter. 2007. Conservation of soil organic matter through cryoturbation in arctic soils in Siberia. Journal of Geophysical Research 112: G02017.

Kaste, J.M., A.M. Heimsath, and B.C. Bostick. 2007. Short-term mixing quantified with fallout radionuclides. Geology 35(3): 243-246.

Kaste, J.M. and M. Baskaran. 2011. Meteoric 7Be and 10Be as process tracers in the environment. Ch 5 in M. Baskaran (ed.), Handbook of Environmental Isotope Geochemistry. Springer-Verlag, Berlin, Germany.

Kimble, J.M., R. Lal, M. Mausbach. 2001. Erosion effects on soil organic carbon pools in soils of Iowa. Pp. 472-475. In: D.E. Stott, R.H. Mohtar and G.C. Steinhardt (eds.): Sustaining the Global Farm. Selected papers from the 10th International Soil Conservation Organization Meeting held May 24-29, 1999 at Purdue University and the USDA-ARS National Soil Erosion Research Laboratory.

Klaminder J, Renberg I, Bindler R, Appleby P, Emteryd O, Grip H. Estimating the mean residence time of lead in the organic horizon of boreal forest soils using 210-lead, stable lead and a soil chronosequence. Biogeochem 2006;78:31–49.

Klaminder, J., R. Bindler, J. Rydberg, I. Renberg. 2008. Is there a chronological record of atmospheric mercury and lead deposition preserved in the mor layer (O-horizon) of boreal forest soils? Geochimica et Cosmochimica Acta 72: 703-712.

Klaminder, J., J.G. Farmer, A.B. MacKenzie. 2011. The origin of lead in the organic horizon of tundra soils: Atmospheric deposition, plant translocation from the mineral soil or soil mineral mixing? Science of the Total Environment 409: 4344-4350.

Klaus, M., Becher, M. and Klaminder, J. (2013), Cryogenic Soil Activity along Bioclimatic Gradients in Northern Sweden: Insights from Eight Different Proxies. Permafrost Periglac. Process., 24: 210–223. doi: 10.1002/ppp.1778

Kokelj, S.V., C.R. Burn and C. Tarnocai. 2007. The structure and dynamics of earth hummocks in the subarctic forest near Inuvik, Northwest Territories, Canada. Arctic, Antarctic, and Alpine Research, 39(1): 99-109.

Kolka, R.K., D.F. Grigal, E.A. Nater and E.S. Verry. 2001. Hydrologic cycling of mercury and organic carbon in a forested upland-bog watershed. Soil Science Society of America Journal 65: 897-905.

Konert, M. and J. Vandenberghe. 1997. Comparison of laser grain size analysis with pipette and sieve analysis: a solution for the underestimation of the clay fraction. Sedimentology 44(3): 523-535.

Koven, C. P. Friedlingstein, P. Ciais, D. Khvorostyanov, G. Krinner, and C. Tarnocai. 2009. On the formation of high-latitude soil carbon stock: Effects of cryoturbation and insulation by organic matter in a land surface model. Geophysical Reserach Letters 36: L21501.

Korschinek, G., A. Bergmaler, I. Dillman, T. Faestermann, U. Gerstmann, K. Knie, and C.L. Gostomski. 2009. Determination of the 10Be half-life by HI-ERD and Liquid Scintillation counting. Geochemica et Cosmochimica Acta 73:A685-A685.

Kreznor, W.R., K.R. Olson, W.L. Banwart, D.L. Johnson. 1989. Soil, landscape and erosion relationships in a Northwest Illinois Watershed. Soil Sceinec Society of America Journal 53: 1763-1771.

Lal, D. 1991. Cosmic ray labeling of erosion surfaces: in situ nuclide production rates and erosion models. Earth and Planetary Science Letters 104, 424–439.

Lal, D. 2007. Recycling of cosmogenic nuclides after their removal from the atmosphere; special case of appreciable transport of 10Be to polar regions by aeolian dust. Earth and Planetary Science Letters 264: 177 - 187.

Lal, R., B.A. Stewart. 2011. World soil resources and food security. Advances in Soil Science, CRC Press, Boca Raton, FL.

Lal, R. and B.A. Stewart. 2012. Sustainable Management of Soil Resources and Food Security. Chapter 1 in: Lal, R. ad B.A. Stewart (Eds.), World Soil Resources and Food Security. Advances in Soil Science v. 18, CRC Press, Boca Raton, FL.

Larsen, I.J., P.C. Almond, A. Eger, J.O. Stone, D.R. Montgomery, B. Malcom. 2013. Rapid soil production and weathering in the Southern Alps, New Zealand. Science 343: 637-640.

Larson, W.E., F.J. Pierce, R.H. Dowdy. 1983. The threat of soil erosion to long-term crop production. Science 219: 458-465.

Lee, J.A., S.J. Woodin. 1988. Vegetation structure and the interception of acidic deposition by ombrotrophic mires. In: Vegetation Structure in Relation to carbon and nutrient economy (J.T.A. Verhoeven, G.W. Heil and M.J.A. Werger, Eds), pp. 137-147. SPB Academic Publsihing, The Hauge.

Lepper, K., T.G. Fisher, I. Hajdas, and T. Lowell. 2007. Ages for the Big Stone Moraine and the oldest beaches of glacial Lake Agassiz: Implications for deglaciation chronology. Geology 35: 667-670.

Leri, A.C., S.C. B. Myneni. 2010. Organochlorine turnover in forest ecosystems: The missing link in the terrestrial chlorine cycle. Global Biogeochemical Cycles 24: GB4021 doi:10.1029/2010GB003882.

Li, L., S. Du., L. Wu, G. Liu. 2009. An overview of soil loss tolerance. Catena 78: 93-99.

Li, S. , D.A. Lobb, M.J. Lindstrom, A. Farenhorst. 2007. Tillage and water erosion on different landscapes in the northern North American Great Plains evaluated using ^{137}Cs technique and soil erosion models. Catena 70: 493-505.

Li, S., D.A. Lobb, M.J. Lindstrom, S.K. Papiernik, A. Farenhorst. 2008. Modeling tillage-induced redistribution of soil mass and its constituents within different landscapes. Soil Science Society of America Journal 72: 167-179.

Li, S., D.A. Lobb, K.H. Tiessen, and B.G. McConkey. 2010. Selecting and applying cesium-137 conversion models to estimate soil erosion rates in cultivated fields. Journal of Environmental Quality 39(1): 204-219.

Lindstrom, M.J., J.A. Schumacher, T.E. Schumacher. 2000. TEP: A Tillage Erosion Prediction model to calculate soil translocation rates from tillage. Journal of Soil and Water Conservation 55(1): 105-108.

Lively, R.S. and L.H. Thorleifson. 2009. Minnesota Soil, Till, and Ground-Water Geochemical Data. Minnesota Geological Survey, Minneapolis, MN.

Lobb, D.A., R.G. Kachanoski, and M.H. Miller. 1995. Tillage translocation and tillage erosion on shoulder slope landscape positions measured using 137Cs as a tracer. Canadian Journal of Soil Science 75: 211-218.

Lobb, D.A., R.G. Kachanoski, and M.H. Miller. 1999. Tillage translocation and tillage erosion in the complex upland landscapes of southwestern Ontario. Soil and Tillage Research 51:189-209.

Lowery, B., J. Swan, T. Schumacher, A. Jones. 1995. Physical properties of selected soils by erosion class. Journal of Soil and Water Conservation 50(3): 306-311.

Lundqvist, J. 2004. Glacial history of Sweden. Pp 401-413 in: Quaternary Glaciations – Extent and Chronology (J. Ehlers and P.L. Gibbard, Eds.), Elsevier.

Luoto, M., and J. Hjort. 2004. Generalized linear modeling in periglacial studies: Terrain

parameters and patterned ground. Permafrost and Periglacial Processes 15: 327-338.

Makoto, K., J. Klaminder. 2012. The influence of non-sorted circles on species diversity of vascular plants, bryophytes and lichens in Sub-Arctic Tundra. Polar Biology 35(11): 1659-1667.

Malmer, N. 1988. Patterns in the growth and the accumulation of inorganic constituents in the Sphagnum cover on ombrothrophic bogs in Scandanavia. Oikos 53: 105-120.

Malmer, N. 1990. Constant or increasing nitrogen concentrations in Sphagnum mosses in mires in Southern Sweden during the last few decades. Aquilo Series Botanici 28: 57-65.

Masarik, J., J. Beer. 2009. An updated simulation of particle fluxes and cosmogenic nuclide production in the Earth's atmosphere. Journal of Geophysical Research 104: 12,099 - 12,111.

Matisoff, G., E.C. Bonniwell, P.J. Whiting. 2002. Soil erosion and sediment sources in an Ohio watershed using beryllium-7, cesium-137, and lead-210. Journal of Environmental Quality 31(1): 54 - 61.

Matisoff, G., P.J. Whiting. 2011. Measuring soil erosion rates using natural (^{7}Be, ^{210}Pb) and anthropogenic (^{137}Cs, ^{239,240}Pu) radionuclides. Chapter 25 in Baskaran, M.: Handbook of Environmental Isotope Geochemistry, Advances in Isotope Geochemistry. Springer-Verlag, Berlin, Heidelberg.

Matshushi, Y., H. Matsuzaki, Y. Matsukura. 2008. Potential of in-situ produced cosmogenic nuclides for quantifying strength reduction of bedrock in soil-mantled hillslopes. Quaternary Geochronology 3: 262-267.

McCormack, D.E., K.K. Young, L.W. Kimberlin. 1982. Current criteria for determining soil loss tolerance. Chapter 9 in D.M. Kral (Ed): Determinants of Soil Loss Tolerance. ASA Publication 45. Soil Science Society of America, Madison, WI.

McGahan, D.G., R.J. Southard, R.J. Zasoski. 2003. Mineralogical comparison of agriculturally acidifed and naturally acidic soils. Geoderma 114 (3-4): 355-368.

McKean, J.A., W.E. Dietrich, R.C. Finkel, J.R. Southton, and M.W. Caffee. 1993. Quantification of soil production and downslope creep rates from cosmogenic 10Be accumulations on a hillslope profile. Geology 21: 343-346.

Melton, M.A. 1965. The geomorphic and paleoclimatic significance of alluvial deposits in Southern Arizona. Journal of Geology 73:1-38.

Meyer, L.D., A. Bauer, R.D. Heil. 1985. Experimental approaches for quantifying the effect of soil erosion on productivity. Chapter 13 (pp. 213-234) in: Follett, R.F. and B.A. Stewart (Eds.): Soil Erosion and Crop Productivity, American Society of Agronomy, Madison, WI

Michaelson, G.J., C.-L. Ping, M. Clark. 2013. Soil pedon carbon and nitrogen data for Alaska: An analysis and update. Open Journal of Soil Science 3: 132-142.

Miller, F.P., W.D. Rasmussen, L.D. Meyer. 1985. Historical perspective of soil erosion in the United States. Chapter 3 (pp. 23-48) in: Follett, R.F. and B.A. Stewart (Eds.): Soil Erosion and Crop Productivity, American Society of Agronomy, Madison, WI.

Miller, W.P., D.M. Miller. 1987. A micro-pipette method for soil mechanical analysis. Communications in Soil Science and Plant Analysis 18(1): 1-15.

Mokma, D.L., T.E. Fenton, K.R. Olson. 1996. Effect of erosion on morphology and classification of soils in the North Central United States. Journal of Soil and Water Conservation 51(2): 171-175.

Monaghan, M.C., J. McKean, W. E. Dietrich and J. Klein. 1992. ^{10}Be Chronometry of bedrock-to-soil conversion rates, Earth Planet. Sci. Lett., v. 111, p. 483-492.

Montgomery, D.R. 2007. Soil erosion and agricultural sustainability. Proceedings of the National Academy of Sciences 104(33): 13268-13272.

Morgan, R.P.C. 2005. Soil Erosion and Conservation (3rd Ed.). Blackwell Publishing, Malden, MA.

Morrás, H., L. Moretti, G. Píccolo, and W. Zech (2009). "Genesis of subtropical soils with stony horizons in NE Argentina: Autochthony and polygenesis". *Quaternary International* **196** (1–2): 137–159.

Munthe, J., et al. 2007. Mercury in Nordic ecosystems, 43 pp., IVL Swed. Environ. Res. Inst. Ltd, Goteborg, Sweden.

Nater, E.A., D.F. Grigal. 1992. Regional trends in mercury distribution across the Great Lake states, north central USA. Nature 358: 139-141.

National Nuclear Data Center. 2011. Chart of Nuclides. Brookhaven National Laboratory. www.nndc.bnl.gov/chart

National Park Service. 2009. An ecological land survey and landcover map of the Arctic network. Natural Resource Technical Report NPS/ARCN/NRTR-2009/270.

Nicolsky, D.J., V.E. Romanovsky, G.S. Tipenko, and D.A. Walker. 2008. Modeling biogeophysical interactions in non-sorted circles in the low Arctic. Journal of Geophysical Research 113: G03S05.

Nishiizumi, K., M. Imamura, M. Caffee, J.R. Southon, R.C. Finkel, J. McAnnich. 2007. Absolute calibration of 10Be AMS standards. Nuclear Instruments and Methods in Physics Research Section B 258, 403-413.

Olsen, B.M., J.H. Mossler. 1982. Geologic Map of Minnesota: Depth to Bedrock, Minnesota Geological Survey Map S-14. Minnesota Geological Survey.

Olsen, C.R., H.J. Simpson, T.-H. Peng, R.F. Bopp, and R.M. Trier. 1981. Sediment mixing and accumulation rate effects on radionuclide depth profiles in Hudson estuary sediments. Journal of Geophysical Research 86(C11): 11020-11028.

Olson, K.R. and A.H. Beavers. 1987. A method to estimate soil loss from erosion. Soil Science Sociey of America Journal 51: 441-445.

Olson, K.R. 1994. Effects of soil formation, erosion, and management on long-term productivity. Chap 9 (pp. 188-214) in McIsaac, G. and W.R. Edwards (Eds.): Sustainable agriculture in the American Midwest: lessons from the past, prospects for the future. University of Illinois Press, Champaign, IL.

Olson, K.R., A.N. Gennadiyev, A.P. Zhidkin, M.V. Markelov, V.N. Golosov, J.M. Lang. 2013. Use f magnetic tracer and radio-cesium methods to determine past cropland soil erosion amounts and rates. Catena 104: 103-110.

Omernik, J.M. 1995. Ecoregions: A spatial framework for environmental management. In: Biological Assessment and Criteria: Tools for Water Resource Planning and Decision Making. Davis, W.S. and T.P. Simon (eds.), Lewis Publishers, Boca Raton, FL. p. 49-62.

Papiernik, S.K., M.J. Lindstrom, J.A. Schumacher, A. Farenhorst, K.D. Stephens, T.E. Schumacher and D.A. Lobb. 2005. Variation in soil properties and crop yield across an eroded prairie landscape. Journal of Soil and Water Conservation 60(6): 388-395.

Papiernik, S.K., M.J. Lindstrom, T.E. Schumacher, J.A. Schumacher, D.D. Malo, D.A. Lobb. 2007. Characterization of soil profiles in a landscape affected by long-term tillage. Soil and Tillage Research 93: 335-345.

Papiernik, S.K., T.E. Schumacher, D.A. Lobb, M.J. Lindstrom, M.L. Lieser, A. Eynard and J.A. Schumacher. 2009. Soil properties and productivity as affected by topsoil movement within an eroded landform. Soil and Tillage Research 102: 67-77.

Pavich, M.J., L. Brown, J.W. Harden, J. Klein and R. Middleton. 1986. ^{10}Be distribution in soils from Merced River terraces, California. Geochimica et Cosmochimica Acta. 50: 1727-1735.

Pennock, D. 1997. Effects of soil redistribution on soil quality: Pedon, Landscape and Regional scales. Chap. 7 (pp. 167-186) In: Gregorich, E.G. and M.R. Carter (Eds.) Soil Quality for Crop Production and Ecosystem Health. Developments in Soil Science 25, Elsevier, Amsterdam, Netherlands.

Peterson, R.A., and W.V. Krantz. 2003. A mechanism for differential frost heave and its implications for patterned-ground formation. Journal of Glaciology 49:69–80.

Ping, C.-L., G.J. Michaelson, J.M. Kimble, V.E. Romanovsky, Y.L. Shur, D.K. Swanson, D.A. Walker. 2008a. Cryogenesis and soil fromation along a bioclimate gradient in Arctic North America. Journal of Geophysical Research 113: G03S12.

Ping, C.-L., G.J. Michaelson, M.T. Jorgenson, J.M. Kimble, H. Epstein, V.E. Romanovsky, and D.E. Walker. 2008b. High stocks of soil organic carbon in the North American Arctic region. Nature Geoscience 1: 615 - 619.

Ping, C.-L. 2013. Gelisols: Part I. Cryogenesis and State Factors of Formation. Soil Horizons 54 (3).

Ping, C.-L., M.H. Clark, J.M. Kimble, G.J. Michaelson, Y. Shur, and C.A. Stiles. 2013. Sampling protocols for permafrost-affected soils. Soil Horizons 54 (1).

Ping, C.-L., J.D. Jastrow, M.T. Jorgenson, G.J. Michaelson, and Y.L. Shur. 2014. Permafrost soils and carbon cycling. SOIL Discussions 1: 709-756.

Prior, J.C. 1991. Landforms of Iowa. University of Iowa Press, Iowa City, IA.

PRISM Climate Group. 2012. Oregon State University, http://prism.oregonstate.edu, created 4 Feb 2004.

Quine, T.A. and K. van Oost. 2007. Quantifying carbon sequestration as a result of soil erosion and deposition: retrospective assessment using caesium-137 and carbon inventories. Global Change Biology 13(12): 2610-2625.

R Development Core Team. 2011. R: A language and environment for statistical computing. R Foundation for Statistical Computing. Vienna, Austria. ISBN 3-900051-07-0, URL http://www.R-project.org.

R Development Core Team. 2014. R: A language and environment for statistical computing. R Foundation for Statistical Computing, Vienna, Austria. ISBN 3-900051-07-0, URL http://www.R-project.org.

Ramankutty, N., A.T. Evan, C. Monfreda, J.A. Foley. 2008. Farming the planet: 1. Geographic distribution of global agricultural lands in the year 2000. Global Biogeochemical Cycles 22(1). DOI: 10.1029/2007GB002952. Available at: http://www.geog.mcgill.ca/~nramankutty/Datasets/Datasets.html

Renard, K.G., G.R. Foster, G.A. Weesies, D.K. McCool, and D.C. Yoder. 1997. Predicting soil erosion by water: A guide to conservation planning with the revised universal soil loss equation (RUSLE). U.S. Department of Agriculture, Agriculture Handbook No. 703, 404 pp.

Rhoton, F.E. and D.D. Tyler. 1990. Erosion-induced changes in the properties of a fragipan soil. Soil Science Society of America Journal 54: 223-228.

Richter, D.D. and D. Markewitz. 2001. Understanding soil change: Soil sustainability over millennia, centuries and decades. Cambridge University Press, Cambridge, UK.

Ritchie, J.C. and J.R. McHenry. 1990. Application of radioactive fallout Cesium-137 fo measuring soil erosion and sediment accumulation rates and patterns: A review. Journal of Environmental Quality 19: 215-233.

Rinke, A., P. Kuhry, K. Dethloff. 2008. Importance of a soil organic layer for Arctic climate: A sensitivity study with an Arctic RCM. Geophysical Research Letters 35: L13709.

Ross, H.B. and L. Granat. 1986. Deposition of atmospheric trace metals in northern Sweden as measured in the snowpack. Tellus 38B: 27-43.

Samonil, P., R.J. Schaetzl, M. Valtera, V. Golias, P. Baldrian, I. Vasickova, D. Adam, D. Janik, L. Hort. 2013. Crossdating of disturbance by tree uprooting: Can treethrow microtopography persist for 6000 years? Forest Ecology and Management 307: 123-135.

Sawyer, C.F. 2007. Frost heaving and surface clast movement in turf-banked terraces, Eastern Glacier National Park, Montana. Ph.D. Dissertation. Texas State University-San Marcos.

Selkirk, Jennifer M. 1998. Active vegetation-banked terraces on Macquarie Island. *Zeitschrift für Geomorphologie* 42, no. 4: 483-96.

Shirazi, M.A. and L. Boersma. 1984. A unifying quantitative analysis of soil texture. Soil Sci. Soc. of Am. J. 48(1):142-147.

Skyllberg, U., K. Xia, P.R. Bloom, E.A. Nater, W.F. Bleam. 2000. Binding of mercury (II) to reduced sulfur in soil organic matter along upland-peat soil transects. Journal of Environmental Quality 29: 855-865.

Smith, C.A.S., C.R. Burn, C. Tarnocai, B. Sproule. 1998. Air and soil temperature relations along an ecological transect through the permafrost zones of northern Canada. pp. 1009 – 1015 in: Proceedings of the Seventh International Conference on Permaforst, Yellowknife, Canada. International Permafrost Association, Potsdam, Germany.

Smith, D. J. 1986. Patterned ground activity in the Mt. Rae area, southern Canadian Rocky Mountians, 1977-1985. In *Current research by western Canadian geographers: The University of Alberta papers*, Edgar L. Jackson, ed.: 99-111. Vancouver: Tantalus Research Limited.

Smith, S.L., V.E. Romanovsky, A.G. Lewkowicz, C.R. Burn, M. Allard, G.D. Clow, K. Yoshikawa and J. Throop. Thermal State of Permafrost in North America: A Contribution to the International Polar Year. Permafrost and Periglacial Processes 21: 117-135.

Soil Survey Division Staff. 1993. Soil survey manual. Soil Conservation Service. U.S. Department of Agriculture Handbook 18.

Soil Survey Staff. 1999. Soil taxonomy: A basic system of soil classification for making and interpreting soil surveys. 2nd edition. Natural Resources Conservation Service. U.S. Department of Agriculture Handbook 436.

Soil Survey Staff. 2002. Field book for describing and sampling soils, Version 2.0. NRCS-NSSC, Lincoln, NE.

Soil Survey Staff. 2010. Keys to soil taxonomy (11th Ed). United States Department of Agriculture – Natural Resources Conservation Service.

Soil Survey Staff, Natural Resources Conservation Service, United States Department of Agriculture. 2014a. Soil Survey Geographic (SSURGO) Database. Available online at http://sdmdataaccess.nrcs.usda.gov/. Accessed 13JUN2014.

Soil Survey Staff - Natural Resources Conservation Service. 2014b. United States Department of Agriculture. Official Soil Series Descriptions. Available online. Accessed 31JUL2014.

Soller, D.R., M.C. Reheis, C.P. Garrity, D.R. Van Sistine. 2009. Map database for surficial materials in the Conterminous United States. U.S. Geological Survey Data Series 425.

Strandberg, M. 1997. Distribution of 137Cs in a low arctic ecosystem in West Greenland. Arctic 50(3): 216 - 223.

Swanson, D.K., C.L. Ping, and G.J. Michaelson. 1999. Diapirism in soils due to thaw of ice-rich material near the permafrost table. Permafrost and Periglacial Processes 10:349–367.

Stohl, A., P. Siebert, G. Wotawa, D. Arnold, J.F. Burkhart, S. Eckhardt, C. Tapia, A. Vargas, and T.J. Yasunari. 2011. Xenon-133 and caesium-137 releases into the atmosphere from the Fukushima Dai-ichi nuclear power plant: determination of the source term, atmospheric dispersion, and deposition. Atospheric Chemistry and Physics Discussions 11: 28319-28394.

Tarnocai, C., J.G. Canadell, E.A.G. Schuur, P. Kuhry, G. Mazhitova, S. Zimov. 2009. Soil organic carbon pools in the northern circumpolar permafrost region. Global Biogeochemical Cycles 23(2): GB2023, doi:10.1029/2008GB003327.

Thakur, P., S. Ballard, R. Nelson. 2012. Radioactive fallout in the United States due to the Fukushima nuclear plant accident. Journal of Environmental Monitoring 14: 1317 - 1324.

Trimble, S.W. 1974. Man-induced soil erosion on the southern Piedmont, 1700-1970. Soil and Water Conservation Society, Ankeny, IA.

Trimble, S.W. 1975. A volumetric estimate of man-induced soil erosion on the southern Piedmont plateau. pp. 142-154 In Present and prospective technology for predicting sediment yields and sources. Proc. Sediment Yield Workshop, U.S. Dept. Agr. Sed. Lab., Oxford, Miss. Nov. 28-30, 1972. U.S. Dept Agr. Agr. Res. Serv. ARS Publ. S-40.

Trimble, S.W. 2008. Man-induced soil erosion on the southern Piedmont, 1700-1970. 2nd Ed. Soil and Water Conservation Society, Ankeny, IA.

Trimble, S.W. 2013. Historical agriculture and soil erosion in the Upper Mississippi Valley hill country. CRC Press, Boca Raton, FL.

Trumbore, S. 2000. Age of soil organic matter and soil respiration: Radiocarbon constraints on belowground C dynamics. Ecological Applications 10(2): 399 - 411.

Trumbore, S. 2009. Radiocarbon and soil carbon dynamics. Annual Review of Earth and Planetary Sciences 37: 47 - 66.

U.S. Census Bureau. 2010. State and County Quickfacts. Retrieved 01JUN2014: http://quickfacts.census.gov/qfd/states.

U.S. Environmental Protection Agency. 2013. Level III and IV ecoregions of the continental United States. U.S. EPA, National Health and Environmental Effects Research Laboratory, Corvallis, Oregon, Map scale 1:3,000,000. Available online at: http://www.epa.gov/wed/pages/ecoregions/level_iii_iv.htm.

USDA National Agricultural Statistics Service. 2013. 2013 Cropland Data Layer. Published national cultivated layer [Online]. Available at http://nassgeodata.gmu.edu/CropScape/ (accessed 01JUN2014; verified 24AUG2014). USDA-NASS, Washington, DC.

U.S. Department of Agriculture. 2013. Summary Report: 2010 National Resources Inventory, Natural Resources Conservation Service, Washington, DC, and Center for Survey Statistics and Methodology, Iowa State University, Ames, Iowa. http://www.nrcs.usda.gov/Internet/FSE_DOCUMENTS/stelprdb1167354.pdf

Vagen, T., L. Winowiecki, J. Tondoh. 2013. Land Degradation Surveillance Framework Field Guide. World Agroforestry Center (ICRAF), Nairobi, Kenya.

Vandenberghe, J. 1992. Cryoturbations: A sediment structural analysis. Permafrost Periglacial Processes 3:343–352.

Van Oost, K., G. Govers, and P. Desmet. 2000. Evaluating the effects of changes in landscape structure on soil erosion by water and tillage, Landscape Ecology, 15: 577-589.

Veenstra, J.J., C.L. Burras. 2012. Effects of agriculture on the classification of Black soils in the Midwestern United States. Canadian Journal of Soil Science 92: 403-411.

Waldrop, M.P., K.P. Wickland, R. White III, A.A. Berhe, J.W. Harden, V.E. Romanovsky. 2010. Molecular investigations into a globally important carbon pool: permafrost-protected carbon in Alaskan soils. Global Change Biology 16: 2543 - 2554.

Walker, D.A., H.E. Epstein, W.A. Gould, A.M. Kelley, A.N. Kade, J.A. Knudson, W.B. Krantz, G. Michaelson, R.A. Peterson, C.-L. Ping, M.K. Raynolds, V.E. Romanovsky, Y. Shur. 2004. Frost-boil ecosystems: Complex interactions between landforms, soils, vegetation and climate. Permafrost and Periglacial Processes 15: 178 - 188.

Walker, D.A., H.E. Epstein, V.E. Romanovsky, C.-L. Ping, G.J. Michaelson, R.P. Daanen, Y. Shur, R.A. Peterson, W.B. Krantz, M.K. Raynolds, W.A. Gould, G. Gonzalez, D.J. Nicolsky, C.M. Vonlanthen, A.H. Kade, P. Kuss, A.M. Kelley, C.A. Munger, C.T. Tarnocai, N.V. Matveyeva, and F.J.A. Daniels. 2008. Arctic patterned-ground ecosystems: A synthesis of field studies and models along a North American Arctic Transect. Journal of Geophysical Research 113: G03S01.

Walling, D.E. and Q. He. 1999. Improved models for estimating soil erosion rates from Cesium-137 measurements. Journal of Environmental Quality 28(2): 611-622.

Walther, S.C., J.J. Roering, P.C. Almond, M.W. Hughes. 2009. Long-term biogenic soil mixing and transport in a hilly, loess-mantled landscape: Blue Mountains of southeastern Washington. Catena 79: 170-178.

Wang, Y., R. Amundson, and S. Trumbore. 1996. Radiocarbon dating of soil organic matter. Quarternary Research 45: 282 - 288.

Washburn, A.L. 1980. Geocryology: A survey of periglacial processes and environments. John Wiley and Sons, New York, N.Y.

Wilkinson, B.H. 2005. Humans as geologic agents: a deep time perspective. Geology 33(3): 161.

Wilkinson, B.H. and B.J. McElroy. 2007. The impact of humans on continental erosion and sedimentation. Geological Society of America Bulletin 119(1-2): 140-156.

Willenbring, J.K., F. von Blanckenburg. 2010. Meteoric cosmogenic beryllium-10 adsorbed to river sediment and soil: applications for earth surface dynamics. Earth Science Reviews 98: 105-122.

Wilson, M.A., S.J. Indorante, B.D. Lee, L. Follmer, D.R. Williams, B.C. Fitch, W.M. McCauley, J.D. Bathgate, D.A. Grimley and K. Kleinschmidt. 2010. Location and expression of fragic soil properties in a loess-covered landscape, Southern Illinois, USA. Geoderma 154: 529-543.

Witzke, B.J., R.R. Anderson, J.P. Pope. 2010. Estimated depth to bedrock of Iowa as a 110 meter pixel_32bit Imagine Format. Iowa Geological Survey. Iowa Department of Natural Resources.

Wolman, M.G. 1985. Soil erosion and crop productivity: a worldwide perspective. Chapter 2 (pp. 10-22) in: Follett, R.F. and B.A. Stewart (Eds.): Soil Erosion and Crop Productivity, American Society of Agronomy, Madison, WI.

Woomer, P.L., A. Martin, A. Albrecht, D.V.S. Resck, H. W. Scharpenseel. 1994. The importance and management of soil organic matter in the tropics. (pp. 47-80 In: Woomer, P.L. and M.J. Swift (Eds.) The biological management of tropical soil fertility. John Wiley and Sns, Chichester, UK.

Wright, H.E. 1962. Role of the Wadena Lobe in the Wisconsin Glaciation of Minnesota. Geological Society of America Bulletin 73: 73-100.

Wright, S.M., B.J. Howard, P. Strand, T. Nylen, M.A.K. Sickel. 1999. Prediction of 137Cs deposition from atmospheric nuclear weapons tests within the Arctic. Environmental Pollution 104: 131-143.

Wynn, J.G., J.W. Harden, T.L. Fries. 2006. Stable carbon depth profiles and soil organic carbon dynamics in the lower Mississippi Basin. Geoderma 131: 89-109.

Verheijen, F.G.A., R.J.A. Jones, R.J. Rickson, C.J. Smith. 2009. Tolerable versus actual soil erosion rates in Europe. Earth-Science Reviews 94: 23-38.

Yoo, K., R. Amundson, A.M. Heimsath, W.E. Dietrich. 2005. Process-based model linking pocket gopher (Thomomys bottae) activity to sediment transport and soil thickness. Geology 33(11): 917-920.

Yoo, K., S.M. Mudd. 2008. Toward process-based modeling of geochemical soil formation across diverse landforms: A new mathematical framework. Geoderma 146: 248-260.

Zachar, D. 1982. Soil Erosion. Developments in Soil Science 10. Elsevier Scientific Publishing Company, New York, NY.

Zdanowicz, C., E. Kruemmel, D. Lean, A. Poulain, C. Kinnard, E. Yumvihoze, J. Chen and H. Hintelmann. 2014. Pre-industrial and recent (1970-2010) atmospheric deposition of sulfate and mercury in snow on southern Baffin Island, Arctic Canada. Science of the Total Environment. 2014 May 15 doi: 10.1016/j.scitotenv.2014.04.092. [Epub ahead of print].

Zhang, J.H., D.A. Lobb, Y. Li, G.C. Liu. 2004. Assessment of tillage translocation and tillage erosion on the steep land in hilly areas of Sichuan, China. Soil and Tillage Research 75(2): 99-107.

Zoltai, S.C., and C. Tarnocai. 1981. Some nonsorted patterned ground types in northern Canada. Arctic and Alpine Research 13(2): 139-151.

APPENDIX A

Protocol: Extraction of Meteoric ^{10}Be from Soils and Sediments

A.1. Introduction

The procedure described herein is a description of standard operating procedures that were utilized to test and validate a meteoric Beryllium-10 (^{10}Be) extraction procedure in the Department of Soil, Water and Climate at the University of Minnesota. This procedure is adapted from the University of Pennsylvania Cosmogenic Isotope Laboratory (CIL) Procedures (J. K. Willenbring, UPenn, written and personal communications 2013-2014), in turn developed from procedures from GFZ Helmholtz-Potsdam (F. von Blanckenburg, BeCook 11 (9-2009), von Blanckenburg et al., 1996). The preliminary draft of this protocol was co-written by N. Jelinski and M. Roser (3-2013). Subsequent and final drafts of this protocol were written solely by N. Jelinski (11-2014).

A.1.1 Relationship to other extraction protocols

This procedure was selected for its simplicity and ease of adaptation. Other procedures for isolating ^{10}Be include the potassium bifuoride fusion method (Stone, 1998, Balco, 2004), and yet other protocols that include a pre- chromatography precipitation step (von Blanckenburg et al., 1996) or single-step column (Chmiel, 2013).

In-situ ^{10}Be extractions from quartz require more extensive sample preparation including the isolation of quartz from samples and the full dissolution of the quartz in HF/HNO_3, along with a certified, dedicated clean room (Bookhagen, 2013). This protocol does not describe those procedures and focuses solely on the extraction of adsorbed *meteoric* ^{10}Be from soil and sediment samples.

A.1.2 Laboratory space and approximate time requirements

Due to the sensitivity to contamination of ^{10}Be measurements and the long period of time that samples must remain open to the laboratory atmosphere in this protocol, this procedure is best accomplished in a dedicated laboratory space to minimize dust and external contamination. If no dedicated space is available, this can be accomplished in a space with no other ongoing procedures as long as the space is thoroughly cleaned prior to use. Entry and exit from this laboratory space should include dust control mats (Table A.1), and all personnel working in the space should be required to wear disposable Tyvek labcoats (Table A.1) which do not leave the space and are exchanged on a regular basis to reduce import of external contaminants. In addition to these controls, Tyvek booties (Table A.1) over shoes can help eliminate external dust contamination. As a general rule, lab space should be cleaned before and after each ^{10}Be run.

If all steps run smoothly, this procedure takes 6 full, dedicated laboratory days (8-10 hours each) to process 8 samples, not including pre-processing and preparation time (often 1 day). If some samples need extra time, this timeframe may be extended to 7 or 8 days. However, this procedure is written under a best-case assumption and a typical timeline of 6 days (plus an extra pre-preparation day) is described here. The protocol is

divided into 6 “process groups”, each of which represents a typical day spent in the laboratory.

A.1.3 Be production and environmental chemistry overview

Beryllium is a monoisotopic (only a single stable nuclide) and mononuclidic (one significantly abundant natural radionuclide) element with z (atomic number) = 4, and A (mass number) = 9 with 5 neutrons. ^{9}Be is the only stable isotope, and of its radioisotopes, only ^{7}Be (t1/2 53 days) and ^{10}Be (t1/2 = 1.36 x10^{6} yrs) have half-lives greater than 1 minute. The expected stable nuclide ^{8}Be has a half-life of only 7 x 10^{-17} s is highly unstable due to it’s extreme disposition towards alpha decay (National Nuclear Data Center, 2011).

Beryllium-10 is a long-lived radioisotope of Beryllium (atomic mass 9) with a half-life of 1.39 x 10^{6} years (Dunai, 2009), which undergoes beta decay (100%) to its daughter isotope ^{10}B (National Nuclear Data Center, 2011). ^{10}Be is produced primarily in the atmosphere (*meteoric* ^{10}Be) when high-energy neutrons from cosmogenic radiation collide with molecular nitrogen and oxygen (Dunai, 2009), and secondarily in the lattices of crystalline minerals (*in-situ* ^{10}Be) via the same process. The spallation reactions that result from this collision break up the target nucleus, producing ^{10}Be and a number of other lighter particles (Willenbring and von Blanckenburg, 2010).

The production of ^{10}Be in the atmosphere depends primarily on 1) the strength of cosmic ray production, which varies in concert with metrics of solar activity and 2) the intensity of the earth’s geomagnetic field, which selectively blocks lower energy cosmic radiation (Lal and Peters, 1967, Willenbring and von Blankenburg, 2010). Because these factors vary predictably, global models of atmospheric ^{10}Be production have successfully reproduced these patterns (Field et al., 2006, Masarik and Beer, 2009). Atmospheric ^{10}Be is sorbed strongly onto aerosols and eventually falls out as both wet and dry deposition (Graham et al., 2003, Lal, 2007). The delivery rate of ^{10}Be to the Earth’s surface is therefore also a function of precipitation and dust deposition patterns (Heikkila et al., 2008). The ^{10}Be that falls out from the atmosphere (termed "meteoric" ^{10}Be) is preferentially sorbed onto the exchange sites of soil minerals (as Be^{2+} for pH values < 6 or as Beryllium hydroxide complexes at higher pH values) or organic materials (as a Be-humate complex in a large pH range between 3 - 10) (Takahashi et al., 1999). Meteoric ^{10}Be can be leached from soils under conditions of high acidity, however understanding of the environmental boundaries characterizing these conditions has improved significantly (Willenbring and von Blanckenburg, 2010). ^{10}Be retention by soil materials under most environmental conditions is high, and therefore due to its long half-life (~ 1.4 Ma), meteoric ^{10}Be accumulates in soils with increasing soil age (Graly, 2010, Willenbring and von Blanckenburg, 2010).

The divalent Be cation (Be^{2+}) in aqueous solution is principally in tetrahedral coordination with its waters of hydration and it can complex easily with a diverse range of ligands (Alderighi et al., 2000). ^{1}H and ^{17}O NMR studies have shown that below pH 3 Be is in tetrahedral coordination with four water molecules as $[Be(H_2O)_4]^{2+}$. This solvated cation, however, is only prominent in acidic conditions (pH 5.5 or less). Beryllium has a very high charge density (charge to atomic radius ratio) so hydrolyzes above a pH of 3. Beryllium hydroxides are therefore formed at higher pH values

($Be(OH)^{+}$, $Be(OH)_2$, $Be(OH)_3^{-}$, $Be(OH)_4^{2-}$, (Willenbring and von Blanckenburg, 2010). Complexing ligands (specifically organic acids) can significantly change the speciation across a wide range of pHs (Willenbring and von Blanckenburg, 2010). These Be-humate complexes are important for retention of ^{10}Be molecules and therefore organic phases must be destroyed for quantitative Be extractions from soil and sediment materials.

A.1.4 Process overview

The extraction and preparation process described here is comprised of 6 process groups (in addition to preparation of reagents and samples), which involve the (1) extraction of ions from the sample adsorbed phase and organic phases to solution, (2,3,4) selective removal of non-Be cations and purification of Be^{2+}, (5) precipitation of $Be(OH)_2$, and (6) flame oxidation to BeO and cathode packing for accelerator mass spectrometry (AMS) analysis. The theory and detailed procedures for each of these process groups are described in each section, below. Due to the complex nature of the process and a series of selective precipitation, sorption and elution steps, it is critical to understand where the Be is (what phase, or what solution fraction) at all times. Notes are added to procedural steps to facilitate this understanding and eliminate major mistakes.

Boron (^{10}B) is the major isobar of ^{10}Be in mass spectrometric analyses, therefore, B must be practically eliminated from every step of this procedure. The major pathway of B contamination in this protocol is through laboratory water as up to 5L of water may be used as a reagent and in the preparation of acids (Table A.2). For this reason, lowering B in laboratory water below analytically detectable limits is a critical component of success. This has been accomplished in the Department of Soil, Water and Climate through the use of a MilliQ Gradient with a Q-GARD Boron cartridge and water input from a MilliQ Elix 5 (water input from facility distilled lines). The resulting high quality water has been proven for use in ^{10}Be extraction procedures through resulting process blanks (Section 10, Table A.4). Validated low-Boron or Boron-free water sources are specifically referred to as $BfddH_2O$ and should not be mixed or substituted with unvalidated water sources (regardless of perceived purity) under any circumstances. Reagent containers that have held unvalidated water sources should not be used for $BfddH_2O$ unless they have been acid-washed.

A.2. Process group 0 – sample and reagent preparation (Day 0)

General concepts. This protocol is designed to run samples in batches of 8 (7 samples + 1 blank). The main reasons for this are: 1) there are 8 spots for columns on each carousel for the ion chromatography step and 2) given existing hotplate capacity, 8-sample runs are about the maximum possible without compromising space which may lead to higher potential for cross-sample contamination.

A large number of acids (and a few other reagents) of differing concentrations must be prepared to execute the entire procedure. Preparing them prior to beginning the extraction protocol allows full concentration to be given to reagent preparation or protocol execution, and is highly recommended. Two of these acids 1.000 M HNO3 and 0.500 M HNO3 must be titrated to within 3 decimal places.

A well homogenized subsample of at least 50 g of the original material should be mixed and dried overnight at 105° C. Homogenization is critical because component

phases of soil and sediment (as well as varying grain sizes – Wittman et al., 2012) can contain different concentrations of ^{10}Be (Balco, 2004).

Notes. Table A.2 details standard amounts of reagents necessary for a single run of 8. This is expanded to 10 samples in order to ensure that enough reagent is available if necessary. Suggested total amounts of mixed acids to be prepared (usually 1L) are also detailed in Table A.2. Adjust volumes according to final desired end volume. Each reagent should have a PFA stock container and a PFA working container in order to keep the stock clean. PFA containers should be color coded with lab tape according to reagent and clearly labeled with concentration/date/preparer's initials: RED = HF, YELLOW = HNO_3, ORANGE = HCl, GREEN = Oxalic, PINK = H_2O_2, BLUE = BfddH_2O, PURPLE = 1:1 NH_4OH:H_2O.

Titration procedure: Titrations should use phenolphthalein as an indicator. If standardized 1.000 M NaOH is available, then nominal 1M HNO3 should be titrated to standardized NaOH. If standardized NaOH is not available, a standardized solution of 1.000 M Oxalic acid should be prepared using oxalic acid dihydrate pellets (cannot prepare a standardized NaOH solution using NaOH pellets because of strong adsorption of moisture from the air), which should be used as a titrant to prepare and adjust a 1.000M NaOH solution as a standard to use for subsequent HNO_3 titration. Titration procedures are detailed in Section 11.

Soil and sediment samples should be oven dried (95° C) after field collection to facilitate preparation for grinding. These samples, depending upon the material, should be hand pulverized and ground to pass a 2mm (#10 U.S. sieve), or ground to analytical fineness (500 um, #35 U.S. sieve). However, grinding to analytical fineness may: 1) influence the measurement of *in-situ* ^{10}Be along with *meteoric* ^{10}Be (remember for *meteoric*, we just want the adsorbed ^{10}Be on the surface, not the ^{10}Be contained in the mineral lattices, although *in-situ* concentrations are generally 2-3 orders of magnitude lower) and 2) increase the difficulties encountered with initial sample loading into PFA vials due to static and sediment removal centrifugation steps. For these reasons, hand pulverization of oven-dried samples and sieving to pass a 2mm sieve is the appropriate sample pre-preparation used for this protocol.

A.2.1 Materials and time requirements

Materials. PFA Containers for stock and working solutions for each reagent (acid washed), graduated cylinders (acid washed), volumetric flasks (acid washed), concentrated analytical grade reagents (Table A.1), titration burettes, ring stand, clamps, phenolphthalein, 50ml beakers, pipettors.

Time requirements. 5-6 hours.

A.2.2 Procedural Steps

1. Prepare reagents according to Table A.1. Titrating instructions in Section 11.
2. Dry 50g of well homogenized sample material (hand pulverized to pass a 2mm sieve) overnight at 105° C. Place in dessicator until ready to weigh.

A.3. Process group 1 – extraction of adsorbed ions/ amorphous iron by HCl leach and removal of organics (Day 1).

General Concepts. In this process group, adsorbed ions are removed from mineral surfaces and organic matter via a strong acid leach (6M HCl) followed by destruction of organic phases by H_2O_2. The 6M HCl leach also dissolves iron oxyhydroxide coatings, bringing significant amounts of Fe into solution (Wagai and Mayer et al., 2007; Deshpande et al., 1968). The predominant exchange phase ions that are likely to be contained in this leach (and thus the major ions of concern in the Be extraction and purification procedure) are Ca, Mg, Na, K, Fe, Al, and Si (Table A.3). Beryllium, while normally at very low levels on the exchange phase and as a elemental constituent of soils (Lively and Thorleifson, 2009, Table A.3), is boosted by 2-3 orders of magnitude with the addition of a Be "spike" or carrier during this process group. The purpose of the carrier is to bring Be to concentrations of similar magnitude as the other major ions as well as the ability to visualize the $Be(OH)_2$ precipitate and achieve mg final yields of BeO powder. Without the carrier, low amounts of native Be would make extraction by the chemical method, quality assurance through visualization, and AMS cathode packing impossible.

Notes. An important assumption in this process is that there is minimal native ^{9}Be adsorbed to mineral grains (Table A.3). This assumption can be checked by an HCl leach where the ^{9}Be carrier is not added and native exchange phase ^{9}Be is measured via inductively coupled plasma-mass spectrometry (ICP-MS). The second major assumption is that sorbed meteoric ^{10}Be is fully and completely desorbed and mixed with the ^{9}Be carrier in the extraction solution (AMS measures ratios of $^{10}Be/^{9}Be$, not absolute amounts). The advantage of measuring ratios is that if assumptions are met, final yield should have little effect on the measured ratio (although it can have an effect on analytical uncertainties).

Due to the difficulty in completely destroying the organic phase from samples high in organic matter (> 8% organic carbon) with H_2O_2 at normal temperatures and pressures, a microwave digest (modified Miller Digest) is recommended for these samples. A modified Miller Digest used by the University of Minnesota Research Analytical Labortatory (Ref. No. 59) has been successfully utilized. In this case, samples should be weighed and spiked with ^{9}Be carrier as described below, but instead of an HCl leach, samples are pre-digested for 60 min with 2ml H_2O_2 and 0.5 ml trace conc HNO_3, then digested in the microwave at 100° C for 8 min followed by 195° C for 12 min. Start at step 14 (below) with these samples.

A.3.1 Materials and time requirements

Materials.10ml PFA containers, Steadler Lumocolor PFA pen, analytical balance, pipettors, SPEX Be standard, 3M HCl, H_2O_2, 6M HCl, hotplate, 15ml Falcon tubes, soil spatula, BfddH_2O, centrifuge, Kim Wipes.

Time requirements. 8-10 hours.

A.3.2 Procedural Steps

Weighing and spiking samples:

1. Label 10 ml Teflon containers with sample names using Steadler Lumocolor permanent markers *(Special – Art. Nr. 319 F-9 – these are the only markers that will reliably write on PFA and withstand the entire process)*.

2. Tare Teflon container *(Note: don't use gloves, gloves will build up static in the Teflon containers*
3. Using analytical balance, add 0.5g of soil (weigh to 4 significant digits). *Make sure that it is a representative sample. Between 0.4800 - 0.5200 g is acceptable. If soil sticks to container sides or top (outside of container), wipe the sides off with a Kim wipe & Boron-free deionized water and re-weigh.*
4. Put container back on balance and record weight of sample to 4 decimal places.
5. Tare sample and container.
6. Set pipette to 250µL and pipette in beryllium standard (SPEX Certiprep Beryllium 2% HNO_3, 1000 mg L^{-1}) into the container with sample. *DO NOT pipette directly out of bottle, pour some standard into an acid washed PFA container and pipette out of that container. (Parafilm SPEX Be standard immediately after use and refrigerate)*
7. Record weight of SPEX Be standard to 4 decimal places.
8. Repeat steps 1 – 6 for each sample.
9. For blanks, only follow steps 5-6 (do not add soil).

Acid leach to remove adsorbed ions, iron oxyhydroxides and destruction of organic phase:

10. Add 3 mL of 3M HCl and 1ml of H_2O_2 to each sample.
11. Heat on hot plate with caps off at 100° C for 2 hrs or until < 1ml of HCl/H_2O_2 remains. (*Beware of violent reactions with carbonates or organic matter at this step – you may need to babysit samples for 30 min – 1 hr, taking them on and off the heat. Avoid reactions which leave significant amounts of material on the sides or cause material to be ejected from PFA container. Samples which contain > 8% organic matter should be considered for Microwave Digestion (see "Notes" section, above) – in this case, follow directions in "Notes" section above and start at step 14, below. Caps can be left on if necessary for violent reactions but enough evaporation/drying must occur so that HCl volume is not significant (> 1ml) when proceeding to step 12.*
12. Add 5mL of 6M HCl to each sample. Heat at 105° C on hot plate for no more than 4 hours with the caps on. *The containers should still have liquid in them*.
13. Turn off hot plate, and transfer solutions and sediment from Teflon containers into 15mL Falcon centrifuge tubes. It is important to get everything out, so use an acid-washed wash bottle with BfddH_2O to rinse out samples. If there is sediment stuck in the container, use a clean pipette tip to remove into the Falcon tube. *Make sure not to use more than 10mL deionized water to rinse PFA container or the sample will not fit in the centrifuge tube.*
14. Centrifuge tubes for 5 minutes at 3200 rpm.
15. Completely wipe out each Teflon container using BfddH_2O and a Kim wipe.
16. Pour supernatant from centrifuge tube back into Teflon containers. Get as much liquid as you can out, but make sure that no sediment comes out. (*Be and all other adsorbed ions are in the supernatant*).
17. OVERNIGHT: Place containers on hot plate and turn hot plate to setting 105° C for 7 hours to overnight. Leave the caps off of the containers. Samples should be

completely dry, with an ion crust at the bottom. (*Note: In this step – and the many other drying steps like it – a balance must be achieved between speed of drying (which influences total process time) and the ability to redissolve the ion crust in the subsequent step. Therefore, as a general rule, drying temperatures should be no greater and drying times no longer than necessary to remove all visual moisture while avoiding "baking" the ion pellet to the PFA container*).

A.4. Process group 2 – removal of Ca and Mg via precipitation as bifluorides (Day 2).

General Concepts. In this process group, large amounts of Ca (Table A.3) and Mg are removed by reaction with HF and precipitated as bifluorides. This process selectively precipitates Ca and Mg as fluorides because they are orders of magnitude less soluble in water (which is used to equilibrate the cake post-treatment) than the alkali metal fluorides (Na, K), Fe and Al fluorides, and Be bifluoride (Sharma, 2014, ILO-ICSC, Oxtoby, 2012, Haynes, 2014). This typically leaves a large white fluoride cake (when soils are calcareous), or a clear to white solid precipitate when the soils are non-calcareous. Cakes can be extensive in calcareous soils and may warrant two HF treatments. Residual organics become apparent in this step due to the strong contrast with the white fluoride cake and are removed with another round of H_2O_2 treatment. Finally, samples are equilibrated with BfddH_2O, releasing to solution any Fe, Al, Be, K, or Na fluorides that have formed.

Notes. HF is a highly dangerous reagent and should only be handled with proper training and personal protective equipment (PPE).

A.4.1 Materials and time requirements

Materials. Sodium bicarbonate, pipettors, HF PPE, calcium gluconate (HF antidote), hotplate, Analytical grade HF, H_2O_2, BfddH_2O, Kim wipes.

Time requirements. 8-10 hours.

A.4.2 Procedural Steps

Precipitating Ca/Mg and Residual Organics: part 1

1. Prepare a solution of ~ 25g sodium bicarbonate in 250mL water. This will be used to neutralize the pipettes used to transfer the hydrofluoric acid (HF).
2. Before starting to handle HF, read the SOP, put on the required PPE (Table A.1), and alert everyone in the room. Follow proper procedures for safely using HF under a hood.
3. CAREFULLY pour a small amount of HF into a labeled working container, and put original HF container back into storage cabinet. ALWAYS use secondary containment!
4. Pipette 1mL HF from working container into each Teflon container. Dispose of pipette tips into the solution of sodium bicarbonate, and change tips between each sample.

5. Gently swirl the containers to mix together HF and sample. To guard against spillage, swirl with container on a flat surface. If not mixing together, use a clean pipette tip to break up solids.
6. Turn on hot plate to setting 100° C. Samples should be allowed to dry down completely, but not "bake" to the PFA.

Removing residual organics
This step is necessary for samples which have darkened fluoride cakes (or dark rings in the cakes) resulting from residual organics.

7. Pour hydrogen peroxide (H_2O_2) into a labeled working container, and then parafilm and refrigerate H_2O_2 original container.
8. Turn on hot plate to setting < 80° C. Add 1mL H_2O_2 to each PFA container, and swirl containers to mix. If sample is high in organics, watch the sample very closely after adding the H_2O_2 as it could foam over. If needed, turn down heat. Use a pipette tip to mix if solids sticking together.
9. Heat containers with caps on until reaction stops.

Precipitating Ca/Mg and Residual Organics: part 2
This step is necessary for calcareous soils, due to the amount of Ca present in the soil sample.

10. Turn on hot plate to setting < 80° C.
11. Ensure that sodium bicarbonate is still on-hand to dispose of pipette tips. Before starting to handle HF, read the SOP, put on the required PPE (Section 12, Table A.1), and alert everyone in the room. Follow proper procedures for safely using HF under a hood.
12. Pipette 2mL of HF from working container into each Teflon container. Dispose of pipette tips into the solution of sodium bicarbonate, and change pipettes between each sample.
13. Gently swirl the containers to mix together HF and sample. To guard against spillage, swirl with container on a flat surface. If not mixing together, use a clean pipette tip to break up solids.
14. Turn hot plate up to setting 100° C. Samples should be allowed to dry down completely, but not "bake" to the PFA.
15. Check the color of the precipitate. If any are still dark, run them through the "Removing residual organics" again before moving on.

Equilibrating fluoride precipitates with water

16. Add 10mL BfddH_2O to all samples.
17. Let sit for 1 hour with gentle < 70° C heat
18. Transfer contents (solution and precipitates) of the Teflon containers into new 15mL Falcon centrifuge tubes.
19. Centrifuge tubes for 5 minutes at 3200 rpm.
20. Completely wipe out each PFA container using BfddH_2O and a Kim wipe.

21. Transfer supernatant from centrifuge tube back into PFA containers. Get as much liquid as you can out, but make sure that no precipitated material comes out (*Be and all other adsorbed ions are in the supernatant*).
22. OVERNIGHT: Place containers on hot plate and turn hot plate to setting 105° C for 7 hours to overnight. Leave the caps off of the containers. Samples should be dry, with an ion pellet at the bottom.

A.5. Process group 3 – removal of Fe via anion exchange (Day 3)

General Concepts. In this process group, the leachate with significantly reduced quantities of Ca/Mg is redissolved in 6M HCl and run through an anion exchange resin. In concentrated HCl, Fe forms tetrahedrally coordinated anionic complexes with chloride, which are readily sorbed to quaternary ammonium-type anion exchange resins (Nicholls, 1975, Dutra et al., 2005, Lee et al., 2003, Moore and Kraus, 1950, Brady et al., 1964). No other ions of concern exhibit this behavior; therefore, in this step the selective removal of Fe is accomplished by preferentially binding $FeCl^{-4}$ complexes to the anion exchange resin through several volumes of 6M HCl while all other cations are leached through. The resin is then cleaned and recharged by flushing with 0.3M HCl, which releases the Fe into a waste collection tube as neutral or positively charged chloride and hydroxide complexes.

Notes. Ion exchange resins must be loaded into columns (Table A.1) prior to procedure. The anion exchange resin used for this procedure is BIORAD AG 1-X8 (Quaternary Ammonium), 100-200 mesh, chloride form. This resin is lighter-colored (yellowish) compared to the cation resin (orangish) used in process group 4. Mix a resin slurry with several scoops of resin and BfddH_2O in a sterile or acid-washed container. Pipette ~ 3ml of the slurry into the column and let the water drain out and the resin settle. Continue to add resin slurry until final resin volume is at the 2 ml mark (above column filter) when drained of gravitational water. To store the columns for future use, fill with BfddH_2O and cap. Store in the refrigerator in an acid-washed Nalgene container.

In a clean lab, ion chromatography steps should be completed in a laminar flow hood. Because columns need to remain open for long periods of time in order to facilitate acid addition, a laminar flow hood provides an environment where no residual dust lands in the columns during the process. In this environment, resins can be regenerated and cleaned (and columns reused) with little concern for contamination. In the absence of a clean lab and laminar flow hood, this process can be completed on a lab bench or fume hood, provided only working solutions of acids are opened and columns/resins are disposed of following the procedure (one-time use).

A.5.1 Materials and time requirements

Materials. BIORAD AG 1-X8 (Quaternary Ammonium), 100-200 mesh, chloride form anion exchange resin, polymer columns with caps, 6M HCl, pipettors, hot plate, centrifuge, lazy susan column holders, 0.3M HCl, BfddH_2O, 15 ml Falcon centrifuge tubes, 50 ml plastic tubes (waste).

Time requirements. 4-6 hours.

A.5.2 Procedural steps

Removal of Fe via anion exchange columns

1. Add 2mL of 6M HCl to the samples in the PFA containers. Samples will look pale to dark yellow, depending on the iron content (dark = high content of iron).
2. Turn the hot plate to < 70° C and let the containers sit for an hour - overnight.
3. Transfer the dissolved portion to a centrifuge tube. *When transferring the liquid from the Teflon containers to the centrifuge tubes, first roll liquid around sides (being careful not to spill the liquid) to ensure all material is captured. If some material sticks to the bottom of the Teflon containers, add 1mL 6M HCl and use a pipette tip to score the surface. Add this to the centrifuge tube. Heating the samples slightly also helps dissolve any remaining precipitate and facilitates transfer into centrifuge tube.*
4. Centrifuge tubes for ~2 minutes at 3500 rpm. Wipe out PFA containers with fresh Kim wipe.
5. Use prepared anion exchange columns and set them up in the 2-tiered Lazy Susan with waste centrifuge tubes (50 ml) underneath. A box of Finntip 5mL pipette tips should be placed under the top tier of the Lazy Susan to raise the columns up (this height will be needed starting in step 7). Uncap anion columns and let water drop out into waste tubes.

6. Add 5 ml 0.3 M HCl *clean resin – discard this acid*
7. Add 5 ml 0.3 M HCl *clean resin – discard this acid*
8. Add 1 ml 6 M HCl *condition resin – discard this acid*
9. Add 5 ml 6 M HCl *condition resin – discard this acid*
10. Pour the contents of the 50 ml waste tubes into a waste container. Set back under the columns and add a new 15mL Falcon centrifuge tube (labeled with sample numbers) to catch the sample containing Be.
11. Add sample (3 ml) *collect Be into labeled tube (sol'n should be clear)*
12. Add 1 ml 6 M HCl *collect Be into labeled tube (sol'n should be clear)*
13. Add 5 ml 6 M HCl *collect Be into labeled tube (sol'n should be clear)*
14. Remove centrifuge tubes from beneath the anion columns, cap, and place in rack. These tubes contain the Be and other cations (Na, K, Al). Place 50ml waste containers back underneath columns.
15. Add 2 ml 0.3 M HCl *clean resin – discard this acid (yellow)*
16. Add 5 ml 0.3 M HCl *clean resin – discard this acid (yellow)*
17. Add 5 ml 0.3 M HCl *clean resin – discard this acid (yellow)*
18. Add 1-3 ml BfddH_2O *cap and store column as before*

19. Transfer solution in 15mL Falcon centrifuge tubes containing Be back to the PFA containers.
20. OVERNIGHT: Place containers on hot plate and turn hot plate to setting 105 C for 7 hours to overnight. Leave the caps off of the containers. Samples should be completely dry, with an ion crust at the bottom. *Beware of baking the sample too hard at this step because the initial part of the next process involves dissolving the sample in 0.4M oxalic acid, which is weak and will not do a good job if the*

sample is firmly pelletized. It is important to dry down completely here, but not at high temperatures for long periods.

A.6. Process group 4 - removal of Al/Na/K and final elution of Be via ion chromatography with a cation exchange resin (Day 4)

General Concepts. In this process group, the ion pellet is initially redissolved in 0.4M oxalic acid. At low pH (< 4.0) in oxalic acid, stable anionic oxalate complexes of Al form and pass through sulfionic cation exchange resins (Korkisch, 1989, Milacic, 2005, Zhu, 1998), while other cations remain in ionic form and are sorbed to the resin. This allows Al to be selectively removed from other cations with several volumes of oxalic acid through a cation exchange resin. Subsequently, Na and K are selectively eluted with 0.5 M HNO3, while Be is selectively eluted with 1M HNO_3, relying on principles of ion chromatography and empirically determined equilibrium distribution coefficients and selectivity scales for cations on sulfonated cation exchange resins in HNO_3 (Strelow, 1960, Strelow et al., 1965). The final elution of high-purity Be is captured.

Note. Because the last portion of this process group relies upon ion chromatographic principles to separate Na and K from Be, it is absolutely critical that the acids used (0.500M HNO3 and 1.00M HNO3) are accurately titrated as described in preparation procedures (Section 11). Untitrated HNO_3 in this step risks complete loss or incomplete elution of Be. Because of the complexity involved in the chromatographic separation of these elements in this process group, all eluents are labeled and saved. In the event that a precipitate is not observed in the next process group, it is possible to analyze the eluents via ICP-MS and recover Be by re-running this procedure on the fraction containing Be.

Ion exchange resins must be loaded into columns prior to procedure. The cation exchange resin used for this procedure is BIORAD 50W-X8 (Sulfonic Acid), 200-400 mesh, hydrogen form. This resin is darker-colored (orangeish) compared to the anion resin (yellowish) used in process group 3. Mix a resin slurry with several scoops of resin and BfddH_2O in a sterile or acid-washed container. Pipette ~ 2ml of the slurry into the column and let the water drain out and the resin settle. Continue to add resin slurry until final resin volume is at the 1 ml mark (above column filter) when drained of gravitational water. To store the columns for future use, fill with BfddH_2O and cap. Store in the refrigerator in an acid-washed Nalgene container.

Selective ion chromatography with exchange resins is dependent upon numerous factors, including solvent concentrations, resin mesh size, ion/exchange site ratio, and volumes passed (Helfferich, 1962). The size of cation exchange resin optimized for this process is 2x smaller than the anion exchange resin utilized in process group 3, significantly increasing the time for solvent filtration through the columns. Therefore, each sample is split into 2 columns, each containing 1ml of resin.

A.6.1 Materials and time requirements

Materials. 0.4M Oxalic acid, 15ml Falcon centrifuge tubes, 50ml tubes (waste), columns with 1ml cation exchange resin (2 per sample), hotplate, centrifuge, pipettors, BfddH_2O, 5M HNO_3, 1M HNO_3, 0.5MHNO_3.

Time requirements. 8-10 hours.

A.6.2 Procedural steps

Removal of Al, Na and K and selective elution of Be via Cation Columns

1. Add 2mL 0.4M oxalic acid to each sample in PFA containers.
2. Turn on hot plate and set to 70° C for 1-2 hours to overnight to dissolve the crust in the oxalic acid. *Note – the longer you can afford to let this dissolve, the higher your yields will be*.
3. For each sample, label (A) 1 clean 15ml Falcon centrifuge tube "Sample xx", (B) 2 clean tubes "Sample xx – Ox", (C) 2 clean tubes "Sample xx – Nit", (D) 2 clean tubes "Sample xx – Be sample", and (E) 1 clean tube "Sample xx – Be ICP". This gives you a total of 8 tubes per sample. Store in racks that are close at hand.
4. Once the ion pellet is dissolved (*note – there may be some recalcitrant oxalates (white-clear) that form, particularly in Ca-rich samples. That is okay…press on*), transfer each sample from the Teflon containers into a clean Falcon centrifuge tube labeled with sample name (A). When transferring the liquid from the Teflon containers to the centrifuge tubes, first roll liquid around sides (being careful not to spill the liquid) to ensure all material is captured. Use a pipette tip and 1mL 0.4M oxalic acid to capture any material stuck to container. It helps to have samples over gentle heat (70° C) to facilitate full dissolution and removal. There are now 3 ml of 0.4M oxalic acid containing the dissolved ion pellet in tube A.
5. Centrifuge tubes for 5min at 3000 rpm. Wipe out PFA containers with fresh Kim wipe and BfddH_2O.
6. Set up prepared cation columns in the 2-tiered Lazy Susan with waste centrifuge tubes underneath. A box of Finntip 5mL pipette tips should be placed under the top tier of the Lazy Susan to raise the columns up (this height will be needed later). *Note – you will be splitting each sample into 2 columns, so a run of 8 samples requires 16 columns*.
7. Uncap cation columns and let water drain out into 50 ml waste centrifuge tubes.

8.	Add 1 ml	5M HNO3	clean resin-discard this acid
9.	Add 5 ml	5M HNO3	clean resin-discard this acid
10.	Add 1 ml	BfddH2O	remove HNO3 from resin – discard
11.	Add 4 ml	BfddH2O	remove HNO3 from resin – discard
12.	Add 1 ml	0.4M Oxalic	condition resin – discard this acid
13.	Add 4 ml	0.4M Oxalic	condition resin – discard this acid

14. Pour contents of waste tubes into a waste container. Set back under columns and place 15mL Falcon tubes labeled "Sample xx – Ox" (B).
15. Each centrifuged sample should have ~3mL of supernatant. Pipette 3mL of each sample's supernatant into 2 columns, 1.5mL into each, which are above its "Sample xx – Ox" (B) 15 ml centrifuge tube (remember, each sample should have 2 of these). Let drain.
16. Add 1mL 0.4M Oxalic collect in Ox. Tube (B) (contains the Al from the sample)

17. Add 5mL 0.4M Oxalic collect in Ox. Tube (B) (contains the Al from the sample)
18. Add 6mL 0.4M Oxalic collect in Ox. Tube (B) (contains the Al from the sample)
19. Remove and cap the "Sample xx – Ox" (B) tubes and set in rack. These should contain the Al from the samples.
20. Put the "Sample xx – Nit" (C) tubes into the waste tubes under the corresponding columns.
21. Add 1ml BfddH2O remove oxalic acid from column into Nit tube (C)
22. Add 2ml BfddH2O remove oxalic acid from column into Nit tube (C)
23. Add 6ml 0.5M HNO3 elute Na/K into Nit tube (C)
24. Remove and cap the "Sample xx – Nit" (C) tubes and set in rack. These should contain the Na and K from the samples.
25. Put the "Sample xx –Be sample" (D) tubes into the waste tubes under the corresponding columns.
26. Add 1ml 1M HNO3 collect Be in 'Be sample' tube (D)
27. Add 6 ml 1M HNO3 collect Be in 'Be sample' tube (D)
28. Add 4 ml 1M HNO3 collect Be in 'Be sample' tube (D)
29. Cap the "Sample xx – Be sample" (D) tubes and set in rack. These should contain the beryllium from the samples.
30. For each sample, pipette 110µL from each "Sample xx – Be sample" (D) tube into the corresponding one "Sample xx – Be ICP" (E); bring up to 10ml with 0.3 M HNO3 for possible OES measurement to check sample's final purity.
31. Set aside all centrifuge tubes and place 50ml waste tube under each column.
32. Add 4 ml 5M HNO3 clean resin – discard this acid
33. Add 6 ml 5M HNO3 clean resin – discard this acid
34. Add 6 ml BfddH2O clean resin – discard

35. OVERNIGHT: Transfer liquid from one of the "Sample xx – Be sample" (D) tubes for each sample into corresponding PFA containers. Evaporate at setting 100° C for 8 hours – overnight. Check frequently to ensure you don't dry down or "bake" the remaining cation pellet – ideally, there should be a very small drop of liquid left when you proceed to step 36.
36. Pour second "Sample xx – Be sample" (D) tube into the PFA container and redissolve Be ion pellet (or just add to remaining drop of liquid). Let it sit for ~ 1-2 hours at > 70° C with the cap on. Transfer back into "Sample xx – Be sample" (D) centrifuge tube.

A.7. Process group 5 – precipitation of $Be(OH)_2$ (Day 5)

General Concepts. In this process group, Be is precipitated from solution as $Be(OH)_2$ by raising the pH to ~ 10 with 1:1 Superpure NH_4OH/BfddH_2O. The current solution pH is ~ 1M HNO_3 with pH < 1 – and almost all of the Be in solution exists as a hydrated ion (Be^{2+}). Raising the pH to ~ 9 results in precipitation of the insoluble hydroxide, $Be(OH)_2$. NH_4OH is used as the base in this titration because the cation impurity can be evaporated from the sample during drying (NH^{4+} (aq) – NH_3 (g)).

Notes. This titration is accomplished most rapidly by smell and visualization. Titration can be accomplished with pH strips, but this requires inserting foreign materials into the sample and/or removing sample volume. In this author's opinion, single pH measurements should be reserved only for samples that are not precipitating in order to judge whether there has been a process error (i.e. no Be precipitate) or whether the titration endpoint has not yet been reached. The blank is done first to gauge the approximate number of drops (at ~ 0.5ml/drop) that are needed to achieve the titration endpoint. Typically a total of 40-80 drops is required, but this can vary depending on the specific conditions of the sample batch.

When titrating the blank, shaking and centrifuging after every 5-10 drops (once 30 drops is reached) will allow the most accurate results and purest yield (extremely high pH values result in the precipitation of remaining impurities with Be, so this is avoided if possible). Essentially, one is looking for the exact point when the smell changes from dull/sweet – predominance of HNO_3 to ammoniac/sour – predominance of NH_4OH. Visually, this coincides with the formation of fizz or bubbles upon shaking. Note: after adding NH_4OH and shaking, uncap and wait ~ 3 seconds before wafting to smell as ammonia offgassing can be very strong. The blank usually requires fewer drops than the samples, so if a precipitate is formed on the blank but not on the samples, continue titrating.

The $Be(OH)_2$ precipitate looks almost "ghosty" or translucent. Impurities manifest themselves as a whiter appearance (Al) or a yellower appearance (Fe). Unless precipitate is extremely dirty, continue processing the sample, as at meteoric concentrations, small amounts of impurities will not affect the final uncertainty.

The importance of using Superpure NH_4OH is that any additions to the sample at this process stage contribute directly to the end impurities; therefore, it is critical that only the highest purity NH_4OH and BfddH_2O is utilized.

Beryllium is dried in either B-free quartz vials, or acid washed/etched quartz vials. B-free quartz is currently extremely expensive, so this process utilizes low-B quartz vials (Table A.1) that have been acid washed/etched. For meteoric concentrations, there is no apparent B isobar signal from the vials. To wash vials, boil them for 24 hours at 110° C in trace grade concentrated HNO_3 in an acid washed PFA jar, followed by boiling at 110° C in BfddH_2O for 24 hours and 3x rinse in BfddH_2O prior to drying. Place on Kim wipes covered by Kim wipes to dry and transfer to a clean plastic bag or acid-washed PFA jar.

A.7.1 Materials and time requirements

Materials. 1:1 ddH2O/Superpure NH_4OH, eyedropper, BfddH_2O, centrifuge, low-Boron quartz vials w/ caps (etched/acid washed), dry block, hotplate.

Time requirements. 3-4 hours.

A.7.2 Procedural Steps

$Be(OH)_2$ precipitation

1. Add 1:1 ddH2O/Superpure NH4OH drop by drop until ~ 30 drops (looking for smell to go from "sweet" to "sour"). Shake vigorously.

2. Do the blank first and then use the blank as a general base for how many to add to the samples.
3. After 30-40 drops, add 5-10 drops, shake, then centrifuge for 1 min at 3600 rpm to see if you get a precipitate. Keep repeating until get a precipitate or if sample continues to smell sweet. Once a good precipitate is formed, move on.
4. Shake vigorously.
5. Centrifuge at 5 min, 3600 rpm.
6. Decant supernate – pour until bead sticks to precip in centrifuge tube.
7. Add 3 ml of BfddH2O and 1-2 drops of 1:1 NH4OH
8. Shake vigorously.
9. Repeat Centrifugation.
10. Decant.
11. Add 4 ml BfddH2O and 1-2 drops of 1:1 NH4OH.
12. Shake Vigorously
13. Repeat centrifugation.
14. Decant and leave small drop at bottom of tube with precipitate. Precipitate should look "ghosty". Whiter = Al contamination and Yellower = Fe contamination.
15. Pipette precipitate (fully mix precipitate with remaining liquid) and liquid into quartz vial (already cleaned and acid washed – to acid wash, boil overnight in 6M HNO3, then 3x wash with ddH2O).
16. OVERNIGHT: Dry down in dry block overnight to 3 days at 80° C.

A.8. Process group 6 - flame oxidation/dehydroxylation and sample packing (Day 6)

General concepts. Beryllium oxide (BeO) is the target material for AMS measurement of Be, so the $Be(OH)_2$ precipitate must be flame oxidized (1000° C) to BeO before packing into cathode holders for AMS analysis. Packing for AMS analysis at Purdue's PRIME Lab utilizes high-purity Niobium (Nb) powder as a binding agent (Nb also increases the current during AMS analysis for PRIME Lab in particular – other labs use different metals).

Notes: The Nb powder used as a binding agent and AMS current booster must also be super-pure analytical grade (Table A.1).

DANGER: The BeO powder produced by the flame oxidation process is toxic and proper PPE and exposure controls must be followed. Although the ~ 1mg amounts of BeO generated in this process are below OSHA exposure limits if released into the laboratory atmosphere, all potential routes of exposure and laboratory contamination should be eliminated. Therefore, a HEPA respirator (Table A.1) should be worn during this process group, and samples should only be uncapped when: 1) flame oxidizing in the fume hood or 2) packing in the glove box. This eliminates the potential for the release of BeO powder into the lab atmosphere. All solid waste from packing in the glove box (Kim Wipes, etc.) should be separately bagged as potential BeO contaminated waste inside the glove box. The glove box should be thoroughly cleaned after each use in the fume hood with 0.1 M HNO_3 and $BfddH_2O$, which will react with any small amounts of residual BeO powder and convert to aqueous Be^{2+} or $Be(OH)_2$.

A.8.1. Materials and time requirements

Materials. MSR Campstove, Pt-tipped tongs, EtOH, tweezers, microspatula, Niobium powder, hammer, packing rods, target press, empty cathode holders, glove box, Kim wipes.

Time requirements. 4-5 hours.

A.8.2 Procedural steps

Flame oxidation

1. Remove everything from hood except for the hot plate and dry block with samples in it.
2. Turn the hot plate off. Let the block cool so it is safe to touch, and take it off the hot plate. Cover samples with their caps. Remove the hot plate from the hood.
3. Set up MSR WhisperLite camp stove in the hood.
4. Light stove. Hold platinum tongs in the flame to burn off any impurities. Clean Pt tongs with EtOH.
5. Using the platinum tongs, carefully hold one sample outside blue flame for 1 min. This allows the sample to heat up and drive off moisture so it doesn't "pop" and jump out of the vial.
6. Hold sample inside blue flame until parts of the sample are glowing red (these are the impurities, so different samples will have more or less).
7. Let sample slightly cool, and set back in block and cap.
8. Repeat steps 5-7 for all samples.

Cathode holder packing

9. Set up portable glove box. Make sure that it is clean and that it can be sealed shut.
10. Place the following items in the glove box
    - Kim wipes
    - Ethanol (in drop bottle)
    - Tweezers*
    - 2 micro spatulas*, labeled with different colored tapes (1 for samples, 1 for Niobium powder)
    - Hammer*
    - Target press*
    - Dry block with sample vials, with caps on
    - Niobium powder – working aliquot
    - Rods for packing cathodes*
    - Cathode holders from PRIME
    - Plastic bags for solid waste contaminated with BeO.

      *if these items are not new, rinse them 3x with Boron-free deionized water and then once with ethanol before placing in box
11. Record the number of the cathode with the corresponding sample that will go in it in the Meteoric 10Be Template (see spreadsheet 1). Label the outside of the plastic cathode sleeves with the corresponding cathode number.
12. Place desired cathode in the target press.

13. With designated micro spatula, scrape quartz vials in an effort to consolidate all of the BeO. It might be helpful to first scrape the ring of BeO down to the bottom of the vial, and then scrape bottom.
14. After all BeO is scraped down, add a ratio of 1:1 to 2:1 Niobium powder to BeO. This will be an estimate from the amount of BeO visible in the vial. When adding the Niobium powder, make sure to use the micro spatula designated for Niobium powder.
15. Scrape together the Niobium powder and BeO in the vial using the micro spatula designated for samples.
16. CAREFULLY tap contents of quartz vial into cathode, making sure not to overfill the conical depression.
17. Using a rod, push down the Niobium/BeO dust into the cathode opening. Then, with the rod centered over the opening, give the rod taps with a hammer to pack the dust into the cathode. Repeat these steps until the cathode is filled.
18. Put cathode in designated plastic tube with the opening FACING DOWN. Pack a Kim Wipe in the top to avoid shaking and loss of material during shipment.
19. Repeat steps 13-19 for each sample.
20. Samples can be shipped for AMS analysis.

A.9. Calculating ^{10}Be concentrations of samples from AMS results

^{10}Be concentrations (atoms g^{-1}) are calculated using observed ^{10}Be/^{9}Be ratios from AMS, ^{9}Be carrier mass, and sample mass:

$$^{10}Be\ (atoms\ g^{-1}) = \frac{^{9}Be_{carrier}(g)\left(\frac{^{10}Be}{^{9}Be}(sample) - \frac{^{10}Be}{^{9}Be}(blank_{ave})\right)N_A(atoms\ mol^{-1})}{M_{^{10}Be}(g\ mol^{-1}) * m_{sample}(g)} \quad (1)$$

Where $^{9}Be_{carrier}$(g) is the total amount of Be carrier added to the sample, ^{10}Be/^{9}Be(sample) and ^{10}Be/^{9}Be(blank$_{ave}$) are the ^{10}Be/^{9}Be ratios of the sample and of all blanks (averaged), N_A is Avogadro's number, M_{10Be} is the molar mass of ^{10}Be, and m_{sample} is the amount of sample added.

Key assumption: This calculation assumes that native adsorbed exchange phase ^{9}Be is negligible. In many soils systems, this is a reasonable assumption. Assumptions can be checked by doing a 6M HCl acid leach with no ^{9}Be carrier spike (Process Group 1) and analyzing for total Be via ICP-MS.

A.10. Process validation – cross-laboratory comparisons and blank ratios

AMS results for 11 process blanks and 2 cross-laboratory comparisons are presented in Table A.4. Due to the expensive and time-consuming nature of ^{10}Be extraction and analysis, extensive cross-laboratory testing is not feasible, however 2 soil samples from Cyrus, MN (subsoil and topsoil) were run both at UMN and at the University of Pennsylvania's CIL.

Results from process blanks show consistently low ^{10}Be/^{9}Be ratios (Range: 8 – 332), with a single outlier blank with a ratio of 332. This high blank is likely due to

contamination from high ^{10}Be organic samples that were run concurrently (with violent H_2O_2 reactions, resulting in the ejection of material), however meteoric ^{10}Be concentrations in the sample run were high enough that even this process blank was 1-2 orders of magnitude below measured concentrations. Including this outlier, UMN process blanks have an average ratio of 49 ± 95, while excluding this outlier, UMN blanks have an average ratio of 22 ± 16; consistently low enough for *meteoric* ^{10}Be but not *in-situ*. *In-situ* blanks should have ratios < 10. The reasonably low values of process blanks provide assurance that B levels in H_2O are low enough that analytical precision is not affected.

Cross-laboratory comparisons are within the 1-sigma analytical uncertainty range for the low level (~1 x 10^7 atoms g-1) Cyrus, MN subsoil and within the 2-sigma analytical uncertainty range for the higher level (~ 2 x 10^8 atoms g-1) Cyrus, MN topsoil. These are excellent cross-laboratory results however it appears that analytical uncertainties are ~ 1-3% higher in the UMN samples (4-5%) than the UPenn samples (1-3%). This is likely due to the fact that sample processing at UPenn takes place in a dedicated clean-laboratory, whereas sample processing at UMN takes place in a dedicated laboratory space, but not a certified clean lab.

Conclusions. Results of process blanks and cross-laboratory comparisons show excellent control of contamination and isobars at UMN. Typical blank ratios at PRIME and UPenn are 5-20 (infrequently to 400 with sample contamination), so UMN blanks are in an expected range for ^{10}Be processing laboratories. Cross-laboratory comparisons show agreement within 1 or 2 sigma analytical uncertainty, with slightly higher uncertainties from UMN process. Although these differences would preclude processing for *in-situ* ^{10}Be (~ 1 x 10^5 atoms g-1), they are negligible for the typical meteoric 10Be concentrations measured here (~ 1 x 10^7 – 1 x 10^9 atoms g^{-1}).

A.11. Detailed procedural notes – titration

General concepts. Titration involves the determination of the molarity of an unknown acid (or base) solution (the *analyte*) by using a known base (or acid) solution (the *titrant*). Briefly, for the purposes of this protocol, precise volumes of base (accurate to 0.005 ml) are added to a precise volume of acid containing 0.2% phenolphthalein indicator (which changes from colorless to pink at pH ~ 8.3) to the titration endpoint (indicator color change). The precise molarity of the analyte is determined and adjusted to the desired molarity. Titration is typically accomplished on a 1:10 dilution of stock solutions (25 ml of stock solution to 250ml total volume w/ ddH2O in a 250ml volumetric flask.

Notes. The end point should be reached as accurately as possible. Prior to reaching the endpoint, color flashes will be apparent, but can be "swirled" away. The endpoint is reached when the faintest color that cannot be swirled away is detected (often facilitated by using a white paper background).

For this procedure, a stock solution of 1.000M NaOH is utilized to determine the molarity of nominal 1M and 0.5M HNO3. These acids are then adjusted to 1.000M and 0.500M. If 1.000M NaOH stock solution is not available, a nominal 1M NaOH solution must be titrated and adjusted to 1.000M using a 1.000M oxalic acid (made by dissolving oxalic acid dihydrate ($H_2C_2O_4 \bullet 2H_2O$) pellets in ddH2O, using an analytical balance). A

1.000M NaOH stock solution cannot be made from pellets due to the strong absorption of atmospheric moisture by NaOH solids.

A.11.1 General procedural steps

1. Quantitatively dilute (10x) titrant and analyte aliquots using ddH2O and volumetric flasks (i.e. 25 ml of stock solution to 250ml total volume).
2. Clean two 10-mL titrating burets by first washing them with deionized water. Then, set up burets on stands with clamps and run deionized water completely through both burets **three times**, capturing waste water in beakers below the burets.
3. Prepare phenolphthalein indicator. If phenolphthalein is in solution, pour some into a drop bottle and move on to next step. If phenolphthalein is in powdered form, prepared a solution of 0.2% (0.2g/100mL), pour it into a drop bottle, and move on to next step.
4. Rinse one buret **three times** with the titrant solution. Drain the titrant solution through the tip of the buret each time, capturing the waste in a beaker. Making sure the stopcock is shut, fill the buret again with titrant solution.
5. Rinse the other buret **three times** with the analyte solution made. Drain analyte solution through the tip of the buret each time, capturing waste in a beaker. Making sure the stopcock is shut, fill the buret again with analyte solution.
6. On both burets, drain out solutions until meniscus is at least at 0mL mark. Record initial readings to 0.001 ml.
7. Remove waste beakers from beneath the burets and pour into designated waste container. Place a clean beaker under the acid buret and run about 4mL out of the buret. Make sure that liquid is not splashing out of beaker. Read the buret and record.
8. Put two to three drops on phenolphthalein indicator into the acid solution. There should be no color change at this point.
9. Move the beaker with acid solution and phenolphthalein under the buret with base solution. You will be looking for a color change in the liquid, so it might help to put a white sheet of paper under the beaker. Add base solution at a moderate rate until you see a flask of pink color in the beaker. At this point, slow the flow of sodium hydroxide solution to a flow of drop by drop. Swirl the beaker between drops; if the pink color dissipates with swirling then keep the stopcock open. Once the pink color persists with swirling, quickly shut off the stopcock. Keep swirling the beaker for 15 seconds; if the pink color dissipates, continuing adding base solution drop by drop. If the pink color persists after 15 seconds, this indicates that the acid and base are at equal molar amounts in the solution.
10. Record the final base solution level in the buret.
11. Calculate the mL used of the acid solution and base solution by subtracting the final reading from the initial reading. Using these volumes, calculate the actual molarity of titrant solution (taking into account molar conversions for di-protic acids if necessary).

12. Repeat 3 times and calculate the average molarity of the analyte stock solution.
13. Adjust analyte stock solution to desired molarity. Utilize titration calculation and stock solution spreadsheet (attached as an electronic .xls file to this dissertation document) to adjust correctly.

A.12. References

Alderighi, L., P. Gans, S. Midollini, A. Vacca. 2000. Aqueous solution chemistry of beryllium. Pp. 109-172 In Advances in Inorganic Chemistry Vol. 50. Elsevier Academic Publishers, Amsterdam, Netherlands.

Balco, G. 2004. Extraction of Beryllium-10 from soil by fusion. University of Washington.

Bookhagen, B. 2013. Chemical Separation of Al and Be from Quartz-bearing rocks, UC Santa Barbara.

Brady, G.W., M.B. Robin, J. Varimbi. 1964. The structure of ferric chloride in neutral and acid solutions. Inorganic Chemistry 3(8): 1168-1173.

Chao, T.T., and Liyi Zhpu. 1983. Extraction techniques for selective dissolution of amorphous iron oxides from soils and sediments. Soil Sci. Soc. Am. J. 47:225-232.

Deshpande, T.L., D.J. Greenland, J.P. Quirk. 1968. Changes in soil properties associated with the removal of iron and aluminum oxides. European Journal of Soil Science 19(1): 108-122.

Dunai, T. 2009. Cosmogenic Nuclides: Principles, Concepts and Applications in the Earth Surface Sciences. Cambridge University Press, Cambridge, UK.

Dutra, P.B., A. T. Toci, C.A.S. Riehl, C.R. Barbosa, F.M.B. Coutinho. 2005. Adsorption of some elements from hydrochloric acid by anion exchange. European Polymer Journal 41: 1943-1946.

Field, C.V., G.A. Schmidt, D. Koch, C. Salyk. 2006. Modeling production and climate-related impacts on 10Be concentration in ice cores. Journal of Geophysical Research 111: D15107.

Graham, I., R. Ditchburn, B. Barry. 2003. Atmospheric deposition of 7Be and 10Be in New Zealand rain (1996-98). Geochimica et Cosmochimica Acta 67: 361 - 373.

Haynes, W.M. (Ed. In-Chief). 2014. CRC Handbook of Chemistry and Physics. 95th Edition 2014-2015. CRC Press, Boca Raton, FL.

Heikkila, U., J. Beer, V. Afimov. 2008. Beryllium-10 and Beryllium-7 in precipitation in Dubendorf (440 m) and at Jungfraujoch (3580 m), Switzerland (1998-2005). Journal of Geophysical Research 113: D111

Helfferich, F. 1962. Ion Echange. McGraw-Hill Book Company, Inc. New York, NY.

Korkisch, J. 1989. Handbook of Ion Exchange Resins Vol 6. CRC Press, Boca Raton, FL.

Lal, D. 2007. Recycling of cosmogenic nuclides after their removal from the atmosphere; special case of appreciable transport of 10Be to polar regions by aeolian dust. Earth and Planetary Science Letters 264: 177 - 187.

Lal, D., B. Peters. 1967. Cosmis ray produced radioactivity on the Earth. In: Site, K. (Ed.) Handbuch der Physik. Springer-Verlag, New York, NY.

Lee, M.-S., J.-G. Ahn, Y.-J. Oh. 2003. Chemical model of the FeCl3-HCl-H2O Solutions at 25o C. Materials Transactions 44(5): 957-961.

Lively, R.S. and L.H. Thorleifson (2009), Minnesota Soil, Till, and Ground-Water Geochemical Data. Minnesota Geological Survey, Minneapolis, MN.

Masarik, J., J. Beer. 2009. An updated simulation of particle fluxes and cosmogenic nuclide production in the Earth's atmosphere. Journal of Geophysical Research 104: 12,099 - 12,111.

Milacic, R. 2005. Speciation of Aluminum in the Environment. Pp 7-19 (Section 2.2.1) In Cornelis, R. (Ed. In-Chief): Handbook of elemental speciation II: Species in the environment, food, medicine and occupational health. John Wiley and Sons, Hoboken, NJ, USA.

Moore, G.E., K.A. Kraus. 1950. Adsoprtion of iron by anion exchange resins from hydrochloric acid solutions. Journal of the American Chemical Society 72(12): 5792-5793.

National Nuclear Data Center. 2011. Chart of Nuclides. Brookhaven National Laboratory. www.nndc.bnl.gov/chart

Nicholls, D. 1975. The Chemistry of Iron, Cobalt and Nickel. Pergamon Texts in Inorganic Chemistry (Vol 24), Pergamon Press, Elmsford, NY.

Oxtoby, David W.; Gillis, H. Pat; Campion, Alan (2012). Principle of Modern Chemistry. Cengage Learning. p. 693. ISBN 9780840049315

Sadzawka, M.A.R., S. Aomine. 1977. Adsorption of silica in river waters by soils in central Chile. Soil Science and Plant Nutrition 23(3): 297-309.

Sharma, B. 2014a. Industrial Chemistry. Krishna Prakachan Media Ltd, Meerut, Utter Pradesh, India.

Sharma, B. 2014b. Objective Pre-engineering Chemistry. Krishna Prakachan Media Ltd, Meerut, Utter Pradesh, India.

Stone, J.O.H. (1998). A rapid fusion method for the extraction of Be-10 from soils and silicates. Geochimica et Cosmochimica Acta (Scientific comment) 62, 555-561.

von Blanckenburg, F., N.S. Belshaw, R.K. O'Nions. 1996. Separation of 9Be and cosmogenic 10Be from environmental materials and SIMS isotope dilution analysis. Chemical Geology 129: 93-99.

Wagai, R., L.M. Mayer. 2007. Sorptive stabilization of organic matter in soils by hydrous iron oxides. Geochimica et Cosmochimica Acta. 71(1): 25-35.

Willenbring, J.K., F. von Blanckenburg. 2010. Meteoric cosmogenic Beryllium-10 adsorbed to river sediment and soil: Applications for earth-surface dynamics. Earth-Science Reviews 98: 105-122.

Wittman, H. F. von Blanckenburg, J. Bouchez, N. Dannhaus, R. Naumann, M. Christl, J. Gaillardet. 2012. The dependence of meteoric 10Be concentrations on particle size in Amazon River bed sediment and the extraction of reactive 10Be/9Be ratios. Chemical Geology 318-319: 126-138.

Zhu, X.P. 1998. The role of citric, lactic and oxalic acids in aluminum mobilization from some Polish and Chinese agricultural soils. Pp. 297-312/Chapter 32 In: Pawlowski, L., M.A. Gonzales, M.R. Dudzinska, W.J. Lacy. Chemistry for the protection of the Environment 3: Environmental Science Research Volume 55. Proceedings of the 11th International Conference on Chemistry for Protection of the Environment, September 10-17, 1997, Cairo, Assuan and Luxor, Egypt. Plenum Press, NY, NY.

Item	Vendor	Catalog #	Notes
		PPE	
Nitrile gloves	Many	-	-
Tyvek laboratory coat	Fisher	0136110C	Size: Large, 30/case
Tyvek coveralls	Fisher	013614C	Size: Large, 25/case, elasticized wrist and ankles
Tyvek booties	Fisher	19813211	Height: 18", 100/case
Splash Apron	Fisher	01353A	Resin-coated, 36 x 27 in
Face shield	Fisher	S66730	-
Laboratory-grade eye protection	Many	-	-
Tyvek sleeves	Fisher	17988108	100/case
		Expendable Reagents and Materials	
HCl: Analytical Grade, Trace	Fisher	A508500	Trace metal grade
2.5% Calcium Gluconate	DEHS	-	HF antidote
HF: Analytical Grade, Trace	Sigma-Aldrich	339261-100ML	Trace metal grade
HNO3: Analytical Grade, Trace	Fisher	A509500	Trace metal grade
Oxalic acid dihydrate solid: Analytical Grade, Trace	Sigma-Aldrich	658537-25G	Trace metal grade
SPEX Beryllium Standard	Fisher	PLBE22Y	SPEX Certiprep Beryllium 2% HNO3, 1000 mg/L, #CLBE2-2Y
Ethanol	Many	-	190 Proof
Superpure NH4OH, Analytical grade, Trace	EMD Millipore	EM-AX1308-7	OmniTrace Ultra
Hydrogen Peroxide, Analytical grade, Trace	Sigma-Aldrich	95321-100ML	30%, Trace SELECT
1.000M NaOH Standard	-	-	-
BIORAD AG 1X8 100-200 mesh, chloride form (Anion)	Bio-Rad	140-1441	-
BIORAD 50W-X8 200-400 mesh, H form (Cation)	Bio-Rad	142-1451	-
Boron-free ddH_2O	-	-	-
Pipette tips (1ml)	-	-	-
Pipette tips (5ml)	-	-	-
Kim wipes	-	-	-

Ion exchange columns	Evergreen	208-3384-060	Medium filter (45-90um), 5" Polypropylene Chromatography Columns
Low-Boron quartz vials	United Silica Products	USP-11-0032	-
Low-Boron quartz caps	United Silica Products	?	-
Niobium powder, high purity analytical grade	Fisher	AA4051009	?
50 ml plastic centrifuge tubes (waste)	Fisher	S99412 (x2)	Self-standing, conical bottom
15 ml plastic centrifuge tubes	Falcon/Fisher	1495970C	BD falcon, in Styrofoam racks
Lab tape (multiple colors for acid labeling)	-	-	-
pH test strips	Fisher	14850111	pHydrion
Q-GARD Boron Carttridge	Fisher	QGARD00B1	
		Durable Items and Equipment	
Hot Plate	-	-	Picotrace?
PFA Containers	Savillex	Many sizes needed	
Acid neutralization carboy	-	-	-
Titrating burettes	-	-	-
Double burette clamp	-	-	-
Ring Stand	-	-	-
Pipettor (0.5-5ml)	-	-	-
Pipettor (100-1000ul)	-	-	-
Fume Hood	-	--	-
Laminar Flow Hood	-	--	-
Column Carousel (Spice Rack)	-	-	-
Glove Box	-	-	-
Target Press	-	-	-
Propane Stove	-	-	MSR-type
HEPA mask + Filter	Fisher	19999206	-
Pt-tipped tongs	-	-	-
Dry bath or dry block	Benchmark Scientific	Custom	11MM x 15MM height
Dropper bottles	Fisher	03402B	-

Microspatulas	-	-	-
Containment Trays	-	-	-

Table A.1. Necessary PPE, expendable reagents and materials and durable items and equipment for meteoric 10Be extraction protocol. Specific vendor and item suggestions are provided as a source reference and not as an endorsement.

Reagent	Amount needed for 10 samples (ml)	Amount of highest concentration needed to prepare (ml)	Total amount of highest concentration needed (ml)	Stock solution	Amount of stock (ml)	Amount of H2O (ml)	Total Amount (ml)
6M HCl	200	200	213.5	32% trace HCl (10.2 M)	588	412	1000
3M HCl	5	2.5	-	6M	100	100	200
0.3M HCl	220	11	-	6M	50	950	1000
H2O2	30	30	30	30%	50	0	50
HF	30	30	30	Trace conc	50	0	50
0.4M Oxalic Acid	370	370	370	Crystalline dehydrate (126.07g/M) or anhydrous (90.03 g/mol)	Dihydrate (50.43 g) Anhydrous (36.012 g)	1000	1000
5M HNO3	320	320	376	70% trace HNO3 (15.8 M)	316	684	1000
1M HNO3	220	44	-	5M	200	800	1000
0.5M HNO3	120	12	-	5M	100	900	1000
1:1 NH4OH BfddH2O	50	50	50	Superpure NH4OH	100	100	200
Boron-free ddH2O	480	480	480	Boron-free di	-	-	~ 5L

Table A.2. Reagent preparation guide.

Ion	Valence	ppm	References
Ca	2	14,500 (0 – 41,000)	Essington, 2003, Batjes, 1995
Mg	2	3500 (0 – 11,000)	Essington, 2003, Batjes, 1995
Na	1	800 (0 – 6,000)	Essington, 2003, Batjes, 1995
K	1	900 (0 – 2,700)	Essington, 2003, Batjes, 1995
Fe	2/3	10,000 (10,000 – 100,000)*	Chao and Zhpu, 1983; Deshpande et al., 1968; Wagai and Mayer, 2007
Al	3	2000 (0 – 8900)	Essington, 2003, Batjes, 1995
Si	4	20 (10 – 40)	Sadzawka and Aomine, 1997
Be (environmental)	2	< 1.5	Lively and Thorleifson, 2009
Be (spiked)	2	500	Calculations in this study.

Table A.3. Typical concentrations of exchange-phase ions in global soils.

Sample	Date	PRIME Lab AMS #	$^{10}Be/^{9}Be$	1-σ Uncertainty $^{10}Be/^{9}Be$	10Be atoms g^{-1}	1-σ Uncertainty ^{10}Be atoms g^{-1}
Process Blanks: UMN						
BLNK 1	01-May-13	201301270	9.6	1.8	-	-
BLNK 3	01-May-13	201301271	21	4	-	-
BLNK 1	05-Nov-13		20	2	-	-
BLNK 2	05-Nov-13		21	5	-	-
124620	11-May-14	201401407	9	1	-	-
124621	11-May-14	201401408	8	1	-	-
BLNK 1	26-Jan-14		332	71	-	-
BLNK 2	26-Jan-14		23	4	-	-
BLANK	03-Sep-14	201402528	20	2	-	-
124628	03-Oct-14	201402730	20	3	-	-
124634	03-Oct-14	201402731	65	7	-	-
Average	-	-	50 (22)	95 (16)	-	-
Cross-Laboratory Comparison UMN:UPenn CIL						
2H1024 – Cyrus, MN Subsoil: UMN	02-May-13	201301272	373	19	1.04×10^{7}	4.67×10^{5}
2H1024 – Cyrus, MN Subsoil: UPenn	21-Sep-12	201202822	361	12	1.07×10^{7}	3.15×10^{5}
2H3030 – Cyrus, MN Topsoil: UMN	01-May-13	201301273	7170	280	2.06×10^{8}	7.98×10^{6}
2H3030 – Cyrus, MN Topsoil: UPenn	21-Sep-12	201202819	6550	70	2.20×10^{8}	2.29×10^{6}

Table A.4. Process Blanks and Cross-Laboratory comparisons.

Page Left Intentionally Blank